

# Large scale physical model tests on the stability of geotextile tubes





# **Large scale physical model tests on the stability of geotextile tubes**

Ir. P. van Steeg  
Ing. E.W. Vastenburg





**Title**

Large scale physical model tests on the stability of geotextile tubes

**Client**

Deltares Kennis-MT

**Project**

1200162-000

**Pages**

54 (excl. appendices)

**Keywords**

Geotextile tube, Delta flume, large scale, stability, wave attack, coastal structure, geotextile.

**Summary**



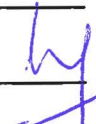
To test the stability of sand filled geotextile tubes under wave attack, tests were performed in the Delta Flume of Deltares on a scale of approximately 1:2 - 1:4. Wave conditions in the model varied up to 1.5 m significant wave height. Seven test series with different geometric conditions were tested. In four test series, single placed tubes with varying filling percentages and sizes were tested. One test series consisted of a single tube with a bar placed at the landward side to simulate a trench. Two other test series consisted of 2 tubes placed behind each other and a so-called 2-1 stack; two tubes placed behind each other with a third tube on top.

During all test series the normative failure mechanism was sliding, although some deformation occurred at the test series with lower filling percentages. The sliding mechanism is studied intensively resulting in a dimensionless stability parameter. This parameter includes the significant wave height ( $H_s$ ), the height ( $D$ ), width ( $B$ ) and relative density ( $\Delta$ ) of the geotextile tube, a reduction parameter to include wave energy transmission ( $\chi$ ), the slope angle of the foundation of the geotextile tube ( $\alpha$ ) and the friction coefficient between the geotextile and the foundation of the geotextile tube ( $f$ ).

Sand migration inside the geotextile tube may decrease its stability when the filling degree is less than approximately 70 %

**References**

Memo "Opdrachtverlening d.d. 5 maart 2009 van T. Minns namens MT-kennis aan MT Operationeel"

Version	Date	Author	Initials Review	Initials Approval	Initials
1	23-12-2009	Ir. P. van Steeg Ing. E.W. Vastenburg			
2	23-2-2010	Ir. P. van Steeg Ing. E.W. Vastenburg			

**State**

final



## Contents

<b>List of Tables</b>	<b>i</b>
<b>List of Figures</b>	<b>iii</b>
<b>List of Photographs</b>	<b>v</b>
<b>List of Symbols</b>	<b>vii</b>
<b>1 Introduction</b>	<b>1</b>
1.1 General	1
1.2 Objective	1
1.3 Outline	1
<b>2 Model set-up</b>	<b>3</b>
2.1 Test facility: the Delta Flume	3
2.2 Test set-up	3
2.2.1 General	3
2.2.2 Construction of a supporting structure	3
2.2.3 Construction of geotextile tubes	4
2.2.4 Geometrical configurations	8
2.3 Hydraulic conditions	12
2.4 Measurements	13
2.4.1 Wave measurements	13
2.4.2 Profile	13
2.4.3 Displacement with the use of camera techniques	17
2.4.4 Sand characteristics	18
2.4.5 Velocity measurements below the supporting structure	18
2.4.6 Sand migration indicated with colour injections	19
2.4.7 Stretches in geotextile	19
<b>3 Experiments and results</b>	<b>21</b>
3.1 Test series F4: single tube ( $R_{100\%} = 0.57$ m, $p_A = 109$ %)	21
3.2 Test series F1: single tube ( $R_{100\%} = 0.75$ m, $p_A = 66$ %)	22
3.3 Test series F3: single tube ( $R_{100\%} = 0.75$ m, $p_A = 80$ %)	23
3.4 Test series T1: single tube with trench ( $R_{100\%} = 0.76$ m, $p_A = 85$ %)	25
3.5 Test series P3: 2-1 stack	26
3.6 Test series P2: 2 tubes placed behind each other	28
3.7 Test series F5: single tube ( $R_{100\%} = 0.76$ m, $p_A = 72$ %)	29
<b>4 Analysis</b>	<b>33</b>
4.1 Introduction	33
4.2 Sliding instability	33
4.2.1 Introduction	33
4.2.2 Overview test results	34
4.2.3 Reduction factor for absorbing wave energy, $\chi$	34
4.2.4 Choice of stability parameter	36
4.2.5 Correction for the slope angle, $\alpha$ , and the friction, $f$	38

4.2.6	Influence location geotextile tube	40
4.2.7	Stability of test series P2 (2 tubes) and test series P3 (2-1 stack)	41
4.2.8	Conclusions on sliding stability	45
4.3	Erosion of fill through the geotextile skin	46
4.4	Deformation of the contained fill	46
4.5	Settlement	47
<b>5</b>	<b>Conclusions and recommendations</b>	<b>49</b>
5.1	Introduction	49
5.2	Stability of single placed tubes	50
5.3	Stability of multiple placed tubes	50
5.4	Overall conclusions with respect to stability	51
5.5	Deformation of the tubes	51
<b>6</b>	<b>References</b>	<b>53</b>

Appendices

**A Tables**

**B Figures**

**C Photos**

**D Description Delta Flume**

**E Analysis colour injections**

- E.1 Theory
- E.2 Measurements and analysis of colour injections
- E.3 Conclusions

**F Specification Geolon PE 180 L**

**G Theoretical derivation stability number with respect to sliding**

- G.1 Analytical model based on stability model of randomly placed rock mounds
  - G.1.1 Introduction
  - G.1.2 Definition of forces
  - G.1.3 Stability based on the drag force
  - G.1.4 Stability based on the drag and lift forces
  - G.1.5 Concluding stability formula
- G.2 Application of theoretical stability formula
  - G.2.1 Introduction
  - G.2.2 Description of relevant parameters
- G.3 Comparison of analytical model and practical application
  - G.3.1 Suggested stability parameter

**H Determination of friction coefficient**

- H.1 Introduction
- H.2 Theory of friction
- H.3 Small scale experiments to determine the friction coefficient

**I Transmission coefficient and Energy losses**

- I.1 Introduction
- I.2 Formula to determine ratio between effective and incoming wave height
- I.3 Graphic presentation of reduction parameter  $\chi$
- I.4 Restrictions for applying the graph



## List of Tables

### *In text*

Table 2.1	Overview of scaling aspects	7
Table 2.2	Summary of geometric specifications of test series F	9
Table 2.3	Geometric specifications of test series T	10
Table 2.4	Geometric specifications of test series P	11
Table 3.1	Overview of measurements related to test series F4	21
Table 3.2	Overview results test series F4	21
Table 3.3	Overview of measurements related to test series F1	22
Table 3.4	Overview results test series F1	23
Table 3.5	Overview of measurements related to test series F3	24
Table 3.6	Overview results test series F3	24
Table 3.7	Overview of measurements related to test series T1	25
Table 3.8	Overview results test series T1	26
Table 3.9	Overview of measurements related to test series P3	27
Table 3.10	Overview results test series P3	27
Table 3.11	Overview of measurements related to test series P2	28
Table 3.12	Overview results test series P2	29
Table 3.13	Overview of measurements related to test series F5	30
Table 3.14	Overview results test series F5	30
Table 5.1	Overview of the main dimensions of the tested configurations	49

### *In appendices*

Table A.1	Measured wave conditions
Table A.2	Measured height of individual tubes (D)
Table A.3	Measured width of individual tubes (B)
Table A.4	Measured exposed circumference of individual tubes (EC)
Table A.5	Measured dimensions of geotextile tube (x)
Table A.6	Measured dimensions of geotextile tube (y)
Table A.7	Measured dimensions of geotextile tube (w)
Table A.8	Measured dimensions of geotextile tube (z)
Table A.9	Derived dimensions of circumference (C)
Table A.10	Overview geometrical parameters of geotextile tubes
Table A.11	Overview relative deformation of geotextile tubes
Table A.12	Dimensions of empty geotextile tube
Table A.13	Overview filling percentages
Table A.14	Measured displacement of geotextile tubes
Table A.15	Unit weight and percentage water in ground samples
Table A.16	Colour injections
Table G.1	Overview stability formula for drag and lift forces with and without a slope
Table G.2	Overview of parameters that influence the stability of an element under wave attack
Table G.3	Overview of length-thickness ratio for several types of geotextile elements
Table H.1	Overview results small scale tests friction coefficient
Table I.1	Value of $\chi$ below a threshold value of $H_s/D$





## List of Figures

### *In text*

Figure 2.1	Impression of test set-up (not on scale)	4
Figure 2.2	Geometric specifications of test series F	9
Figure 2.3	Geometric specifications of test series T	10
Figure 2.4	Geometric specifications of test series P	11
Figure 2.5	Position of profile lines (top view)	14
Figure 2.6	Profiler runs and recognizable points	14
Figure 2.7	Overview of characteristic parameters of a geotextile tube	15
Figure 2.8	Example colour injection after a test series	19
Figure 4.1	Schematization of geometry that will be analysed for the mechanism sliding	33
Figure 4.2	Results as function of the significant wave height, $H_s$	34
Figure 4.3	Design curve to determine $\chi$ (assuming perpendicular wave attack and a water level equal to the top of the tube)	35
Figure 4.4	Results based on the dimensionless parameter $\chi H_s / (\Delta B)$	37
Figure 4.5	Results based on the dimensionless parameter $\chi H_s / \sqrt{(\Delta B D)}$	38
Figure 4.6	Determination of $\alpha$	39
Figure 4.7	Results based on the dimensionless parameter $\chi H_s / (\Delta \sqrt{(B D)} (f \cos \alpha + \sin \alpha))$	39
Figure 4.8	Results based on the dimensionless parameter $\chi H_s / (\Delta \sqrt{(B D)} (f \cos \alpha + \sin \alpha))$ and the dimensionless parameter $\Delta x_{avg} / B_{avg}$	40
Figure 4.9	Schematized geotextile tube and foreshore	40
Figure 4.10	Schematisation of test series P2	41
Figure 4.11	Schematization of test series P3 (tube C)	43
Figure 4.12	Schematization of test series P3 (tube B)	44
Figure 4.13	Stability calculation 2-1 stack	45
Figure 4.14	The Froude scaling law and the importance of sand transport within the geotextile element according to Venis (1968)	47
Figure 4.15	Relative vertical deformation of the geotextile tubes	48
Figure 5.1	Configurations that have been tested	49
Figure 5.2	Design curve to determine $\chi$ (assuming perpendicular wave attack and a water level equal to the top of the tube)	50

### *In appendices*

Figure B.1	Overall set-up of the model
Figure B.2	Wave height exceedance curves and energy density spectra
Figure B.3	Overview of profile measurements
Figure B.4	Results top view camera
Figure B.5	Overview displacements based on top view camera analysis
Figure B.6	Penetrologger data
Figure B.7	Grain distribution
Figure B.8	Stretches in geotextile
Figure E.1	Colour injection characteristics.
Figure G.1	Forces on an element
Figure G.2	Relevance of lift and drag
Figure H.1	Forces on an element placed on a slope

- Figure H.2 Impression of small scale model tests to determine friction coefficients
- Figure I.1 Definition of energy
- Figure I.2 Design graph for determining  $\chi$

## List of Photographs

### *In text*

Photo 2.1	Impression of configuration F (F1, F3, F4, F5)	10
Photo 2.2	Impression of test configuration T	10
Photo 2.3	Impression of test configuration P (P2 and P3)	11
Photo 3.1	Geotextile tube after test P3-9	28

### *In appendices*

Photo C.1	Lining out the Back flow structure
Photo C.2	Building the Back flow structure
Photo C.3	Placing concrete plates
Photo C.4	Back flow structure
Photo C.5	Geotextile on the concrete plates to avoid erosion
Photo C.6	Building the sand core
Photo C.7	Compacting the sand core
Photo C.8	Installing the reinforcement
Photo C.9	Application of the concrete
Photo C.10	Lay out geotextile tube
Photo C.11	Temporarily fixation geotextile tube
Photo C.12	Sand-water mixture
Photo C.13	Filling the geotextile tube and measuring the actual height
Photo C.14	Filling (over pressure) hose
Photo C.15	Walking over geotextile tube to prevent blocking
Photo C.16	Process water flows trough the geotextile during filling
Photo C.17	Markers on filled geotextile tube for image processing
Photo C.18	Bar behind geotextile tube to simulate trench
Photo C.19	Use of a slat at the landside to prevent damaging the profiler and geotextile tube.
Photo C.20	Use of a block at the seaside to prevent damaging the profiler
Photo C.21	Calibrating profiler
Photo C.22	Profiling geotextile tube
Photo C.23	Marking block
Photo C.24	Determine outermost point geotextile tube
Photo C.25	Measurements with Penetrologger
Photo C.26	Use of split ring
Photo C.27	Example of color injections
Photo C.28	During test series F4-1
Photo C.29	After test series F4-1
Photo C.30	During test series F1-6
Photo C.31	After test series F1-10
Photo C.32	After examining the geotextile tube (F1)
Photo C.33	During test series F3-9
Photo C.34	After test series F3-9
Photo C.35	Measuring height geotextile tube after test series F3-9
Photo C.36	During test series T1-6

- Photo C.37 During test series T1-6
- Photo C.38 During test series T1-6
- Photo C.39 During test series T1-6
- Photo C.40 Geotextile tube partly on bar after test series T1-9
- Photo C.41 Determine dimensions after test series T1-9
- Photo C.42 During test series P3-8
- Photo C.43 During test series P3-9
- Photo C.44 Sliding of geotextile tube during test series P3-9
- Photo C.45 Prepared geotextile tubes before test series P2-1
- Photo C.46 Movement of geotextile tube (left tube) after test series P2-4-2
- Photo C.47 During test series F5-5
- Photo C.48 During test series F5-5
- Photo C.49 Deformed geotextile tube after test series F5-6
- Photo C.50 Color injection test series F1. Injection at line 4, point 3
- Photo C.51 Color injection test series F1. Injection at line 4, point 3
- Photo C.52 Color injection test series F3. Injection at line1, point 3
- Photo C.53 Color injection test series F4. Injection at line3, point 5
- Photo C.54 Color injection test series F4. Injection at line 3, point 5

## List of Symbols

Symbol	Unit	Description
$a$	m	measured distance between geotextile tube and seaward side of the supporting structure
$A$	$m^2$	derived surface of cross section of an actual filled tube
$A_{100\%}$	$m^2$	derived theoretical surface of cross-section of a tube which is 100 % filled
$B_i$	m	measured width of geotextile tube at line $i$
$C_{empty}$	m	measured circumference of empty geotextile tube
$C_i$	m	derived circumference of a filled tube at line $i$
$C_u$	-	uniformity coefficient ( $D_{60}/D_{10}$ )
$d$	m	water depth
$d_1$	m	deepest point of coloured sand below the geotextile
$d_2$	m	the highest point below the geotextile
$d_p$	m	penetration depth
$D_{deformed}$	m	tube height after deformation
$D_{initial}$	m	tube height before deformation
$D_i$	m	measured height of the geotextile tube at line $i$
$D_x$	m	sieve size of the theoretical sieve with rectangular openings where $x$ % of the grains of the sand passes through
$EC_i$	m	measured exposed circumference at line $i$
$F$	N	force
$F_f$	N	frictional forces
$F_g$	N	gravitational forces
$F_H$	N	hydraulic forces
$F_w$	N	forces due to static water pressure
$F_p$	kN	penetration force
$F^*$	-	densimetric Froude number
$g$	$m/s^2$	acceleration due to gravity
$h_{bar}$	m	height of the bar
$H_{max}$	m	the maximum measured wave height in a wave record
$H_s$	m	significant wave height
$H_{s,N}$	m	representing characteristic wave height for a combination of tests
$H_{s,sm}$	m	significant wave height at which sand starts to migrate within the geotextile element
$i$	-	marker number
$j$	-	test number
$K$	m/s	permeability
$L$	m	length
$L$	m	measured length of geotextile tube
$L_o$	m	deep water wave length
$L_{toe,p}$	m	wave length at the toe of the structure
$L_x$	m	wave length at position $x$
$L_n$	m	length of colour injection needle
$m$	m	mass

Symbol	Unit	Description
$m_0$	m <sup>2</sup>	zero <sup>th</sup> moment of the wave spectrum
$m_s$	kg	mass of ground sample
$m_{s,dry}$	kg	mass of dry ground sample after drying for 24 hours in an oven
$m_{split}$	kg	mass of split ring
$n$	-	number of markers on the tube
$N$	-	number of waves during a test
$N$	-	scale
$O_{90}$	m	the opening size which corresponds to the $D_{90}$ of the soil passing the geotextile
$p_A$	%	filling degree based on the cross-sectional surface
$p_{h,avg}$	%	filling degree based on the height of the tube averaged over the situation before and after testing
$p_{h,a}$	%	filling degree based on the height of the tube after testing
$p_{h,b}$	%	filling degree based on the height of the tube before testing
$P$	Pa	ground pressure
$P_{ave}$	Pa	averaged ground pressure based on $n$ measurements
$R_{100\%}$	m	theoretical diameter when tube is 100 % filled
$R_c$	m	crest height above the mean water level
$S_p$	-	wave steepness based on the wave length at deep water
$S_{toe,p}$	-	wave steepness based on the wave length at the toe of the structure
$S_x$	-	wave steepness based on the wave length at position $x$
$S(f)$	m <sup>2</sup> /Hz	variance spectral density
$S_{tube}$	-	relative settlement ( $= \frac{D_{deformed} - D_{initial}}{D_{initial}}$ )
$t$	s	time
$T$	N	tensile strength
$T_{pd}$	s	wave peak-period
$T_{pd}$	s	representing peak period for a combination of tests
$u_{crit}$	m/s	critical velocity with respect to stability
$u_{crit,CP}$	m/s	critical velocity with respect to the Caterpillar mechanism
$V$	m <sup>3</sup>	volume of cross section
$V_s$	m <sup>3</sup>	volume of split ring
$w_i$	m	measured characteristic distance at line $i$
$W$	%	percentage water in sample
$x_i$	m	measured characteristic distance at line $i$
$X$	m	distance from the wave board
$x$	m	relative distance between the needle insertion point in the geotextile and the highest point of coloured sand parallel to the geotextile
$X_{a,i,j}$	m	position of marker $i$ after test $j$
$X_{b,i,j}$	m	position of marker $i$ before test $j$
$y_i$	m	measured characteristic distance at line $i$
$Y$	m	distance from the western flume wall
$z_i$	m	measured characteristic distance at line $i$
$Z$	m	height with respect to the bottom of the flume
$\alpha$	-	slope of the structure

Symbol	Unit	Description
$\alpha_{\text{bar}}$	-	slope of the bar
$\alpha_{\text{ss,seaside}}$	-	slope of supporting structure at seaward side (structure below geotextile tube)
$\alpha_{\text{ss,landside}}$	-	slope of supporting structure table at landward side (structure below geotextile tube)
$\alpha_{\text{T}}$	-	slope of the tube = $\tan^{-1}(D/B)$
$\gamma$	kg/m <sup>3</sup>	unit weight of the soil
$\Delta$	-	relative buoyance $(=\rho - \rho_w) / \rho_w$
$\Delta x_{\text{cum},i,j}$	m	cumulative displacement of marker $i$ during test 1 until test $j$
$\Delta x_{\text{avg,cum},j}$	m	average cumulative displacement of tube during test 1 until test $j$
$\Delta x_{\text{min,cum},j}$	m	minimum cumulative displacement of tube during test 1 until test $j$
$\Delta x_{\text{max,cum},j}$	m	maximum cumulative displacement of tube during test 1 until test $j$
$\Delta x_{i,j}$	m	displacement of marker $i$ during test $j$
$\Delta x_{\text{avg},j}$	m	average displacement of tube during test $j$
$\Delta x_{\text{min},j}$	m	minimum displacement of tube during test $j$
$\Delta x_{\text{max},j}$	m	maximum displacement of tube during test $j$
$\lambda$	-	shape factor $(B / D)$
$\xi_{o,p}$	-	breaker parameter at deep water
$\xi_{\text{toe},p}$	-	breaker parameter at the toe of the structure
$\rho$	kg/m <sup>3</sup>	density
$\zeta$	-	buoyancy factor
$\zeta$	-	ratio between friction forces and resisting water forces
$\sigma$	N/m	stress

## Commonly used indices

Indices	Description
a	after a test series
A	tube A
avg	average
b	before a test series
B	tube B
C	tube C
cum	cumulative
crit	critical
G	geotechnical
H	hydraulic
m	model
max	maximum
min	minimum
N	normal (w.r.t. forces)
p	prototype
pe	permeability
rep	representative
s	sand
ss	supporting structure
T	tube
w	water





# 1 Introduction

## 1.1 General

Geotextile encapsulated sand elements, such as geotextile tubes, geotextile containers, geotextile bags or geotextile mattresses can be used in several hydraulic applications. Examples and suggestions are given in CUR (2004), CUR (2006), Pilarczyk (2000) and Oh and Shin (2006). However, the elements are hardly used for coastal defence works. Several reasons for this are given in Bezuijen and Vastenburg (2008). One of the main reasons given in that paper is the uncertainty on the behaviour of geotextile encapsulated sand elements under wave load.

Therefore, it is decided to focus on the stability of geotextile encapsulated sand elements under wave load. The most commonly used geosystems in coastal protection structures are geotextile containers and geotextile tubes, therefore those elements have been studied in two large scale physical model test series. The first series covers the stability of geotextile containers under wave load and is described in Van Steeg and Klein Breteler (2008). The second series, stability of geotextile tubes under wave load, is subject of this report.

The physical model tests are performed in the Delta Flume of Deltares (see Appendix D) under supervision of ir. A. Bezuijen, ir. M. Klein Breteler, ir. P. van Steeg and ing. E.W. Vastenburg. This report is written by ir. P. van Steeg and ing. E.W. Vastenburg and is based on discussions, meetings and writings with ir. A. Bezuijen, ir. M. Klein Breteler and dr. ir. B. Hofland. During all phases of the research, an expert panel gave constructive feedback on the project. The members of this panel were:

Ir. E. Berendsen	RWS / Bouwdienst
Ir. J.G. de Gijt	Gemeentewerken Rotterdam / Delft University of Technology
F.A.S.D. Hemstra	De Vries en van de Wiel
R. Veldhoen	Van den Herik
Ing. E.L.F. Zengering	Ten Cate

Ten Cate Geosynthetics supplied the geotextile tubes and the geotextile required for this research. The filling process of the geotextile tubes is performed by a contractor who is experienced with the construction of geotextile tubes; de Vries en van de Wiel.

## 1.2 Objective

The main objective of this project is to determine the stability of geotextile tubes and the possible migration of sand in the geotextile tubes during wave attack by performing large scale physical model tests.

## 1.3 Outline

Chapter 2 describes the model setup of the experiments. The experiments and test results are given in Chapter 3. In Chapter 4, the analysis of the test results is described and stability formulae are suggested. Conclusions are given in Chapter 5.



## 2 Model set-up

### 2.1 Test facility: the Delta Flume

The physical model tests were carried out in the Delta Flume of Deltares. The flume has a width of 5 m, a height of 7 m and the overall length is 240 m. In this flume, waves can be generated, depending on several hydraulic conditions, up to a significant wave height of  $H_s = 1.5$  m.

Waves, as described in Section 2.3, were generated by the wave board. At the wave board, active re-reflection compensation was used to compensate for waves that reflect from the structure back to the wave board. In this way waves were generated that resemble natural waves very closely. This system has been validated and applied in a large number of experimental investigations. Details of the Delta Flume and the wave board are given in Appendix D.

### 2.2 Test set-up

#### 2.2.1 General

In this report, a coordinate system is used as follows:

$X$  = distance from the wave board in neutral position (m)

$Y$  = distance from the western flume wall (m)

$Z$  = height with respect to the bottom of the flume (m)

All values given in this report are model values. The present set-up is thought to represent structures up to four times larger than tested.

An overview of the test set-up is given in Figure B.1 of Appendix B.

#### 2.2.2 Construction of a supporting structure

Sufficient water depth is required to ensure that the wave height is not limited by depth induced wave breaking. Therefore a supporting structure with a height of  $Z = 3.60$  m has been created in the Delta Flume. From  $Z = 0.00$  m until  $Z = 1.00$  m, the supporting structure has a width of 19.70 m (from  $X = 109.40$  m to  $X = 129.10$  m). At its maximum height,  $Z = 3.60$  m, the width of the supporting structure is 8.00 m (from  $X = 115.90$  m to  $X = 123.90$  m). The seaward slope has an angle of  $\cot(\alpha_{ss,seaside}) = 2.5$ , the landward slope has an angle of  $\cot(\alpha_{ss,landside}) = 2$ .

Since it was expected that much water would overtop during the different test series, a back flow channel was implemented in the supporting structure (see Photo 1 to Photo 5 in Appendix C). This system is based on a physical model that has been performed in the past and is described in Kuiper et al. (2006). In this way, overtopping water flows back through this channel and levels the water column at both sides of the supporting structure. The back flow channel is formed by concrete walls as can be seen on Photo 1 and Photo 2 in Appendix C. The back flow channel has a height of 1m (from  $Z = 0.00$  m to  $Z = 1.00$  m).

On top of the back flow channel concrete plates were placed. This is shown on Photo 3 and Photo 4 in Appendix C. On top of the concrete plates, a geotextile was placed to avoid erosion of the core material which is placed on top.

A compacted sand core with a reinforced concrete layer was placed on top of the concrete plates. The construction of the sand core is shown on Photo 6. The compacting of the sand core is shown on Photo

7. A reinforced concrete layer was placed on and around the sand core, which is shown on Photo 8 and Photo 9.

This supporting structure simulates a part of a structure, for example other geotextile tubes, geotextile containers or a different structure. The choice for this type of structure is made since it would take too long to build up a stack of geotextile tubes or containers after each test series (in case the stack collapses). In addition, the shape of the sand/concrete structure is more constant, which avoids side effects caused by an irregular stack of geotextile tubes and makes comparing of the results more difficult. Most damage is expected at the top of a stack of tubes, where interlocking is minimal and wave attack most severe.

At the landward side of the supporting structure, a slope with an angle of approximately 1:3 and a height of  $Z = 8.30$  m was present. The toe of this slope was situated at  $X = 169.84$  m. The crest of this slope was at  $X = 194.94$  m. This structure was a residue of a previous project in the Delta Flume and was used as a wave-damping element.

An overview of the supporting structure and the wave damping structure is shown in Figure 2.1 and Figure B.1 in Appendix B.

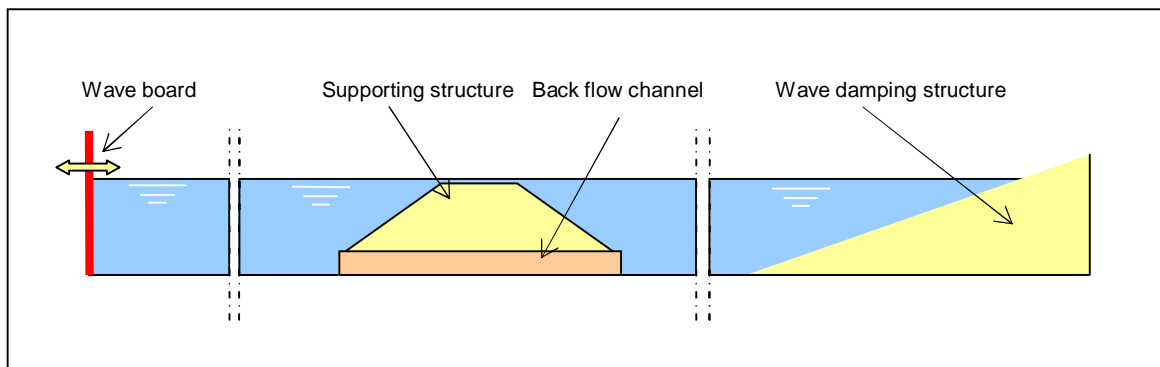


Figure 2.1 Impression of test set-up (not on scale)

### 2.2.3 Construction of geotextile tubes

On top of the supporting structure, one or more geotextile tubes were placed. The empty geotextile tubes were prefabricated by Ten Cate based on specifications given by Deltares. During the filling process the water level in the flume was lowered to a level just below the crest of the supporting structure. This was done for safety reasons. During the filling and emptying process a temporarily door (at  $X = 102$  m) was used to divide the flume in two parts. The advantage of this approach is that the water level in only one compartment of the flume needs to be lowered. After lowering the water level, the empty geotextile was aligned between two beams. The location of the beams was determined by using the Timoshenko method; CUR (2006). This method estimates the theoretical shape of the geotextile tube by a given degree of filling and geotextile properties as stiffness etc. The distance between the beams is given by the width of the theoretical shape of the geotextile tube. To avoid rolling and sliding away during the filling process, the geotextile tube was temporarily fixated at the beams, which is shown in Photo 10 and 11.

Next, the tubes were filled hydraulically by pumping a sand-water mixture into the geotextile tube. Therefore a container has been placed along the flume. This container was filled with sand which was selected for the experiment. The characteristics of the sand are:

$$D_{10} = 0.133 \text{ mm}$$

$$D_{50} = 0.194 \text{ mm}$$

$$D_{60} = 0.206 \text{ mm}$$

$$D_{90} = 0.292 \text{ mm}$$

A sieving curve of the sand is given in Appendix B.7.

To create a sand-water mixture, water was pumped from the Delta Flume into the container. Subsequently the mixture was transported by using another pump through a hose which was fixated to the filling hose of the geotextile tube (see photo 12).

First, water with a low concentration of sand was pumped into the tube. The sand filled the pores and avoided that most of the process water flowed away. Some of the water left the tube through the pores and the overpressure hose (see photo 14 en 16). Due to the water pressure the geotextile tube obtained its shape. At this point the concentration of sand in the sand-water mixture needed to be increased to fill the geotextile tube. After a small layer of sand in the geotextile tube was formed, the fixation as described above was removed to prevent tearing of the geotextile.

During the filling process, the actual height of the tube was monitored by measuring the distance from the top of the tube to the crest of the supporting structure. When the desired height (filling percentage) was reached, the filling process has been stopped (see photo 13). To avoid blocking of the pores of the geotextile an employee walked over on the tube during the filling process.

After completion of the filling process, the beams that fixated the tube were removed and the filling hoses were closed. To avoid chatter of the hoses, which could lead to tearing of the geotextile, the hoses were fixated with a rope around the geotextile tube. This is shown at Photo 18.

The working method followed is the same as during normal practice. The work has been performed by an external contractor, de Vries en van de Wiel, experienced with this process from field applications. Reference is made to Photo 12 to 16 in Appendix C.

#### *Geotextile*

Since the model and the prototype are not on the same scale, it is not possible to use geotextile that is used in the prototype. Three scaling aspects were considered:

- 1 Stiffness and tensile strength of the geotextile during wave experiments
- 2 Stiffness and tensile strength of the geotextile during filling
- 3 Sand tightness

#### Ad1 Stiffness and tensile strength of the geotextile during wave experiments

To get a proper model, scaling of the strength and stiffness of the geotextile is necessary. In a scale 1: $N$  model, where the prototype geometric dimensions are  $N$  times higher in the prototype compared to the model, the volume and thus the weight of the model scales with  $1:N^3$ . This means that the forces scale with  $1:N^3$ . Thus in formula:

$$L_m = \frac{1}{N} L_p \quad (2.1)$$

$$F_m = \frac{1}{N^3} F_p \quad (2.2)$$

Where  $L$  indicates a length and  $F$  a force. The index  $m$  indicates model and  $p$  prototype.

With these starting points it is possible to calculate the scaling of other parameters which includes the dimensions force or length. The stress ( $\sigma$ ) is force/area and thus is the scaling factor for the stress:

$$\sigma_m = \frac{F_m}{L_m^2} = \frac{1/N^3 F_p}{1/N^2 L_p^2} = \frac{1}{N} \sigma_p \quad (2.3)$$

Thus the stresses are  $N$  times less in the model compared with prototype. The dimension of a tensile strength in a geotextile ( $T$ ) as well as the dimension of the stiffness is stress/length and this results in:

$$T_m = \frac{F_m}{L_m} = \frac{1/N^3 F_p}{1/N L_p} = \frac{1}{N^2} T_p \quad (2.4)$$

This result means that applying proper scaling rules would result into an impractical non-existing geotextile (at a geometric scale of, for example 1:4, the tensile force is 1:16). Therefore, a choice was made for a thinner geotextile, which is more flexible than the geotextile used in the field. The strength was  $1/3^{\text{rd}}$  to  $1/5^{\text{th}}$  of the strength of geotextiles used in the field. This means that the geotextile in the model is relatively too strong. Since the geotextile is not loaded to rupture this is not a problem.

#### Ad2 Stiffness and tensile strength of the geotextile during filling

The scaling rule mentioned above is valid for the situation where the stresses in the model are  $N$  times smaller than the stresses in the prototype (where  $N$  is the geometric scale). This was the case during the wave experiments. It is assumed that during the filling process, the pressure is more or less the same in the model as in the prototype and determined by the pump capacity. For such a situation the scaling laws become:

$$L_m = \frac{1}{N} L_p \quad (2.5)$$

$$\sigma_m = \sigma_p \quad (2.6)$$

And thus is for this situation the appropriate scaling rule for the tensile force:

$$T_m = \frac{F_m}{L_m} = \sigma_m L_m = \frac{1}{N} T_p \quad (2.7)$$

The tensile force scales with the geometric scale. A geometric scale of, for example, 1:4 leads to a tensile force of 1:4. This is conflicting with the scaling rules given for the tubes under water attack.

It was expected that the geotextile would be strong enough during the filling process. However, to ensure that no damage to the geotextile would occur, the external contractor, de Vries en van de Wiel, did a fill test before the experiments to determine the strength of the geotextile tube. From these tests, it was concluded that the geotextile tubes were strong enough to survive the filling procedure in the Delta Flume.

#### Ad3 Scaling of sand

The scaling rules used for the sand depends on the phenomena that are expected. The following aspects have to be considered:

- 1 For geotechnical reasons it is most convenient when the model sand and the prototype sand are the same, since the friction angle and dilatancy angle are the same.
- 2 To properly test the possibility of sand migration it would be the best to scale the grain size based on sediment transport scaling rules such as described in Kamphuis (1996) and Hughes (1993) and reviewed by Alsina et.al. (2007). The similarity in these transport models is obtained by fulfilling similitude in the following dimensionless parameters

Densimetric Froude number:

$$F_* = \frac{u_*^2}{\Delta g d_{50}} \quad (2.8)$$

Where  $u_*$  = bottom shear velocity,  $\Delta$  = relative buoyant density of material  $(= (\rho_s - \rho_w)/\rho_w)$ ,  $g$  = acceleration due to gravity and  $d_{50}$  = medium grain size.

Densimetric Froude number similitude give arise to a geometric scaling of the sediment size. Following Equation (2.8) it is obtained that

$$N_{d50} = N \quad (2.9)$$

- 3 When the permeability of the sand is of dominant importance it would be necessary to scale the grains with  $(1/N)^{0.25}$ . Since Froude scaling is applied, this means that the relation for the time is:

$$t_m = \frac{1}{\sqrt{N}} t_p \quad (2.10)$$

which means that the relation for the permeability ( $K$  with dimension m/s) is:

$$K_m = \frac{1}{\sqrt{N}} K_p \quad (2.11)$$

For laminar low through a granular medium the permeability scales with the  $D^2$  where  $D$  is the diameter of the grain. This means that the grains should scale with  $(1/N)^{0.25}$ . For a scale of, for example, 1:4 this means that the grain diameter in the model must be 1.4 times smaller than the grain diameter in prototype. However, it is expected that there is hardly any flow through the sand and that the scaling rules with respect to the permeability can be neglected.

It is not possible to fulfil all these scaling rules, so a compromise is necessary. Here it is assumed that hydraulic properties are of importance in a way that unprotected sand has to move under wave attack in the model as well as in prototype, but that it is not really necessary that the densimetric Froude number  $F_*$  is the same. This means that the geotechnical scaling rules may prevail. Therefore a choice is made for sand with prototype scale. The model represents a sand with the scales as indicated in Table 2.1.

Table 2.1 Overview of scaling aspects

<b>N</b>	<b>Geotechnical scale (friction and dilatancy angle)</b>	<b>Hydraulic scale (sediment transport)</b>	<b>Permeability scale</b>
	$N_G = 1$	$N_H = N_L$	$N_{Pe} = (N_L)^{0.25}$
1	1	1	1
2	1	2	1.2
4	1	4	1.4

### Ad3 Sand tightness

Requirements regarding sand tightness of the geotextile, which are based on CUR (2006) are:

$$O_{90} \leq D_{90} \quad (2.12)$$

and

$$O_{90} < 1.5 \cdot D_{10} \cdot C_u^{1/2} \quad (2.13)$$

Wherein:

$O_{90}$	=	the opening size which corresponds to the $D_{90}$ of the soil passing the geotextile
$D_x$	=	sieve size of the theoretical sieve with rectangular openings where $x$ % of the grains of the sand passes through
$C_u$	=	uniformity coefficient ( $D_{60}/D_{10}$ )

According to the grain distribution (see Appendix B7), the  $D_{90} = 0.292$  mm,  $D_{10} = 0.133$  mm,  $D_{60} = 0.206$  mm and  $C_u = 0.206/0.133 = 1.55$ . The chosen geotextile has an opening size of  $O_{90} = 0.17$  mm. According to the requirements given in Equation (2.12) and Equation (2.13) this should be sufficient. In this situation, approximately 20 % of the grains (by weight) can theoretically pass the openings in the geotextile. It was assumed that the real percentage that passes the geotextile would be much lower due to clogging and blocking of the sand.

The geotextile used for the geotextile tubes is Geolon® P180L and was fabricated by Ten Cate. Specifications of the geotextile used are given in Appendix F.

#### *Filling material*

The filling material consists of sand. A sieving curve of the sand is given in Figure B.1 in Appendix B.

#### 2.2.4 Geometrical configurations

Seven geometrical configurations, divided in 3 categories, have been tested. The categories are:

- Test series F: single tubes without trench (4x)
- Test series T: single tube with trench (1x)
- Test series P: multiple tubes (2x)

A description of each category is given below. In this report, the filling percentage is defined as the actual fill divided by the maximum fill that is possible given the circumference of the geotextile ( $p_A$ ), or as the actual height divided by the maximum possible height ( $p_h$ ). The size of a tube is indicated with the radius of a 100% filled tube ( $R_{100\%}$ ), the average measured width ( $B_{avg}$ ) and the average measured height ( $D_{avg}$ ). Figure 2.2 (test series F), Figure 2.3 (test series T) and Figure 2.4 (test series P) are plotted on scale and are based on the measurements performed before the tests as described in Section 2.4.

#### *Test series F: Single tubes without trench*

Four configurations with a single tube were tested. Variations were made in the filling percentage ( $p_A$ ) and the size, characterized by the radius ( $R_{100\%}$ ). An impression is given in Figure 2.2 and Photo 2.1. The main dimensions of the tubes are given in Table 2.2.

After finishing test series P2, there was still one tube left that could be used for the testing of a single tube under wave attack. This tube was, due to the severe wave attack during test series P2, a little deformed. It was decided to use this tube for test series F5.



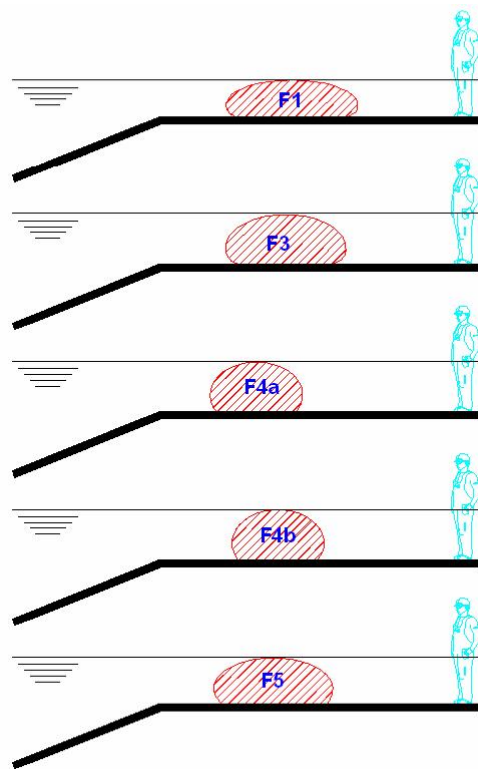


Figure 2.2 Geometric specifications of test series F

Table 2.2 Summary of geometric specifications of test series F

series	$D_{avg}$ (m)	$B_{avg}$ (m)	$R_{100\%}$ (m)	$p_h$ (%)	$p_A$ (%)
F1	0.57	2.19	0.75	38	66
F3	0.79	2.04	0.75	53	80
F4	0.82	1.52	0.57	73	109
F5	0.74	2.02	0.76	48	72



Photo 2.1 Impression of configuration F (F1, F3, F4, F5)

### Test series T: Single tube with trench

One configuration with a single tube resembling test series F3 and a bar, which simulates a trench, was tested. The bar was placed at the landside of the tube (see Appendix C, photo 18) and has a slope of  $\cot\alpha_{\text{bar}} = 2$  and a height of  $h_{\text{bar}} = 0.175$  m.

An impression is given in Figure 2.3 and Photo 2.2. The main dimensions of the tubes are given in Table 2.3.

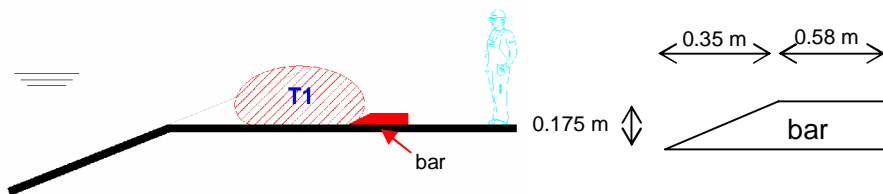


Figure 2.3 Geometric specifications of test series T

Table 2.3 Geometric specifications of test series T

series	$D_{\text{avg}}$ (m)	$B_{\text{avg}}$ (m)	$R_{100\%}$ (m)	$p_h$ (%)	$p_A$ (%)
T1	0.88	2.03	0.76	58	85

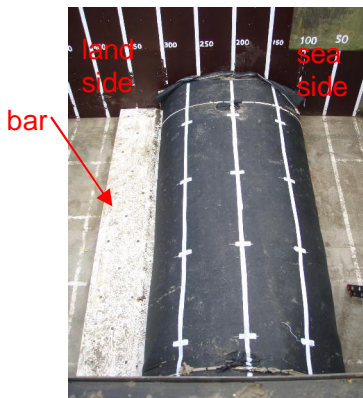


Photo 2.2 Impression of test configuration T

**Series P: Multiple tubes**

Two configurations with multiple tubes were tested (see Figure 2.4):

- Series P2: two tubes placed behind each other
- Series P3: two tubes placed behind each other and a third tube on top (2-1 stack).

Besides the number of tubes used, the radius ( $R_{100\%}$ ) was different during both test set-ups (see Table 2.4).

At series P3 a bar was placed at the landward side of tube A. The bar has a slope of  $\cot\alpha_{\text{bar}} = 2$  and a height of  $h_{\text{bar}} = 0.120$  m. A smaller bar (compared with test series T1) was chosen since the tubes used at test series P3 are smaller.

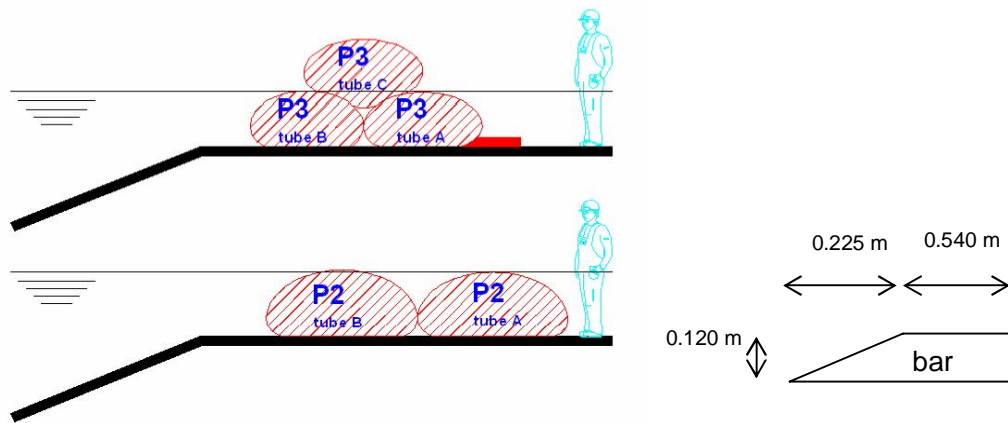


Figure 2.4 Geometric specifications of test series P

Table 2.4 Geometric specifications of test series P

series	$D_{\text{avg}}$ (m)	$B_{\text{avg}}$ (m)	$R_{100\%}$ (m)	$p_h$ (%)	$p_A$ (%)
P3 tube A	0.71	1.49	0.58	61	86
P3 tube B	0.70	1.56	0.57	61	89
P3 tube C	-	1.41	0.57	-	99
P3 average	0.71	1.47	0.57	61	91
P2 tube A	0.86	1.98	0.77	56	78
P2 tube B	0.82	1.99	0.76	54	76
P2 average	0.84	1.99	0.77	55	77

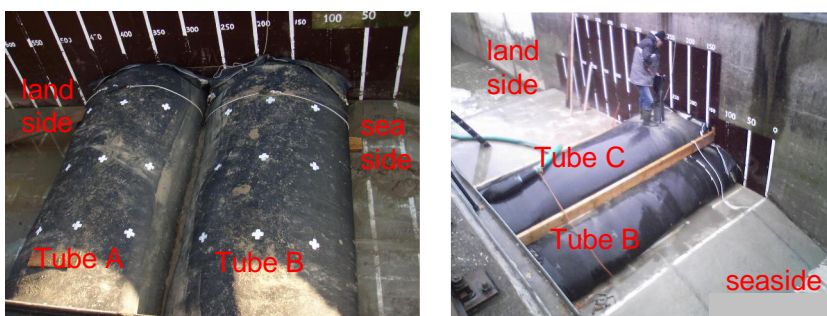


Photo 2.3 Impression of test configuration P (P2 and P3)

## 2.3 Hydraulic conditions

Several hydraulic conditions were used during the test series. Each test series started with a relatively low wave height that was increased after every test. The water level was always equal to the top of the geotextile tube. The water level at series P3 was equal to the top of tube B. For all tests, irregular waves (JONSWAP spectrum with a peak enhancement factor of 3.3) were used. The wave steepness is based on the breaker parameter at the toe of the structure, which is kept constant at  $\xi_{toe,p} = 2$  ( $s_{toe,p} = 0.04$ ). The deepwater breaker parameter varies between  $\xi_{o,p} = 1.95$  ( $s_{o,p} = 0.042$ ) and  $\xi_{o,p} = 2.60$  ( $s_{o,p} = 0.024$ ).

An overview of the hydraulic conditions is given in Appendix A, Table A.1. The wave conditions are specified by a wave height,  $H_s$  (m), and a wave peak period,  $T_p$  (s). The water depth,  $d$ , is specified in metres relative to the bottom of the flume. The test duration is given as a number of waves,  $N$  (-). The breaker parameter ( $\xi_{o,p}$  and  $\xi_{toe,p}$ ) and wave steepness ( $s_{o,p}$  and  $s_{toe,p}$ ) are calculated with the use of Equation (2.14) until Equation (2.18).

$$\xi_{o,p} = \frac{\tan \alpha}{\sqrt{s_{o,p}}} \quad (2.14)$$

$$\xi_{toe,p} = \frac{\tan \alpha}{\sqrt{s_{toe,p}}} \quad (2.15)$$

$$s_{o,p} = \frac{H_s}{L_{o,p}}, \quad s_{toe,p} = \frac{H_s}{L_{toe,p}} \quad (2.16)$$

$$L_o = \frac{gT_p^2}{2\pi} \quad (2.17)$$

$$L_{toe,p} = L_o \tanh\left(\frac{2\pi d}{L_{toe,p}}\right) \quad (2.18)$$

Where:

- $d$  = water level relative to the bottom of the flume (m)
- $H_s$  = significant wave height (m)
- $L_{o,p}$  = deep water wave length based on the peak wave period (m)
- $L_{toe,p}$  = wave length at the toe of the structure (m)
- $s_{o,p}$  = wave steepness based on the wave length at deep water (-)
- $s_{toe,p}$  = wave steepness based on the wave length at the toe of the structure (-)
- $T_p$  = peak wave period
- $\xi_{o,p}$  = breaker parameter at deep water (-)
- $\xi_{toe,p}$  = breaker parameter at the toe of the structure (-)

## 2.4 Measurements

### 2.4.1 Wave measurements

The wave characteristics were measured by means of three wave gauges in front of the structure. The wave gauges were placed at  $X = 85.0$  m,  $X = 88.0$  m and  $X = 89.5$  m. Each wave gauge is a pair of vertical wires near the wave flume, which measures the surface elevation of the water at a fixed location. To separate the incident and reflected waves a cross-correlation technique was used as described by Mansard and Funke (1980). The signals from the three wave gauges were used to determine the following wave characteristics of the incoming waves:

$H_s$	=	the significant wave height $H_s$ (m), based on the wave spectrum, including the wave height exceedance curves.
$H_{\max}$	=	the maximum measured wave height in the wave record (m)
$N$	=	number of waves during a test (-)
$S_{0,p}$	=	deep water wave steepness based on the wave peak period (-). The wave steepness has been determined with the use of Equation (2.16) and (2.17)
$S(f)$	=	the variance spectral density ( $\text{m}^2/\text{Hz}$ )
$T_p$	=	the peak period, the wave period corresponding to the peak of the variance spectral density (s)
$\xi_{0,p}$	=	deep water breaker parameter (-). The breaker parameter has been determined with the use of Equation (2.14), (2.16) and (2.17)

During some tests technical problems occurred with the wave machine. When these problems occurred the test was aborted and restarted. During some tests the problem occurred several times. These specific tests are shown in the tables with an extra digit. For example: test F1-9 was aborted and restarted two times. This resulted in the test name coding F1-91 and F1-92. A corresponding representing value of the significant wave height ( $H_{s,N}$ ) and the wave peak period ( $T_{p,N}$ ) for the combination of subtests is shown by adding a 't'. (For example: F1-9\_t). This is done for tests F1-9 (3 subtests), F3-2 (2 subtests), F3-6 (2 subtests), P2-1 (2 subtests), P2-2 (4 subtests), P2-3 (3 subtests) and P2-4 (3 subtests). The significant wave height and peak periods for these tests have been calculated based on Klein Breteler (2006) using Equation (2.19) and (2.20):

$$H_{s,N} = \sqrt{\frac{\sum_{i=1}^n N_i H_{s,i}^2 T_i}{\sum_{i=1}^n N_i T_i}} \quad (2.19)$$

$$T_{p,N} \approx \frac{\sum_{i=1}^n (N_i H_{s,i}^2 T_{pd,i})}{H_{s,N}^2 \sum_{i=1}^n N_i} \quad (2.20)$$

Equation (2.19) is based on an exact summation of the wave signals. Equation (2.20) would be an exact determination of the wave period if  $T_{m-1.0}$  would be used. Since the ratio  $T_p/T_{m-1.0}$  is usually constant this is a good approximation.

### 2.4.2 Profile

The profile of every structure is determined with the use of a mechanical profile tracker combined with hand measurements.

### Mechanical profile tracker

The mechanical profile tracker uses a small wheel that follows the structure in a seaward direction and logs the profile of the structure very accurately (~ 1 mm). The machine was used before a test series and after several tests. The profiler was used at four different lines perpendicular to the structure, Line 1, (Y = 4.00 m), Line 2 (Y = 3.00 m), Line 3 (Y = 2.00 m) and Line 4 (Y = 1.00 m). The distance between each line is 1 meter. An illustration of the position of the profile lines is given in Figure 2.5 and Appendix C, photo 17.

Due to the round shape of the geotextile tube and the configuration of the profiler, it was necessary to lift the profiler a bit, to prevent damage to the device and the geotextile tube. To this end, a wooden board was used at the landward side and a wooden block at the seaward side (see Figure 2.6 and Appendix C, photo 19 and 20). When the profiler reached the widest point at the seaside of the tube, the device made a “free fall” downwards and landed on the wooden block. This resulted in a straight line in the profiler data.

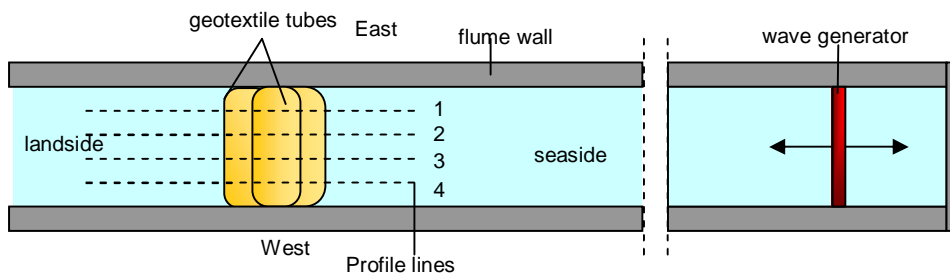


Figure 2.5 Position of profile lines (top view)

To calibrate the profiler it was leveled at a benchmark (see Appendix C, photo 21).

On beforehand, based on the results of the tests with geotextile containers, it was expected that the geotextile tubes could turn over and / or deform. To mark a fixed point on the tube, a small marking block was used (see Appendix C, photo 23). This marker was clearly recognizable in the profiler data as can be seen in Figure 2.6.

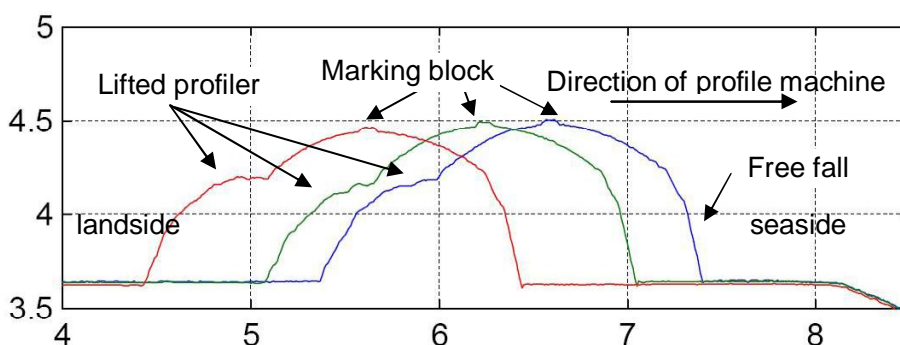


Figure 2.6 Profiler runs and recognizable points

Because of the round shape of the geotextile tube and the geometry of the profiler, the profiler was not able to measure the total circumference of the tube. To determine the length of the base of the tube (part of the geotextile tube which has direct contact with the floor) the distance between the outermost point of the tube (see Appendix C, photo 24) and the base has been measured before each test series.

The shape of the geotextile tube between the end of the profiler data and the base of the tube is determined by using the calculated shape, based on the Timoshenko method (see CUR2006, Appendix E).

#### Hand measurements

Before and after each test several hand measurements have been carried out to determine the characteristics of the geotextile tube. An overview of the characteristic parameters is given in Figure 2.7.

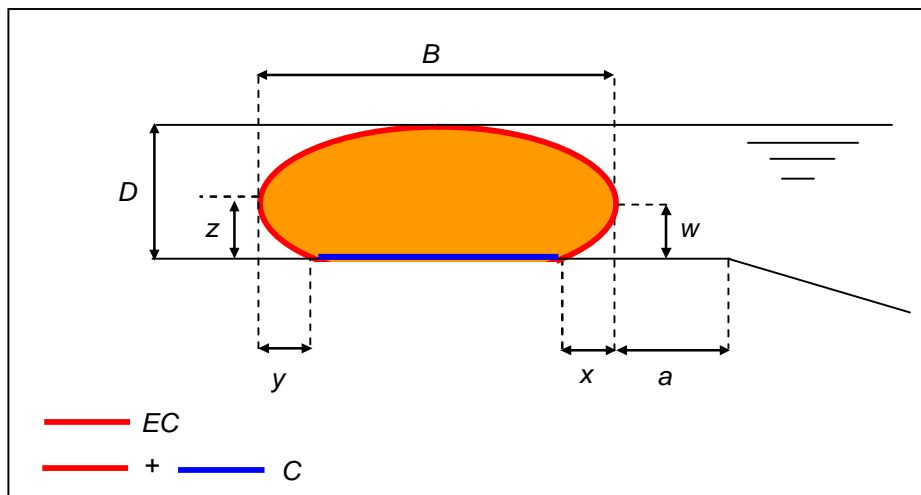


Figure 2.7 Overview of characteristic parameters of a geotextile tube

The characteristic dimensions of the geotextile tubes are indicated with the measured and derived geometric parameters:

#### Measured geometric parameters:

$a$	=	distance between geotextile tube and seaward side of the supporting structure table (m)
$B_i$	=	width of the geotextile tube at line $i$ (m)
$D_i$	=	height of the geotextile tube at line $i$ (m)
$C_{empty}$	=	circumference of empty geotextile tube (m)
$EC_i$	=	exposed circumference at line $i$ (m)
$L$	=	length of the geotextile tube (m)
$x_i$	=	characteristic distance as shown in Figure 2.7 at line $i$ (m)
$y_i$	=	characteristic distance as shown in Figure 2.7 at line $i$ (m)
$w_i$	=	characteristic distance as shown in Figure 2.7 at line $i$ (m)
$z_i$	=	characteristic distance as shown in Figure 2.7 at line $i$ (m)

Parameters  $B_i$ ,  $D_i$ ,  $EC_i$ ,  $x_i$ ,  $y_i$ ,  $w_i$ ,  $z_i$  have been measured before and after each test series. This is indicated with a 'b' (before a test series) or an 'a' (after a test series) i.e.  $B_{1,a}$  is the measured width of the geotextile tube at line 1 (see Figure 2.5) after a test series,  $B_{1,b}$  is the measured width at line 1 before a test series. The parameters that have been measured at four positions are averaged i.e.  $B_{a,avg}$  is the averaged width after a test series. The averaged values before and after each test are also averaged resulting in an 'overall' averaged parameter, i.e.  $B_{avg}$ . This is summarized in the equations (2.21) (2.22) and (2.23).

$$P_{a,avg} = \frac{\sum_{i=1}^n P_{a,i}}{n} \quad (2.21)$$

$$P_{b,avg} = \frac{\sum_{i=1}^n P_{b,i}}{n} \quad (2.22)$$

$$P_{avg} = \frac{P_{a,avg} + P_{b,avg}}{2} \quad (2.23)$$

Where  $P$  indicates one of the parameters  $B_i$ ,  $C_i$ ,  $D_i$ ,  $EC_i$ ,  $x_i$ ,  $y_i$ ,  $w_i$ , or  $z_i$ .

### Derived geometric parameters:

Based on the hand measurements the following parameters have been derived:

$A$  = Derived surface of cross section of an actual filled tube ( $m^2$ ). This surface is determined based on the theoretical graphs shown in Figure B.1 of Appendix B

$A_{100\%}$  = Derived theoretical surface of cross section of a tube which is 100% filled ( $m^2$ ). Stretching of the geotextile is not taken into account. The surface is determined with the following formula:

$$A_{100\%} = \pi R_{100\%}^2 \quad (2.24)$$

$C_i$  = Derived circumference of a filled tube at line  $i$  (m). This length is calculated with the following formula:

$$C_i = B_i - x_i - y_i + EC_i \quad (2.25)$$

$p_A$  (%) = The filling percentage based on the cross sectional area (%). This is determined by the following formula:

$$p_A = \frac{A}{A_{100\%}} \cdot 100\% \quad (2.26)$$

$p_h$  = The filling percentage based on the height (%). This is determined by the following formula:

$$p_h = \frac{h}{h_{100\%}} \quad (2.27)$$

$R_{100\%}$  = The radius when a geotextile tube is (theoretically) 100 % filled (m). Stretching of the geotextile tube is not taken into account in this approach. The radius is determined by measuring the circumference ( $C_{empty}$ ) of an empty geotextile tube. The radius has been determined with the use of Equation (2.28):

$$R_{100\%} = \frac{C_{empty}}{2 \cdot \pi} \quad (2.28)$$

$dU$  = Relative deformation of parameter  $U$ , where  $U$  indicates the parameter  $B_i$ ,  $C_i$ ,  $D_i$ ,  $EC_i$ ,  $x_i$ ,  $y_i$ ,  $w_i$ , or  $z_i$  (%). This relative deformation has been determined with the use of Equation (2.29):

$$dU = \frac{U_a - U_b}{U_b} \cdot 100\% \quad (2.29)$$



### 2.4.3 Displacement with the use of camera techniques

During the experiments a video camera recorded the test series from above. Several marker points were added on the geotextile tubes (see Appendix C, photo 17). By using these marker points in post processing software, the positions of the markers before and after a test have been determined. By subtracting the positions of the markers before and after each test, the displacements have been derived. From the displacements of the individual marker points the average displacement of the tube as well as the maximum and the minimum displacement are obtained. All the presented displacements are parallel to the flume axis. It was visually observed that the tubes were only shifted and did not roll.

Displacement individual marker:

$$\Delta x_{i,j} = X_{a,i,j} - X_{b,i,j} \quad (2.30)$$

The average displacement of the tube is:

$$\Delta x_{avg,j} = \frac{\sum_{i=1}^n \Delta x_{i,j}}{n} \quad (2.31)$$

The minimum displacement of the tube is:

$$\Delta x_{min,j} = \min(\Delta x_{i,j}, \Delta x_{i+1,j}, \dots, \Delta x_{n,j}) \quad (2.32)$$

The maximum displacement of the tube is:

$$\Delta x_{max,j} = \max(\Delta x_{i,j}, \Delta x_{i+1,j}, \dots, \Delta x_{n,j}) \quad (2.33)$$

Where:

$i$	=	marker number
$j$	=	test number
$n$	=	number of markers on the tube
$\Delta x_{i,i}$	=	displacement of marker $i$ during test $j$ (m)
$\Delta x_{avg,j}$	=	averaged displacement of tube during test $j$ (m)
$\Delta x_{min,j}$	=	minimum displacement of tube during test $j$ (m)
$\Delta x_{max,j}$	=	maximal displacement of tube during test $j$ (m)
$X_{a,i,j}$	=	position of marker $i$ after the test $j$ (m)
$X_{b,i,j}$	=	position of marker $i$ before test $j$ (m)

Also the averaged, minimum and maximum cumulative displacements have been determined. The cumulative displacement represents the total displacement during a test series.

The cumulative displacement individual marker is:

$$\Delta x_{cum,i,j} = X_{a,i,j} - X_{b,1,j} \quad (2.34)$$

The cumulative average displacement of the tube is:

$$\Delta x_{avg,cum,j} = \frac{\sum_{i=1}^n \Delta x_{cum,i,j}}{n} \quad (2.35)$$

The cumulative minimum displacement of the tube is:

$$\Delta x_{min,cum,j} = \min(\Delta x_{cum,i,j}, \Delta x_{cum,i+1,j}, \dots, \Delta x_{cum,n,j}) \quad (2.36)$$

The cumulative maximum displacement of the tube is:

$$\Delta x_{\max,cum,j} = \max(\Delta x_{cum,i,j}, \Delta x_{cum,i+1,j}, \dots, \Delta x_{cum,n,j}) \quad (2.37)$$

Where:

$\Delta x_{cum,i,j}$	=	cumulative displacement of marker $i$ during test 1 until test $j$
$\Delta x_{avg,cum,j}$	=	average cumulative displacement of tube during test 1 until test $j$
$\Delta x_{\min,cum,j}$	=	minimum cumulative displacement of tube during test 1 until test $j$
$\Delta x_{\max,cum,j}$	=	maximum cumulative displacement of tube during test 1 until test $j$

#### 2.4.4 Sand characteristics

A Penetrologger was used to investigate geotechnical aspects of the sand. A Penetrologger measures the penetration force,  $F_p$  (kN), as function of the penetration depth,  $d_p$  (m), by pressing a cone through the sand (see Appendix C, photo 25). Based on the measured penetration force and the known cone surface, the pressure is calculated,  $P$  (Pa). This is an indication for the compaction of the soil. The measurements were performed before and after some test series. Before the Penetrologger measurements the water level was lowered to a level below the tube. For each measurement, three penetrations were performed per location. The measurements of the three samples are averaged,  $P_{ave}$  (Pa).

In addition, the unit weight,  $\gamma$  (kg/m<sup>3</sup>) of the sand was determined by using a split ring. The split ring has a volume of  $V_s = 5.74 \cdot 10^{-4} \text{ m}^3$  (see Appendix C, photo 26). The mass of a sample taken,  $m_s$  (kg) has been determined. After storing the sample in an oven for 24 hours the dry mass  $m_{s,dry}$  (kg) of the sample has been measured again. The difference between the weights gives the percentage of water,  $W$  (%) in the sample:

$$W = \frac{m_s - m_{s,dry}}{m_{s,dry} - m_{ring}} \cdot 100\% \quad (2.38)$$

Where:

$W$	=	percentage of water in sample (%)
$m_s$	=	mass of soil sample including the split ring (kg)
$m_{s,dry}$	=	mass of dry soil sample after drying for 24 hours in an oven including the split ring (kg)
$m_{ring}$	=	mass of split ring (kg)

To investigate a possible change in compaction during the test, samples were taken before and after a test series and the dry unit weights were compared with each other. Appendix A15 gives an overview of the samples taken and their locations.

To investigate the loss of sand (fine fraction) during a test series, a sample has been taken before and after a test. These samples are used to determine the grain distribution. The comparison between the different curves could tell something about the possible loss of fine fraction.

#### 2.4.5 Velocity measurements below the supporting structure

The water velocity below the supporting structure is measured with the use of three EMF (Electro Magnetic Flow) measuring instruments which were placed in the back flow channel. Since the averaged measured velocities were relatively low (below 1 m/s) no further analysis of this data was performed.

#### 2.4.6 Sand migration indicated with colour injections

To determine possible sand migration, the geotextile tubes were, prior to a test series, injected (three injections per location) with ink at specific locations indicated with the crossings of marking lines. The injections, with a length of  $L_{\text{needle}} = 20$  cm, formed several vertical coloured lines (see Appendix C, photo 27). After a test series, the geotextile was removed and three characteristics of the colour injection were determined. These are the deepest point of coloured sand below the geotextile,  $d_1$  (m), the highest point of coloured sand below the geotextile,  $d_2$  (m), and the relative distance between the needle insertion point in the geotextile and the highest point of coloured sand parallel to the geotextile,  $x$  (m). These characteristics are shown in Figure E.1. Figure 2.8 shows an example of a colour injection after a test series.

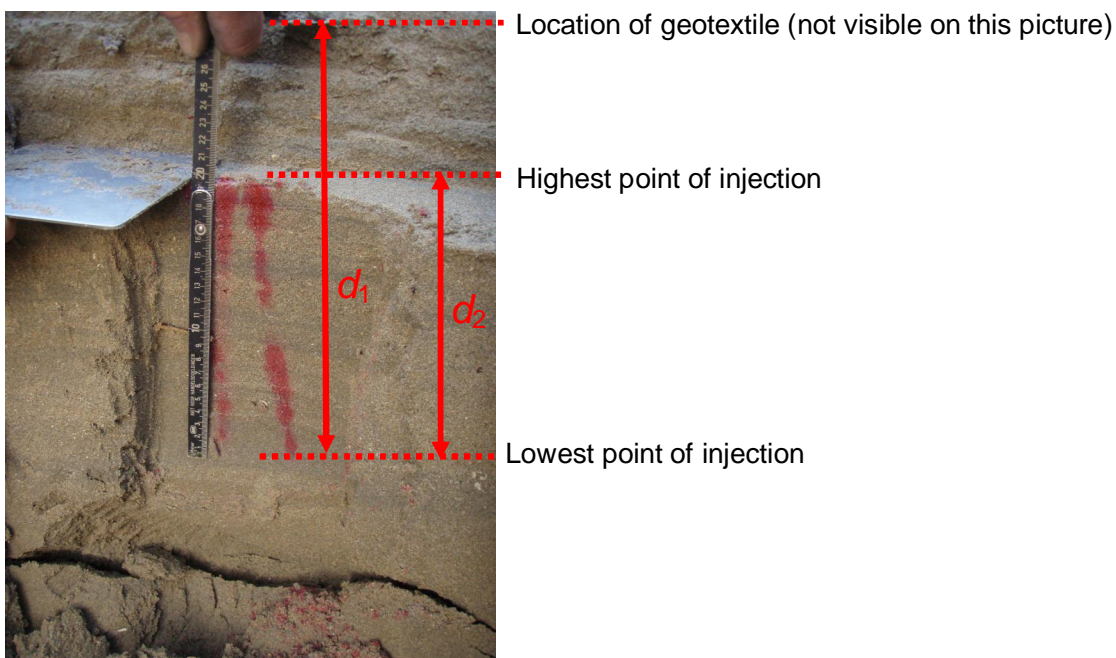


Figure 2.8 Example colour injection after a test series

For more details on the colour injections one is referred to Appendix E.

#### 2.4.7 Stretches in geotextile

Before and after each test the length between several marker lines were measured. An overview of the locations is given in Appendix B.8.



### 3 Experiments and results

In this chapter an overview of the experiments and the results are given. Only tests with special events are mentioned in the description.

#### 3.1 Test series F4: single tube ( $R_{100\%} = 0.57$ m, $p_A = 109$ %)

Test series F4 consisted of a single tube with an averaged width of  $B_{avg} = 1.52$  m and an average height of  $D_{avg} = 0.82$  m. The radius is  $R_{100\%} = 0.57$  m. The filling percentage based on the height is  $p_{h,avg} = 73$  %, the filling percentage based on the cross-section is  $p_A = 109$  % which indicates that the geotextile is stretched significantly during the filling process.

An overview of the measurements and the results are given in Table 3.1. Photographs are given in Appendix C, photo 28-29. A brief overview of the wave conditions and displacements are given in Table 3.2.

Table 3.1 Overview of measurements related to test series F4

Type of measurement	Performed?	When	Table	Figure	Photo
Profile machine	x	Before F4-1, after F4-6	-	B.3c	
Hand measurement (empty tube)	x	Before filling process	A.12	-	-
Hand measurement (filled tube)	x	Before and after test series	A.2-A.13	-	-
Wave measurements	x	During each test	A.1c	B.2e, B.2f	-
Penetrologger	x	Before F4-1 and after F4-6	-	B.6a-B.6c	-
Split ring	x	Before F4-1 and after F4-6	A.15a	-	
Grain distribution	x	Before F4-1 and after F4-6	-	B7	-
Stretches in geotextile	-	-	-	-	-
Colour injections	x	After test F4-6	A.16a	-	C, photo 53-54
Video camera	x	Before and after each test	A.14c	B.4c, B.5	-

Table 3.2 Overview results test series F4

Testname	$H_s$ (m)	$T_p$ (s)	$N$ (-)	$\Delta x_{avg}$ (m)	$\Delta x_{cum}$ (m)
F4-1	0.57	3.07	994	0.365	0.365
F4-2	0.41	3.02	696	-0.013	0.352
F4-3	0.48	2.84	966	0.006	0.358
F4-4	0.57	3.07	983	0.030	0.388
F4-5	0.67	3.34	1010	0.204	0.592
F4-6	0.75	3.65	1021	0.467	1.059

### Test description

Since test F4-1 was the first test in this test series and a significant displacement has been measured it was decided to perform the test F4-2 with a lower wave height.

The observed failure mechanism during test series F4 is horizontal sliding. The tube slid away in a landward direction. Almost no deformation of the geotextile tube occurred. Based on the sand colour injections it is concluded that hardly any sand movement occurred in the tubes (see appendix E).

### 3.2 Test series F1: single tube ( $R_{100\%} = 0.75$ m, $\rho_A = 66$ %)

Test series F1 consisted of a single placed tube with an averaged width of  $B_{avg} = 2.19$  m and an averaged height of  $D_{avg} = 0.57$  m. The radius is  $R_{100\%} = 0.75$  m, The filling percentage based on the height is  $\rho_h = 38$  %, and the filling percentage based on the cross-section is  $\rho_A = 66$  %.

Photographs are given in Appendix C, photo 30-32. A brief overview of the wave conditions and displacements are given in Table 3.4.

Table 3.3 Overview of measurements related to test series F1

Type of measurement	Performed?	When	Table	Figure	Photo
Profile machine	x	Before F1-1, after F1-1, F1-4, F1-6, F1-8	-	B.3a	-
Hand measurement (empty tube)	x	Before filling process	A.12	-	-
Hand measurement (filled tube)	x	Before and after test series	A.2-A.13	-	-
Wave measurements	x	During each test	A.1a	B.2a, B.2b	-
Penetrologger	x	Before F1-1, after F1-8	-	B.6d-B.6k	-
Split ring	x	Before F1-1, after F1-8	A.15b	-	-
Grain distribution	-	-	-	-	-
Stretches in geotextile	x	Before F1-1, after F1-8	-	B.8a	-
Colour injections	x	After test F1-8	A.16b	-	C, photo 50-51
Video camera	x	Before and after each test	A.14a	B.4a, B.5	-

Table 3.4 Overview results test series F1

Testname	$H_s$ (m)	$T_p$ (s)	$N$ (-)	$\Delta x_{avg}$ (m)	$\Delta x_{cum}$ (m)
F1-1	0.36	2.47	935	0.003	0.003
F1-2	0.42	2.63	1029	0.011	0.013
F1-3	0.49	2.88	1030	0.015	0.028
F1-4	0.56	3.11	979	0.010	0.038
F1-5	0.67	3.37	998	0.030	0.068
F1-6	0.76	3.63	1013	0.016	0.084
F1-7	0.88	4.02	998	0.026	0.110
F1-8	1.00	4.46	1047	0.037	0.147
F1-9	1.17	5.01	1037	0.377	0.524
F1-10	1.28	5.33	75	1.069	1.593

#### Test description

Due to technical problems test F1-9 was aborted after a number of waves of  $N = 391$  and restarted as test F1-91. After a number of waves of  $N = 400$ , the same technical problems occurred and the test was aborted and restarted again as test F1-92 which consisted of a number of waves of  $N = 246$ .

Since the geotextile tube moved almost directly after the start of test F1-10, it was decided to abort the test.

The observed failure mechanism during test series F1 is horizontal sliding. The tube slid away in a landward direction. During Test F1-10 the geotextile tube was lifted by an individual wave and “dropped” 1 m further. After this movement the geotextile tube was deformed heavily (see Appendix C, photo 31). Based on the sand colour injections it is concluded that a lot of sand movement occurred in the tubes (see appendix E).

### 3.3 Test series F3: single tube ( $R_{100\%} = 0.75$ m, $p_A = 80$ %)

Test series F3 consisted of a single placed tube with an averaged width of  $B_{avg} = 2.04$  m and the averaged height of  $D_{avg} = 0.79$  m and a radius of  $R_{100\%} = 0.75$  m. The filling percentage based on the height is  $p_h = 53$  %, and the filling percentage based on the cross-section is  $p_A = 80$  %.

Photographs are given in Appendix C, photo 33-35. A brief overview of the wave conditions and displacements are given in Table 3.6.

Table 3.5 Overview of measurements related to test series F3

Type of measurement	Performed?	When	Table	Figure	Photo	Appendix
Profile machine	x	After F3-1, F3-5, F3-6, F3-8, F3-9	-	B.3b	-	-
Hand measurement (empty tube)	x	Before filling process	A.12	-	-	-
Hand measurement (filled tube)	x	Before and after test series	A.2-A.13	-	-	-
Wave measurements	x	During each test	A.1b	B.2c, B.2d	-	-
Penetrologger	x	Before F3-1, after F3-9	-	B.6l-B.6r	-	-
Split ring	x	Before F3-1, after F3-9	A.15c			
Grain distribution	-	-	-	-	-	-
Stretches in geotextile	x	Before F3-1, after F3-9	-	B.8b	-	-
Colour injections	x	After test F3-9	A.16c	-	C, photo 52	A.16b
Video camera	x	Before and after each test	A.14b	B.4b, B.5	-	-

Table 3.6 Overview results test series F3

Testname	$H_s$ (m)	$T_p$ (s)	$N$ (-)	$\Delta x_{avg}$ (m)	$\Delta x_{cum}$ (m)
F3-1	0.42	2.64	985	0.002	0.002
F3-2	0.52	2.91	963	0.021	0.023
F3-21	0.49	2.88	985	0.006	0.029
F3-3	0.56	3.10	975	-0.001	0.029
F3-4	0.66	3.34	992	0.031	0.060
F3-5	0.77	3.67	983	0.037	0.097
F3-6	0.87	4.02	1011	0.055	0.151
F3-61	0.87	4.02	1009	0.087	0.238
F3-7	1.00	4.45	1033	0.038	0.276
F3-8	1.17	5.02	990	0.070	0.347
F3-9	1.32	5.59	1034	1.198	1.544

### Test description

Since it was assumed that wrong conditions were used during test F3-2, this test is repeated as test F3-21. An adapted steering file was used.

Since some shifting of the tube occurred during test F3-6, it was decided to re-run test F3-6 as F3-61.



The observed failure mechanism during test series F3 is horizontal sliding. The tube slid away in a landward direction. The geotextile tube deformed noticeable. Based on the sand colour injections it is concluded that some sand movement occurred in the tubes (see appendix E).

### 3.4 Test series T1: single tube with trench ( $R_{100\%} = 0.76$ m, $p_A = 85$ %)

Test series T1 consisted of a single placed tube with an averaged width of  $B_{avg} = 2.03$  m, an averaged height of  $D_{avg} = 0.88$  m and a radius of  $R_{100\%} = 0.76$  m. The filling percentage based on the height is  $p_{h,avg} = 58$  %, the filling percentage based on the cross-section is  $p_A = 85$  %. At the landward side of the tube a bar has been placed to simulate a trench.

Photographs are given in Appendix C, photo 36-41. A brief overview of the wave conditions and displacements are given in Table 3.8

Table 3.7 Overview of measurements related to test series T1

Type of measurement	Performed?	When	Table	Figure
Profile machine	x	Before T1-1, after T1-1, T1-5, T1-8, T1-9	-	B.3e
Hand measurement (empty tube)	x	Before filling process	A.12	-
Hand measurement (filled tube)	x	Before and after test series	A.2-A.13	-
Wave measurements	x	During each test	A.1g	B.2l, B.2m
Penetrologger	x	Before and after test series	-	B.6s-B.6v
Split ring	-	-	-	-
Grain distribution	-	-	-	-
Stretches in geotextile	-	-	-	-
Colour injections	-	-	A.16d	-
Video camera	x	Before and after each test	A.14e	B.4e, B.5

Table 3.8 Overview results test series T1

Testname	$H_s$ (m)	$T_p$ (s)	$N$ (-)	$\Delta x_{avg}$ (m)	$\Delta x_{cum}$ (m)
T1-0	0.61	3.04	414	0.051	0.051
T1-1	0.56	3.07	1038	0.016	0.067
T1-2	0.68	3.34	1008	0.011	0.078
T1-3	0.76	3.72	1033	0.025	0.103
T1-4	0.87	4.02	1014	0.057	0.160
T1-5	1.01	4.47	993	0.050	0.210
T1-6	1.15	5.04	1001	0.370	0.247
T1-7	1.35	5.64	1027	0.091	0.338
T1-8	1.49	6.39	1023	0.149	0.487
T1-9	1.50	6.36	2021	0.241	0.728

### Test description

During the first test (test T1-0) it was realized that a wrong input file has been used and the test was aborted after  $N = 414$  waves.

Since the maximum capacity of the wave machine was reached with test T1-8, it was not possible to increase the wave height. Therefore, it was decided to perform the same test as test T1-9 with around 2000 waves.

The observed failure mechanism during test series T1 is horizontal sliding. The tube slid away in a landward direction and shifted partly on the bar. The tube deformed heavily. Based on the sand colour injections it is concluded that some sand movement occurred in the tubes (see appendix E).

### 3.5 Test series P3: 2-1 stack

Test series P3 consisted of three tubes. The averaged radius derived from measurements is  $R_{100\%} = 0.57$  m (based on tube B), the averaged width per element is  $B_{avg} = 1.47$  m and the averaged height per element is  $D_{avg} = 0.71$  m. The filling percentage based on the height is  $p_{h,avg} = 62$  % and  $p_{h,avg} = 61$  % for respectively tube A and tube B. The filling percentage based on the cross-section is  $p_A = 86$  % and 89 % for respectively tube A and tube B.

Photographs are given in Appendix C, photo 42-44. A brief overview of the wave conditions and displacements are given in Table 3.10.

Table 3.9 Overview of measurements related to test series P3

Type of measurement	Performed?	When	Table	Figure
Profile machine	x	Before P3-1, after P3-9	-	B.3g
Hand measurement (empty tube)	x	Before filling process	A.12	-
Hand measurement (filled tube)	x	Before and after test series	A.2-A.13	-
Wave measurements	x	During each test	A.1f	B.2j, B.2k
Penetrologger	-	-	-	-
Split ring	-	-	-	-
Grain distribution	-	-	-	-
Stretches in geotextile	-	-	-	-
Colour injections	-	-	-	-
Video camera	x	Before and after each test	-	-

Table 3.10 Overview results test series P3

Testname	$H_s$ (m)	$T_p$ (s)	$N$ (-)	$\Delta x_{avg}$ (m)	$\Delta x_{cum}$ (m)
P3-1	0.44	2.64	1013	0.00	0.00
P3-2	0.51	2.88	1006	0.00	0.00
P3-3	0.58	3.08	1048	0.00	0.00
P3-4	0.66	3.34	1030	0.00	0.00
P3-5	0.76	3.64	1035	0.00	0.00
P3-6	0.89	4.05	979	0.00	0.00
P3-7	1.02	4.48	1012	0.00	0.00
P3-8	1.16	5.04	1012	see description	
P3-9	1.37	5.50	282	see description	

### Test description

No significant movements were observed until test P3-7.

During test P3-8 slight movements of the tubes were observed. Tube A moved 0.04 m in landward direction on Line 1 and Line 2 and 0.02 m on landward direction on Line 3 and Line 4. Tube B did not move on Line 1 but moved 0.04 m in seaward direction on Line 2 and 0.10 m in seaward direction on Line 3 and Line 4. Tube C did not move on Line 1 but moved 0.01 m, 0.02 m and 0.03 m in seaward direction on respectively Line 2, Line 3 and Line 4. The position of Line 1,2,3 and 4 is given in Figure 2.5 on page 14.

During test P3-9, tube B and tube C slid in seaward direction as shown on Photo 3.1.

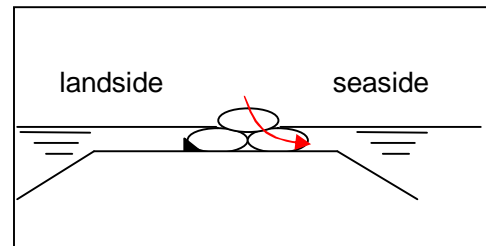
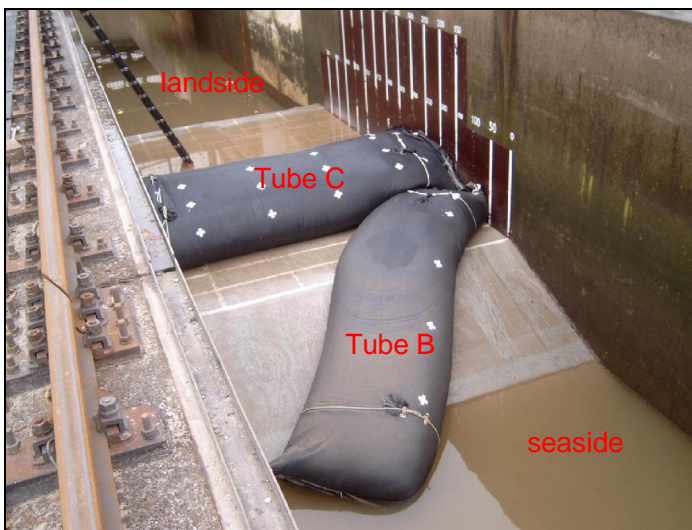


Photo 3.1 Geotextile tube after test P3-9

The observed failure mechanism during test series P3 is comparable with a slip circle, where the lowest tube at the seaward side (B) slides away, followed by the top tube (C) of the stack. The observed deformations for tube A are marginal. Due to the failure tube B and C were deformed.

### 3.6 Test series P2: 2 tubes placed behind each other

Test series P2 consisted of two tubes placed behind each other. The radius derived from measurements is  $R_{100\%} = 0.77$  m, the averaged width is  $B_{avg} = 1.99$  m and the averaged height is  $D_{avg} = 0.84$  m. The filling percentage based on the height is  $p_{h,avg} = 57\%$  and  $p_{h,avg} = 55\%$  for respectively tube A and tube B. The filling percentage based on the cross-section is  $p_A = 78\%$  and  $p_B = 76\%$  for respectively tube A and tube B.

Photographs are given in Appendix C, photo 45-46. A brief overview of the wave conditions and displacements are given in Table 3.12.

Table 3.11 Overview of measurements related to test series P2

Type of measurement	Performed?	When	Table	Figure
Profile machine	x	Before P2-1, after P2-42	-	B.3f
Hand measurement (empty tube)	x	Before filling process	A.12	-
Hand measurement (filled tube)	x	Before and after test series	A.2-A.13	-
Wave measurements	x	During each test	A.1e	B.2i
Penetrologger	-	-	-	-
Split ring	-	-	-	-
Grain distribution	-	-	-	-
Stretches in geotextile	-	-	-	-
Colour injections	-	-	-	-
Video camera	x	Before and after each test	A.14f	B.4f,B5

Table 3.12 Overview results test series P2

Testname	$H_s$ (m)	$T_p$ (s)	$N$ (-)	$\Delta x_{avg}$ (m) (tube A)	$\Delta x_{cum}$ (m) (tube A)
P2-1	0.88	3.99	1016	0.018	0.018
P2-2	1.00	4.44	1003	0.219	0.237
P2-3	1.14	4.96	1011	0.063	0.300
P2-4	1.38	5.63	568	1.08	1.380

#### Test description

Due to technical problems test P2-1 was aborted after a number of waves of  $N = 592$  and restarted as test P2-21, which consisted of a number of waves of  $N = 420$ .

Due to technical problems test P2-2 was aborted and restarted three times as test P2-21, P2-22 and P2-23. Due to a human error a wrong signal was sent to the wave board during test P2-21. This caused the generation of a single wave with a wave height of  $H = 1.83$  m which resulted in a severe displacement of tube A. Tube B did not move.

Due to technical problems test P2-3 was aborted and restarted two times as test P2-31, P2-32. Tube B did not move.

Due to technical problems test P2-4 was aborted and restarted two times as test P2-41 and P2-42. Tube B did not move but was heavily deformed.

The observed failure mechanism during test series P2 is horizontal sliding. This is only the case for tube A. Tube A slide away in a landward direction. Tube B did not move at all during the test. Tube A and tube B deformed heavily.

### 3.7 Test series F5: single tube ( $R_{100\%} = 0.76$ m, $p_A = 72$ %)

Test series F5 consisted of a single placed tube which is filled to its (practical) maximum. The tube used is tube B of test series P2 and was already heavily deformed. The radius derived from measurements is  $R_{100\%} = 0.76$  m, the averaged width is  $B_{avg} = 2.02$  m and the averaged height is  $D_{avg} = 0.74$  m. The filling percentage based on the height is  $p_{h,avg} = 48$  %, the filling percentage based on the cross-section is  $p_A = 72$  %.

Photographs are given in Appendix C, photo 47-49. A brief overview of the wave conditions and displacements are given in Table 3.14.

Table 3.13 Overview of measurements related to test series F5

Type of measurement	Performed?	When	Table	Figure
Profile machine	x	Before F5-1 (=after P2-4), After F5-6	-	B.3d
Hand measurement (empty tube)	x	Before filling process	A.12	-
Hand measurement (filled tube)	x	Before and after test series	A.2-A.13	-
Wave measurements	x	During each test	A.1d	B.2g, B.2h
Penetrologger	-	-	-	-
Split ring	-	-	-	-
Grain distribution	-	-	-	-
Stretches in geotextile	-	-	-	-
Colour injections	-	-	-	-
Video camera	x	Before and after each test	A.14d	B.4d, B5

Table 3.14 Overview results test series F5

Testname	$H_s$ (m)	$T_p$ (s)	$N$ (-)	$\Delta x_{avg}$ (m)	$\Delta x_{cum}$ (m)
F5-1	0.67	3.35	1005	0.029	0.029
F5-2	0.77	3.70	984	-0.004	0.025
F5-3	0.88	4.05	999	0.045	0.070
F5-4	1.03	4.50	999	0.013	0.082
F5-5	1.16	5.06	997	0.050	0.132
F5-6	1.36	5.65	991	0.645	0.777

### Test description

The observed failure mechanism during test series F5 is horizontal sliding. The tube slide in a landward direction. The tube deformed significantly.







## 4 Analysis

### 4.1 Introduction

In Lawson (2008), nine failure mechanisms are discussed. Six failure mechanisms are related to external loads:

- sliding instability
- overturning instability
- bearing instability
- global instability
- scour of the subsurface
- subsurface settlement.

Three failure mechanisms are internal:

- tearing of geotextile,
- loss of fill material through the geotextile
- deformation of the sand core (fill material).

This chapter focuses on two failure mechanisms that are relevant with respect to the results obtained from the experiments:

- Sliding instability
- Deformation of the contained fill

### 4.2 Sliding instability

#### 4.2.1 Introduction

This section focuses on a geometry such as described in Chapter 2. A schematization of this typical geometry is given in Figure 4.1.

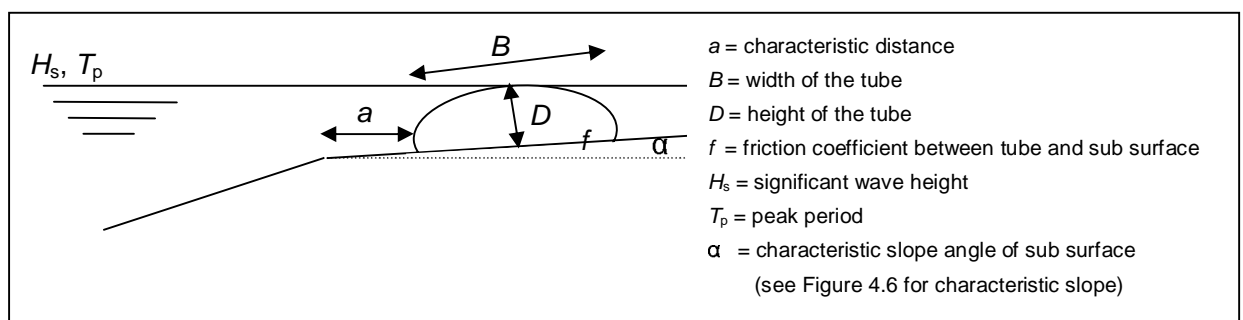


Figure 4.1 Schematization of geometry that will be analysed for the mechanism sliding

Several tests have been performed and are described in this report. During all the tests the observed failure mechanism was sliding of the tubes. This failure mechanism will be discussed extensively in this section. The analysis is based on the average displacement per test,  $\Delta x_{avg}$  (during a loading of approximately 1000 waves) and the cumulative displacement after a test,  $\Delta x_{cum}$ . Since test series F4 was restarted after test F4-1 with a lower significant wave height this series is considered as two series; F4a consisting of test F4-1 and F4b consisting of test F4-2 until F4-6.

The main goal of this section is to find a physically sound dimensionless parameter, based on the data derived from the present Delta Flume tests, and which can be used for engineering purposes.

In the next sections, the wave height is corrected for the absorbed wave energy (Section 4.2.3) and is made dimensionless with the dimensions of the tube (Section 4.2.4). The dimensionless parameter found is corrected for the slope of the supporting structure (see Figure 2.1) on which the tube is placed and the friction coefficient between the geotextile and its subsoil (Section 4.2.5). Limitations of this research are given in Section 4.2.6.

## 4.2.2 Overview test results

The results of the tests, based on the significant wave height,  $H_s$ , are shown in Figure 4.2.

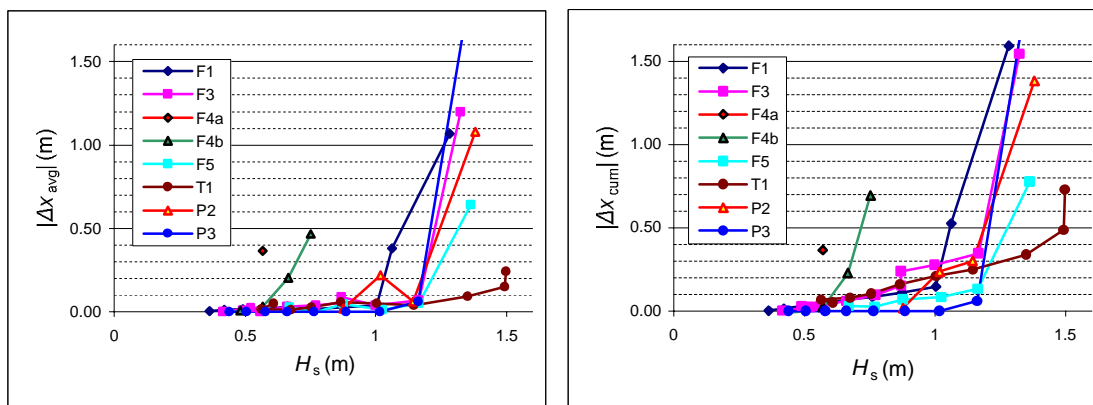


Figure 4.2 Results as function of the significant wave height,  $H_s$

In Figure 4.2, the significant wave height is plotted against the displacement per test (left figure) and the cumulative displacement (right figure). It can be seen that the horizontal axes is not dimensionless and that the results are not uniform.

## 4.2.3 Reduction factor for absorbing wave energy, $\chi$

During the tests the waves break on the structure. This results in transmitted wave energy over the structure, reflected wave energy and dissipated wave energy. The dissipated and reflected wave energy leads to forces on the structure. Not all the dissipated and reflected energy leads to forces on the geotextile tube since a part of this wave energy leads to forces on the supporting structure placed under the geotextile tube. Therefore, it is stated that the real wave load is not characterized by the incoming wave height,  $H_s$ , but by a reduced wave load,  $\chi H_s$ , with  $\chi$  being a reduction parameter. The values of  $\chi$  are determined with an empirical formula for wave transmission. This formula is based on Van der Meer et. al. (2004). Appendix I describes how the reduction parameter  $\chi$  is determined. This results in the following two formulae:

$$\chi = \sqrt{C_{t,ss}^2 - C_{t,ss+tube}^2} \quad (4.1)$$

$$C_t = \left( -0.3 \frac{R_c}{H_s} + 0.75(1 - e^{-0.5\xi_p}) \right) \cos^{2/3} \beta \quad (4.2)$$

Where  $C_t$  has a minimum ( $C_t = 0.075$ ) and a maximum value ( $C_t = 0.8$ ). In addition the following limitations apply:  $1 < \xi_p < 3$ ;  $0^\circ \leq \beta \leq 70^\circ$ ;  $1 < B_{crest}/H_s < 4$ .

Where

$C_t$	=	transmission coefficient
$C_{t,ss}$	=	transmission coefficient in a situation with only the supporting Structure (-)
$C_{t,ss+tube}$	=	transmission coefficient in a situation with the supporting structure and the tube (-)
$H_s$	=	significant wave height (m)
$R_c$	=	crest height (m)
$\beta$	=	angle of wave incidence ( $^\circ$ )
$\xi_p$	=	breaker parameter (-)
$\chi$	=	wave absorption correction factor (-)

Since it can be unpractical to determine  $\chi$  with the use of the given formulae a design curve has been derived. The background of this curve is given in Appendix I. The following assumptions have been made to create this graph:

- Perpendicular wave attack on the structure is assumed ( $\beta = 0^\circ$ ).
- The water level is equal to the highest point of the tube
- The formula given in Van der Meer et. al. (2004) serves as a basis for the transmission of wave energy over the structure.

The graph is shown in Figure 4.3.

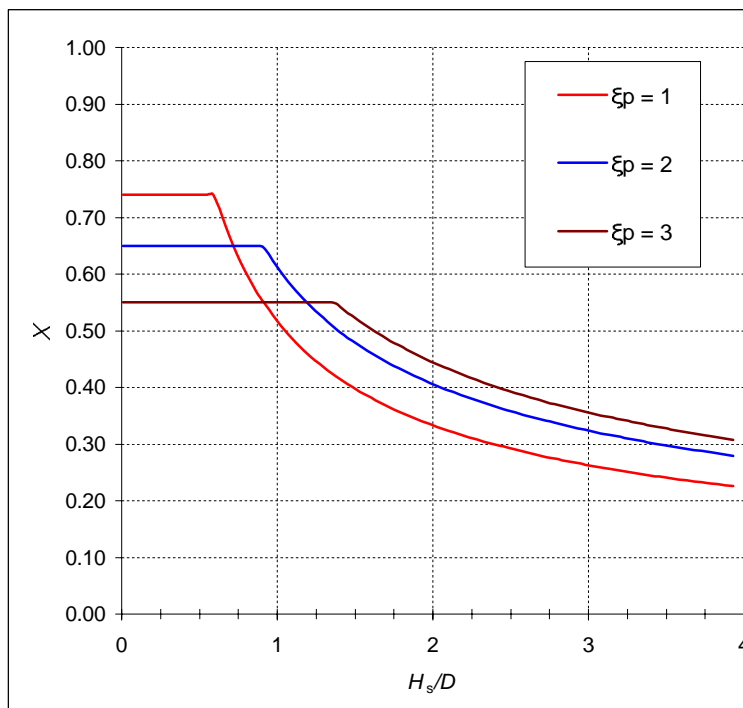
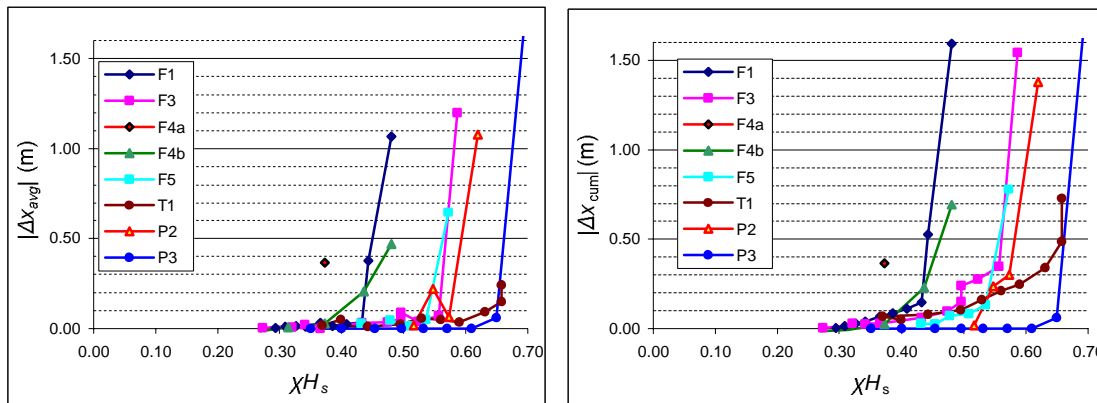


Figure 4.3 Design curve to determine  $\chi$  (assuming perpendicular wave attack and a water level equal to the top of the tube)

On the horizontal axis the ratio between the wave height,  $H_s$  and the tube height,  $D$ , is shown. The wave height reduction parameter,  $\chi$ , is plotted on the vertical axis.

The above described wave height reduction parameter,  $\chi$ , is applied in the following sections.



#### 4.2.4 Choice of stability parameter

Stability formulae based on several small-scale model tests have been described and summarized in Pilarczyk (2000) and CUR (2006). The derived stability parameters are usually based on Froude scaling laws, in e.g.  $H_s/(\Delta D) = \text{constant}$  or  $H_s/(\Delta B) = \text{constant}$ . In Van Steeg and Klein Breteler (2008) a stability number  $H_s/(\Delta\sqrt{BD})$  is suggested. This is based on a large-scale physical model test on the stability of geotextile containers described in the same report. Since literature does not give an unambiguous answer which parameter should be used a theoretical analysis is performed and described in Appendix G. This theoretical derivation, based on the stability of rubble mound slopes against sliding, resulted in Equation (4.3)

$$\frac{H}{\Delta\sqrt{BD}} < \frac{\sqrt{\lambda}}{\varphi^2(C_D + fC_L\lambda)} (f \cos \alpha \pm \sin \alpha) \quad (4.3)$$

Where

- $H$  = wave height (m)
- $\Delta$  = relative density ( $\Delta = (\rho_s - \rho_w)/\rho_w$ ) (-)
- $B$  = width of element (m)
- $D$  = thickness or height of elements (m)
- $\lambda$  = shape factor ( $\lambda = B/D$ ) (-)
- $\varphi$  = wave-velocity coefficient (-)
- $C_D$  = drag coefficient (-)
- $C_L$  = lift coefficient (-)
- $f$  = friction coefficient (-)
- $\alpha$  = slope ( $^\circ$ )

For an extensive description of the parameters, reference is made to Appendix G. The theoretical background of this Equation (4.3) gives a better insight in some important physical processes that occur during a breaking wave on a geotextile encapsulated sand element. Equation (4.3) can be considered as a basis for more applied stability parameters. However, for practical applications the formula is not suitable since it is very difficult to determine several parameters such as the drag coefficient,  $C_D$ , the lift coefficient,  $C_L$ , and the wave-

velocity parameter  $\varphi$ . Equation (4.3) shows that the use of  $H/(\Delta\sqrt{BD})$  is not a proper dimensionless parameter since this parameter is a function of the shape factor,  $\lambda (= B/D)$ , of the element. The main question that is raised is which dimensionless stability number can be used for engineering purposes (for example  $H_s/(\Delta D)$ ,  $H_s/(\Delta B)$  or  $H_s/(\Delta\sqrt{BD})$ ).

It is possible to simplify Equation (4.3) by assuming that no lift forces or no drag forces occur. In case no lift forces occur, the lift coefficient is equal to  $C_L = 0$  and Equation (4.3) is rewritten:

$$\text{No lift forces: } \frac{H}{\Delta B} < \frac{1}{\varphi^2 C_D} (f \cos \alpha \pm \sin \alpha) \quad (4.4)$$

In case that no drag forces occur, the drag coefficient is equal to  $C_D = 0$  and Equation (4.3) is rewritten

$$\text{No drag forces: } \frac{H}{\Delta D} < \frac{1}{f \varphi^2 C_L} (f \cos \alpha \pm \sin \alpha) \quad (4.5)$$

It is quite unlikely that  $H_s/(\Delta D)$  is a representative parameter since this assumes that drag forces can be neglected (see analysis in Appendix G). Therefore a choice has to be made between  $H_s/(\Delta\sqrt{BD})$  and  $H_s/(\Delta B)$ . When using the parameter  $H_s/(\Delta B)$  it implies that lift forces play no significant roll and can be neglected. It is unknown whether lift forces were significant during the test series or not. This will be determined based on the test results, plotted in Figure 4.4.

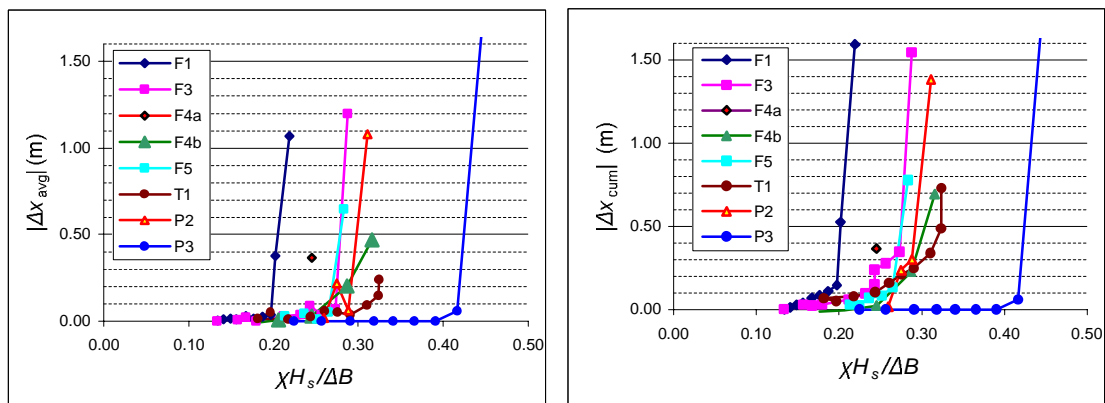


Figure 4.4 Results based on the dimensionless parameter  $\chi H_s / (\Delta B)$

In Figure 4.4 it can be seen that all the test series except F1 (lowest filling rate), P3 (2-1 stack) and F4a, fit in this figure. Since the failure mechanism in series P3 was different from the other test series, this series is not included in the analysis. Series F1 does not fit well in Figure 4.4. This is explained by the lift mechanism which is excluded when choosing the dimensionless parameter  $\chi H_s / \Delta B$ . However, it is very likely that the lift mechanism did play an important role at test series F1. The lift mechanism becomes more significant when applying a tube with a lower filling rate. Reference is made to Appendix G. To include the lift mechanism, the parameter  $\chi H_s / (\sqrt{\Delta BD})$  is used. The results are shown in Figure 4.5.

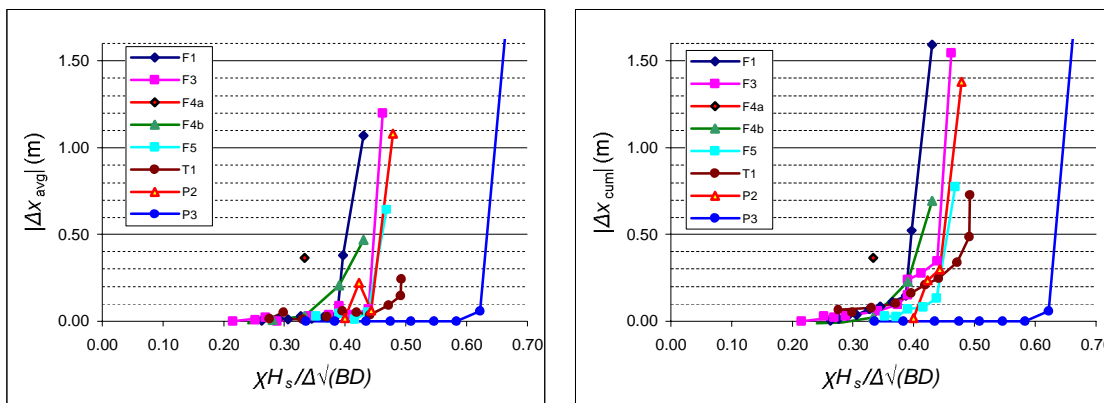


Figure 4.5 Results based on the dimensionless parameter  $\chi H_s / \Delta \sqrt{BD}$

It can be seen that there is a better data collapse in Figure 4.5 than in Figure 4.4.

#### 4.2.5 Correction for the slope angle, $\alpha$ , and the friction, $f$

The results shown in Figure 4.5 are not corrected for friction and the presence of a slope under the geotextile tube. A theoretical approach how to include the friction and the presence of a slope is given in Appendix G. This analysis resulted in Equation (4.3) and is rewritten as:

$$\frac{H}{\Delta \sqrt{BD} (f \cos \alpha \pm \sin \alpha)} < \frac{\sqrt{\lambda}}{\varphi^2 (C_D + f C_L \lambda)} \quad (4.6)$$

Or, when the slope angle is equal to  $\alpha = 0^\circ$ :

$$\frac{H}{f \Delta \sqrt{BD}} < \frac{\sqrt{\lambda}}{\varphi^2 (C_D + f C_L \lambda)} \quad (4.7)$$

Following the process described above, the stability criterion becomes:

$$\frac{\chi H_s}{\Delta \sqrt{BD} (f \cos \alpha + \sin \alpha)} \leq C \quad (\text{assuming no severe wave run down}) \quad (4.8)$$

$$\text{with } C = \frac{\sqrt{\lambda}}{\varphi^2 (C_D + f C_L \lambda)} \quad (4.9)$$

$\alpha$  is determined as indicated in Figure 4.6.

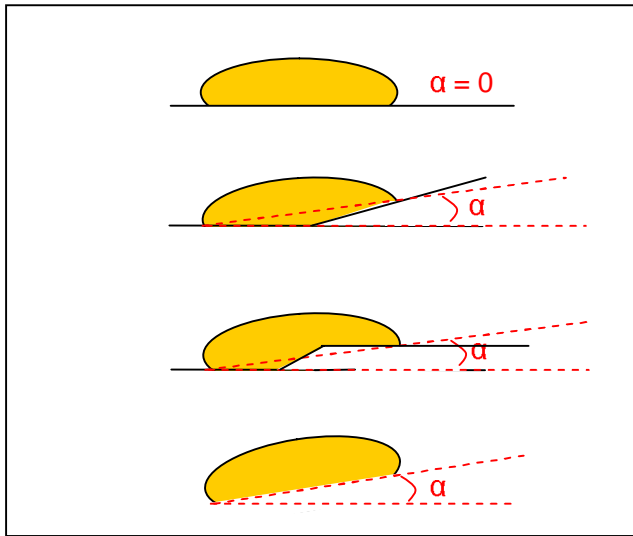


Figure 4.6 Determination of  $\alpha$

Since it is very unlikely that  $C_D$ ,  $C_L$  and  $\varphi$  will be determined for each specific situation and the fact that the coefficient  $f$  has not much influence since the lift forces are relatively small ( $fC_L\lambda$ ), these parameters are put into the 'dustbin' coefficient  $C$  which can be determined based on the experiments. The results are given in Figure 4.7.

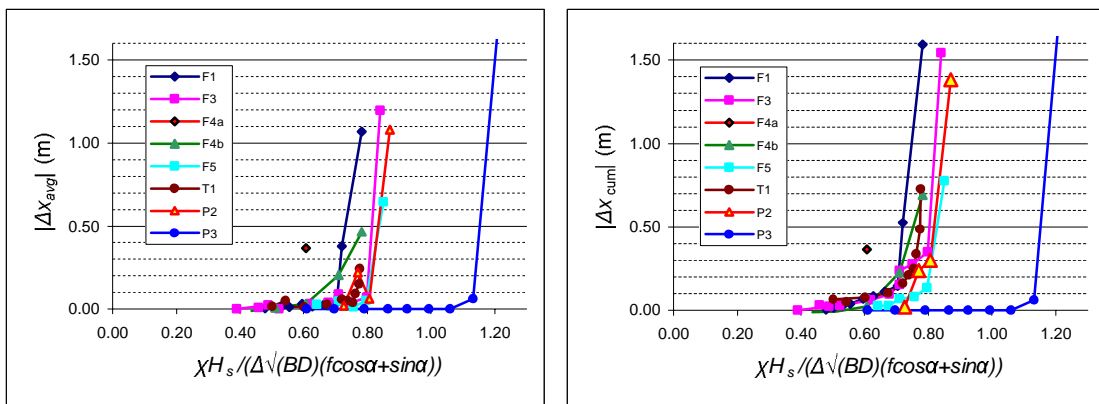


Figure 4.7 Results based on the dimensionless parameter  $\chi H_s / (\Delta \sqrt{BD})(f \cos \alpha + \sin \alpha)$

The displacements on the vertical axes have been made dimensionless with the width of the geotextile tubes. This is shown in Figure 4.8.

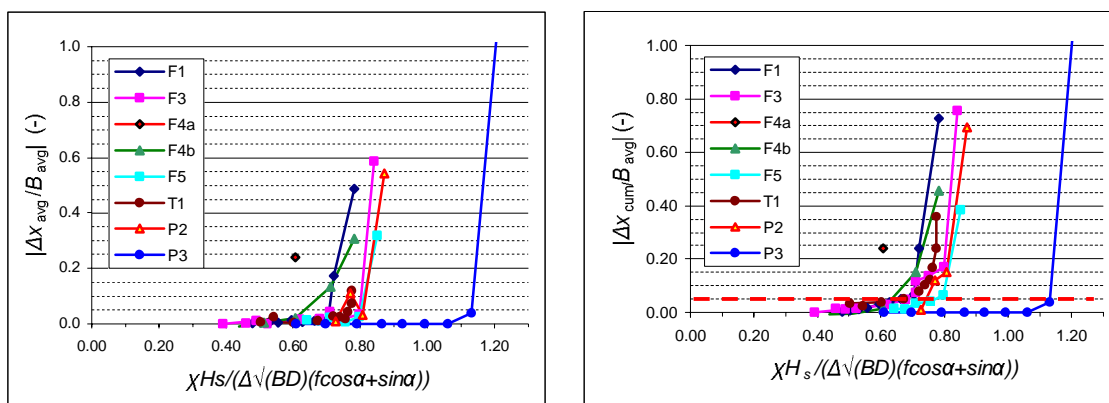


Figure 4.8 Results based on the dimensionless parameter  $\chi H_s / (\Delta \sqrt{BD} (f \cos \alpha + \sin \alpha))$  and the dimensionless parameter  $\Delta x_{avg} / B_{avg}$

In Figure 4.8, it can be seen that all test series except series F4a and P3 are comparable. Test F4a distinguishes from the other tests since the tube was placed in a more seaward direction and therefore under heavier wave attack (see also figure B.1a). This is discussed in the following section.

#### 4.2.6 Influence location geotextile tube

To determine the influence of the location of the geotextile tube on the stability a relation between the wave energy and the forces on the tube is assumed.

A schematized geometry of a geotextile tube and a foreshore is given in Figure 4.9.

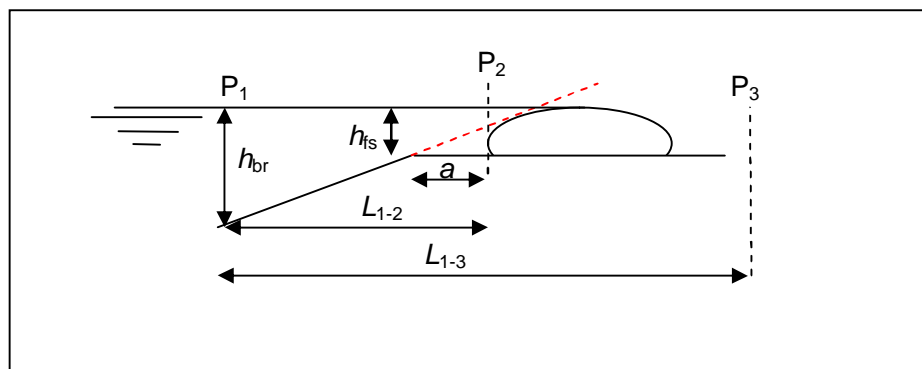


Figure 4.9 Schematized geotextile tube and foreshore

It is assumed that waves start to break at a certain point  $P_1$ , at a distance  $L_{1-2}$  from the seaward side of the geotextile tube. At point  $P_1$ , the wave energy is still 100% of its initial energy. From point  $P_1$ , the wave energy is dissipated by breaking. At a certain (fictitious) point  $P_2$ , the wave energy becomes constant low. The ratio between  $L_{1-2}$  and  $L_{1-3}$  and the shape of the declination of the wave energy (e.g. linear) determines which fraction of the wave energy reaches the front of the geotextile tube. Therefore there is a need to include the relevant parameters such as  $a$ ,  $L_{1-2}$  and  $L_{1-3}$  in the dimensionless parameter. It is very likely that these parameters depend on several other parameters (e.g. the breaker depth,  $h_{br}$ , the breaker parameter,  $\xi_p$ ). The distance  $L_{1-2}$  is strongly dependent on the parameter  $a$ . The analysis of the influence of this parameter is not the scope of this report. However, it is strongly recommended to perform a study to the influence of this parameter and include it in the dimensionless parameter.



The above-described phenomenon has been observed in test series F4a. The tube was relatively close to the seaward side of the supporting structure and therefore the geotextile tube absorbed a larger proportion of the wave energy. This is also visible in the results presented in Figure 4.7 where test F4a does not fit in the other test results.

It is assumed that the derived dimensionless parameter is valid for situations where the whole tube is placed at the landward side of the extension of the slope line (the red dotted line in Figure 4.9). In the test sections the tube was a little bit on the seaward side of the red dotted lines which implies that the suggested condition is conservative.

#### 4.2.7 Stability of test series P2 (2 tubes) and test series P3 (2-1 stack)

Test series P2 (2 tubes placed behind each other) and test series P3 (2-1 stack) differ from the other tests which all consisted of a single tube. A theoretical analysis on both series will be described in this section

##### *Test series P2*

Test series P2 is given schematically in Figure 4.10.

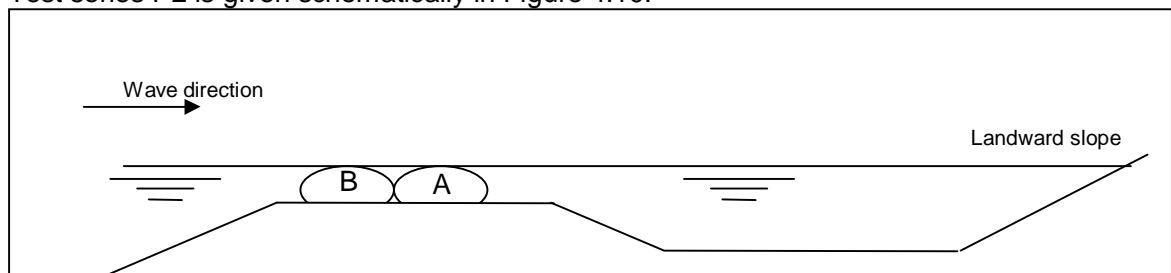
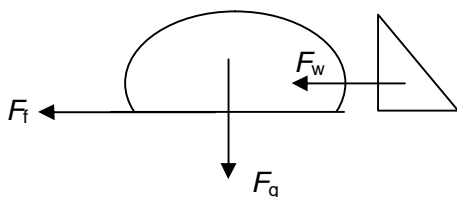


Figure 4.10 Schematisation of test series P2

Surprisingly, during the tests tube A started to shift in landward direction and tube B did not shift at all. This is explained by the fact that the water pressure at the landward side was different for both tubes.

The waves that overtopped the tubes travelled until the landward slope and reflected back to the tubes, resulting in a wave trough near tube A. It was visually observed that in some cases tube A was totally 'dry' at the landward side. Therefore, no resisting water pressure was present at the landward side of tube A. At the landward side of tube B there was a seaward force due to the water that was trapped in between tube A and tube B.

The ratio between the friction forces and resisting water forces is calculated below for tubes A and B, assuming a hydrostatic pressure at the landward side of the tube.



It is assumed that a tube which is dry on one side, and under water at the other side, can be considered as a tube under water (thus taking the underwater weight in Equation (4.10))

$$F_g = mg = (\rho_s - \rho_w) \cdot p_{AVG} \cdot \pi A_{100\%}^2 \cdot g = 14.0 \text{ kN} / \text{m} \quad (4.10)$$

$$F_f = fF_g = 7.7 \text{ kN} / \text{m} \quad (4.11)$$

$$F_w = \frac{1}{2} \rho g D^2 = 3.5 \text{ kN} / \text{m} \quad (4.12)$$

$$F_w + F_f = 11.1 \text{ kN} / \text{m} \quad (4.13)$$

$$\zeta = \frac{F_w}{F_w + F_f} = 0.32 \quad (4.14)$$

This suggests that the resisting forces against sliding are approximately 32 % higher for tube B than for tube A explaining why tube A shifted and tube B did not shift. Therefore, it has no added value to place two tubes behind each other when severe waves at the landward side of the tubes can occur. This can also be seen on the test results in Figure 4.8 where the relative displacement of test series F5 (the tube in test series F5 is tube B from test series P2) is almost equal to the relative displacement of tube A in test series P2.

In the above-described analysis, the dynamic forces are not taken into account. It should be realized that the dynamic forces on tube A were significant (based on visual observations).

### *Test series P3*

The set-up of test series P3 is given schematically in Figure 4.11.

The following situation is assumed:

- The water level at the seaward side is below the geotextile tubes indicating a wave trough at the seaside (wave run down).
- The water level at the landward side of the stack of geotextile tubes is equal to the top of tube C indicating a high wave reflecting against the stack of tubes.
- The schematisation of interaction of forces between tube B and C is assumed to be such as given in Figure 4.11 and Figure 4.12.
- To determine the relative weight it is assumed that the tubes are 50 % under water ( $\zeta = 0.5$ )

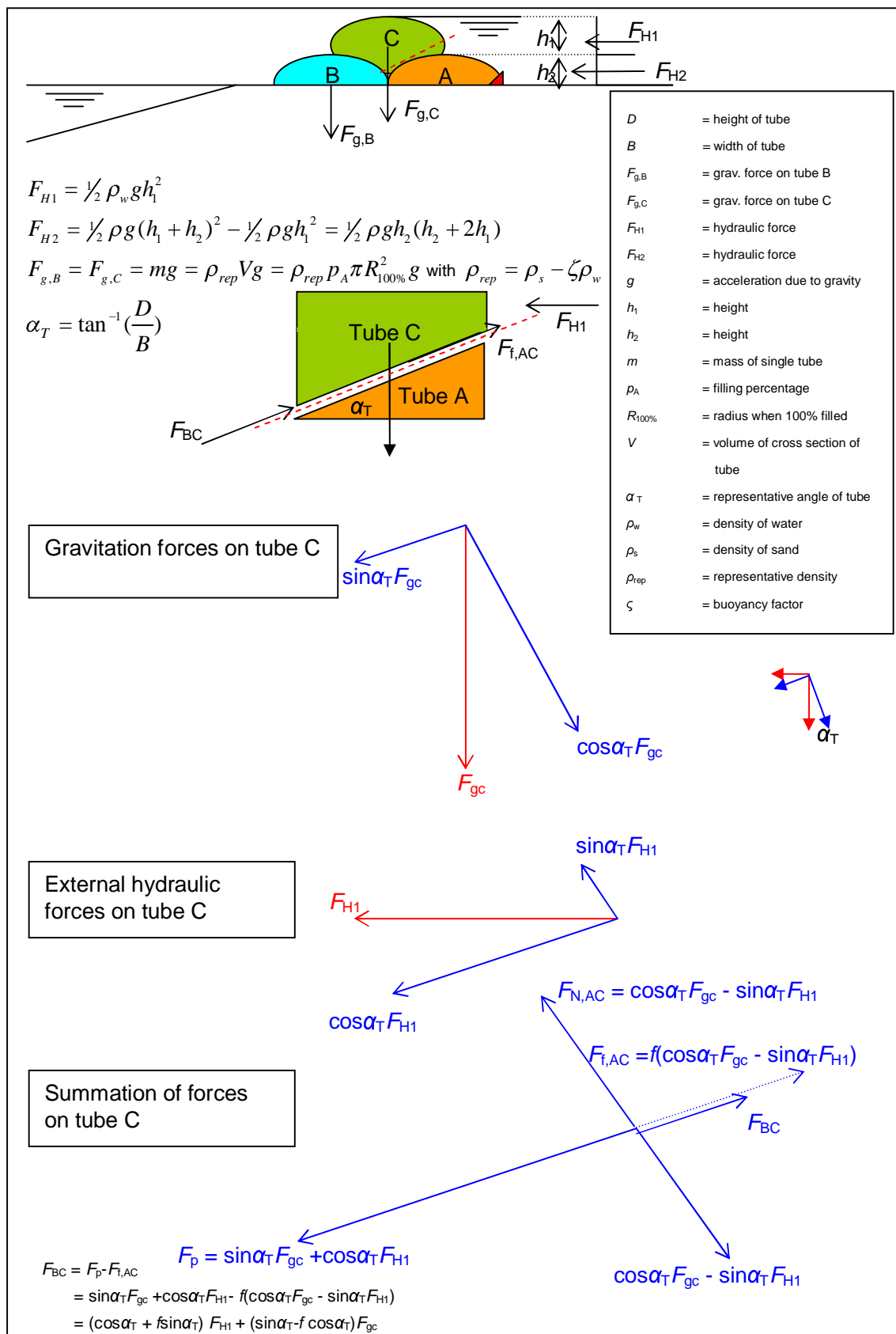


Figure 4.11 Schematization of test series P3 (tube C)

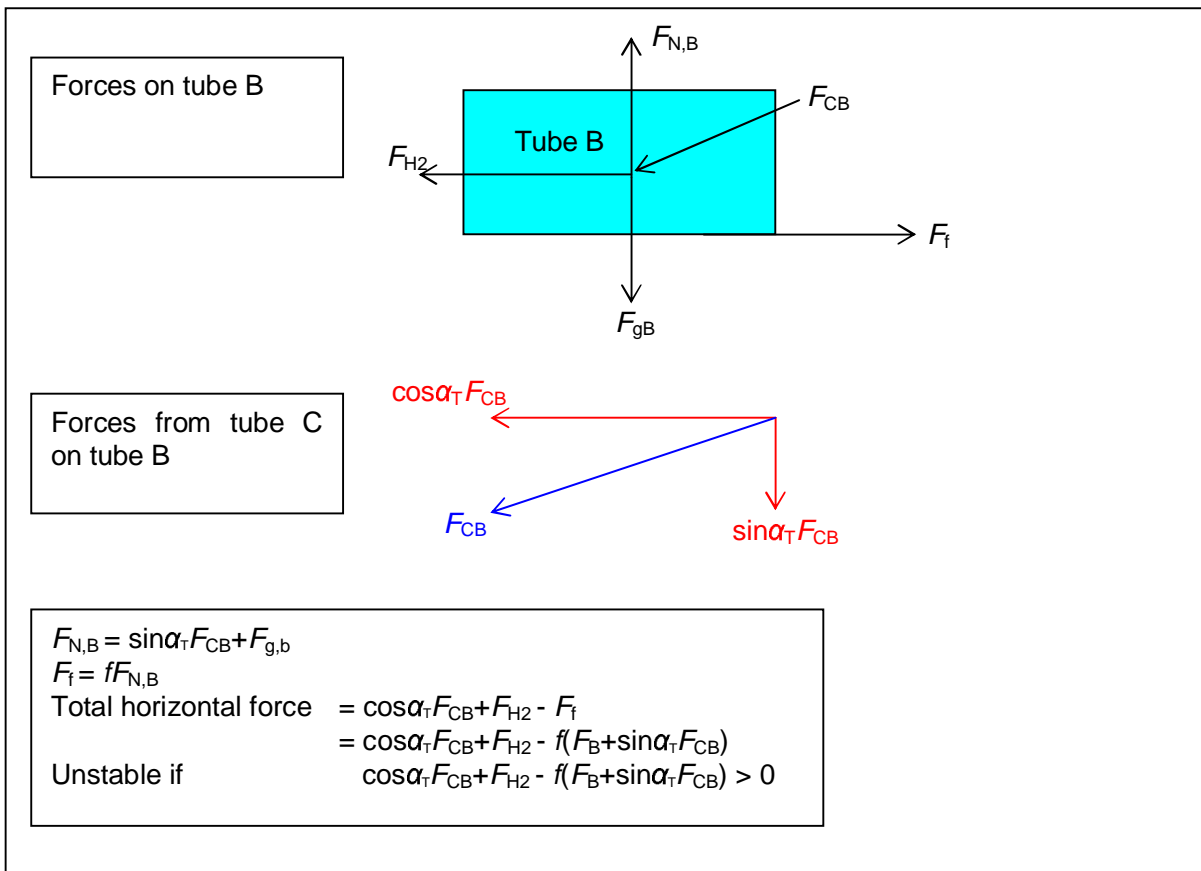


Figure 4.12 Schematization of test series P3 (tube B)

<b>Fixed parameters</b>				
Acceleration due to gravity	$g$	9.81 m/s <sup>2</sup>		
Density water	$\rho_w$	1000 N/kg		
<b>Variable parameter</b>				
Height of tube A	$D$	0.71		
Width of tube A	$B$	1.49		
Representative height	$h_1$	0.55 m	$h_{tot}$	1.25 m
Representative height	$h_2$	0.70 m		
Filling percentage	$\rho_A$	0.81 -	$V$	0.83 m <sup>2</sup>
Radius	$R_{100\%}$	0.57 m	$\rho_{rep}$	1500
Density of tube	$\rho_s$	2000 kg/m <sup>3</sup>	$m_{rep}$	1240 kg/m
Slope angle	$\alpha$	25°	$\cos\alpha$	0.90
Friction coefficient	$f$	0.50	$\sin\alpha$	0.43
Buoyancy factor	$\zeta$	0.50		
<b>External hydraulic forces</b>				
Hydraulic force	$F_{h1}$	1484 N/m	$\cos\alpha F_{h1}$	1339 N/m
Hydraulic force	$F_{h2}$	6180 N/m	$\sin\alpha F_{h1}$	638 N/m
Hydraulic force	$F_{htot}$	7664 N/m	$\cos\alpha F_{h2}$	5579 N/m
			$\sin\alpha F_{h2}$	2659 N/m
<b>Gravitational forces</b>				
Gravitational force on tube C	$F_{g,C}$	12166 N/m	$\cos\alpha F_{gc}$	10983 N/m
Gravitational force on tube B	$F_{g,B}$	12166 N/m	$\sin\alpha F_{gc}$	5233 N/m
<b>Calculations (tube C and A)</b>				
Force parallel to slope tube A and C	$F_p$	6573 N/m		
Frictional force between tube A and C	$F_{fAC}$	5172 N/m	$\cos\alpha F_{BC}$	1264 N/m
Force between tube B and C	$F_{BC}$	1401 N/m	$\sin\alpha F_{BC}$	603 N/m
<b>Calculations (tube C and B)</b>				
Normal force on tube B	$F_{N,B}$	12768 N/m		
Resulting horizontal force on tube B	$F_{tot,hor}$	1060 N/m	<b>UNSTABLE</b>	

Figure 4.13 Stability calculation 2-1 stack

#### 4.2.8 Conclusions on sliding stability

A stability parameter has been derived with respect to the sliding of a geotextile tube under wave attack. This dimensionless parameter fits with the data derived from the experiments. The following design rule is suggested with respect to the sliding mechanism of geotextile tubes under wave attack.

It is assumed that a sliding distance of 5% or less of the width of the geotextile tube is accepted ( $\Delta x/B < 0.05$ ) per storm. It is assumed that a storm consists of approximately 1000 waves.

$$\frac{\chi H_s}{\Delta \sqrt{BD} (f \cos \alpha + \sin \alpha)} \leq 0.65 \quad (4.15)$$

Where (see also Figure 4.1):

$H_s$  = significant wave height

$\Delta$	=	relative density of the geotextile tube
$B$	=	width of the geotextile tube
$D$	=	height of the geotextile tube
$f$	=	friction coefficient of the geotextile tube and subsoil
$\alpha$	=	representative slope of the underlying floor of the geotextile tube
$X$	=	correction factor for overtopping wave energy as given in Equation (4.1) or Figure 4.3

Equation (4.15) is based on tests with the following characteristics:

Crest height	$R_c$	=	0
Breakerparameter	$\xi_{p,toe}$	=	2
Friction coefficient	$f$	=	0.55
Angle of underground	$0^\circ$	<	$\alpha$ < $5^\circ$
Filling percentage	66 %	<	$p_A$ < 109 %
Radius when 100% filled	0.57	<	$R_{100\%}$ < 0.75
Characteristic distance	1.2	<	$a/D$ < 2.0 m

It is also possible to accept a larger sliding distance. Whether this can be accepted depends on the criteria specific for each situation. However, accepting a larger sliding distance does not lead to a significant larger stability. For example, if a sliding distance of 20 % of the width of a geotextile tube is accepted, the stability parameter becomes 0.70 (instead of 0.65). A sliding distance of 50% of the width of a geotextile tube leads to a stability parameter of 0.75.

### 4.3 Erosion of fill through the geotextile skin

Loss of fill material (fine fraction) through the geotextile is described in CUR (2006) and Van Steeg and Klein Breteler (2008). To examine possible loss of fill material, grain size distribution graphs have been made before test series F4 (see Appendix B7-A, B7-B and B7-C) and after the test series F4 (Appendix B7-D and B7-E). No significant differences between the graphs were found indicating that there was no significant loss of sand through the geotextile. In addition, no visual signs of erosion (loss of fill material) have been observed.

### 4.4 Deformation of the contained fill

An almost forgotten failure mechanism is described in Venis (1968). Venis performed several tests with various sizes of sandbags under current attack. He found that the point at where the sandbag started to shift was almost independent of the model scale. At a certain velocity,  $u_{crit,cp}$ , the sand in the bags became unstable. This mechanism only occurred when applying larger sand bags. This is illustrated in Figure 4.14. This mechanism has also been found at the tests performed on geotextile containers described in Van Steeg and Klein Breteler (2008). In these tests, wave run-down caused a severe sand transport within the geotextile containers resulting in instability of the elements.

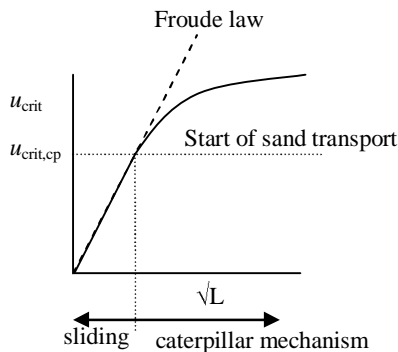


Figure 4.14 The Froude scaling law and the importance of sand transport within the geotextile element according to Venis (1968)

It is assumed that the sand transport in the geotextile elements is highly dependent on the filling percentage. A low filling percentages enables the sand to move within the geotextile element resulting in deformation and a potential 'Caterpillar mechanism'.

Based on the color injections and the calculated erosion it is clear that no erosion occurs in the case of a geotextile tube with a high degree of filling. Test series F4, where the geotextile tube was filled to its maximum, does not show any erosion or sand migration (see Appendix C, photo 53-54 and Appendix E). The tubes with a lower degree of filling, for example test series F1, shows clear signs of sand migration (see Appendix E). This is in agreement with the theory as described by Van Steeg and Klein Breteler (2008). A lower filling rate results in more sand migration within the tubes. This could induce the caterpillar mechanism as described in Van Steeg and Klein Breteler (2008).

In most cases a geotextile tube will be filled to its (practical) maximum. This will lead to high degrees of filling (~80% on basis of area). Therefore, it is unlikely that internal sand migration within a geotextile tube will be a realistic failure mechanism for a structure consisting of geotextile tubes. Although this is not guaranteed for larger tubes (for example a factor four larger than tested) it is likely that this mechanism is not dominating. This mechanism is not investigated further, although the migration mechanism is not fully understood, since there was a minimal influence on the stability of the tested configurations.

#### 4.5 Settlement

Based on the tests with a single tube the relative vertical deformation is determined and plotted in Figure 4.15.

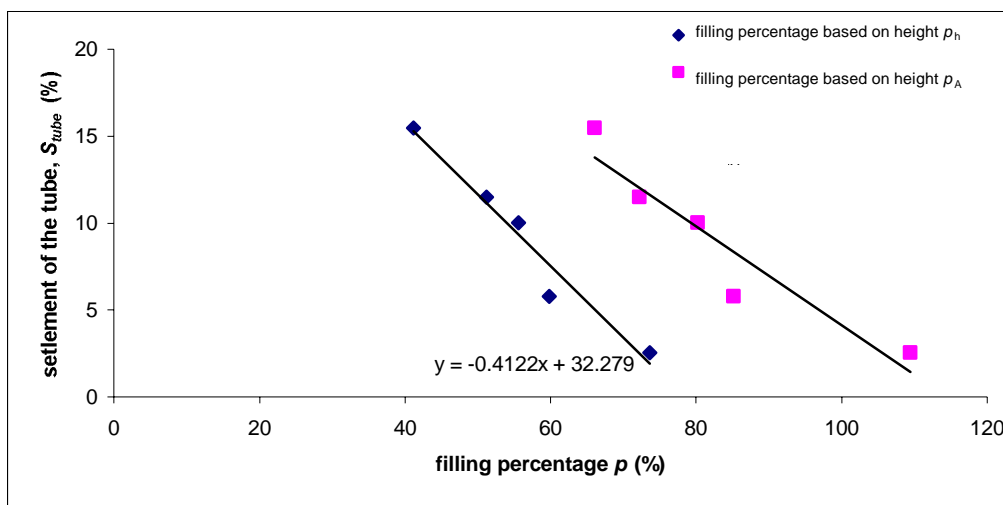


Figure 4.15 Relative vertical deformation of the geotextile tubes

It can be seen that there is a good correlation between the filling percentage based on the height before wave loading ( $p_{h,b}$ ) and the relative settlement of the tube ( $S_{tube}$ ). The following formula with respect to deformation is suggested (based on regression analysis through the measurement points):

$$S_{tube} = -0.41p_{h,b} + 32.3 \quad (4.16)$$

With minimum and maximum values of  $p_{h,b} = 41\%$  and  $p_{h,b} = 74\%$ .

Where:

$$S_{tube} = \text{relative settlement} \left( = \frac{D_{deformed} - D_{initial}}{D_{initial}} \right)$$

$$p_{h,b} = \text{filling percentage directly after constructing based on the height of the tube (\%)}$$

Based on the results from the split rings (see Appendix A15) and the Penetrologger (see Appendix B06-w) measurements before and after the tests series, it is concluded that during the tests, due to the hydraulic loads, the compaction within the geotextile tube increases. The Penetrologger data can be used as a qualitative indication of the compaction, but not quantitative. Due to the unknown water content in the sand the registered conus resistance may only be used as indicative values.

Based on these observations it is important to take compaction of the elements in account during the design stage. As indication Figure 4.15 can be used.



## 5 Conclusions and recommendations

### 5.1 Introduction

Seven structures consisting of geotextile tubes have been tested at large scale. In four configurations, single placed tubes with varying filling percentages and sizes were tested. One configuration consisted of a single tube with a bar placed at the landward side to simulate a trench. Two other configurations consisted of two tubes placed behind each other and a so-called 2-1 stack; two tubes placed behind each other with a third tube on top. These configurations are shown in Figure 5.1.

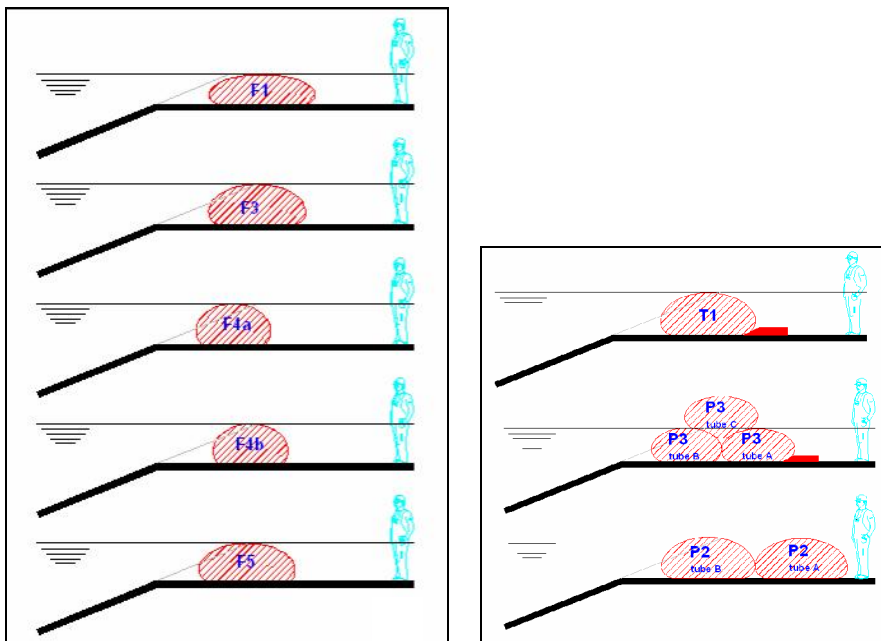


Figure 5.1 Configurations that have been tested

Table 5.1 Overview of the main dimensions of the tested configurations

series	$D_{avg}$ (m)	$B_{avg}$ (m)	$a$ (m)	$R_{100\%}$ (m)	$A$ (m <sup>2</sup> )	$A_{100\%}$ (m <sup>2</sup> )	$p_{h,avg}$ (%)	$p_A$ (%)
F1	0.57	2.19	1.12	0.75	1.16	1.76	38	66
F3	0.79	2.04	1.11	0.75	1.42	1.77	53	80
F4	0.82	1.52	0.85	0.57	1.10	1.01	73	109
F5	0.74	2.02	0.91	0.76	1.33	1.83	48	72
T1	0.88	2.03	1.03	0.76	1.54	1.80	58	85
P3-tube A	0.71	1.49	-	0.58	0.90	1.04	62	86
P3-tube B	0.70	1.56	-	0.57	0.91	1.03	61	89
P3-tube C	-	1.41	-	0.57	1.03	1.03	-	99
P3-mean	0.70	1.47	0.65	0.57	0.95	1.04	61	91
P2-tube A	0.86	1.98	-	0.77	1.45	1.86	57	78
P2-tube B	0.82	1.99	-	0.76	1.39	1.81	55	76
P2-mean	0.84	1.99	0.86	0.77	1.42	1.84	56	77

All structures were tested by creating wave fields consisting of approximately 1000 waves. The tests were repeated with higher waves until failure occurred.

## 5.2 Stability of single placed tubes

All single placed tubes (F1, F3, F4a, F4b, F5) slide in a landward direction. A stability relation based on physical reasoning has been derived and led to the best data collapse. This stability relation is based on the width ( $B$ ) and height ( $D$ ) of the geotextile tube, the slope angle of the support of the tube ( $\alpha$ ), the friction coefficient of the geotextile tube and its support ( $f$ ), the significant wave height ( $H_s$ ) corrected with the amount of overtopping energy ( $\chi$ ) and the relative density of the tube ( $\Delta$ ). It is assumed that a maximum displacement of the geotextile tube of 5 % of its width during a storm consisting of approximately 1000 waves is accepted. The derived stability formula, is:

$$\frac{\chi H_s}{\Delta \sqrt{BD} (f \cos \alpha + \sin \alpha)} \leq 0.65 \quad (5.1)$$

With

- $H_s$  = significant wave height
- $\Delta$  = relative density of the geotextile tube
- $B$  = width of the geotextile tube
- $D$  = height of the geotextile tube
- $f$  = friction coefficient of the geotextile tube
- $\alpha$  = representative slope of the supporting structure of the geotextile tube
- $\chi$  = correction factor for overtopping wave energy as given in Equation (4.1) or Figure 5.2.

Accepting larger displacements of the tube leads to only slightly higher stability numbers.

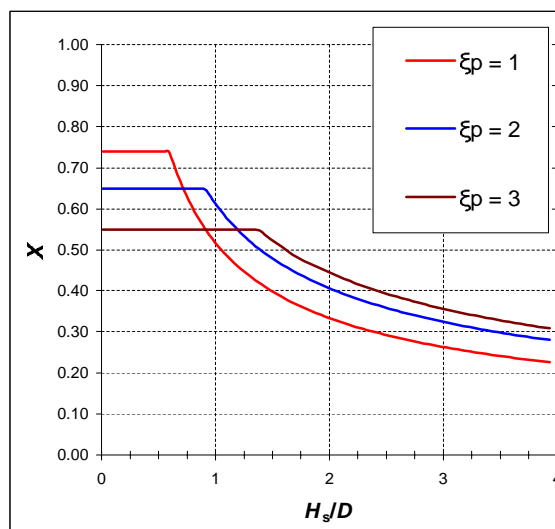


Figure 5.2 Design curve to determine  $\chi$  (assuming perpendicular wave attack and a water level equal to the top of the tube)

## 5.3 Stability of multiple placed tubes

Applying two tubes behind each other does not significantly increase the stability. The tube at the landward side will start to shift due to a hydrostatic pressure caused by the water entrapped between the two tubes and the hydrodynamic water pressures caused by the wave action at the landward side of the tubes. Therefore the stability relationship as given in

Section 5.2 should be also used for a structure consisting of two tube placed behind each other.

Placing two tubes behind each other with a third tube on top (P3) will result into a so-called slip circle failure mechanism during heavy wave attack. In the performed tests, the slip circle in landward direction was blocked by applying a fixed bar at the landward side of the tube which simulated a trench (for example formed due to settlement of the subsoil of the tubes or a commonly used dredged trench). At the seaside, such a bar was not placed resulting in a slip circle in seaward direction. A stability analysis is carried out and the calculated results approximated the results obtained from the physical model.

#### 5.4 Overall conclusions with respect to stability

All the tested configurations failed due to the sliding mechanism. Migration of sand within the tube was observed but did not cause any failure. A lower filling percentage resulted in more sand movement within the geotextile element. In most cases a geotextile tube will be filled to its (practical) maximum. This will lead to high degrees of filling (~80 % on basis of area). Therefore, it is unlikely that internal sand migration within a geotextile tube will be a realistic failure mechanism for a structure consisting of geotextile tubes with higher filling degrees. Although this is not guaranteed for larger tubes (for example a factor four larger than tested), it is likely that this mechanism is not dominating.

Assuming that sand migration can be ignored for tubes with a high filling percentage, Froude scaling can be applied and more specific research (for example other configurations) can be carried out in small-scale physical models. Besides filling percentage and density, parameters that require attention are the shape of the element (depends partly on the elasticity and thickness of the geotextile), the friction coefficient between the tubes and the friction coefficient between the tube and its foundation. For geotextile elements with lower filling percentages (for example geotextile containers) large-scale physical modelling is required to include the effect of internal sand migration and deformation on the elements.

#### 5.5 Deformation of the tubes

The deformation of the tubes is a function of the filling percentage; a higher filling percentage leads to less deformation. The deformation of geotextile tubes leads to a loss in height of the tubes. For single placed tubes a relation between the filling percentage based on the height of the tube before wave loading ( $p_{h,b}$ ) and the relative loss in height ( $P$ ) has been derived:

$$S_{tube} = -0.41p_{h,b} + 31.3 \quad (5.2)$$

With

$$S_{tube} = \text{relative settlement} \left( = \frac{D_{deformed} - D_{initial}}{D_{initial}} \right)$$

$$p_{h,b} = \text{filling percentage directly after constructing based on the height of the tube (\%)}$$

With minimum and maximum values of  $p_{h,b} = 41 \%$  and  $p_{h,b} = 74 \%$ .



## 6 References

- Alsina, J.M., Sánchez-Arcilla, A., Gironella, X. and Baldock, T.E. (2007), '*Design of scaled movable bed experiments using numerical models*', Journal of Coastal Research, SI 50 (Proceedings of the 9<sup>th</sup> International Coastal Symposium), Gold Coast Australia
- Bezuijen, A. and Vastenburch, E. (2008) '*Geosystems, Possibilities and limitations for applications*', EuroGeo 4, paper number 282
- CUR (2004) '*CUR214: Geotextiele zandelementen*', Stichting CUR, Gouda
- CUR (2006) '*CUR 217: Ontwerpen met geotextiele zandelementen*', Stichting CUR, Gouda
- CIRIA, CUR, CETMEF (2007) '*The Rock Manual. The use of rock in hydraulic engineering (2<sup>nd</sup> edition)*' C683, CIRIA, London
- Hughes, R.Y. (1993), '*Physical models and laboratory techniques in coastal engineering*' World Scientific, 588p
- Irribarren (1938) '*Una Formula para el Calculo de los Diques de Escollera*' M. Bermejillo-Pasajes, Madrid, Spain
- Kamphuis, J.W. (1996), '*Physical Modeling of Coastal Processes*' In: LIU, P.L. (ed.), *Advance in Coastal and Ocean Engineering*, World Scientific
- Klein Breteler, M. (2006) '*Het optellen van belastingperioden met verschillende golfhoogte*', memo February 2006, WL|Delft Hydraulics, Delft
- Kuiper, C., Klein Breteler, M., Booster L.N., Eysink, W. (2006) '*Stabiliteit van gezette steenbekledingen op havendammen*', WL|Delft Hydraulics report H4432, February 2006, Delft
- Mansard, E.P.D. and Funke, E.R. (1980) '*The measurement of incident waves and reflected spectra using a least square method*', 17<sup>th</sup> Int. Conf. of Coastal Engineering, Proc. ICCE'80, ASCE, pp.154-172, Sydney.
- Lawson, C.R. (2008) '*Geotextile containment for hydraulic and environmental engineering*', Geosynthetics International, 15, No 6, 384-427
- Oh, Y. I., Shin, E. C. (2006) '*Using submerged geotextile tubes in the protection of the E. Korean shore*', Coastal Engineering 53, 879-895, Elsevier.
- Pilarczyk, K. (2000) '*Geosynthetics and Geosystems in Hydraulic and Coastal Engineering*', 2000, Balkema Rotterdam
- Recio, J. (2008) '*Hydraulic Stability of Geotextile Sand containers for Coastal Structures - Effect of Deformations and Stability Formulae*' PhD Thesis, Leichweiß Institute for Hydraulic Engineering and Water resources, www.digibib.tu-bs.de/?docid=00021899

Schiereck, G.J. (2001) '*Introduction to bed, bank and shore protection*', Delft University Press

Van der Meer, J.W., Wang, B., Wolters, A., Zanuttigh, B. and Kramer, M. (2003) 'Oblique wave transmission over low-crested structures'. In: J.A. Melby (ed) Proc 4<sup>th</sup> int coastal structures conf, Portland, OR, 26-30 Aug 2003. ASCE, reston, VA, pp567-579

Van Steeg, P., Klein Breteler, M. (2008) '*Large scale physical model tests on the stability of geocontainers*', Deltares report H4595, May 2008, Delft

Venis, W.A. (1968) '*Closure of estuarine channels in tidal regions, Behaviour of dumping material when exposed to currents and wave action*', De ingenieur, 50

## A Tables

<i>Table A.1</i>	<i>Measured wave conditions</i>
<i>Table A.2</i>	<i>Measured height of individual tubes (D)</i>
<i>Table A.3</i>	<i>Measured width of individual tubes (B)</i>
<i>Table A.4</i>	<i>Measured exposed circumference of individual tubes (EC)</i>
<i>Table A.5</i>	<i>Measured dimensions of geotextile tube (x)</i>
<i>Table A.6</i>	<i>Measured dimensions of geotextile tube (y)</i>
<i>Table A.7</i>	<i>Measured dimensions of geotextile tube (w)</i>
<i>Table A.8</i>	<i>Measured dimensions of geotextile tube (z)</i>
<i>Table A.9</i>	<i>Derived dimensions of circumference (C)</i>
<i>Table A.10</i>	<i>Overview geometrical parameters of geotextile tubes</i>
<i>Table A.11</i>	<i>Overview relative deformation of geotextile tubes</i>
<i>Table A.12</i>	<i>Dimensions of empty geotextile tube</i>
<i>Table A.13</i>	<i>Overview filling percentages</i>
<i>Table A.14</i>	<i>Measured displacement of geotextile tubes</i>
<i>Table A.15</i>	<i>Unit weight and percentage water in ground samples</i>
<i>Table A.16</i>	<i>Colour injections</i>





Test	water level (m)	$H_s$ (m)	$T_{pd}$ (s)	$H_{max}$ (m)	$s_{0,p}$ (-)	$\xi_{o,p}$ (-)	$N$ (-)
F1-1	4.22	0.364	2.47	0.67	0.038	2.04	935
F1-2	4.22	0.421	2.63	0.75	0.039	2.03	1029
F1-3	4.22	0.491	2.88	0.87	0.038	2.06	1030
F1-4	4.22	0.558	3.11	0.96	0.037	2.08	979
F1-5	4.22	0.665	3.37	1.11	0.038	2.06	998
F1-6	4.22	0.761	3.63	1.14	0.037	2.08	1013
F1-7	4.22	0.875	4.02	1.34	0.035	2.15	998
F1-8	4.22	1.004	4.46	1.65	0.032	2.23	1047
F1-9	4.22	1.179	5.01	1.81	0.030	2.30	391
F1-9 <sub>1</sub>	4.22	1.213	5.03	1.78	0.031	2.28	400
F1-9 <sub>2</sub>	4.22	1.062	4.99	1.51	0.027	2.42	246
F1-9 <sub>t</sub>	4.22	1.166	5.01	1.81	0.030	2.32	1037
F1-10	4.22	1.283	5.33	1.61	0.029	2.35	75

Table A.1a: measured wave conditions for test series F1

Test	water level (m)	$H_s$ (m)	$T_{pd}$ (s)	$H_{max}$ (m)	$s_{0,p}$ (-)	$\xi_{o,p}$ (-)	$N$ (-)
F3-1	4.45	0.416	2.64	0.686	0.038	2.04	985
F3-2	4.45	0.522	2.91	0.935	0.040	2.01	963
F3-2 <sub>1</sub>	4.45	0.490	2.88	0.840	0.038	2.06	985
F3-2 <sub>t</sub>	4.45	0.506	2.90	0.94	0.039	2.03	1948
F3-3	4.45	0.559	3.10	0.980	0.037	2.07	975
F3-4	4.45	0.661	3.34	1.080	0.038	2.05	992
F3-5	4.45	0.772	3.67	1.172	0.037	2.09	983
F3-6	4.45	0.871	4.02	1.288	0.035	2.15	1011
F3-6 <sub>1</sub>	4.45	0.870	4.02	1.309	0.034	2.15	1009
F3-6 <sub>t</sub>	4.45	0.871	4.02	1.31	0.035	2.15	2020
F3-7	4.45	0.999	4.45	1.610	0.032	2.22	1033
F3-8	4.45	1.166	5.02	1.825	0.030	2.32	990
F3-9	4.45	1.323	5.59	1.958	0.027	2.43	1034

Table A.1b: measured wave conditions for test series F3

Test	water level (m)	$H_s$ (m)	$T_{pd}$ (s)	$H_{max}$ (m)	$s_{0,p}$ (-)	$\xi_{o,p}$ (-)	$N$ (-)
F4-1	4.45	0.570	3.07	0.96	0.039	2.03	994
F4-2	4.45	0.410	3.02	0.72	0.029	2.36	969
F4-3	4.45	0.480	2.84	0.90	0.038	2.05	966
F4-4	4.45	0.570	3.07	0.99	0.039	2.03	983
F4-5	4.45	0.667	3.34	1.12	0.038	2.04	1010
F4-6	4.45	0.753	3.65	1.29	0.036	2.10	1021

Table A.1c: measured wave conditions for test series F4

Test	water level	$H_s$	$T_{pd}$	$H_{max}$	$s_{0,p}$	$\xi_{0,p}$	$N$
	(m)	(m)	(s)	(m)	(-)	(-)	(-)
F5-1	4.390	0.671	3.35	1.139	0.038	2.04	1005
F5-2	4.390	0.770	3.70	1.272	0.036	2.11	984
F5-3	4.390	0.877	4.05	1.319	0.034	2.16	999
F5-4	4.390	1.025	4.50	1.603	0.032	2.22	999
F5-5	4.390	1.164	5.06	1.789	0.029	2.34	997
F5-6	4.390	1.363	5.65	1.916	0.027	2.42	991

Table 1d: measured wave conditions for test series F5

Test	water level	$H_s$	$T_{pd}$	$H_{max}$	$s_{0,p}$	$\xi_{0,p}$	$N$
	(m)	(m)	(s)	(m)	(-)	(-)	(-)
P2-1	4.460	0.881	4.00	1.313	0.035	2.13	596
P2-11	4.460	0.874	4.00	1.304	0.035	2.14	420
P2-1_t	4.460	0.878	4.00	1.31	0.035	2.13	1016
P2-2	4.460	1.036	4.41	1.524	0.034	2.16	152
P2-21	4.460	-	-	-	-	-	18
P2-22	4.460	0.994	4.60	1.827	0.030	2.31	274
P2-23	4.460	1.026	4.51	1.867	0.032	2.23	559
P2-2_t	4.460	1.019	4.52	1.867	0.032	2.24	1003
P2-3	4.460	1.117	5.00	1.779	0.029	2.37	450
P2-31	4.460	1.060	5.00	1.378	0.027	2.43	122
P2-32	4.460	1.192	4.90	1.834	0.032	2.24	439
P2-3_t	4.460	1.144	4.96	1.83	0.030	2.32	1011
P2-4	4.460	1.510	5.54	1.737	0.032	2.25	80
P2-41	4.460	1.204	5.40	1.480	0.026	2.46	41
P2-42	4.460	1.372	5.66	1.841	0.027	2.42	447
P2-4_t	4.460	1.381	5.63	1.84	0.028	2.39	568

Table A.1e: measured wave conditions for test series P2

Test	water level	$H_s$	$T_{pd}$	$H_{max}$	$s_{0,p}$	$\xi_{0,p}$	$N$
	(m)	(m)	(s)	(m)	(-)	(-)	(-)
P3-1	4.310	0.440	2.642	0.723	0.040	1.99	1013
P3-2	4.310	0.506	2.880	0.861	0.039	2.02	1006
P3-3	4.310	0.580	3.077	0.985	0.039	2.02	1048
P3-4	4.310	0.661	3.342	1.138	0.038	2.05	1030
P3-5	4.310	0.764	3.643	1.173	0.037	2.08	1035
P3-6	4.310	0.886	4.050	1.300	0.035	2.15	979
P3-7	4.310	1.017	4.478	1.621	0.032	2.22	1012
P3-8	4.310	1.162	5.037	1.746	0.029	2.34	1012
P3-9	4.310	1.368	5.500	1.860	0.029	2.35	282

Table A.1f: measured wave conditions for test series P3

Test	water level	$H_s$	$T_{pd}$	$H_{max}$	$s_{0,p}$	$\xi_{0,p}$	$N$
	(m)	(m)	(s)	(m)	(-)	(-)	(-)
<b>T1-1oud</b>	<b>4.52</b>	<b>0.61</b>	<b>3.04</b>		0.042	1.95	<b>414</b>
T1-1	4.52	0.564	3.070	1.003	0.038	2.04	1038
T1-2	4.52	0.676	3.335	1.227	0.039	2.03	1008
T1-3	4.52	0.756	3.715	1.139	0.035	2.14	1033
T1-4	4.52	0.866	4.021	1.262	0.034	2.16	1014
T1-5	4.52	1.005	4.465	1.550	0.032	2.23	993
T1-6	4.52	1.146	5.035	1.781	0.029	2.35	1001
T1-7	4.52	1.350	5.639	2.004	0.027	2.43	1027
T1-8	4.52	1.492	6.386	1.983	0.023	2.61	1023
T1-9	4.42	1.497	6.364	2.126	0.024	2.60	2021

**Table A.1g: measured wave conditions for test series T1**

series	height before test ( $D_b$ )					height after test ( $D_a$ )					mean $D_{avg}$ (m)	dD (%)
	line 1 $D_{b,1}$ (m)	line 2 $D_{b,2}$ (m)	line 3 $D_{b,3}$ (m)	line 4 $D_{b,4}$ (m)	mean $D_{b,avg}$ (m)	line 1 $D_{a,1}$ (m)	line 2 $D_{a,2}$ (m)	line 3 $D_{a,3}$ (m)	line 4 $D_{a,4}$ (m)	mean $D_{a,avg}$ (m)		
F1	0.60	0.62	0.64	0.61	0.62	0.50	0.57	0.53	0.49	0.52	0.57	-15.5
F3	0.80	0.83	0.84	0.88	0.83	0.79	0.75	0.74	0.73	0.75	0.79	-10.0
F4	0.83	0.84	0.85	0.82	0.84	0.79	0.82	0.84	0.80	0.81	0.82	-2.5
F5	0.78	0.80	0.80	0.75	0.78	0.68	0.70	0.72	0.67	0.69	0.74	-11.5
T1	0.89	0.89	0.91	0.94	0.91	0.84	0.85	0.85	0.89	0.86	0.88	-5.8
P3-tube A	0.72	0.69	0.72	0.72	0.72	0.69	0.69	0.70	0.70	0.70	0.71	-2.7
P3-tube B	0.71	0.70	0.68	0.69	0.70	-	-	-	-	-	0.70	-
P3-tube C	-	-	-	-	-	-	-	-	-	-	-	-
P3-mean	0.71	0.70	0.70	0.71	0.71	0.69	0.69	0.70	0.70	0.70	0.70	-2.69
P2-tube A	0.96	0.83	0.84	0.89	0.88	0.87	0.83	0.82	0.83	0.84	0.86	-4.8
P2-tube B	0.85	0.88	0.83	0.84	0.85	0.78	0.80	0.80	0.75	0.78	0.82	-7.6
P2-mean	0.90	0.85	0.83	0.86	0.86	0.83	0.81	0.81	0.79	0.81	0.84	-6.2

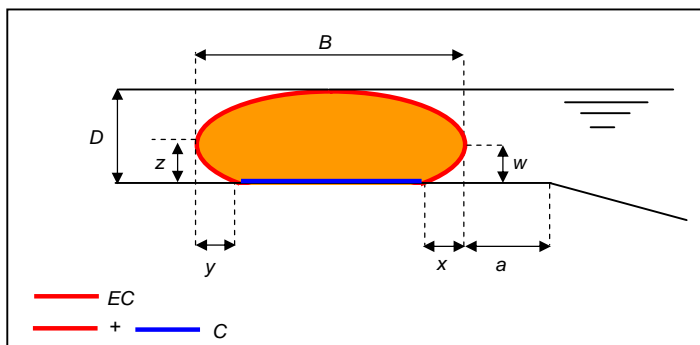
Table A.2: Measured height of individual tubes (D)

series	width before test ( $B_b$ )					width after test ( $B_a$ )					mean $B_{avg}$ (m)	dB (%)
	line 1 $B_{b,1}$ (m)	line 2 $B_{b,2}$ (m)	line 3 $B_{b,3}$ (m)	line 4 $B_{b,4}$ (m)	mean $B_{b,avg}$ (m)	line 1 $B_{a,1}$ (m)	line 2 $B_{a,2}$ (m)	line 3 $B_{a,3}$ (m)	line 4 $B_{a,4}$ (m)	mean $B_{a,avg}$ (m)		
F1	2.23	2.21	2.21	2.22	2.22	2.20	2.14	2.16	2.18	2.17	2.19	-2.1
F3	2.02	2.04	2.05	2.03	2.03	2.03	2.04	2.06	2.07	2.05	2.04	0.9
F4	1.50	1.52	1.49	1.75	1.56	1.49	1.50	1.47	1.47	1.48	1.52	-5.1
F5	2.02	2.00	2.00	2.01	2.01	2.04	2.02	2.01	2.04	2.03	2.02	0.9
T1	2.03	2.02	2.00	2.05	2.02	2.05	2.05	2.04	2.03	2.04	2.03	0.7
P3-tube A	1.50	1.51	1.48	1.48	1.49	-	-	-	-	-	1.49	-
P3-tube B	1.54	1.56	1.59	1.57	1.56	-	-	-	-	-	1.56	-
P3-tube C	-	-	-	-	-	1.50	1.40	1.35	1.40	1.41	1.41	-
P3-mean	1.52	1.54	1.53	1.53	1.53	1.50	1.40	1.35	1.40	1.41	1.47	-
P2-tube A	1.96	1.99	2.00	2.01	1.99	1.96	1.92	1.99	2.03	1.97	1.98	-0.9
P2-tube B	1.96	1.98	1.98	1.97	1.97	2.02	2.00	2.00	2.01	2.01	1.99	1.7
P2-mean	1.96	1.99	1.99	1.99	1.98	1.99	1.96	2.00	2.02	1.99	1.99	0.4

Table A.3: Measured width of individual tubes (B)

series	exposed circumf. before test ( $EC_b$ )					exposed circumf. after test ( $EC_a$ )					mean $EC_{avg}$ (m)	dEC (%)
	line 1 $EC_{b,1}$ (m)	line 2 $EC_{b,2}$ (m)	line 3 $EC_{b,3}$ (m)	line 4 $EC_{b,4}$ (m)	mean $EC_{b,avg}$ (m)	line 1 $EC_{a,1}$ (m)	line 2 $EC_{a,2}$ (m)	line 3 $EC_{a,3}$ (m)	line 4 $EC_{a,4}$ (m)	mean $EC_{a,avg}$ (m)		
F1	2.99	2.95	2.98	2.98	2.97	3.03	3.02	3.01	3.03	3.02	3.00	1.7
F3	3.24	3.17	3.16	3.20	3.19	3.21	3.25	3.21	3.22	3.22	3.21	1.0
F4	2.68	2.71	2.73	2.78	2.72	2.59	2.68	2.70	2.69	2.66	2.69	-2.2
F5	3.04	3.00	3.01	3.03	3.02	3.18	3.11	3.15	3.12	3.14	3.08	4.1
T1	3.21	3.19	3.24	3.22	3.22	3.26	3.24	3.27	3.28	3.26	3.24	1.3
P3-tube A	2.46	2.36	2.43	2.39	2.41	-	-	-	-	-	2.41	-
P3-tube B	-	-	-	2.57	2.57	-	-	-	-	-	2.57	-
P3-tube C	-	-	-	-	-	-	-	-	-	-	-	-
P3-mean	2.46	2.36	2.43	2.48	2.49	-	-	-	-	-	2.49	-
P2-tube A	-	-	-	-	-	3.11	3.09	3.13	3.27	3.15	3.15	-
P2-tube B	-	-	-	-	-	3.04	3.00	3.01	3.03	3.02	3.02	-
P2-mean	-	-	-	-	-	3.07	3.04	3.07	3.15	3.08	3.08	-

Table A.4: Measured exposed circumference of individual tubes (EC)



series	$x_b$ before test					$x_a$ after test					mean $x_{avg}$ (m)	dx (%)
	line 1	line 2	line 3	line 4	mean	line 1	line 2	line 3	line 4	mean		
	$x_{b,1}$ (m)	$x_{b,2}$ (m)	$x_{b,3}$ (m)	$x_{b,4}$ (m)	$x_{b,avg}$ (m)	$x_{a,1}$ (m)	$x_{a,2}$ (m)	$x_{a,3}$ (m)	$x_{a,4}$ (m)	$x_{a,avg}$ (m)		
F1	0.21	0.22	0.17	0.16	0.19	0.18	0.19	0.17	0.17	0.18	0.18	-5.6
F3	0.25	0.20	0.18	0.22	0.21	0.21	0.24	0.20	0.19	0.21	0.21	-1.2
F4	-	-	-	-	-	-	-	-	-	-	-	-
F5	0.15	0.12	0.11	0.12	0.13	0.215	0.202	0.222	0.205	0.21	0.17	66.8
T1	0.27	0.21	0.21	0.25	0.23	0.24	0.23	0.23	0.21	0.23	0.23	-3.5
P3-tube A	0.22	0.19	0.23	0.21	0.21	-	-	-	-	-	0.21	-
P3-tube B	0.19	0.25	0.25	0.21	0.22	-	-	-	-	-	0.22	-
P3-tube C	-	-	-	-	-	-	0.21	0.22	0.22	0.22	0.22	-
P2-tube A	-	-	-	-	-	0.18	0.23	0.22	0.22	0.21	0.21	-
P2-tube B	0.22	0.18	0.18	0.21	0.20	0.15	0.12	0.11	0.12	0.13	0.16	-35.6

Table A.5: Measured dimensions of geotextile tube (x)

series	$y_b$ before test					$y_a$ after test					mean $y_{avg}$ (m)	dy (%)
	line 1	line 2	line 3	line 4	mean	line 1	line 2	line 3	line 4	mean		
	$y_{b,1}$ (m)	$y_{b,2}$ (m)	$y_{b,3}$ (m)	$y_{b,4}$ (m)	$y_{b,avg}$ (m)	$y_{a,1}$ (m)	$y_{a,2}$ (m)	$y_{a,3}$ (m)	$y_{a,4}$ (m)	$y_{a,avg}$ (m)		
F1	0.20	0.18	0.24	0.20	0.20	0.14	0.11	0.14	0.15	0.14	0.17	-33.6
F3	0.22	0.20	0.20	0.25	0.22	0.17	0.16	0.15	0.17	0.16	0.19	-27.0
F4	-	-	-	-	-	-	-	-	-	-	-	-
F5	0.12	0.07	0.09	0.08	0.09	0.132	0.111	0.116	0.102	0.12	0.10	29.5
T1	0.21	0.27	0.25	0.24	0.24	0.16	0.18	0.20	0.16	0.18	0.21	-25.9
P3-tube A	0.14	0.11	0.18	0.18	0.15	0.10	0.08	0.07	0.05	0.08	0.11	-48.9
P3-tube B	-	-	0.24	0.33	0.28	-	-	-	-	-	0.28	-
P3-tube C	-	-	-	-	-	-	-	-	-	-	-	-
P2-tube A	0.28	0.28	0.23	0.26	0.26	0.17	0.20	0.14	0.14	0.16	0.21	-37.5
P2-tube B	-	-	-	-	-	0.12	0.07	0.09	0.08	0.09	0.09	-

Table A.6: Measured dimensions of geotextile tube (y)

series	$w_b$ before test					$w_a$ after test					mean $w_{avg}$ (m)	dw (%)
	line 1	line 2	line 3	line 4	mean	line 1	line 2	line 3	line 4	mean		
	$w_{b,1}$ (m)	$w_{b,2}$ (m)	$w_{b,3}$ (m)	$w_{b,4}$ (m)	$w_{b,5}$ (m)	$w_{a,1}$ (m)	$w_{a,2}$ (m)	$w_{a,3}$ (m)	$w_{a,4}$ (m)	$w_{a,avg}$ (m)		
F1	-	-	-	-	-	-	-	-	-	-	-	-
F3	-	-	-	-	-	-	-	-	-	-	-	-
F4	-	-	-	-	-	-	-	-	-	-	-	-
F5	0.17	0.16	0.16	0.13	0.16	0.165	0.17	0.16	0.16	0.16	0.16	5.6
T1	-	-	-	-	-	-	-	-	-	-	-	-
P3-tube A	0.28	0.28	0.28	0.30	0.28	-	-	-	-	-	0.28	-
P3-tube B	0.12	0.18	0.15	0.15	0.15	-	-	-	-	-	0.15	-
P3-tube C	-	-	-	-	-	-	0.23	0.23	0.14	0.20	0.20	-
P2-tube A	-	-	-	-	-	0.25	0.18	0.17	0.14	0.18	0.18	-
P2-tube B	0.26	0.21	0.20	0.24	0.23	0.17	0.16	0.16	0.13	0.16	0.19	-31.9

Table A.7: Measured dimensions of geotextile tube (w)

series	$z_b$ before test					$z_a$ after test					mean $z_{avg}$ (m)	dz (%)
	line 1	line 2	line 3	line 4	mean	line 1	line 2	line 3	line 4	mean		
	$z_{b,1}$ (m)	$z_{b,2}$ (m)	$z_{b,3}$ (m)	$z_{b,4}$ (m)	$z_{b,avg}$ (m)	$z_{a,1}$ (m)	$z_{a,2}$ (m)	$z_{a,3}$ (m)	$z_{a,4}$ (m)	$z_{a,avg}$ (m)		
F1	-	-	-	-	-	-	-	-	-	-	-	-
F3	-	-	-	-	-	-	-	-	-	-	-	-
F4	-	-	-	-	-	-	-	-	-	-	-	-
F5	0.11	0.06	0.09	0.05	0.08	0.168	0.163	0.181	0.158	0.17	0.12	114.7
T1	-	-	-	-	-	-	-	-	-	-	-	-
P3-tube A	0.29	0.26	0.25	0.26	0.26	0.16	0.13	0.12	0.13	0.13	0.20	-48.6
P3-tube B	0.23	0.22	0.18	0.21	0.21	-	-	-	-	-	0.21	-
P3-tube C	-	-	-	-	-	-	-	-	-	-	-	-
P2-tube A	0.22	0.20	0.22	0.27	0.23	0.20	0.16	0.14	0.21	0.18	0.20	-22.0
P2-tube B	-	-	-	-	-	0.11	0.06	0.09	0.05	0.08	0.08	-

Table A.8: Measured dimensions of geotextile tube (z)

series	Circumference before test ( $C_b$ )					Circumference after test ( $C_a$ )					mean (C) $C_{avg}$ (m)	dC (%)
	line 1	line 2	line 3	line 4	mean	line 1	line 2	line 3	line 4	mean		
	$C_{b,1}$ (m)	$C_{b,2}$ (m)	$C_{b,3}$ (m)	$C_{b,4}$ (m)	$C_{b,avg}$ (m)	$C_{a,1}$ (m)	$C_{a,2}$ (m)	$C_{a,3}$ (m)	$C_{a,4}$ (m)	$C_{a,avg}$ (m)		
F1	4.81	4.76	4.78	4.84	4.80	4.90	4.86	4.86	4.89	4.88	4.84	1.7
F3	4.79	4.81	4.84	4.75	4.80	4.87	4.90	4.93	4.94	4.91	4.85	2.3
F4	-	-	-	-	-	-	-	-	-	-	-	-
F5	4.79	4.81	4.81	4.83	4.81	4.88	4.82	4.81	4.86	4.84	4.83	0.6
T1	4.76	4.73	4.78	4.78	4.77	4.90	4.87	4.87	4.93	4.89	4.83	2.7
P3-tube A	3.61	3.58	3.51	3.49	3.55	-	-	-	-	-	3.55	-
P3-tube B	-	-	-	3.60	3.60	-	-	-	-	-	3.60	-
P3-tube C	-	-	-	-	-	-	-	-	-	-	-	-
P2-tube A	-	-	-	-	-	4.72	4.57	4.77	4.94	4.75	4.75	-
P2-tube B	-	-	-	-	-	4.79	4.81	4.81	4.83	4.81	4.81	-

Table A.9: Derived dimensions of circumference (C)

series	$D_{avg}$ (m)	$B_{avg}$ (m)	$x_{avg}$ (m)	$y_{avg}$ (m)	$w_{avg}$ (m)	$z_{avg}$ (m)	$EC_{avg}$ (m)	$C_{avg}$ (m)	$a$ (m)	$R_{100\%}$ (m)	$A$ (m <sup>2</sup> )	$A_{100\%}$ (m <sup>2</sup> )	$p_{h,avg}$ (%)	$p_A$ (%)
F1	0.57	2.19	0.18	0.17	-	-	3.00	4.84	1.12	0.75	1.16	1.76	38	66
F3	0.79	2.04	0.21	0.19	-	-	3.21	4.85	1.11	0.75	1.42	1.77	53	80
F4	0.82	1.52	-	-	-	-	2.69	-	0.85	0.57	1.10	1.01	73	109
F5	0.74	2.02	0.17	0.10	0.16	0.12	3.08	4.83	0.91	0.76	1.33	1.83	48	72
T1	0.88	2.03	0.23	0.21	-	-	3.24	4.83	1.03	0.76	1.54	1.80	58	85
P3-tube A	0.71	1.49	0.21	0.11	0.28	0.20	2.41	3.55	-	0.58	0.90	1.04	62	86
P3-tube B	0.70	1.56	0.22	0.28	0.15	0.21	2.57	3.60	-	0.57	0.91	1.03	61	89
P3-tube C	-	1.41	0.22	-	0.20	-	-	-	-	0.57	1.03	1.03	-	99
P3-mean	0.70	1.47	0.21	0.20	0.28	-	2.41	3.55	0.65	0.57	0.95	1.04	61	91
P2-tube A	0.86	1.98	0.21	0.21	0.18	0.20	3.15	4.75	-	0.77	1.45	1.86	57	78
P2-tube B	0.82	1.99	0.16	0.09	0.19	0.08	3.02	4.81	-	0.76	1.39	1.81	55	76
P2-mean	0.84	1.99	0.22	0.28	0.15	0.21	2.57	3.60	0.86	0.77	1.42	1.84	56	77

Table A.10: Overview geometrical parameters of geotextile tubes

series	dD (%)	dB (%)	dx (%)	dy (%)	dw (%)	dz (%)	dEC (%)	dC (%)
F1	-15.5	-2.1	-5.6	-33.6	-	-	1.7	1.7
F3	-10.0	0.9	-1.2	-27.0	-	-	1.0	2.3
F4	-2.5	-5.1	-	-	-	-	-2.2	-
F5	-11.5	0.9	66.8	29.5	5.6	114.7	4.1	0.6
T1	-5.8	0.7	-3.5	-25.9	-	-	1.3	2.7

Table A.11: Overview relative deformation of geotextile tubes

series	width $w_{gt}$ (m)	length $L_{gt}$ (m)	circumf. $C_{empty}$ (m)	radius $R_{100\%}$ (m)	diameter $D_{100\%}$ (m)	volume $A_{100\%}$ (m <sup>2</sup> )
F1	2.35	5.90	4.70	0.75	1.50	1.76
F3	2.36	5.54	4.71	0.75	1.50	1.77
F4	1.78	5.50	3.56	0.57	1.13	1.01
F5	2.40	5.85	4.80	0.76	1.53	1.83
T1	2.38	5.75	4.76	0.76	1.52	1.80
P3-tube A	1.81	5.60	3.62	0.58	1.15	1.04
P3-tube B	1.80	5.71	3.60	0.57	1.15	1.03
P3-tube C	1.80	5.64	3.60	0.57	1.15	1.03
P3-mean	1.80	5.65	3.61	0.57	1.15	1.04
P2-tube A	2.41	6.00	4.82	0.77	1.53	1.85
P2-tube B	2.40	5.85	4.80	0.76	1.53	1.83
P2-mean	2.41	5.93	4.81	0.77	1.53	1.84

Table A.12: Dimensions of empty geotextile tube

series	$A$ (m <sup>2</sup> )	$p_{h,b}$ (%)	$p_{h,a}$ (%)	$p_{h,avg}$ (%)	$dp_h$ (%)	$p_A$ (%)
F1	1.16	41	35	38	-15.5	66
F3	1.42	56	50	53	-10.0	80
F4	1.10	74	72	73	-2.5	109
F5	1.33	51	45	48	-11.5	72
T1	1.54	60	56	58	-5.8	85
P3-tube A	0.90	62	60	61	-2.7	86
P3-tube B	0.91	61	-	61	-	89
P3-tube C	1.03	-	-	-	-	99
P3-mean	0.95	61	60	61	-2.7	91
P2-tube A	1.45	57	54	56	-4.8	78
P2-tube B	1.39	55	51	53	-7.6	76
P2-mean	1.42	56	53	55	-6.2	77

Table A.13: Overview filling percentages

after testnr	F1-1	F1-2	F1-3	F1-4	F1-5	F1-6	F1-7	F1-8	F1-92	F1-10
$\Delta x_{avg}$	0.003	0.011	0.015	0.010	0.030	0.016	0.026	0.037	0.377	1.069
$\Delta x_{avg,cum}$	0.003	0.013	0.028	0.038	0.068	0.084	0.110	0.147	0.524	1.593

**Tabel A.14a: Averaged displacement ( $\Delta x_{avg}$ ) and cumulative averaged displacement ( $\Delta x_{avg,cum}$ ) of geotextile tube for test series F1 (m)**

after testnr	F3-1	F3-2	F3-21	F3-3	F3-4	F3-5	F3-6	F3-61	F3-7	F3-8	F3-9
$\Delta x_{avg}$	0.002	0.021	0.006	-0.001	0.031	0.037	0.055	0.087	0.038	0.070	1.198
$\Delta x_{avg,cum}$	0.002	0.023	0.029	0.029	0.060	0.097	0.151	0.238	0.276	0.347	1.544

**Tabel A.14b: Averaged displacement ( $\Delta x_{avg}$ ) and cumulative averaged displacement ( $\Delta x_{avg,cum}$ ) of geotextile tube for test series F3 (m)**

after testnr	F4-1	F4-2	F4-3	F4-4	F4-5	F4-6
$\Delta x_{avg}$	0.365	-0.013	0.006	0.030	0.204	0.467
$\Delta x_{avg,cum}$	0.365	0.352	0.358	0.388	0.592	1.059

**Tabel A.14c: Averaged displacement ( $\Delta x_{avg}$ ) and cumulative averaged displacement ( $\Delta x_{avg,cum}$ ) of geotextile tube for test series F4 (m)**

after testnr	F5-1	F5-2	F5-3	F5-4	F5-5	F5-6
$\Delta x_{avg}$	0.029	-0.004	0.045	0.013	0.050	0.645
$\Delta x_{avg,cum}$	0.029	0.025	0.070	0.082	0.132	0.777

**Tabel A.14d: Averaged displacement ( $\Delta x_{avg}$ ) and cumulative averaged displacement ( $\Delta x_{avg,cum}$ ) of geotextile tube for test series F5 (m)**

after testnr	T1-oud	T1-1	T1-2	T1-3	T1-4	T1-5	T1-6	T1-7	T1-8	T1-9
$\Delta x_{avg}$	0.051	0.016	0.011	0.025	0.057	0.050	0.037	0.091	0.149	0.241
$\Delta x_{avg,cum}$	0.051	0.067	0.078	0.103	0.160	0.210	0.247	0.338	0.487	0.728

**Tabel A.14e: Averaged displacement ( $\Delta x_{avg}$ ) and cumulative averaged displacement ( $\Delta x_{avg,cum}$ ) of geotextile tube for test series T1 (m)**

after testnr	P2-11	P2-23	P2-32	P2-42
$\Delta x_{avg}$	0.018	0.219	0.063	1.080
$\Delta x_{avg,cum}$	0.018	0.237	0.300	1.380

**Tabel A.14f: Averaged displacement ( $\Delta x_{avg}$ ) and cumulative averaged displacement ( $\Delta x_{avg,cum}$ ) of geotextile tube for test series P2 (m)**



## Table A15 Unit weight and percentage water in ground samples

Test series: F4

Table A15.a

Monster	Before/after test	Location	$\gamma_{dry}$ [kg/m <sup>3</sup> ]	W [%]
F4-1	Before test	Filling hose, line 1	2198.41	5.18
F4-2	Before test	Filling hose, line 4	2156.00	3.08
F4-3	After test	Middle of tube	2310.05	5.82
F4-4	After test		1655.70	4.41

Test series: F1

Table A15.b

Monster	Before/after test	Location	$\gamma_{dry}$ [kg/m <sup>3</sup> ]
F1-1	Before test	Filling hose, line 4	1649.95
F1-2	Before test	Filling hose, line 1	1642.47
F1-3	After test	Close to the hose, line 4	1745.17
F1-4	After test	Close to the hose, line 1	1706.09

Test series: F3

Table A15.c

Monster	Before/after test	Location	$\gamma_{dry}$ [kg/m <sup>3</sup> ]
F3-1	Before test	Filling hose, line 4	1537.82
F3-2	After test	Close to the hose, line 4	1506.95
F3-3	After test	Top of ring at 0.2 below surface. Location close to hose at line 1	1514.31

## Appendix A16a - F4 Estimation erosion based on colour injections

location	line				mean	min	max
	1	2	3	4			
1	0	-	-	-	0	0	0
2	0	0	0	0	0	0	0
3	0	-	-	-	0	0	0

Table A.16a.1: Depth of injections below geotextile,  $d_2$  at testseries F4 (cm)

location	line				mean	min	max
	1	2	3	4			
1	20	-	-	-	20	20	20
2	20	18	20	20	20	18	20
3	18	-	-	-	18	18	18

Table A.16a.2: Length of injection,  $d_1$  at testseries F4 (cm)

location	line				mean	min	max
	1	2	3	4			
1	0	-	-	-	0	0	0
2	0	2	0	0	1	0	2
3	2	-	-	-	2	2	2

Table A.16a.3: Derived erosion depth  $d_{\text{erosion}}$  (= Length injection needle -  $d_1$ ) at testseries F4 (cm)

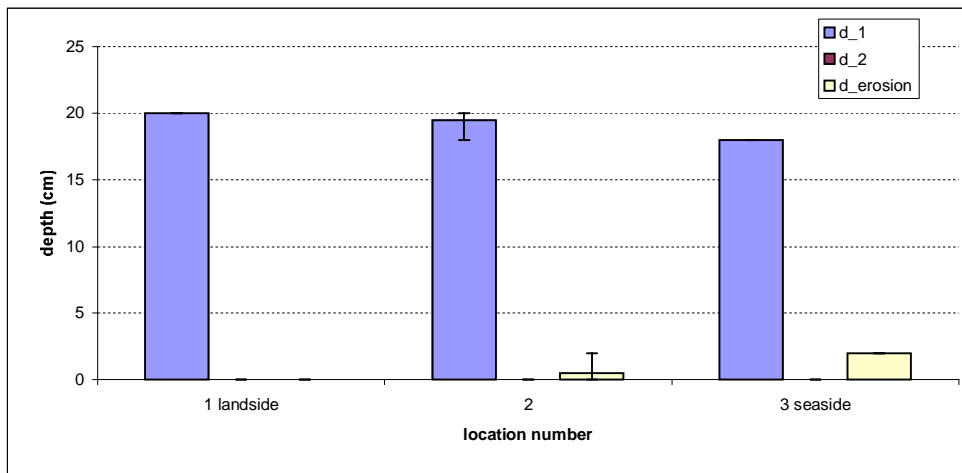


Figure A.16a.1:  $d_1$ ,  $d_2$  and  $d_{\text{erosion}}$  for all positions at testseries F4

## Appendix A16b - F1 Estimation erosion based on colour injections

location	line				mean	min	max
	1	2	3	4			
1	-	8	-	7	7	7	8
2	-	-	7	-	7	7	7
3	-	4	1	-	3	1	4
4	-	-	-	-	-	-	-
5	-	7	8	7	7	7	8

Table A.16b.1: Depth of injections below geotextile,  $d_2$  at testseries F1 (cm)

location	line				mean	min	max
	1	2	3	4			
1	-	20	-	20	20	20	20
2	-	-	9	-	9	9	9
3	-	6	5	-	5	5	6
4	-	-	-	-	-	-	-
5	-	20	20	20	20	20	20

Table A.16b.2: Length of injection,  $d_1$  at testseries F1 (cm)

location	line				mean	min	max
	1	2	3	4			
1	-	0	-	0	0	0	0
2	-	-	11	-	11	11	11
3	-	14	16	-	15	14	16
4	-	-	-	-	-	-	-
5	-	0	0	0	0	0	0

Table A.16b.3: Derived erosion depth  $d_{erosion}$  (= Length injection needle -  $d_1$ ) at testseries F1 (cm)

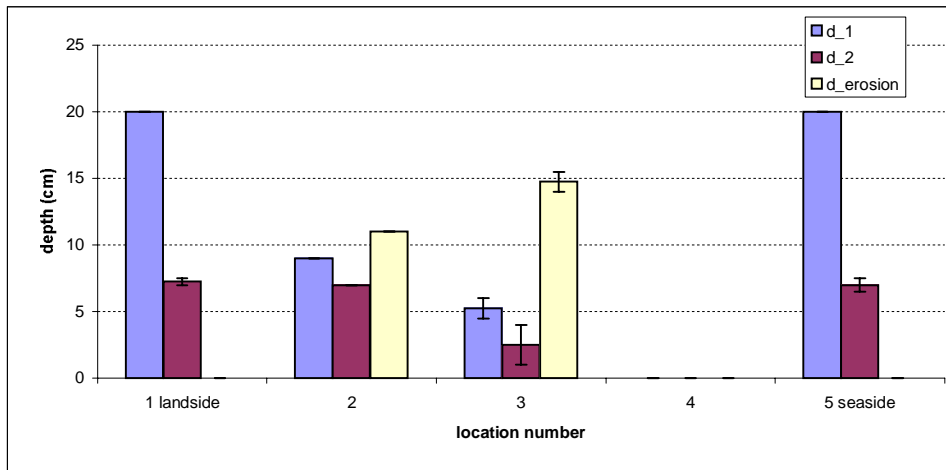


Figure A.16b.1:  $d_1$ ,  $d_2$  and  $d_{erosion}$  for all positions at testseries F1 (cm)

## Appendix A16c - F3 Estimation erosion based on colour injections

location	line				mean	min	max
	1	2	3	4			
1	0	2	0	1	1	0	2
2	7	10	12	12	10	7	12
3	5	1	1	4	3	1	5
4	1	5	3	4	3	1	5
5	1	not measured	3	6	3	1	6

Table A.16c.1: Depth of injections below geotextile,  $d_2$  at testseries F3 (cm)

location	line				mean	min	max
	1	2	3	4			
1	-	23	-	-	23	23	23
2	-	30	-	-	30	30	30
3	12	9	7	16	11	7	16
4	-	-	20	18	19	18	20
5	-	-	-	-	-	-	-

Table A.16c.2: Length of injection,  $d_1$  at testseries F3 (cm)

location	line				mean	min	max
	1	2	3	4			
1	-	-1	-	-	-1	-1	-1
2	-	-1	-	-	-1	-1	-1
3	13	13	15	8	12	8	15
4	-	-	3	6	4	3	6
5	-	-	-	-	-	-	-

Table A.16c.3: Derived erosion depth  $d_{erosion}$  at testseries F3 (cm)

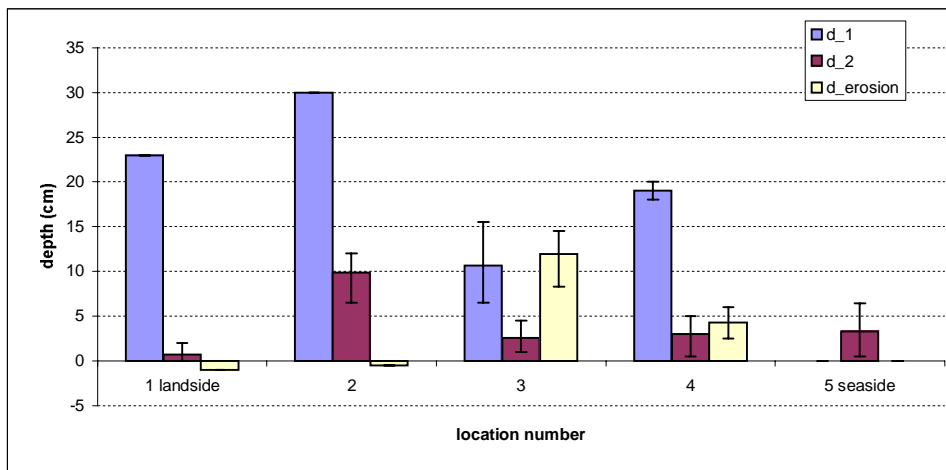


Figure A.16c.1:  $d_1$ ,  $d_2$  and  $d_{erosion}$  for all positions at testseries F3 (cm)

## Appendix A16d - T1 Estimation erosion based on colour injections

location	line				mean	min	max
	1	2	3	4			
1	3.9	18.5	24	21	17	4	24
2	2.5	2.5	NaN	NaN	3	3	3
3	5	11.2	8.1	11.9	9	5	12

Table A.16d.1: Depth of injections below geotextile,  $d_2$  at testseries T1(cm)

location	line				mean	min	max
	1	2	3	4			
1	27	25	29	29	28	25	29
2	-	-	-	-	-	-	-
3	29	22	22	23	24	22	29

Table A.16d.2: Length of injection,  $d_1$  at testseries T1 (cm)

location	line				mean	min	max
	1	2	3	4			
1	-	14	-	-	14	14	14
2	-	-	-	-	-	-	-
3	-4	9	6	9	5	-4	9

Table A.16d.3: Derived erosion depth  $d_{erosion}$  (= Length injection needle -  $d_1$ ) at testseries T1 (cm)

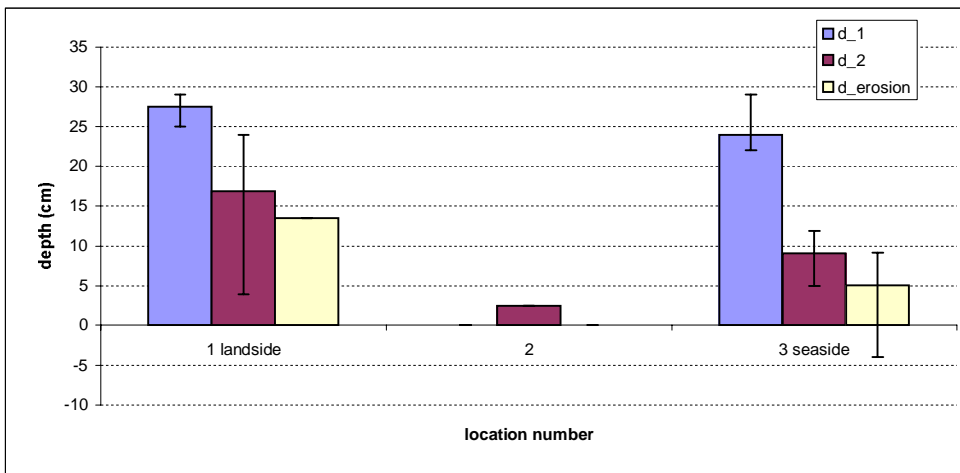


Figure A.16d.1:  $d_1$ ,  $d_2$  and  $d_{erosion}$  for all positions at testseries T1



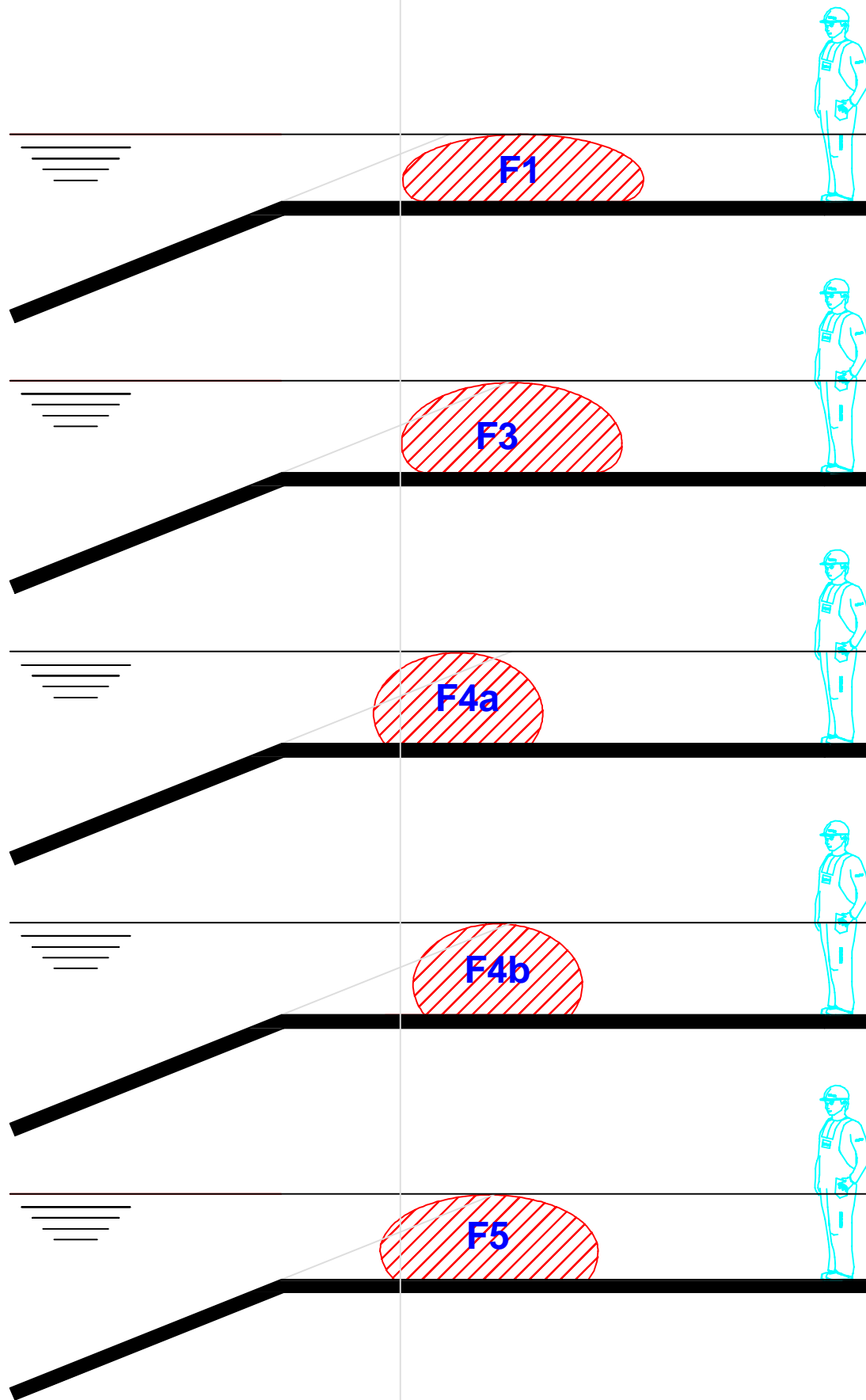
## B Figures

<i>Figure B.1</i>	<i>Overall set-up of the model</i>
<i>Figure B.2</i>	<i>Wave height exceedance curves and energy density spectra</i>
<i>Figure B.3</i>	<i>Overview of profile measurements</i>
<i>Figure B.4</i>	<i>Results top view camera</i>
<i>Figure B.5</i>	<i>Overview displacements based on top view camera analysis</i>
<i>Figure B.6</i>	<i>Penetrologger data</i>
<i>Figure B.7</i>	<i>Grain distribution</i>
<i>Figure B.8</i>	<i>Stretches in geotextile</i>









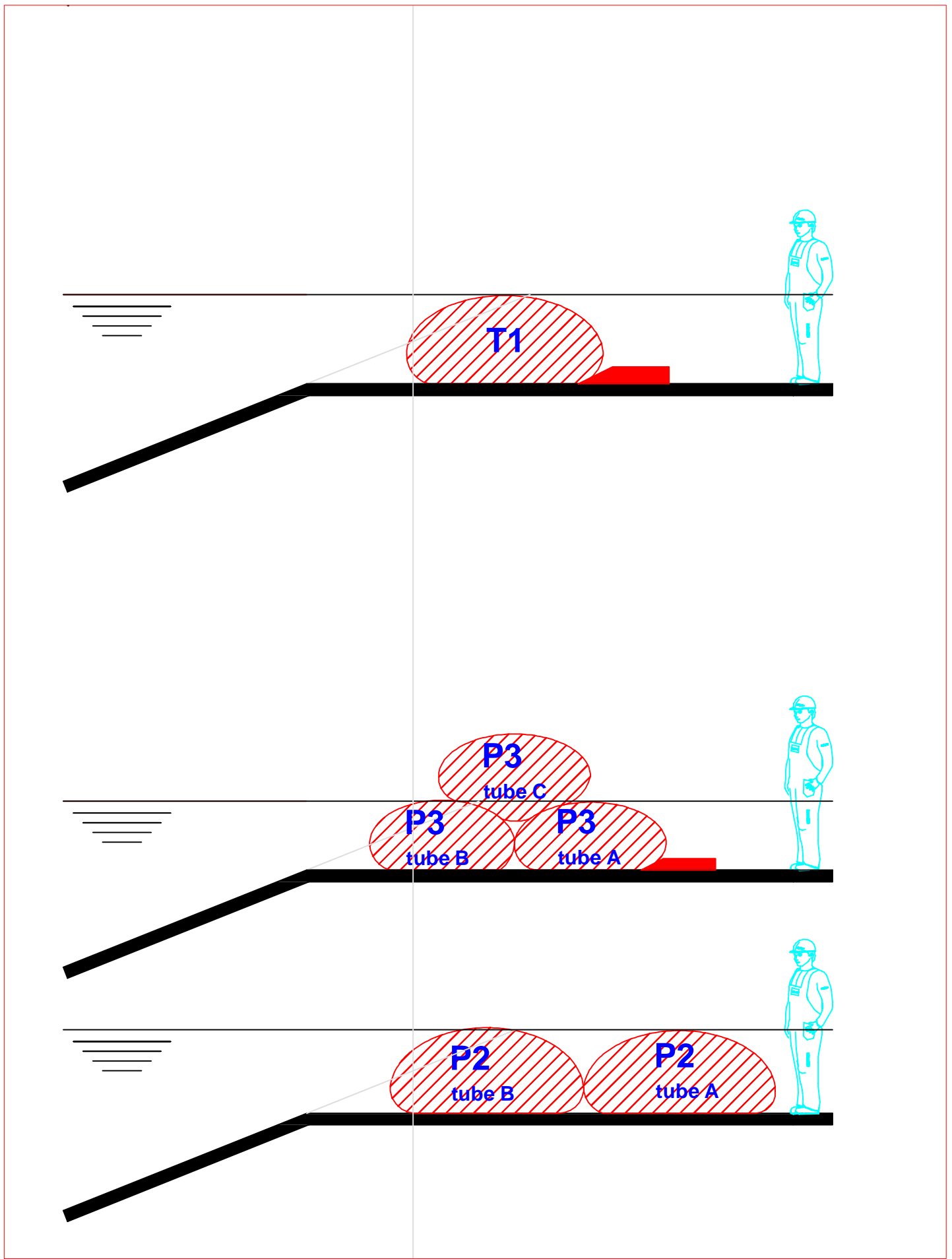
Geometrical variations in the test set-up

Geotextile tubes

Deltares

H5153

Fig B.1b



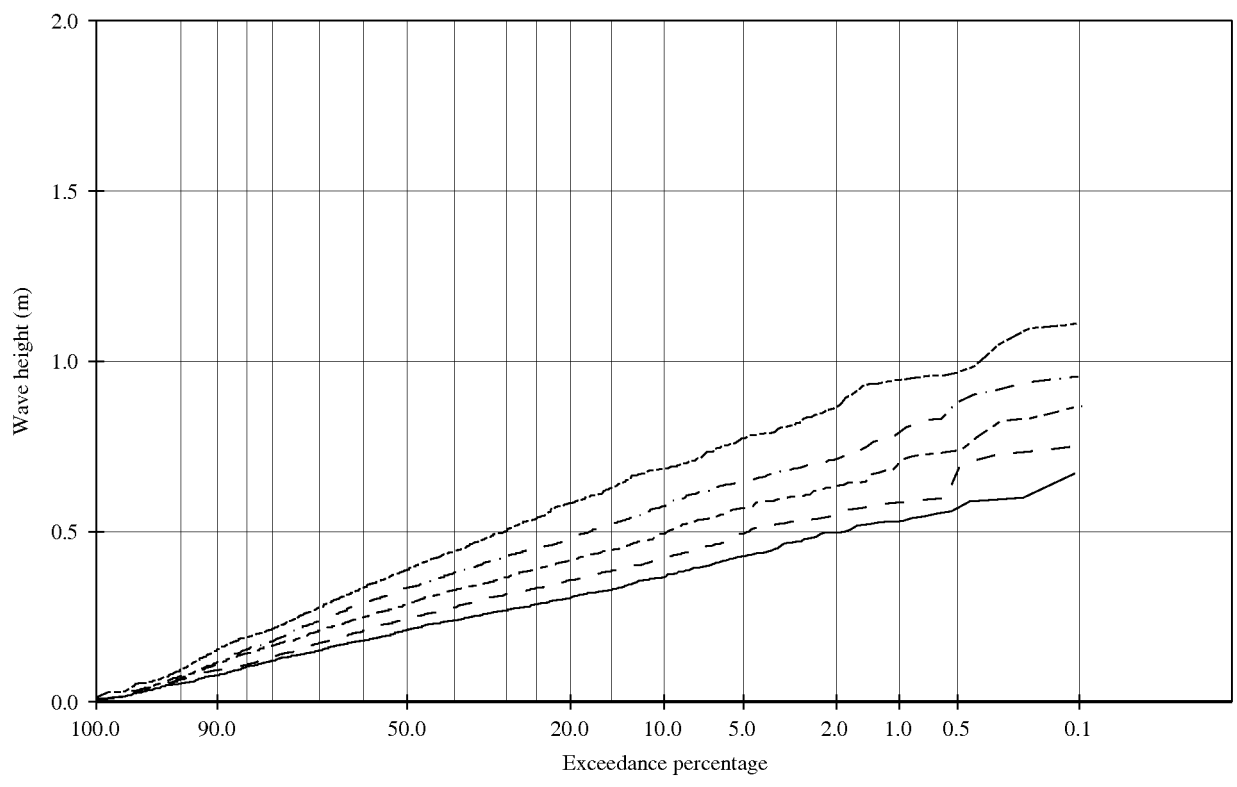
Geometrical variations in the test set-up

Geotextile tubes

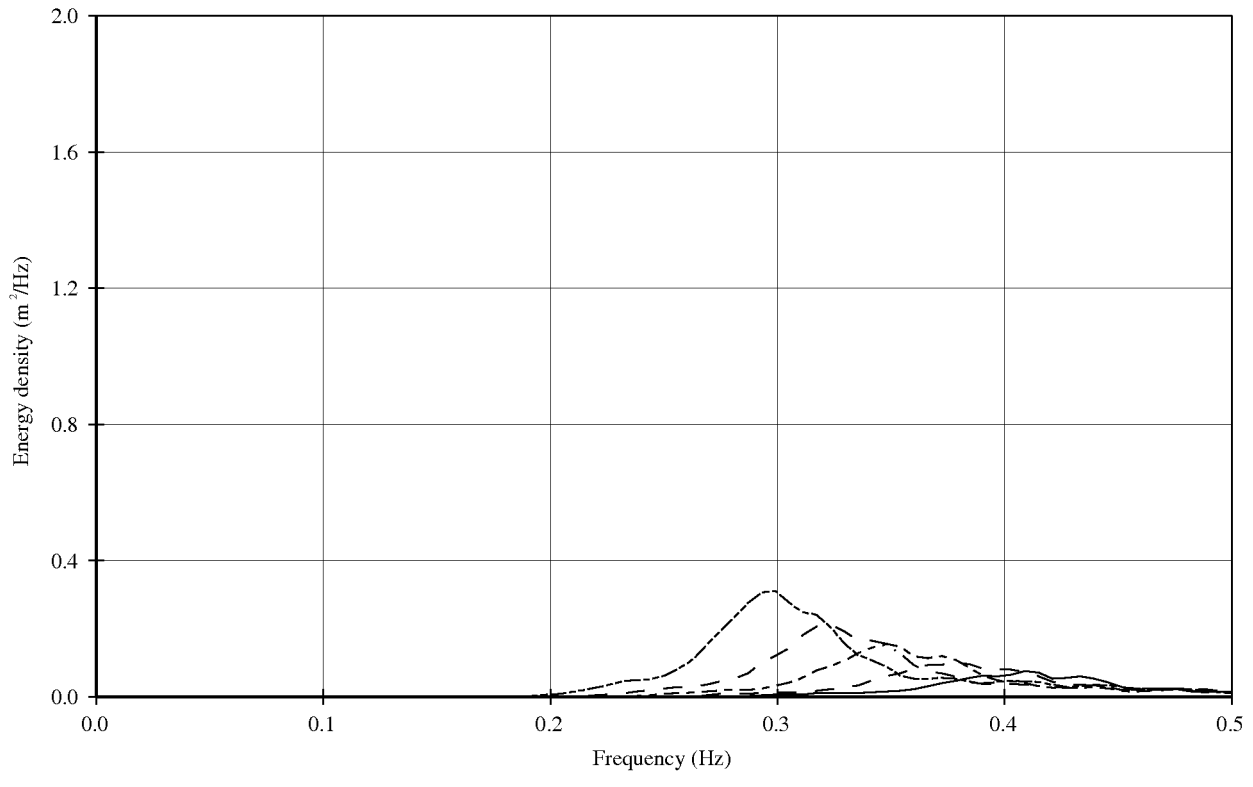
Deltares

H5153

Fig B.1c



- Test F1-1
- - - Test F1-2
- - - Test F1-3
- · - Test F1-4
- · · Test F1-5



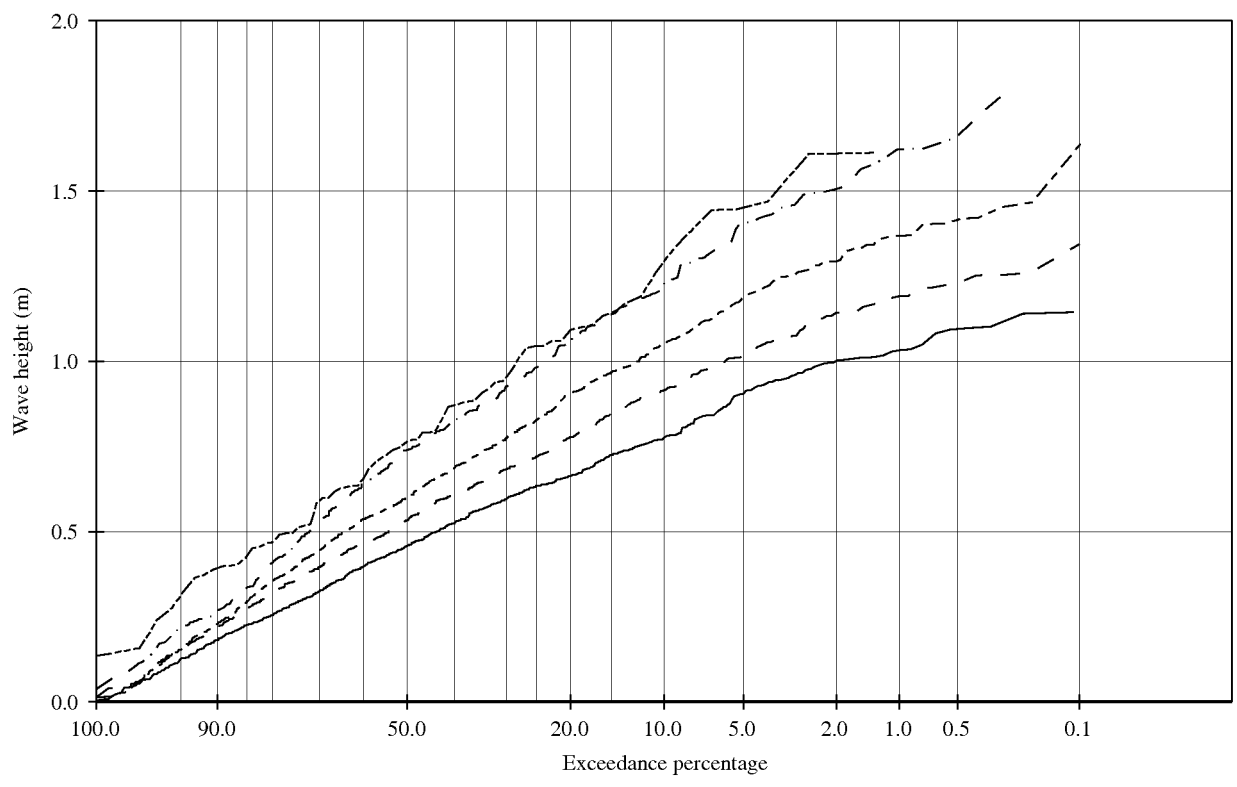
Wave height exceedance curves and  
energy spectra

Series F1  
Incoming waves

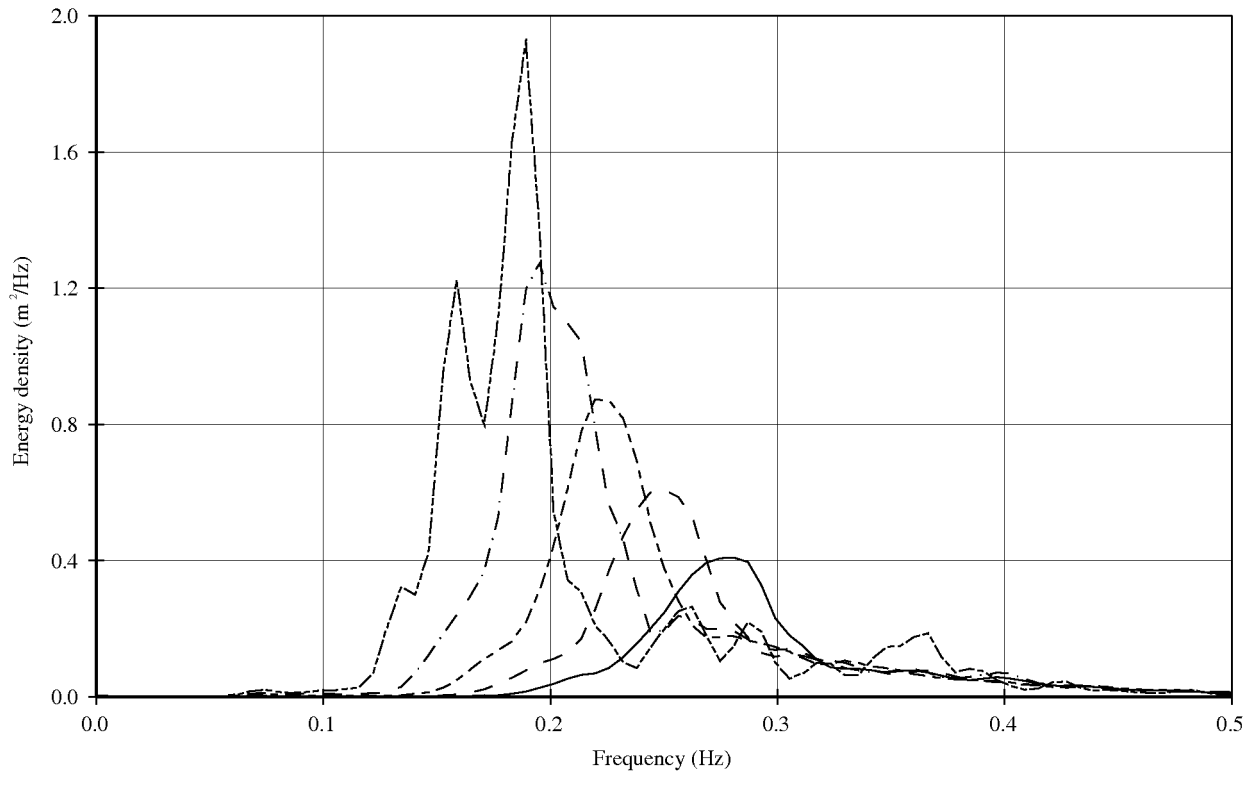
**Deltares**

H5188

Fig.B2a



- Test F1-6
- - - Test F1-7
- - - Test F1-8
- · - · Test F1-9
- - - Test F1-10



Wave height exceedance curves and  
energy spectra

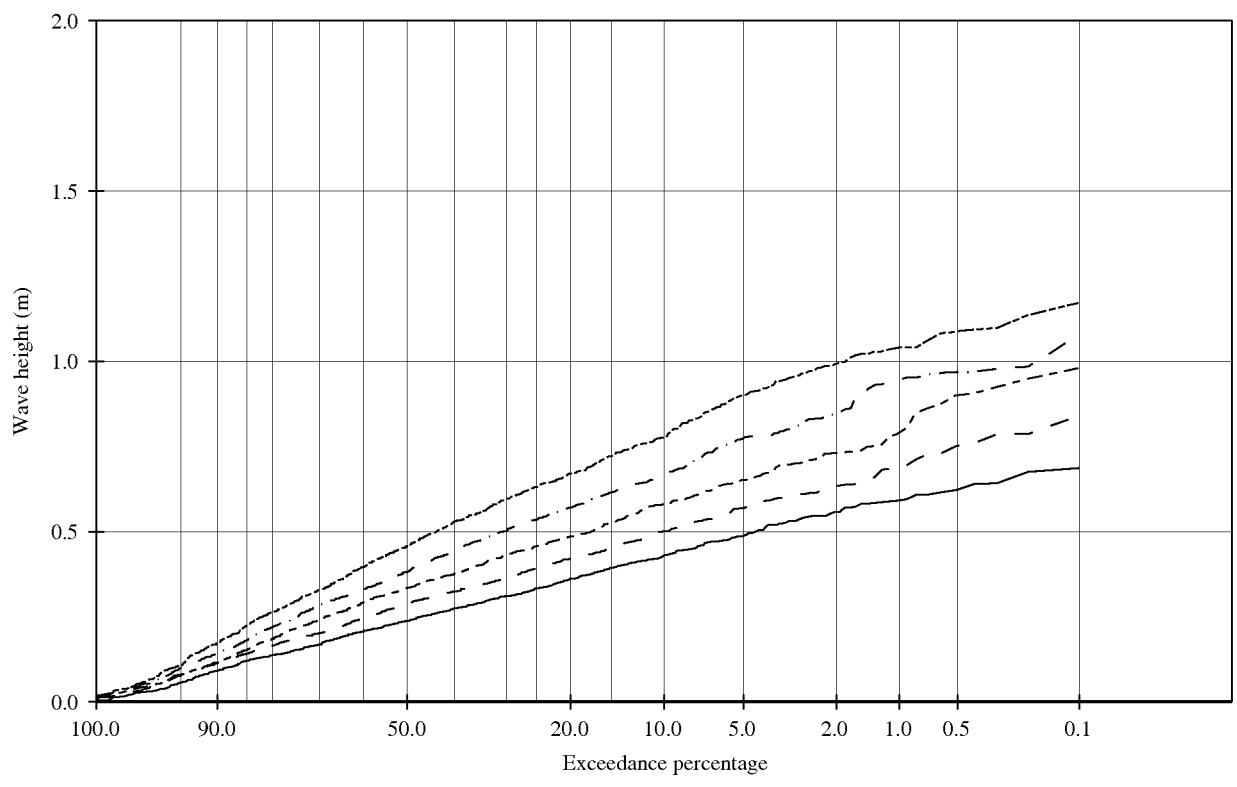
Series F1

Incoming waves

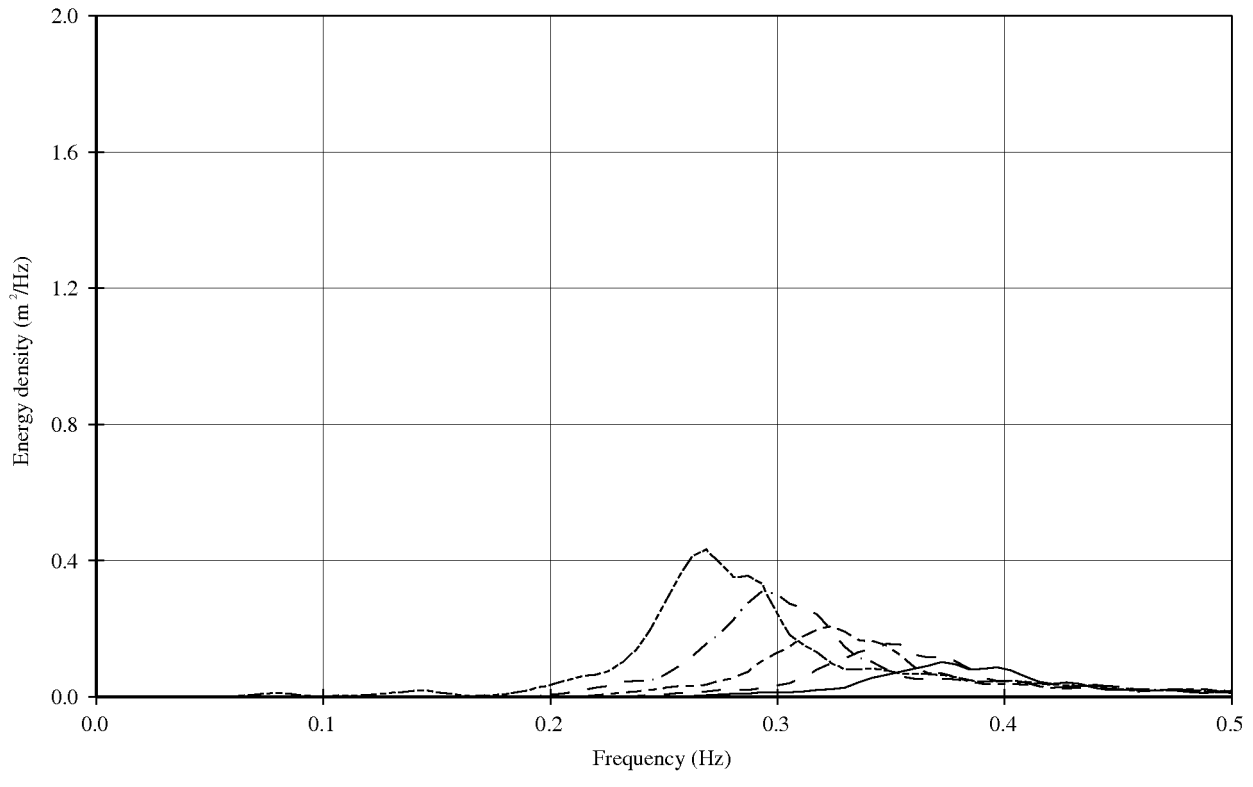
**Deltares**

H5188

Fig.B2b



- Test F3-1
- - - Test F3-21
- - - Test F3-3
- · - Test F3-4
- · · Test F3-5



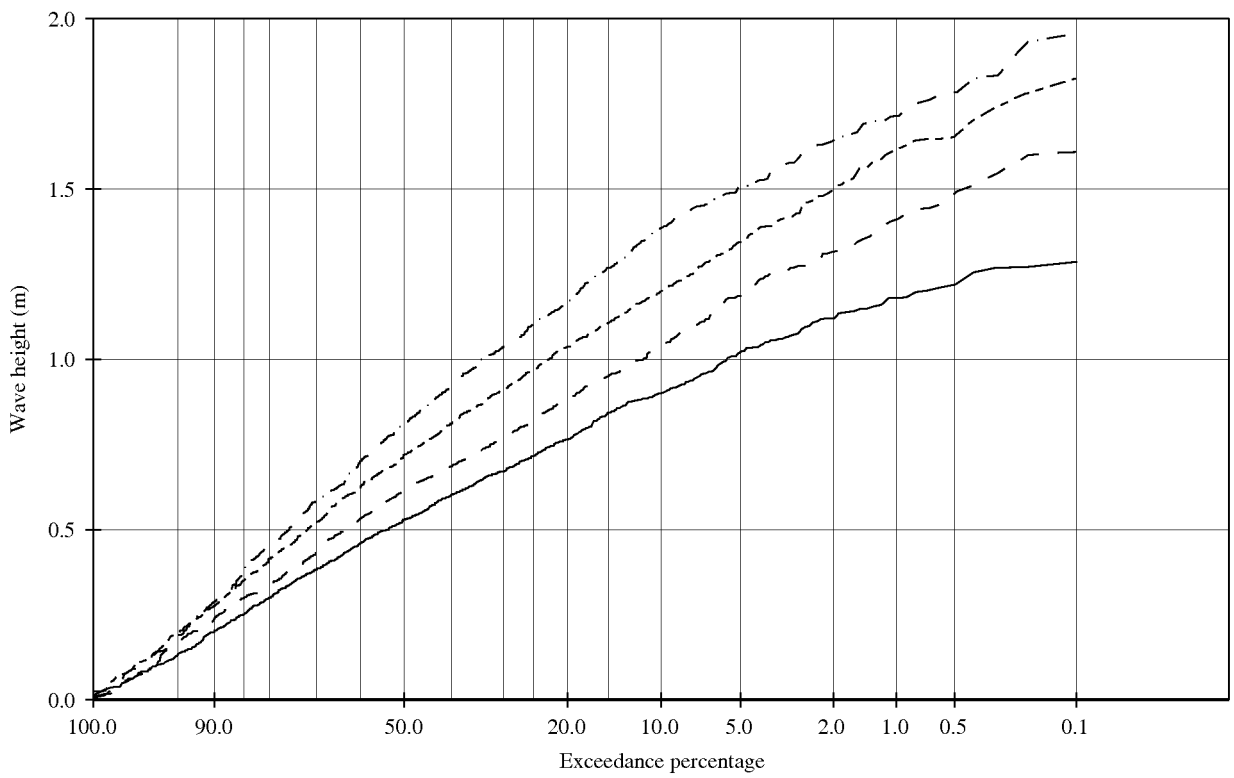
Wave height exceedance curves and  
energy spectra

Series F3  
Incoming waves

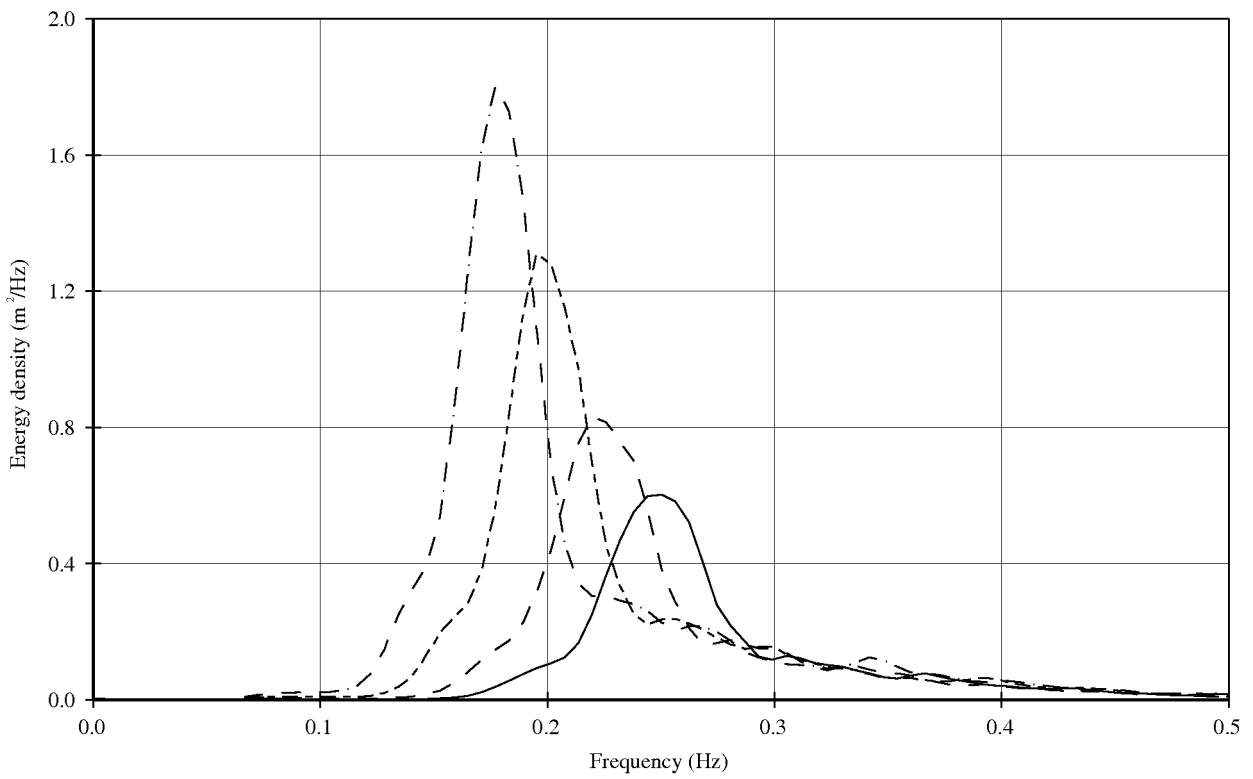
**Deltares**

H5188

Fig.B.2c



- Test F3-6
- - - Test F3-7
- · - Test F3-8
- - - - Test F3-9



Wave height exceedance curves and  
energy spectra

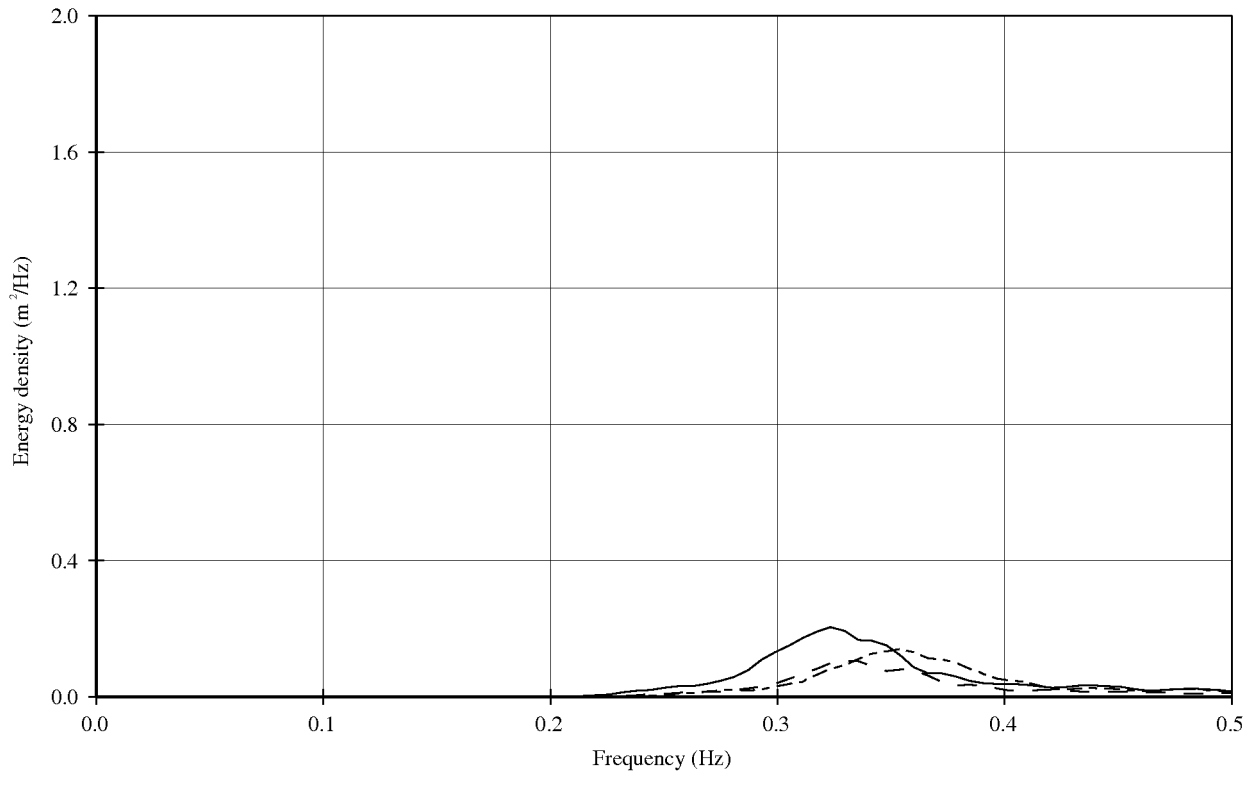
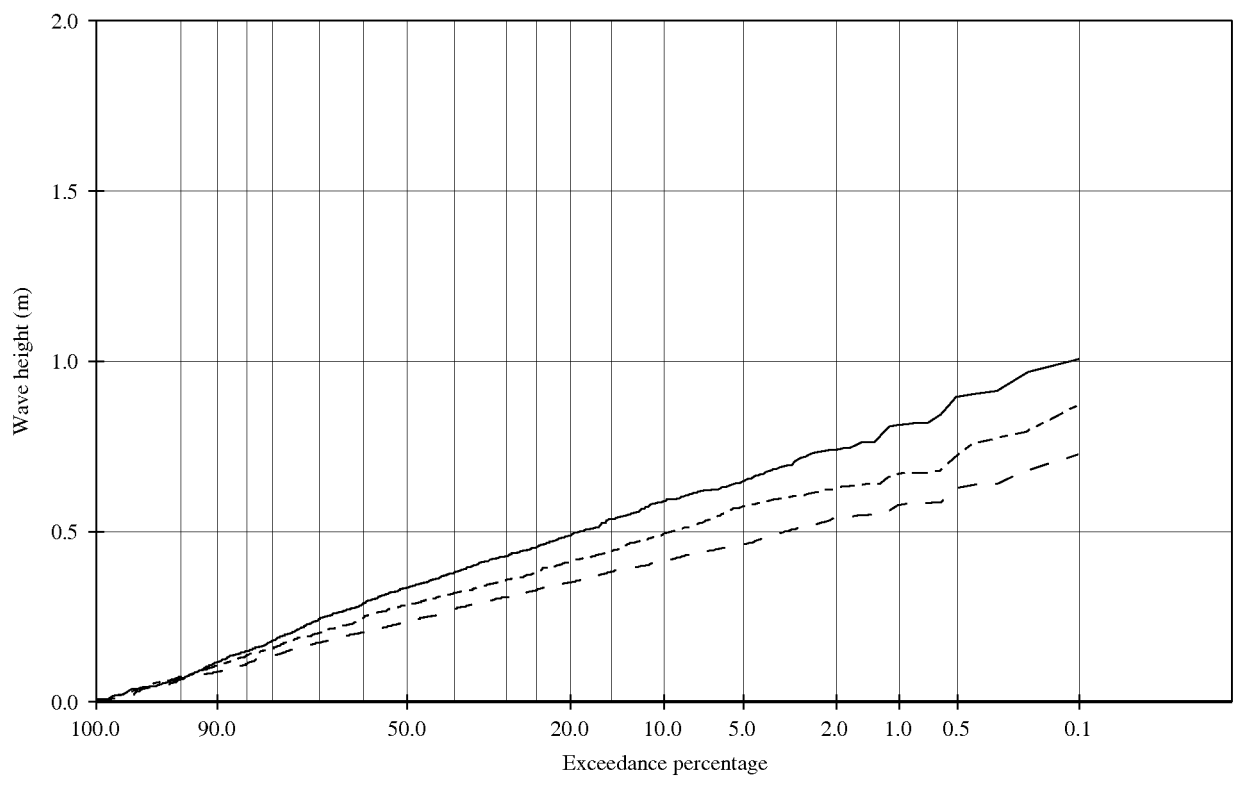
Series F3

Incoming waves

**Deltares**

H5188

FIG.B.2d



Wave height exceedance curves and  
 energy spectra

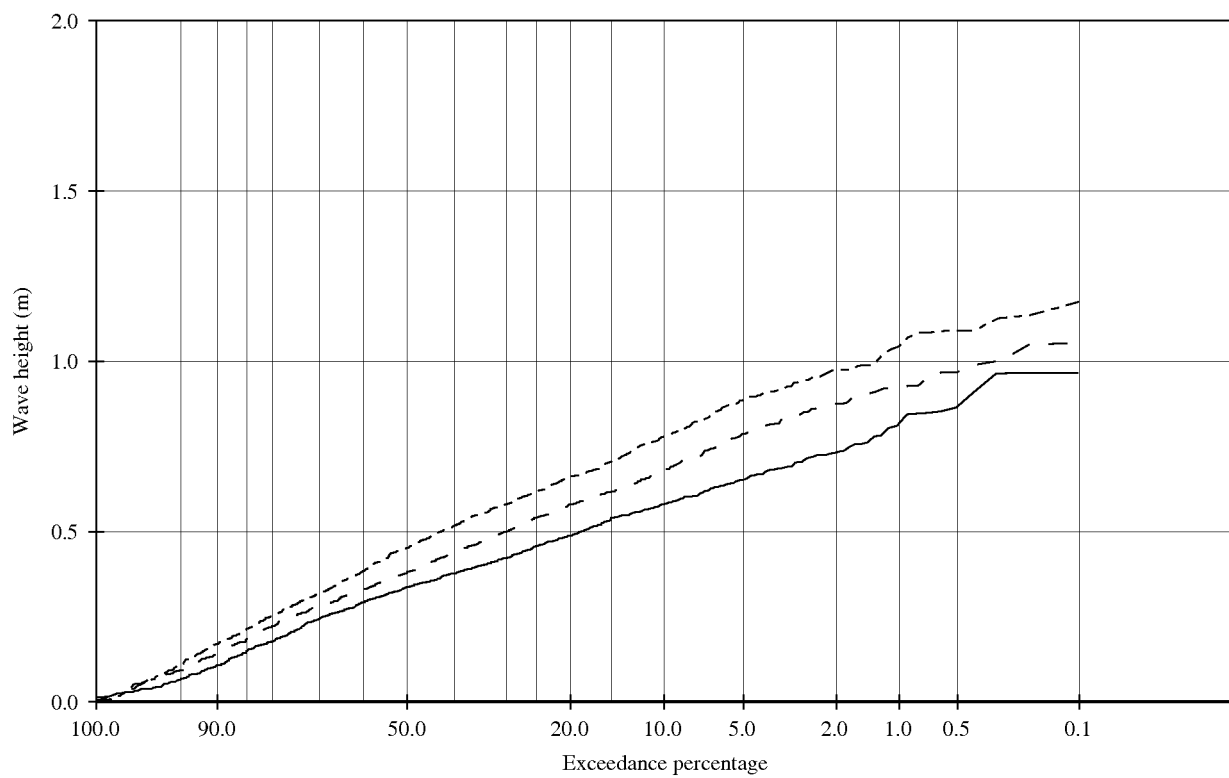
Series F4  
 Incoming waves

**Deltares**

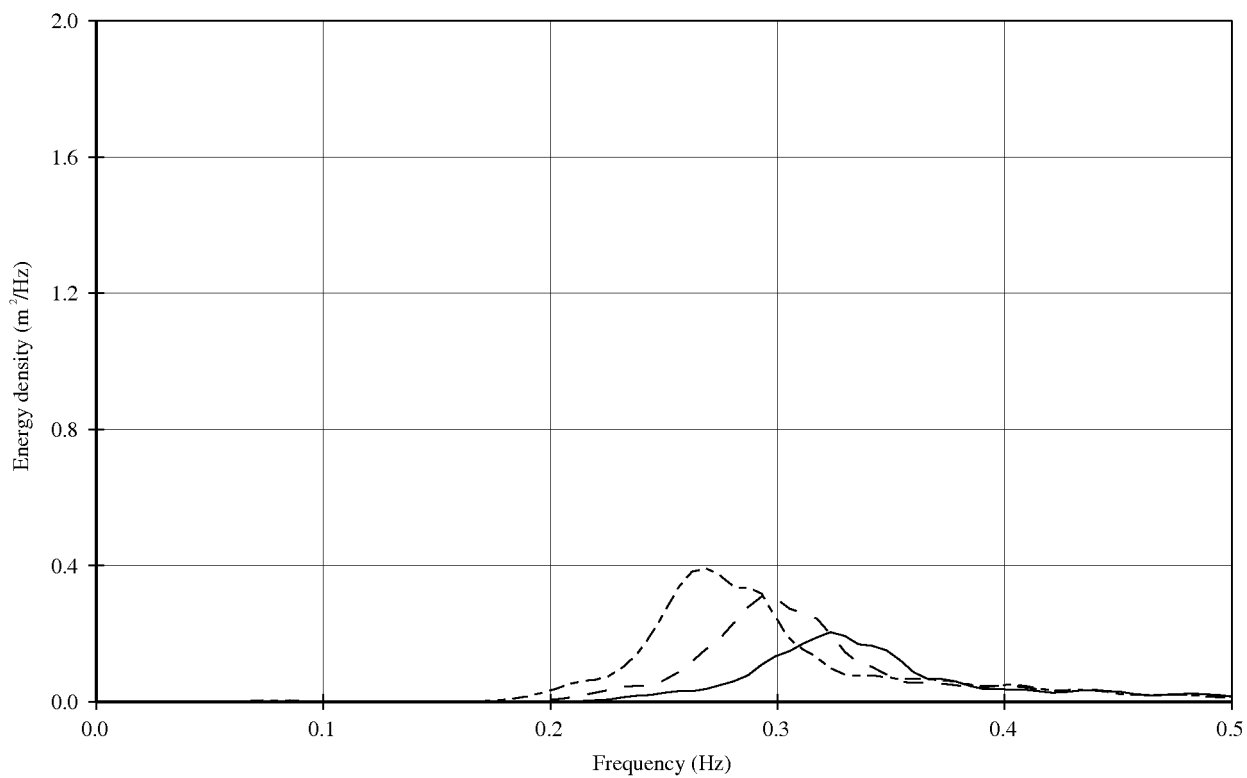
H5188

Fig.B.2e





— Test F4-4  
 - - - Test F4-5  
 - - - Test F4-6



Wave height exceedance curves and  
energy spectra

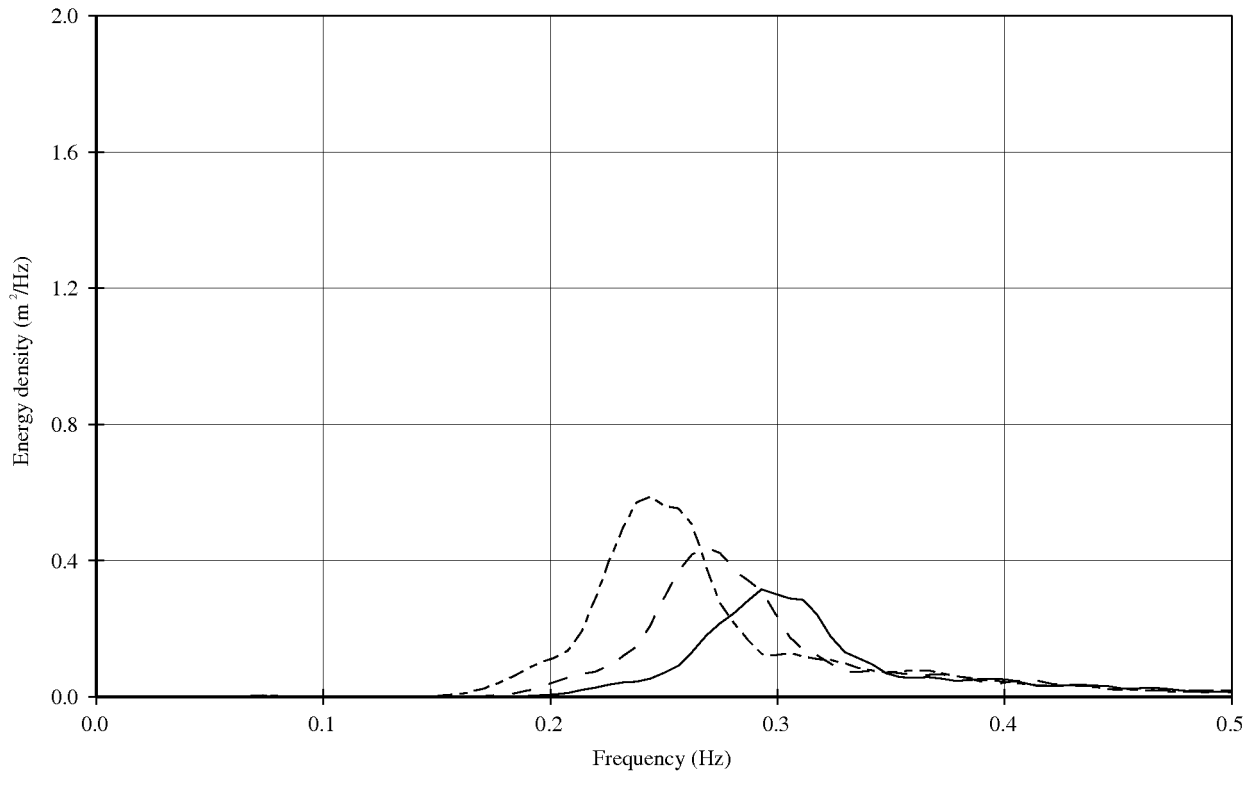
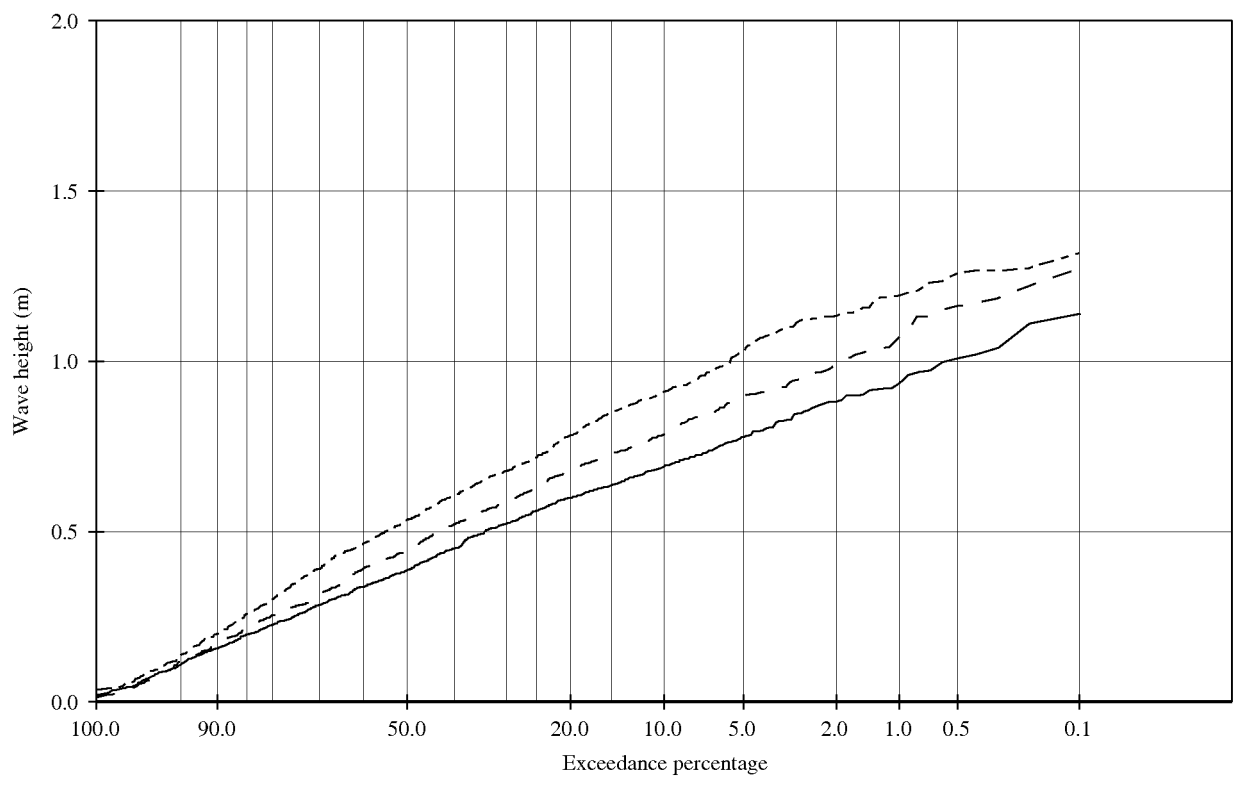
Series F4

Incoming waves

**Deltares**

H5188

Fig.B.2f



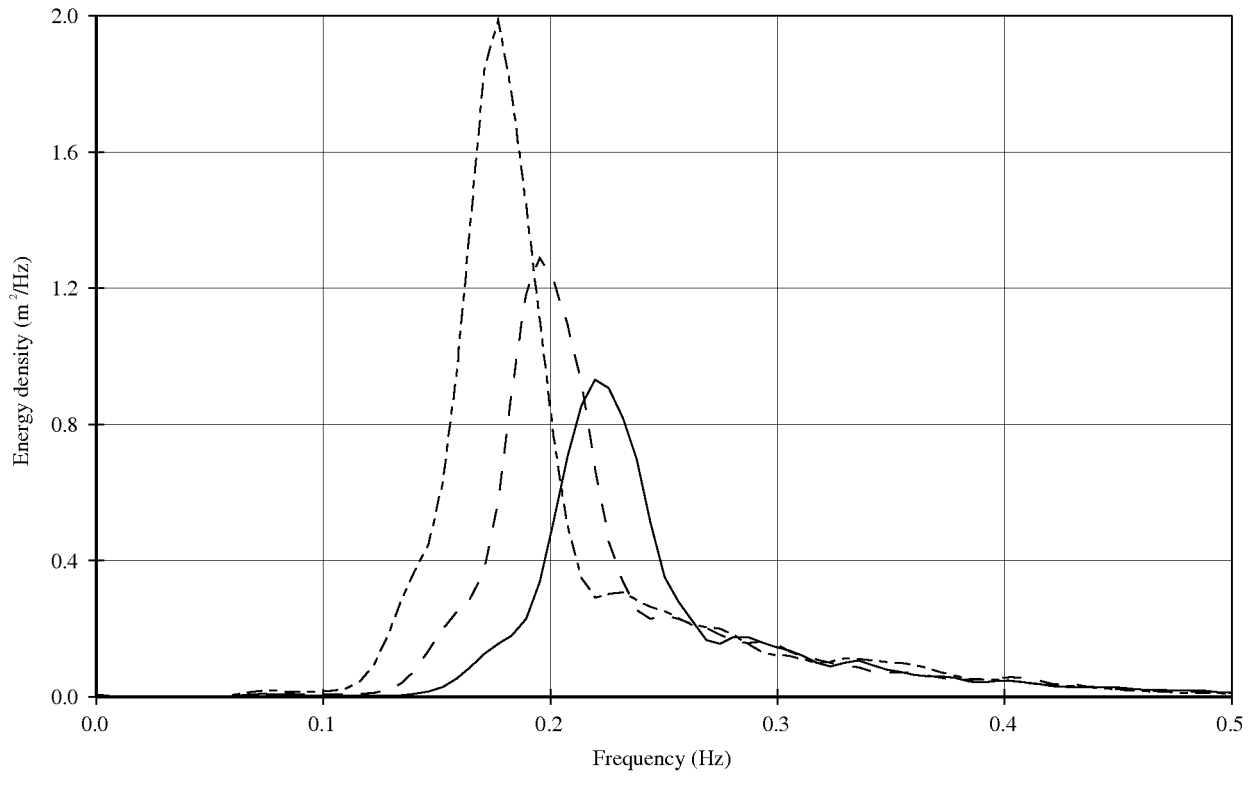
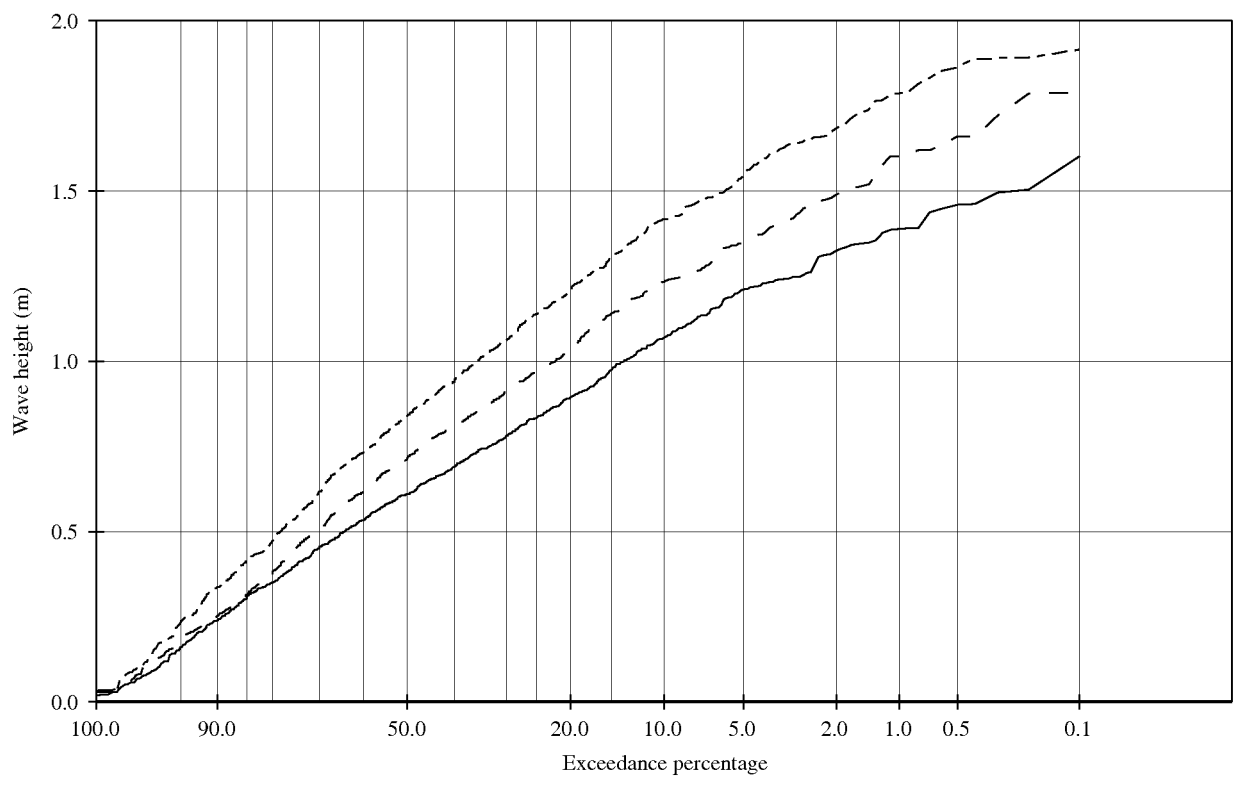
Wave height exceedance curves and  
 energy spectra

Series F5  
 Incoming waves

**Deltares**

H5188

Fig.B.2g



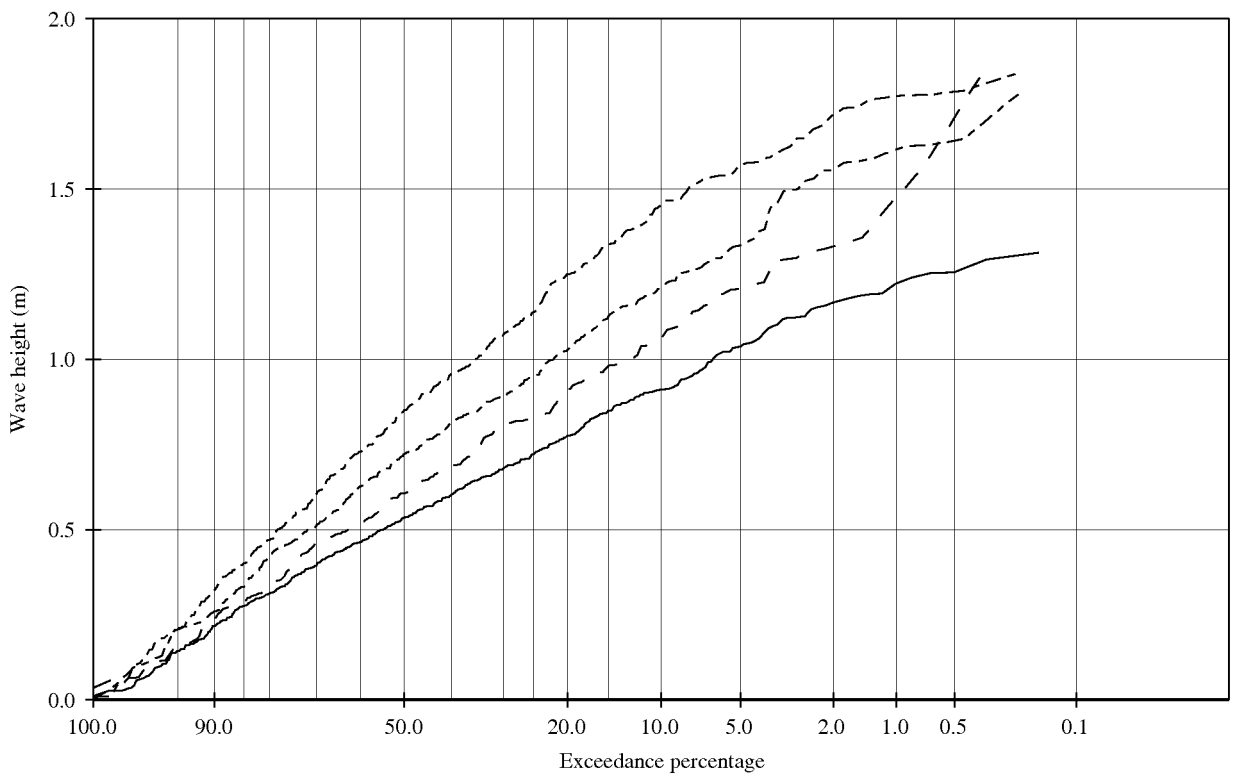
Wave height exceedance curves and  
 energy spectra

Series F5  
 Incoming waves

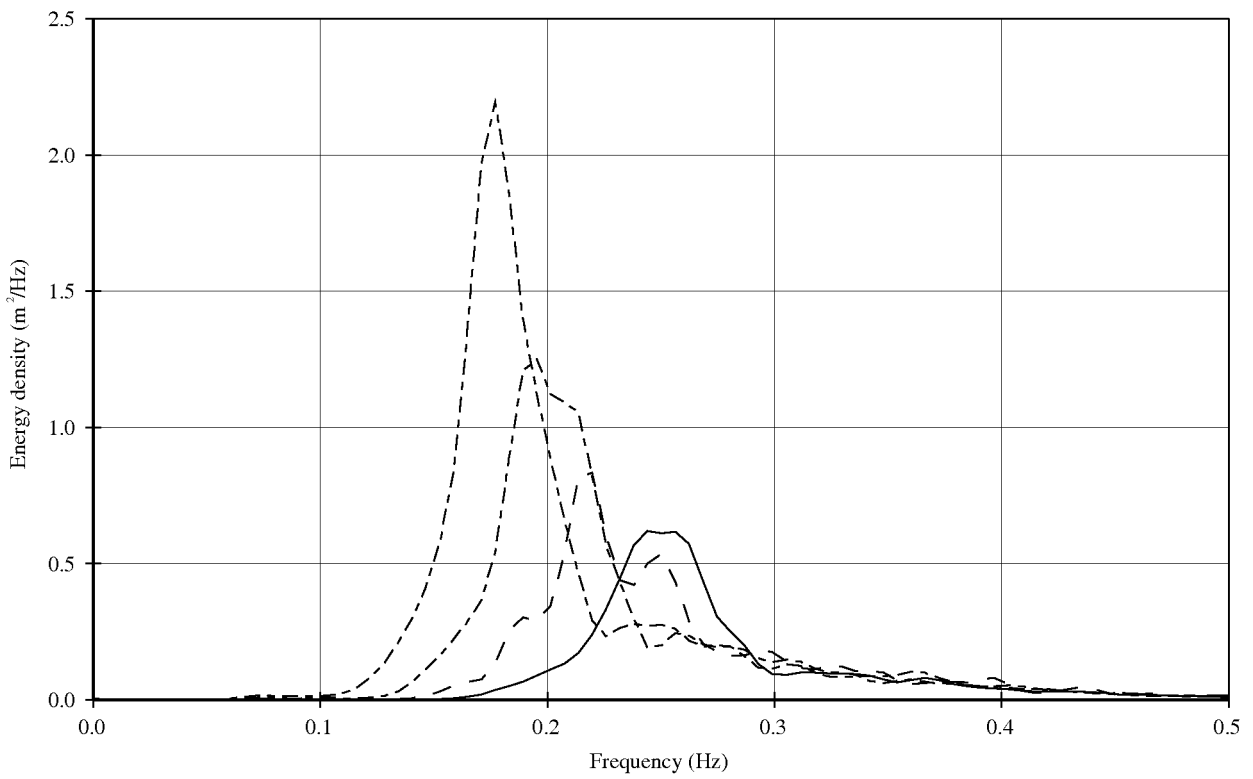
**Deltares**

H5188

Fig.B.2h



- Test P2-1
- - - Test P2-22
- - - Test P2-3
- · - Test P2-42



Wave height exceedance curves and  
energy spectra

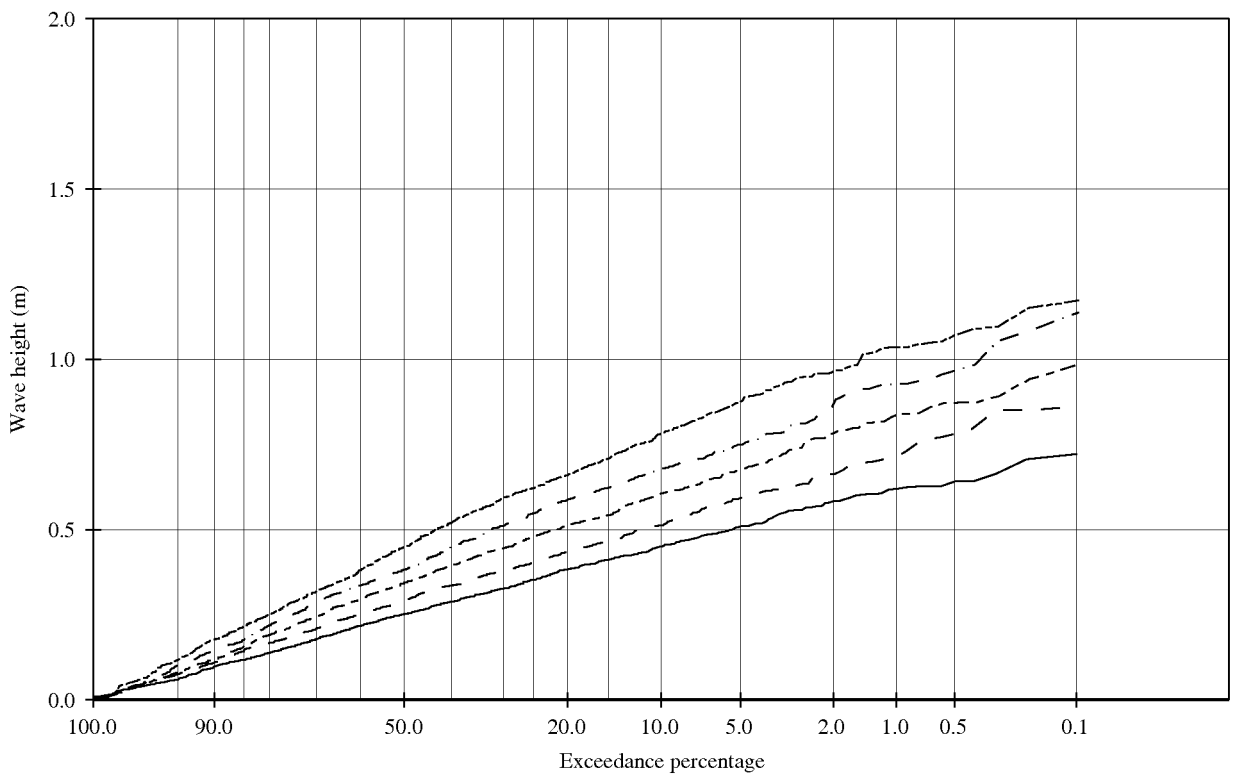
Series P2

Incoming waves

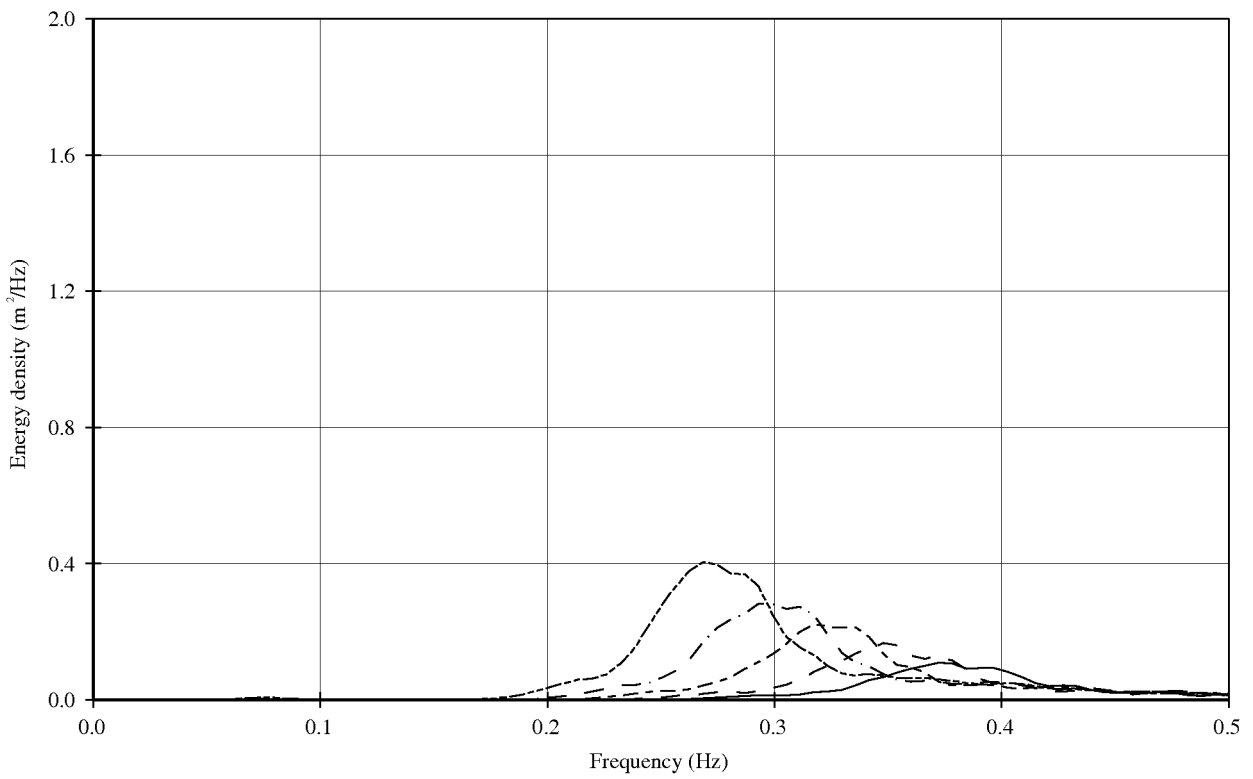
**Deltares**

H5188

Fig.B.2i



- Test P3-1
- - - Test P3-2
- - - Test P3-3
- · - Test P3-4
- · · Test P3-5



Wave height exceedance curves and  
energy spectra

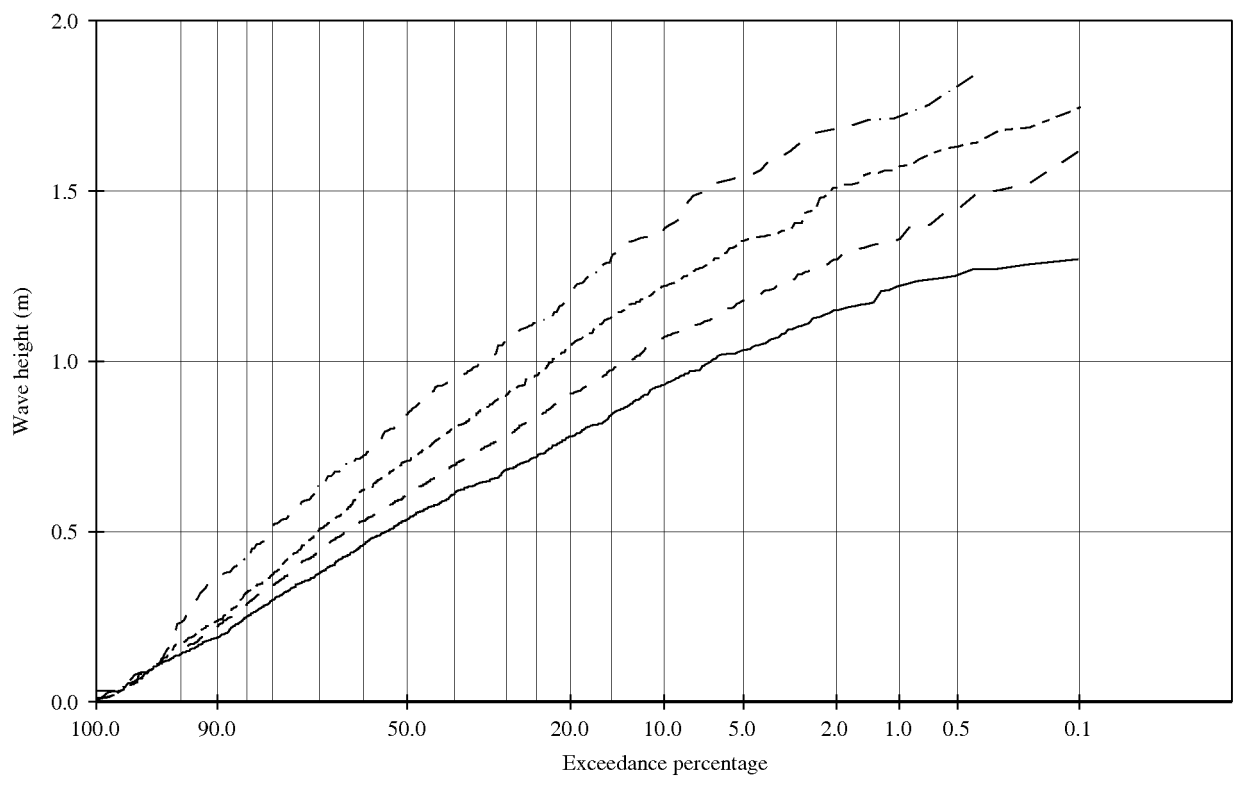
Series P3

Incoming waves

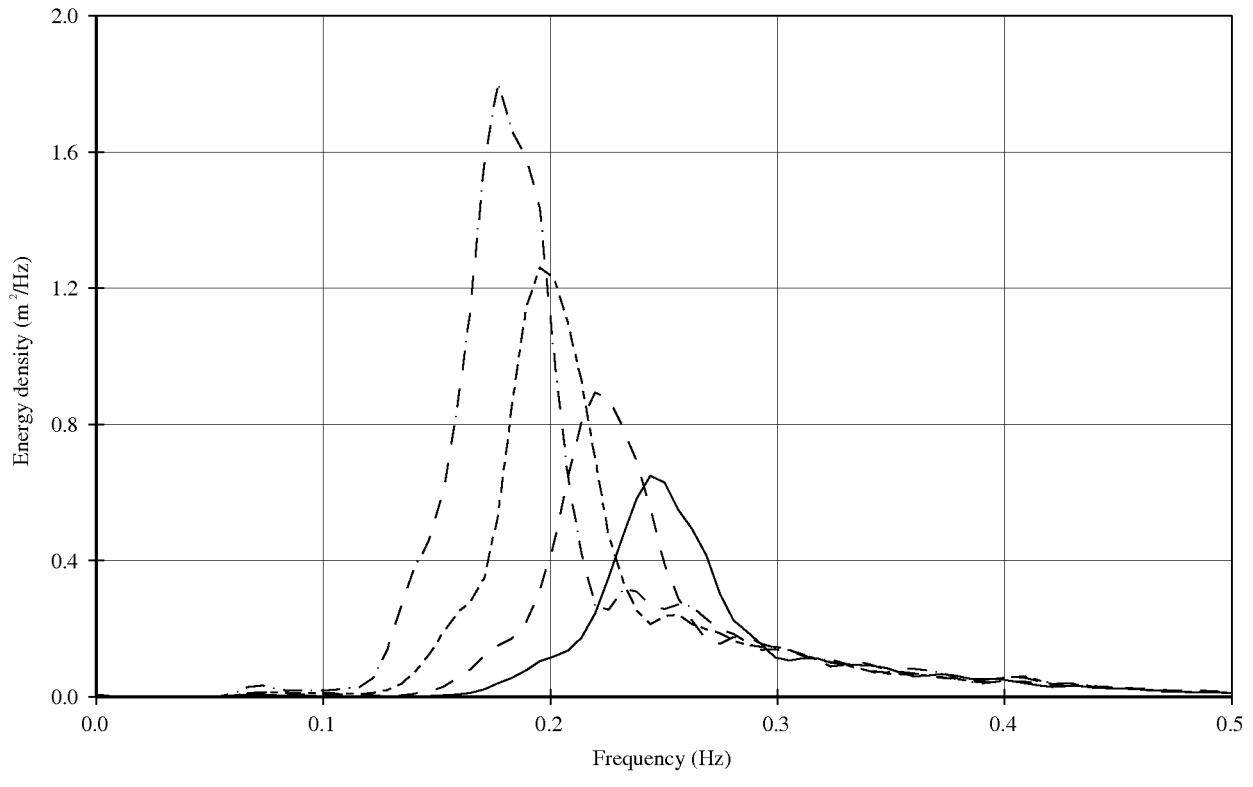
**Deltares**

H5188

Fig.B.2j



- Test P3-6
- - - Test P3-7
- · - Test P3-8
- - - - Test P3-9



Wave height exceedance curves and  
energy spectra

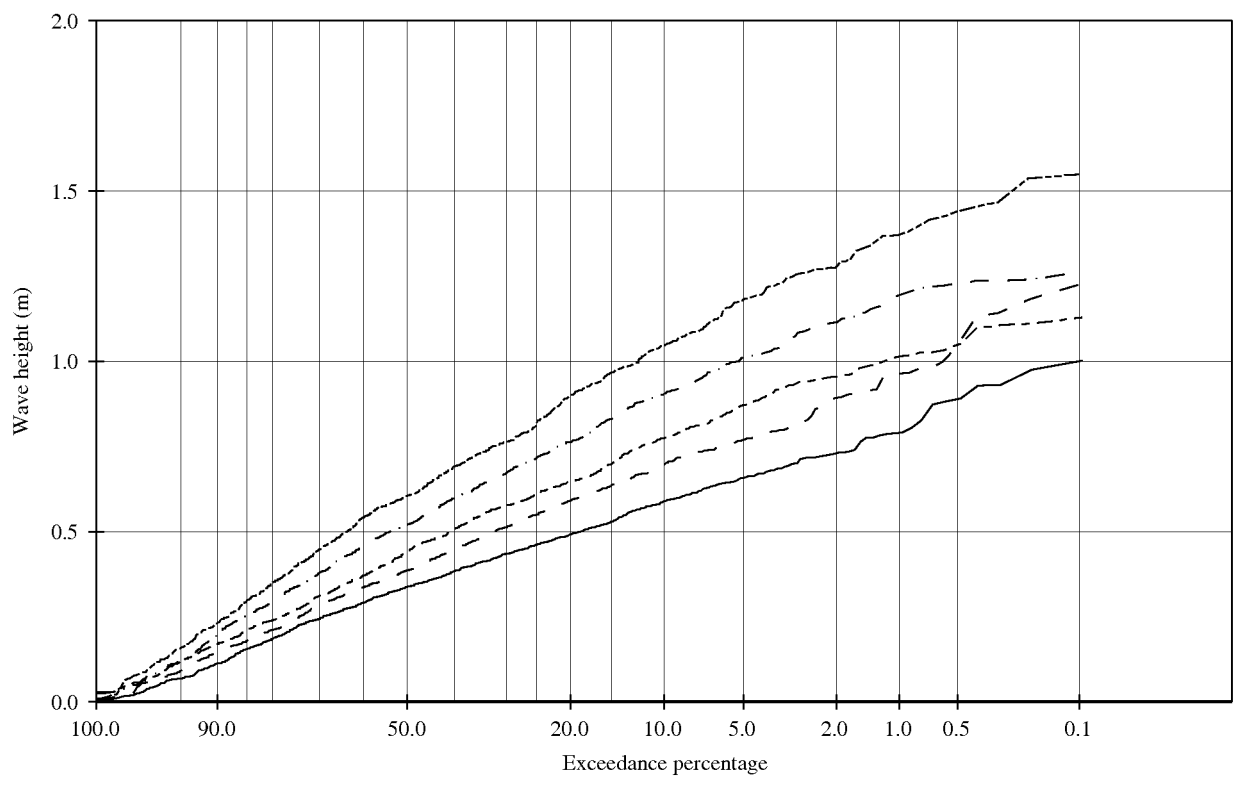
Series P3

Incoming waves

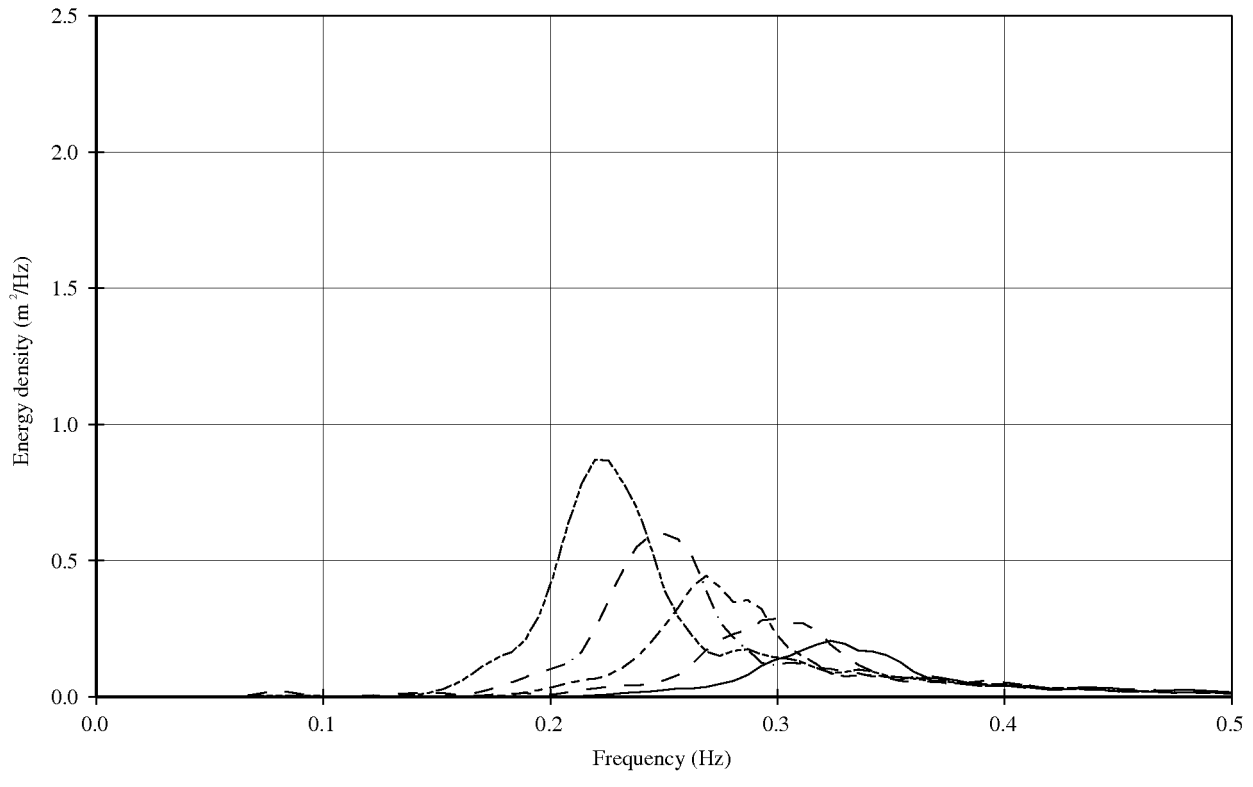
**Deltares**

H5188

Fig.B.2k

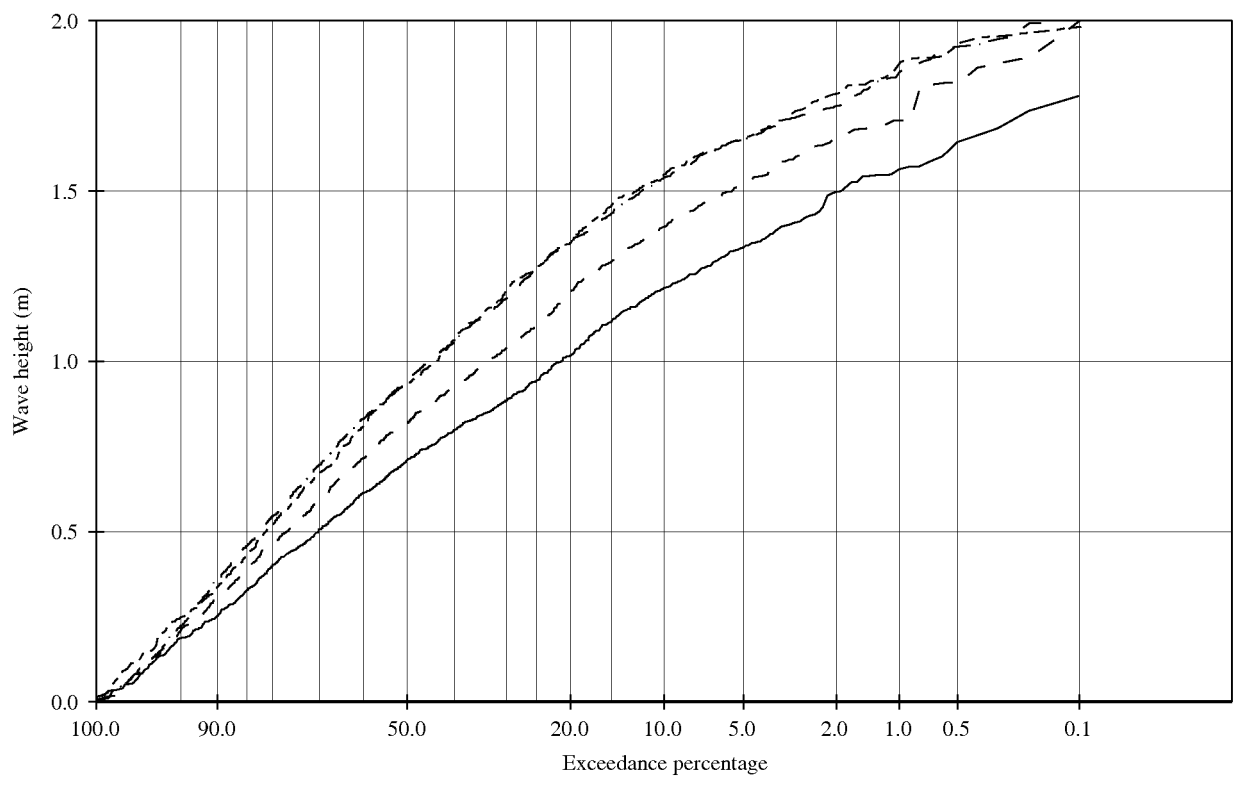


- Test T1-1
- - - Test T1-2
- - - Test T1-3
- · - Test T1-4
- · · Test T1-5

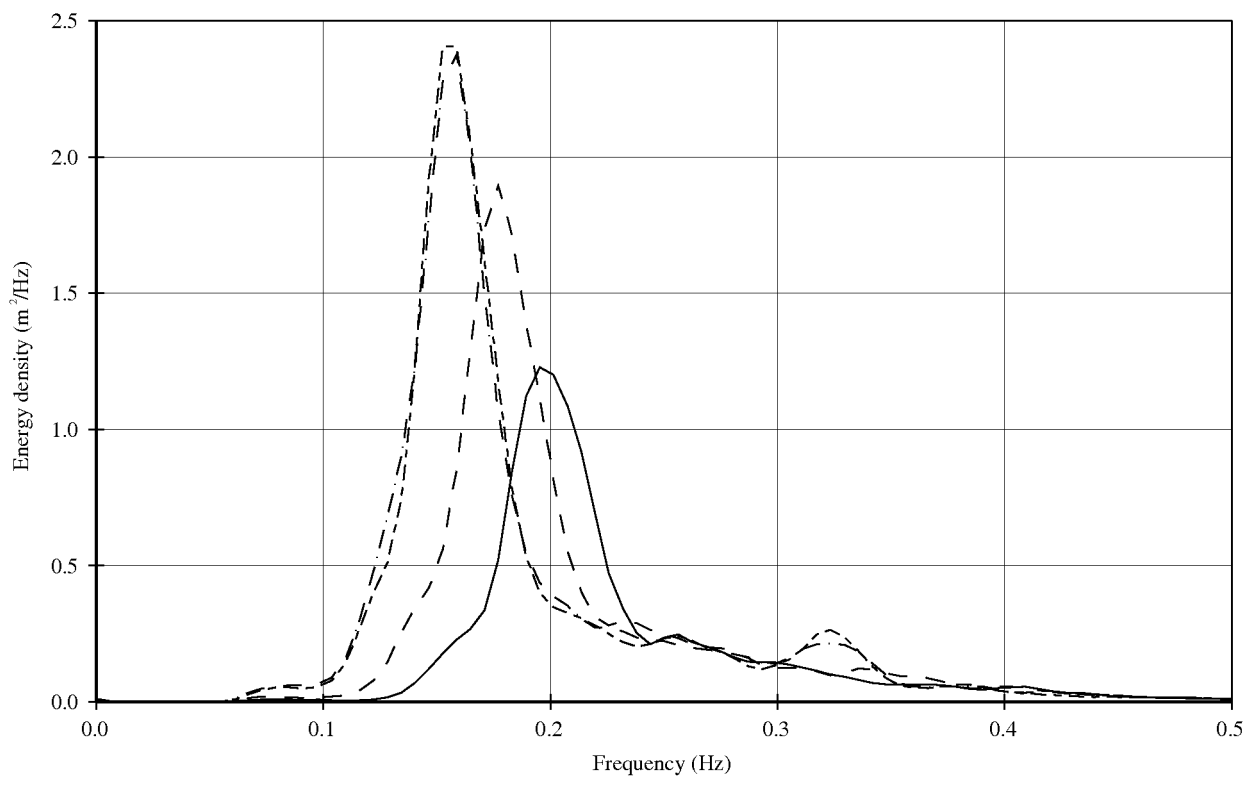


Wave height exceedance curves and  
energy spectra

Series T1  
Incoming waves



- Test T1-6
- - - Test T1-7
- - - Test T1-8
- · - · Test T1-9



Wave height exceedance curves and  
energy spectra

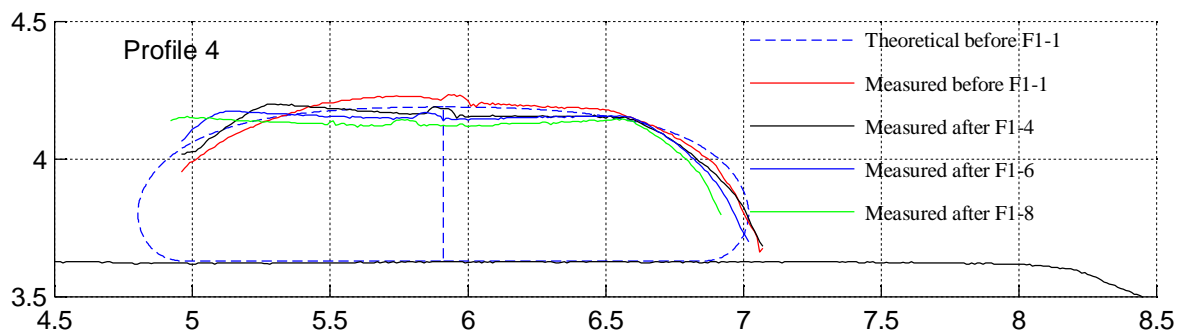
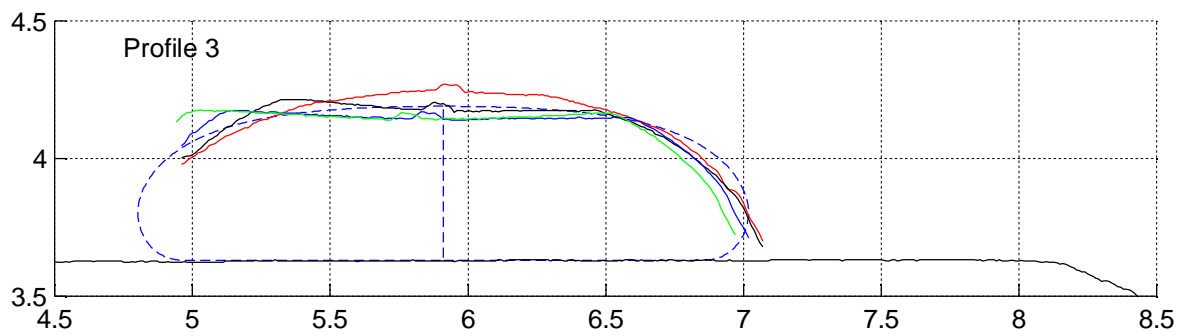
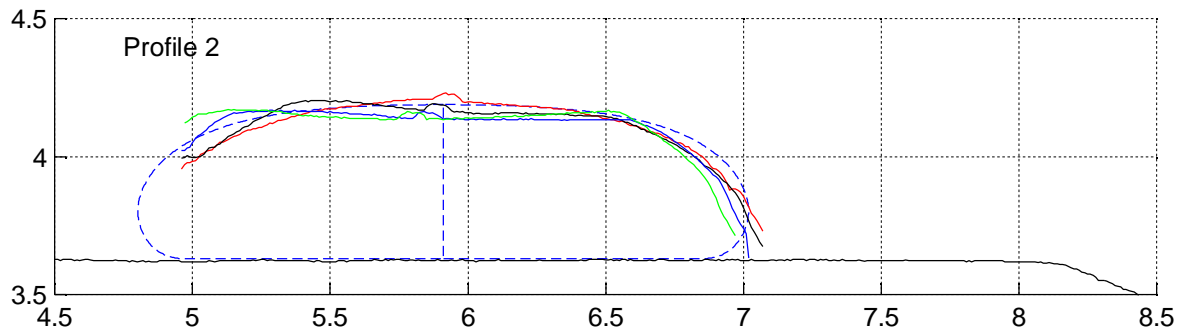
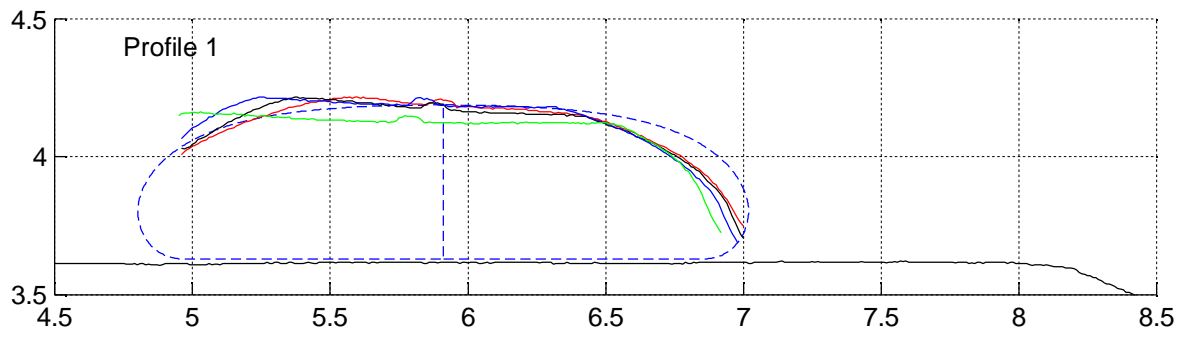
Series T1  
Incoming waves

**Deltares**

H5188

Fig.B.2m





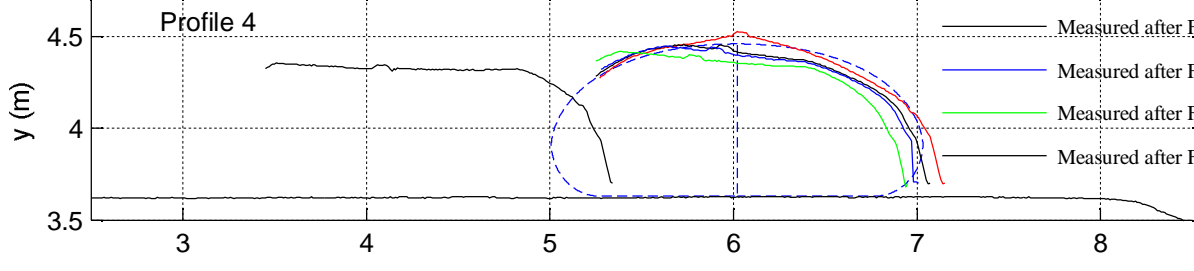
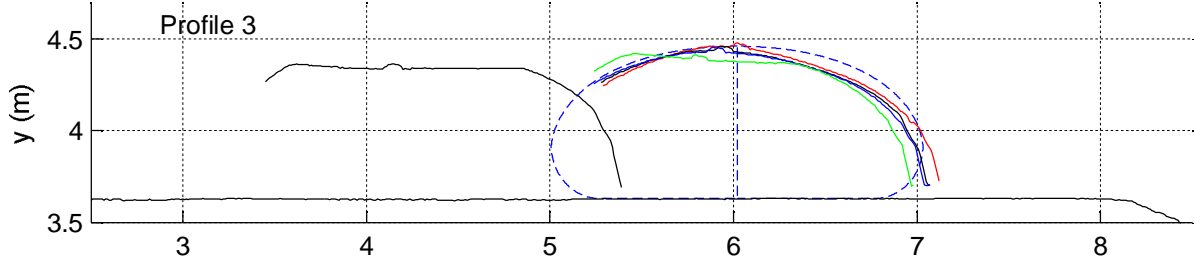
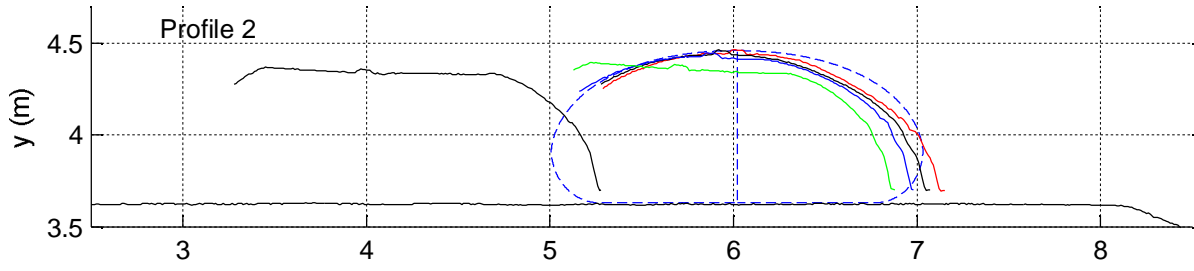
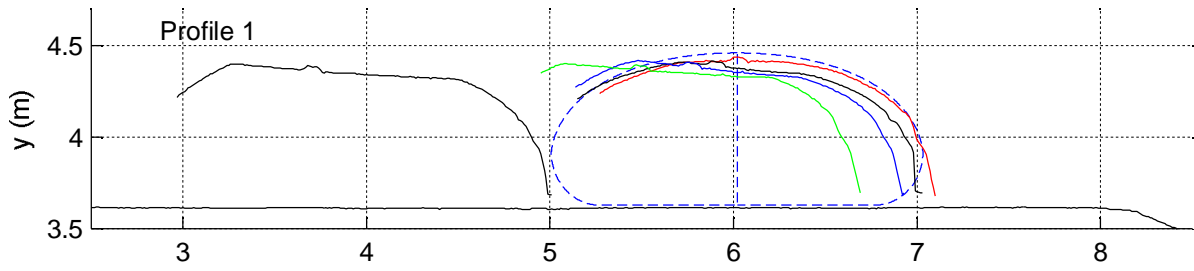
Results profiler Test Series F1

Geotextile tubes

Deltares

H5153

Fig. B.3a



- Theoretical before F3-1
- Measured after F3-1
- Measured after F3-5
- Measured after F3-6
- Measured after F3-8
- Measured after F3-9

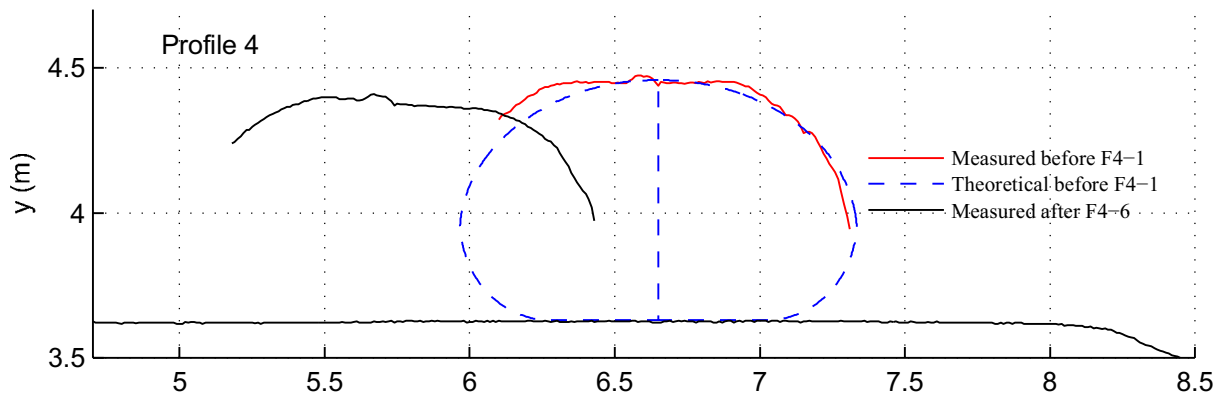
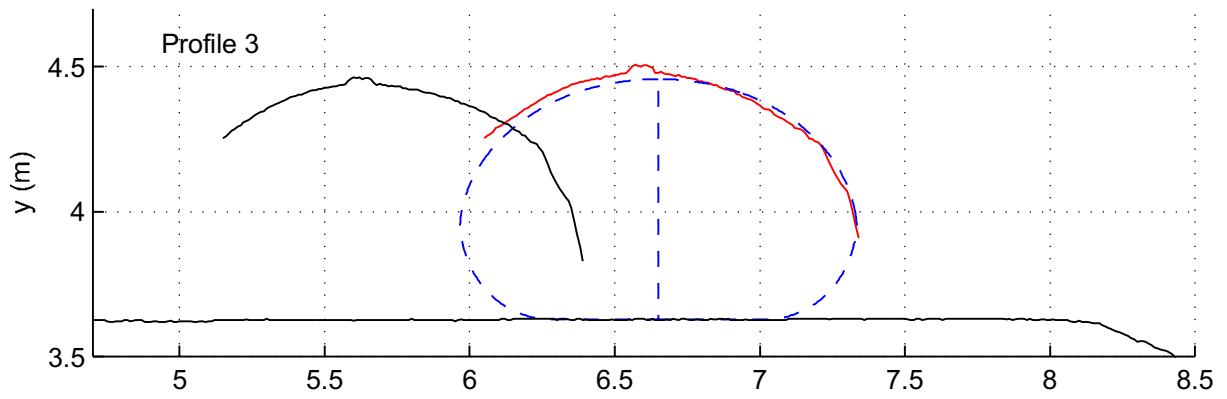
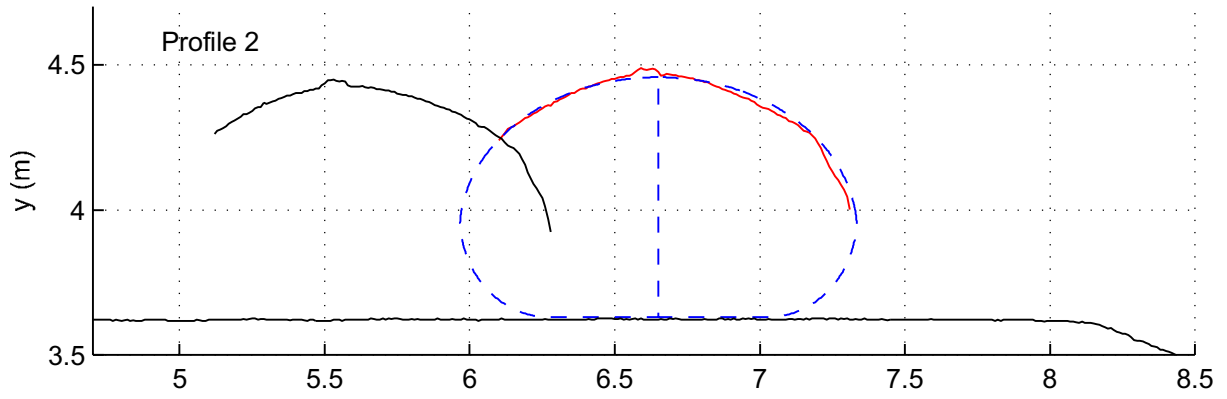
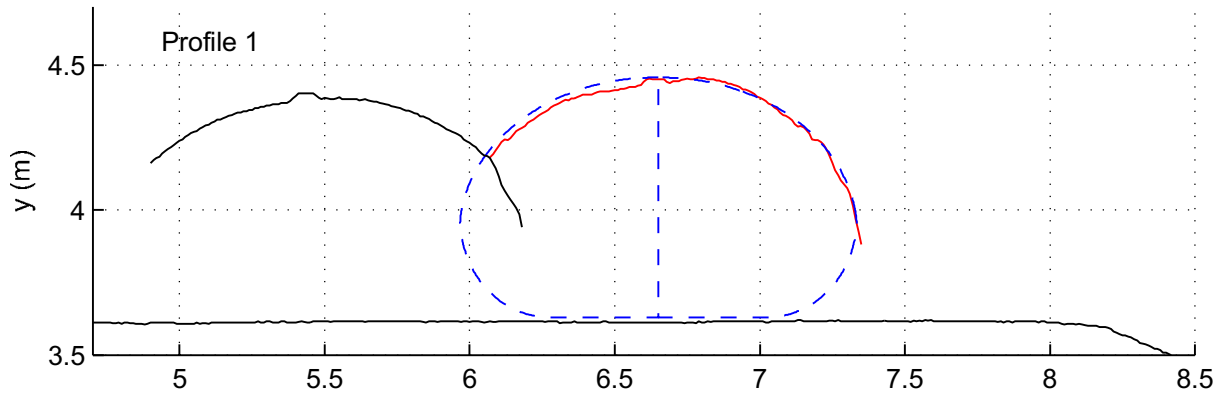
Results profiler Test Series F3

Geotextile tubes

**Deltares**

H5153

Fig. B.3b



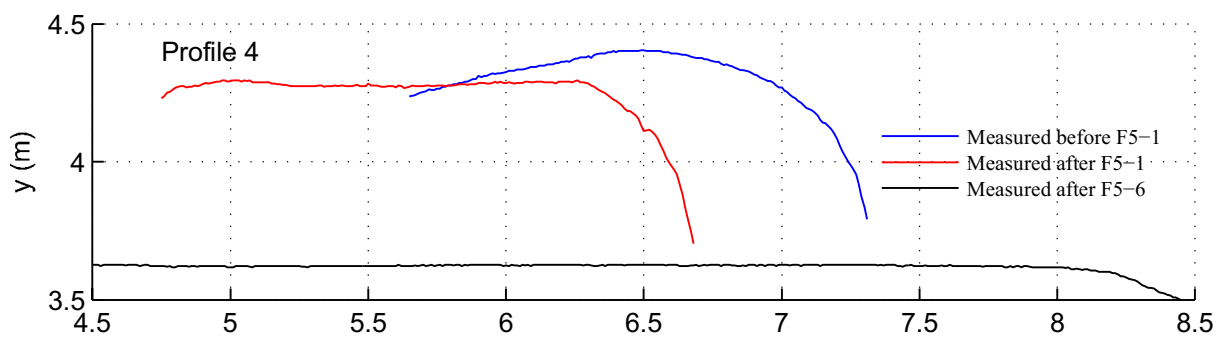
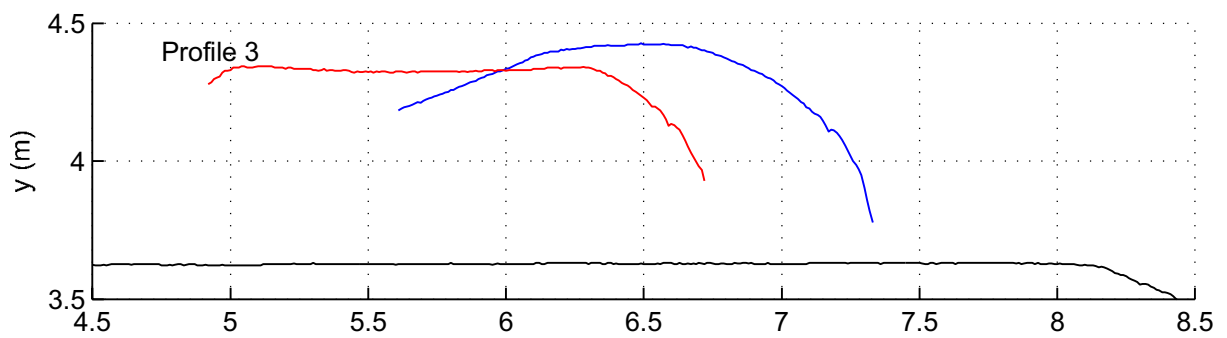
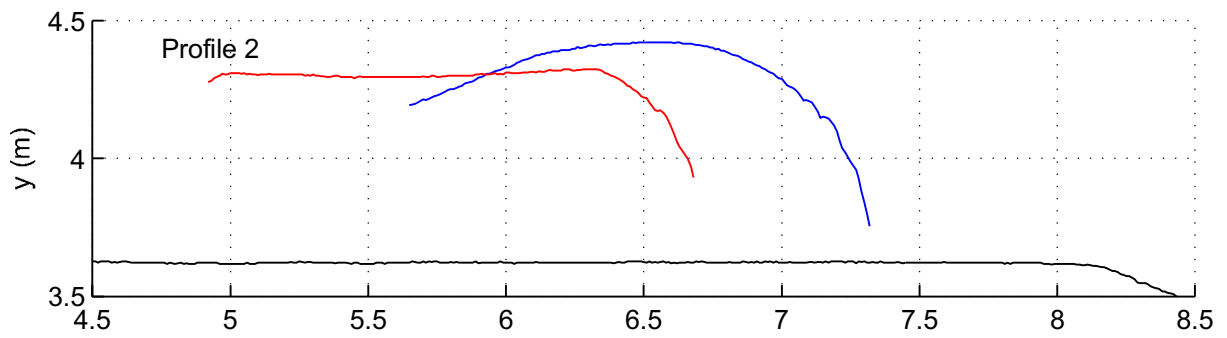
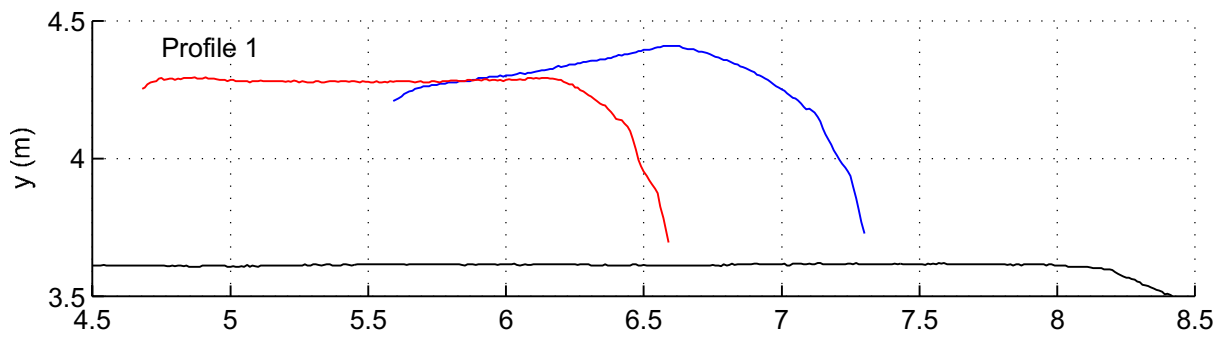
Results profiler Test Series F4

Geotextile tubes

Deltares

H5153

Fig. B.3c



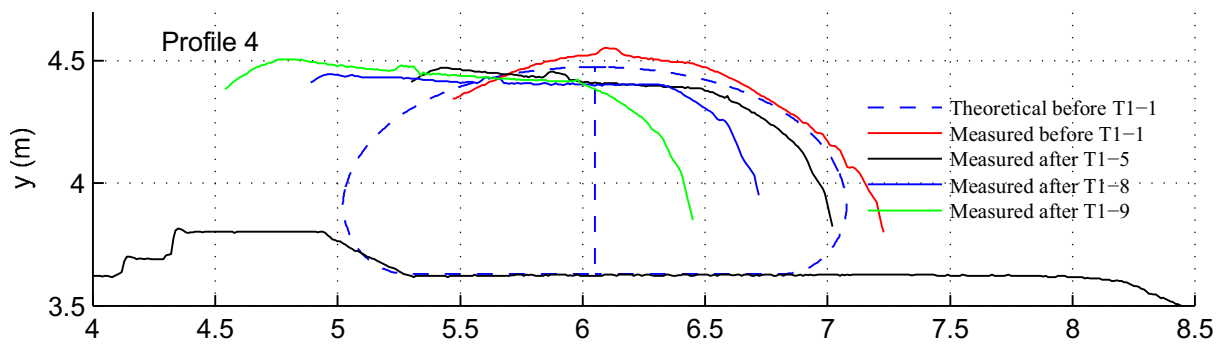
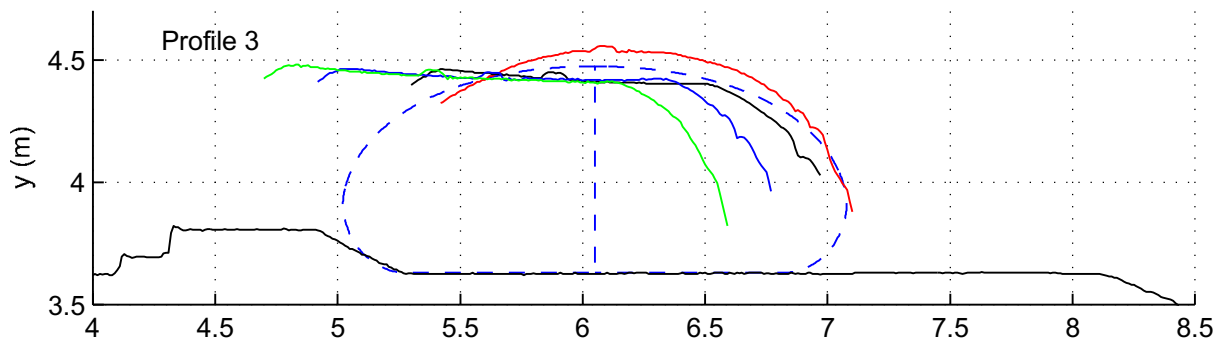
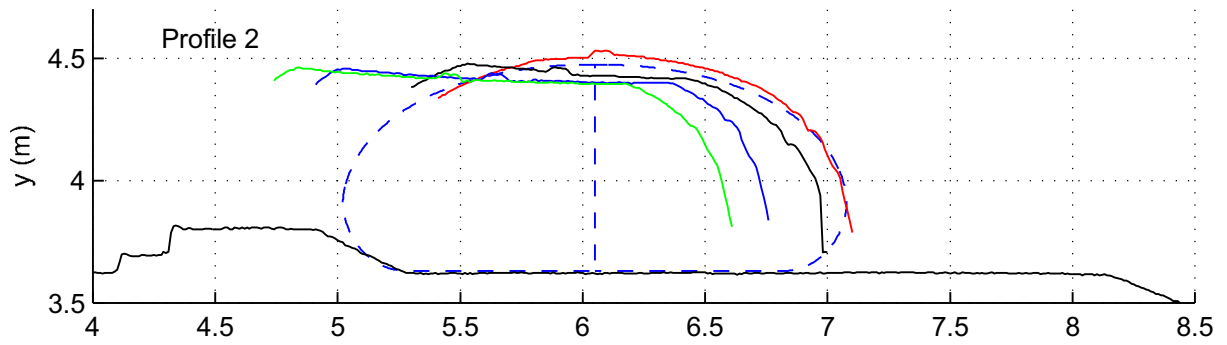
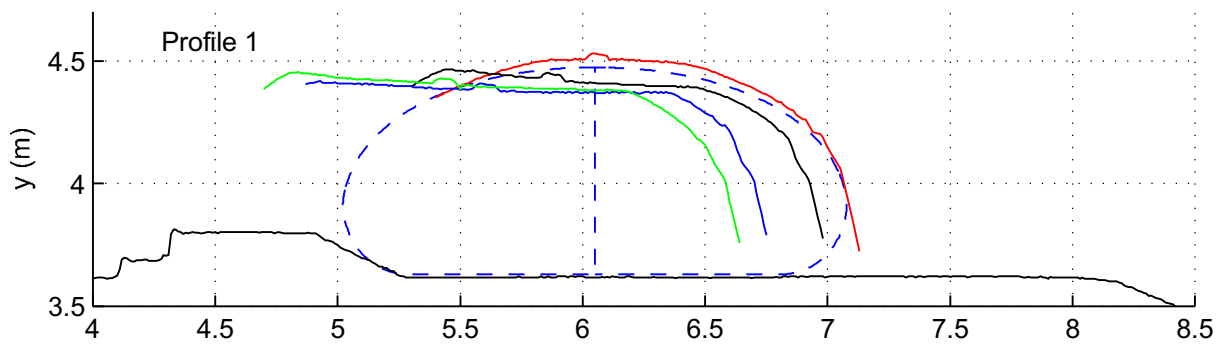
Results profiler Test Series F5

Geotextile tubes

Deltares

H5153

Fig. B.3d



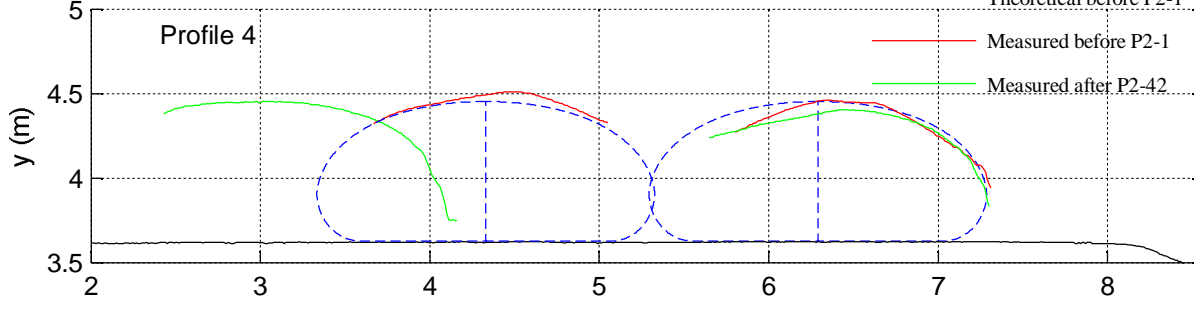
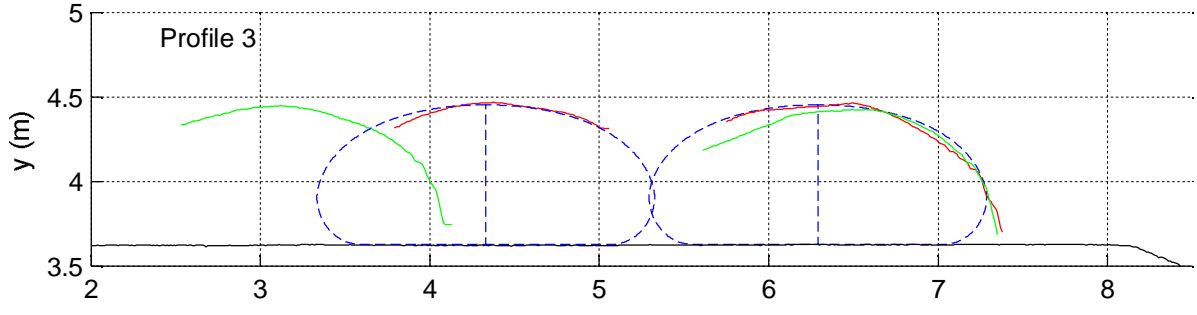
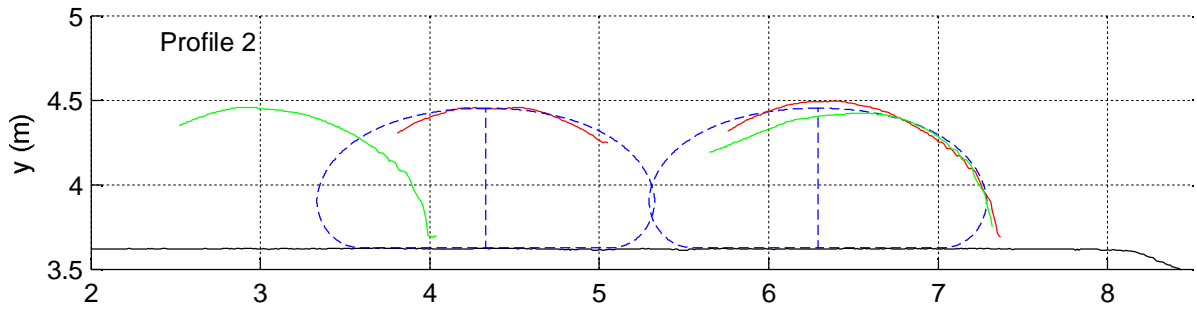
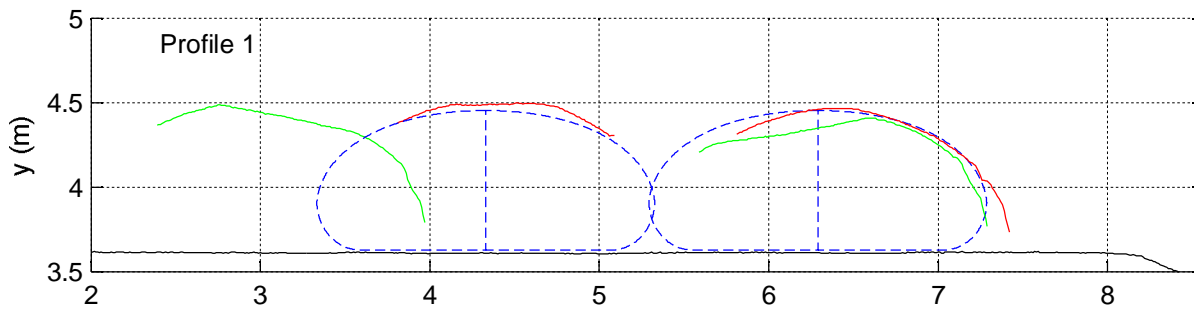
Results profiler Test Series T1

Geotextile tubes

**Deltares**

H5153

Fig. B.3e



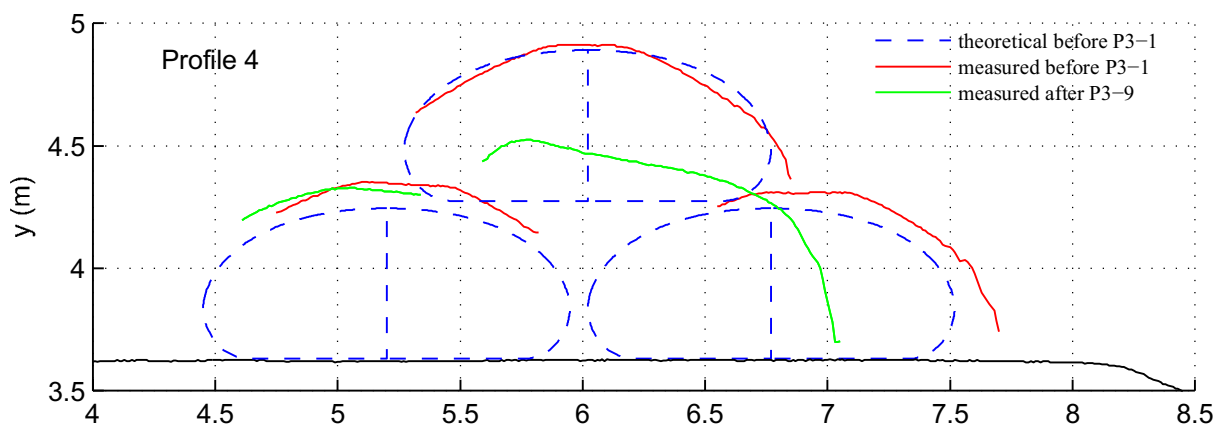
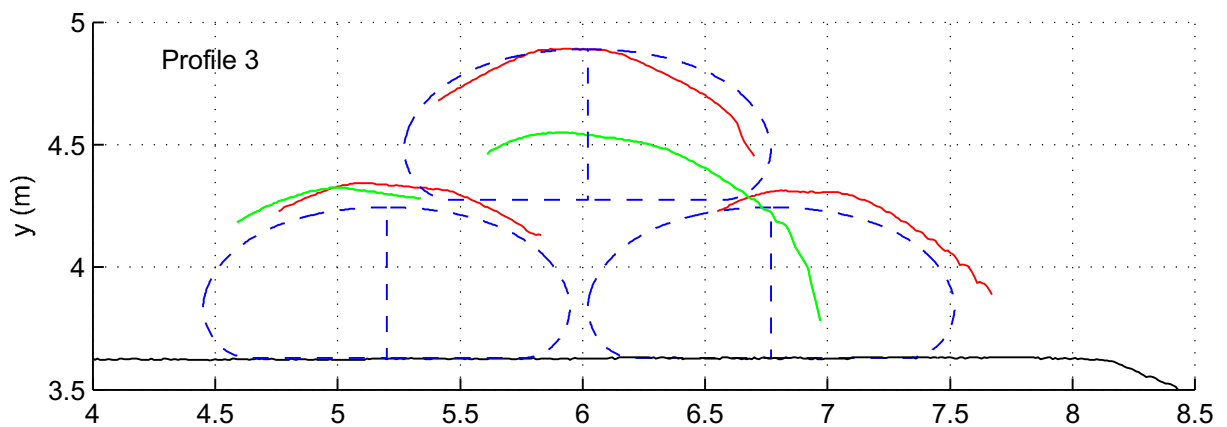
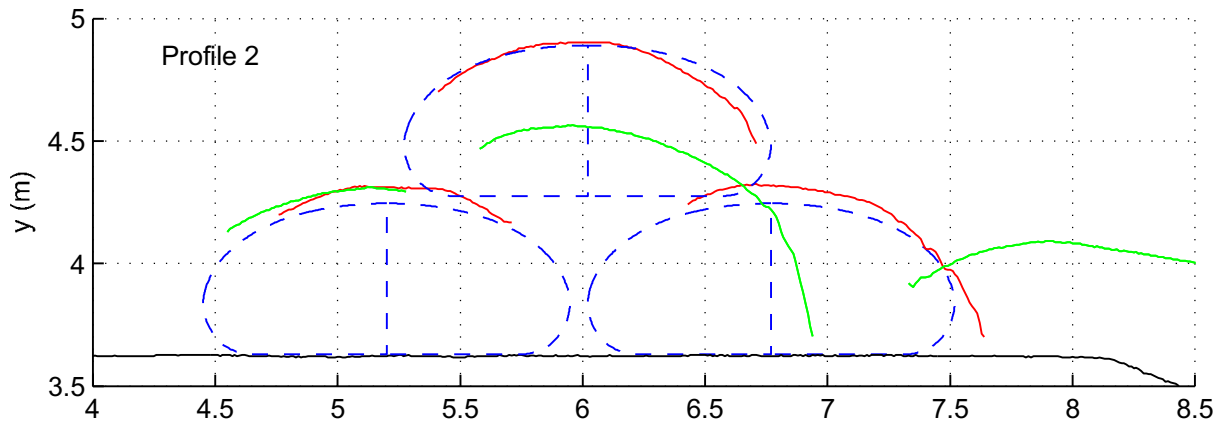
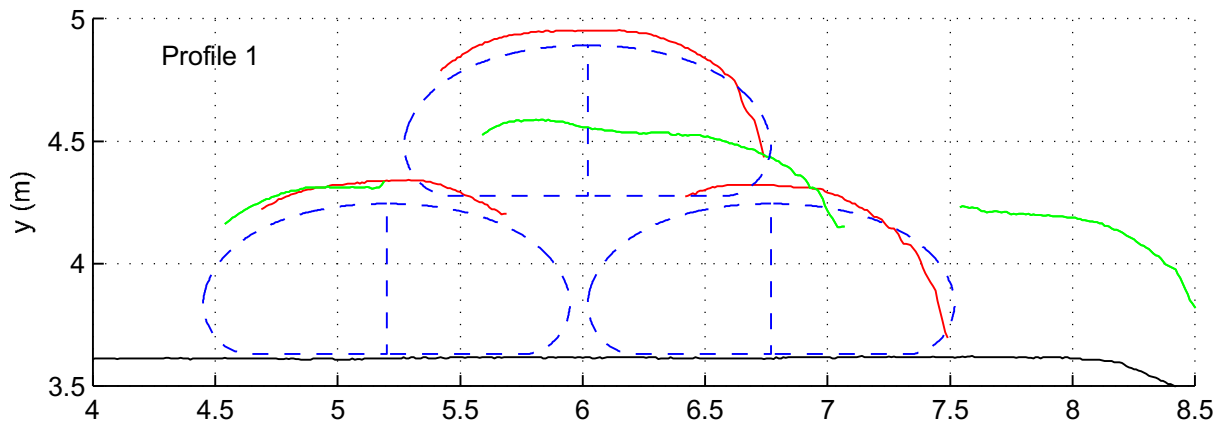
Results profiler Test Series P2

Geotextile tubes

**Deltares**

H5153

Fig. B.3f



Results profiler Test Series P3

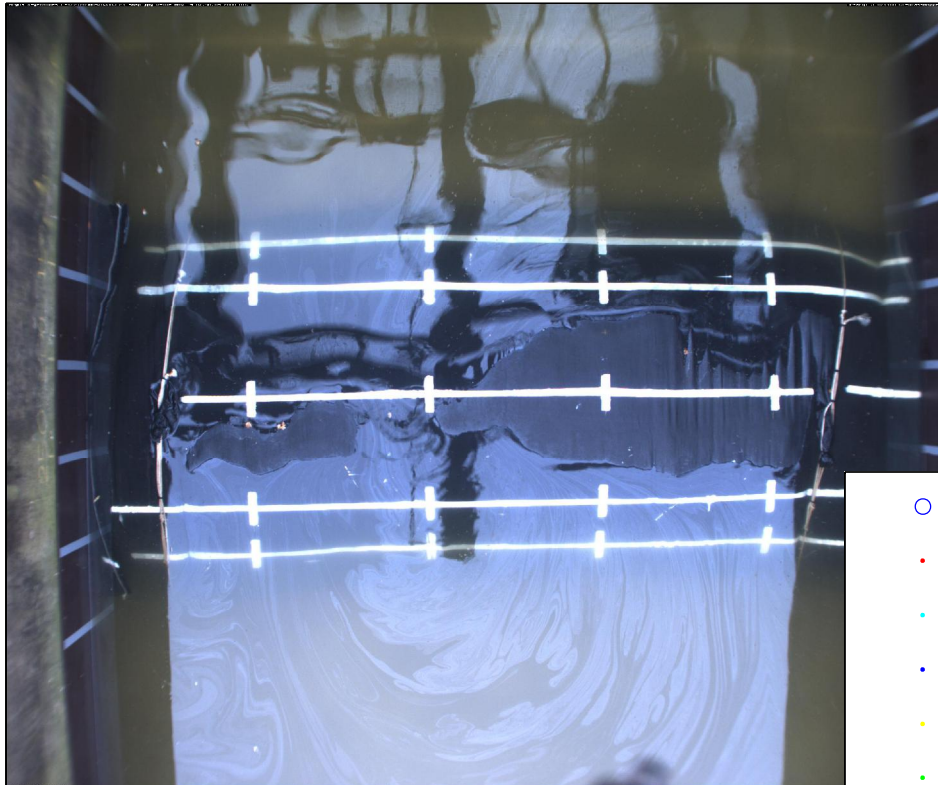
Geotextile tubes

**Deltares**

H5153

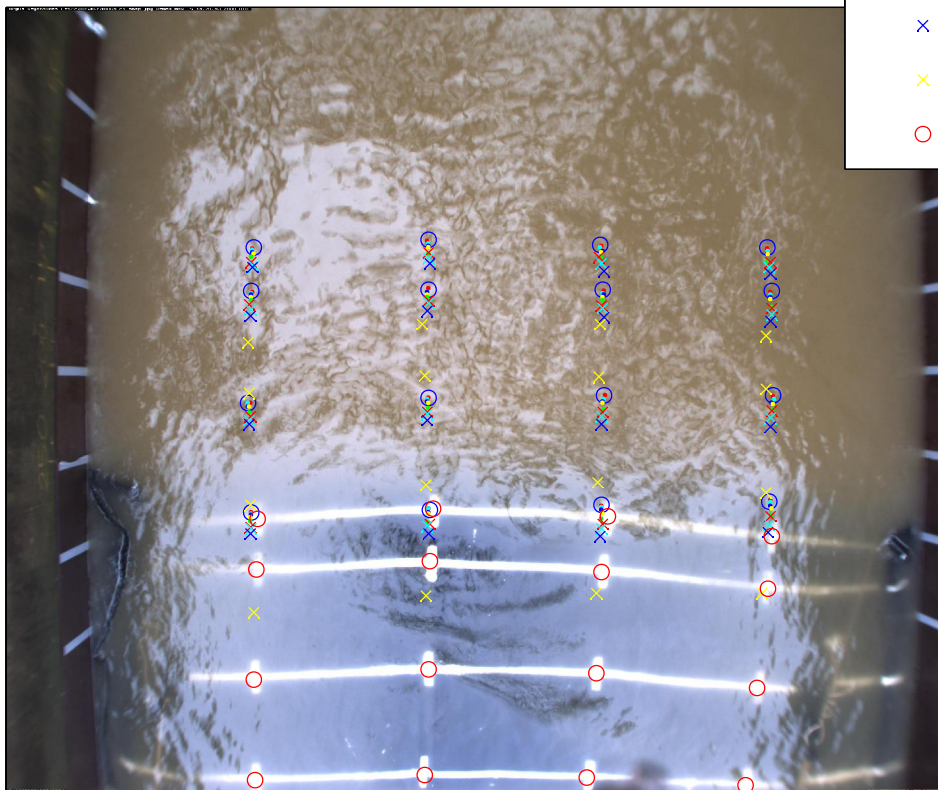
Fig. B.3g

before F1-1



- Before F1-1
- After F1-1
- After F1-2
- After F1-3
- After F1-4
- After F1-5
- × After F1-6
- × After F1-7
- × After F1-8
- × After F1-9
- After F1-10

After F1-10



Results top view camera

Series F1

Geotextile Tubes

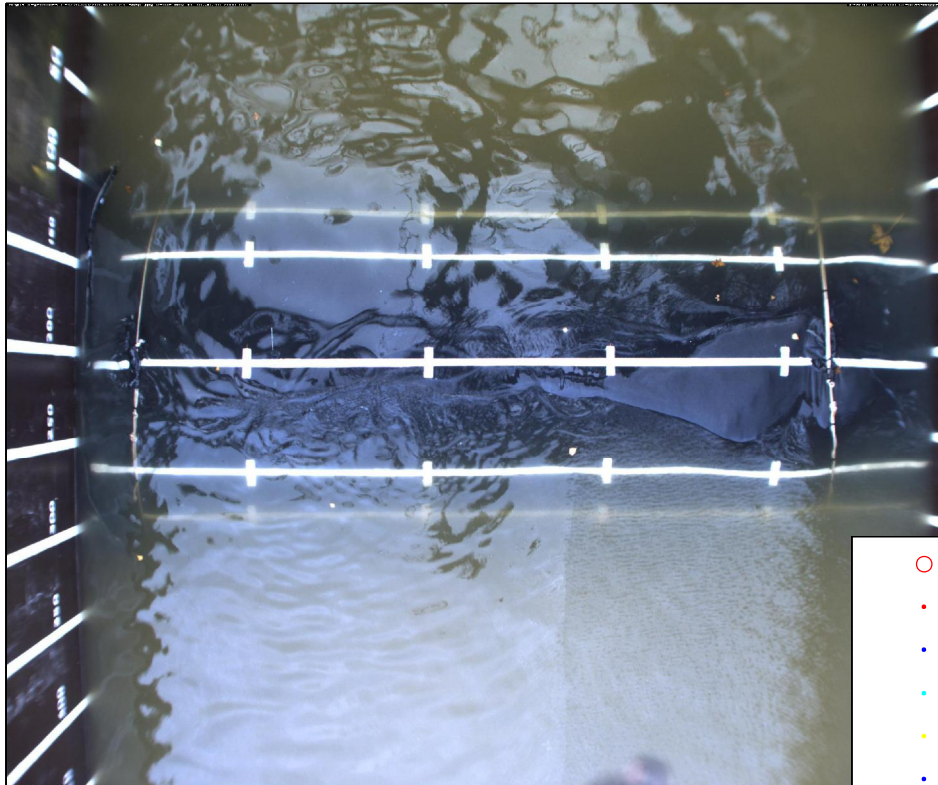
**Deltares**

H5153

Fig B.4a

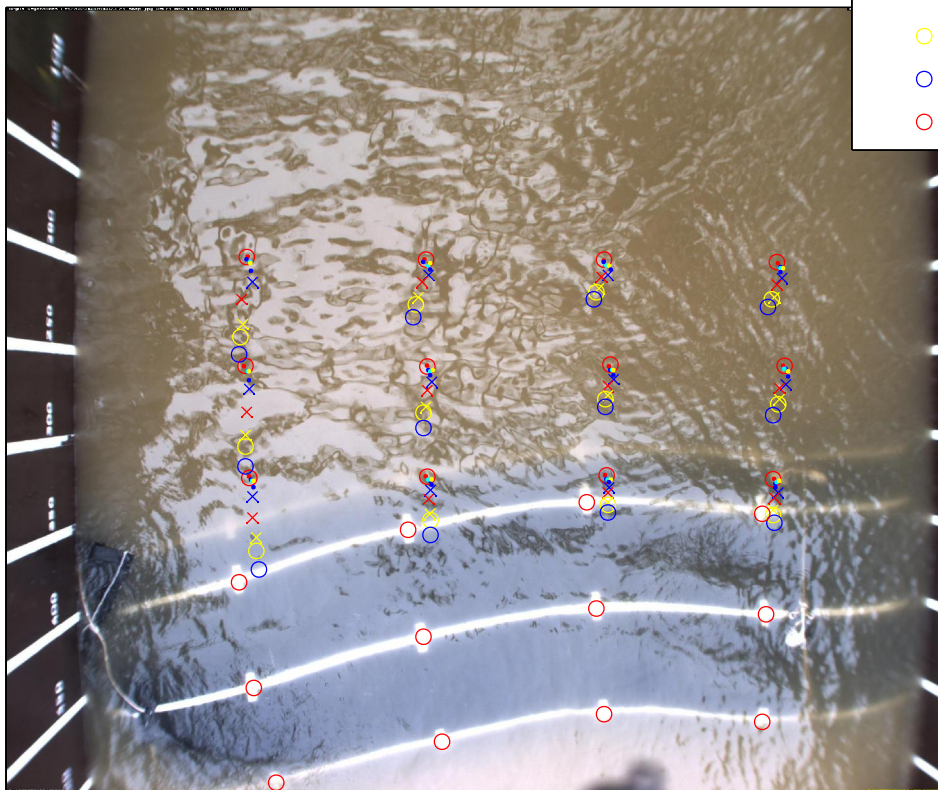


before F3-1



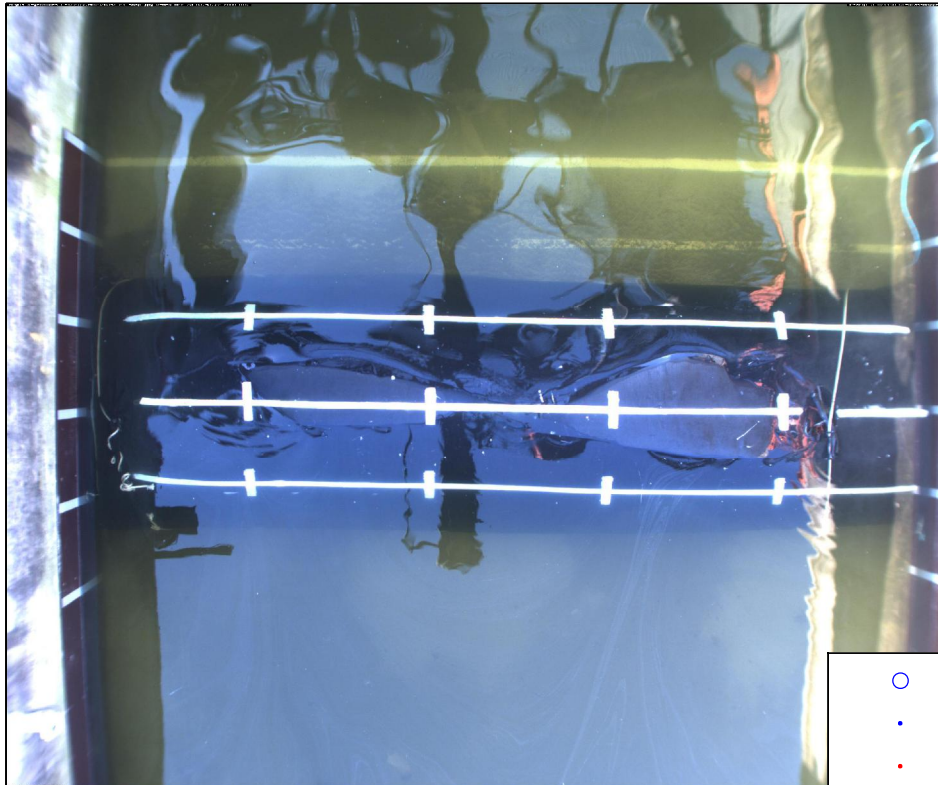
- Before F3-1
- After F3-1
- After F3-2
- After F3-21
- After F3-3
- After F3-4
- × After F3-5
- × After F3-6
- × After F3-61
- After F3-7
- After F3-8
- After F3-9

After F3-9



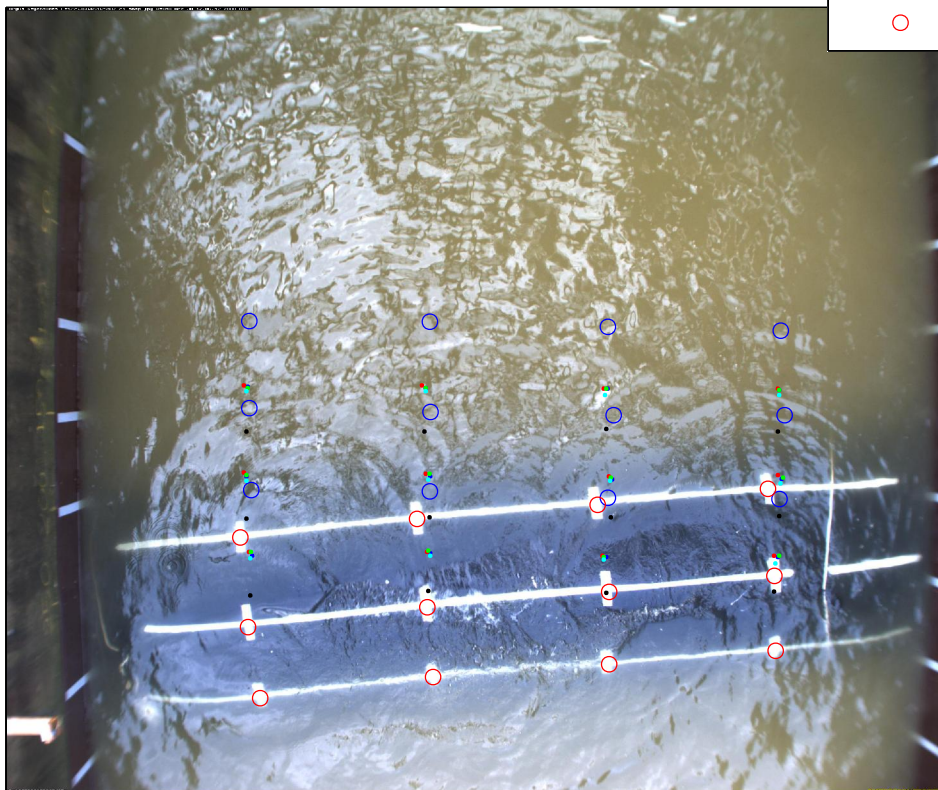
	Series F3	Results top view camera
Geotextile Tubes		
Fig B.4b	H5153	<b>Deltares</b>

before F4-1



- Before F4-1
- After F4-1
- After F4-2
- After F4-3
- After F4-4
- After F4-5
- After F4-6

After F4-6



Results top view camera

Series F4

Geotextile Tubes

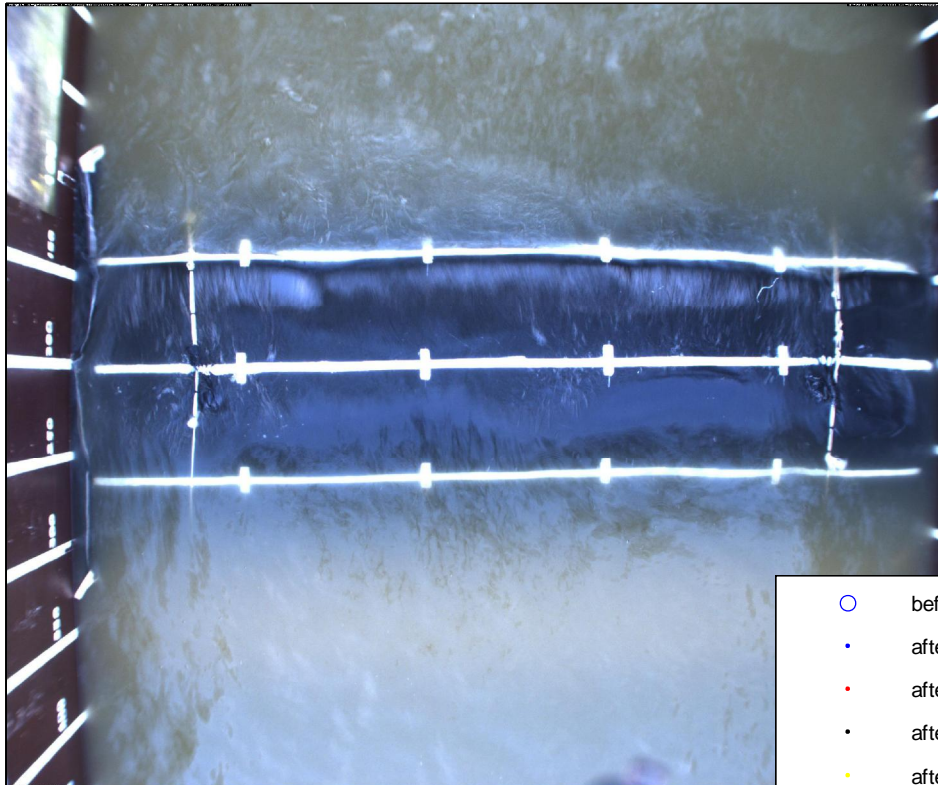
Deltares

H5153

Fig B.4c

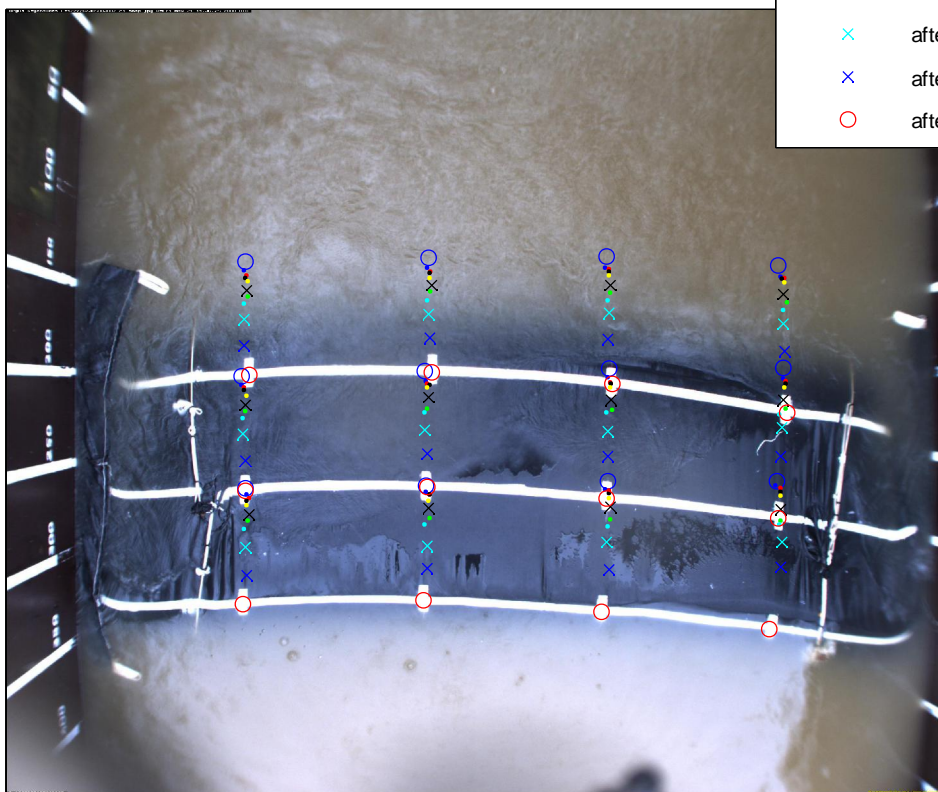


Before T1-1



- before T1-1oud
- after T1-1oud
- after T1-1
- after T1-2
- after T1-3
- × after T1-4
- after T1-5
- after T1-6
- × after T1-7
- × after T1-8
- after T1-9

After T1-9



Results top view camera

Series T1

Geotextile Tubes

**Deltares**

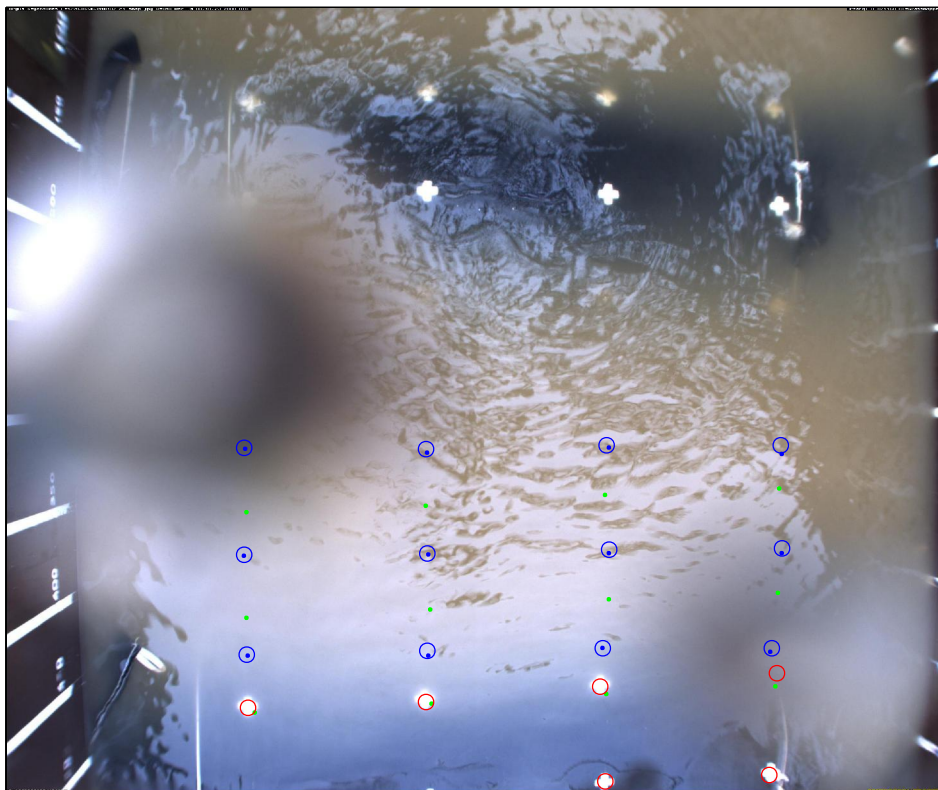
H5153

Fig B.4e

before P2-1

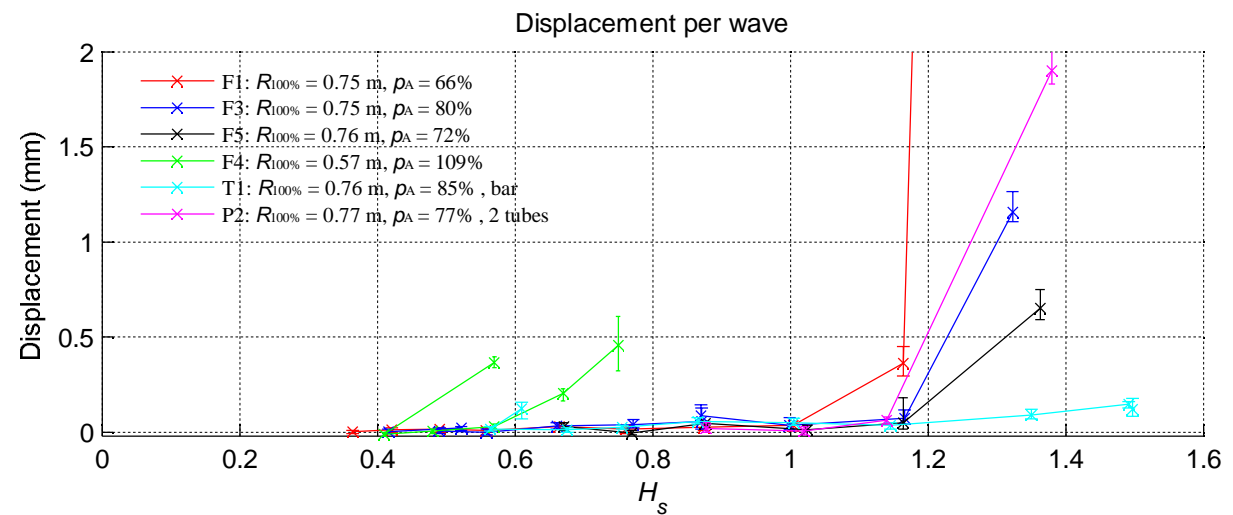
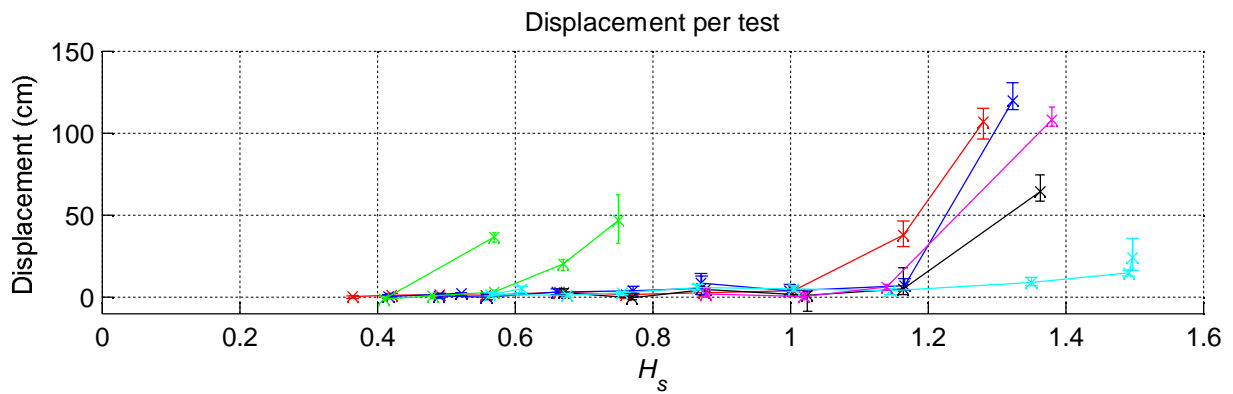
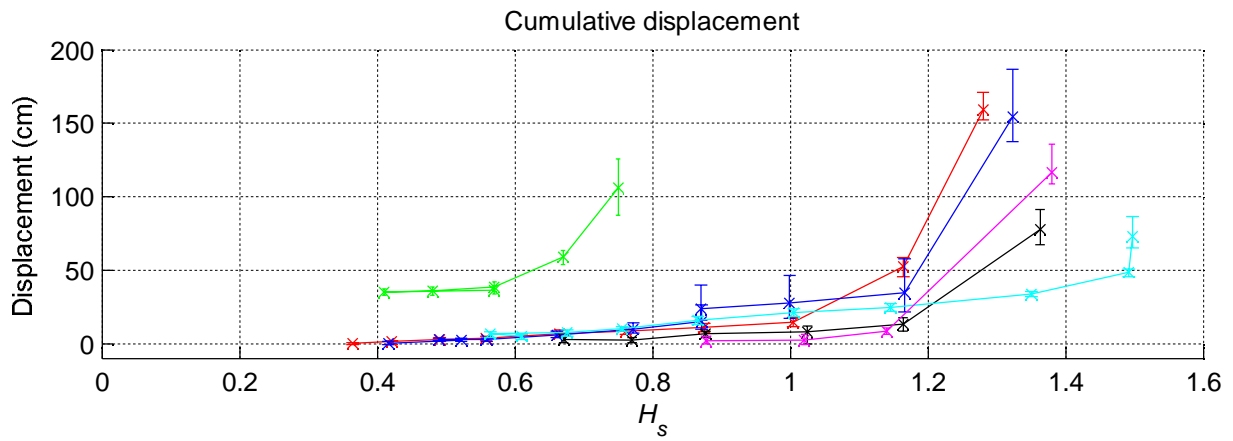


after P2-42



- Before P2-1
- After P2-1
- After P2-23
- After P2-42

	Series P2	Results top view camera
Geotextile Tubes		
Fig B.4f	H5153	<b>Deltares</b>



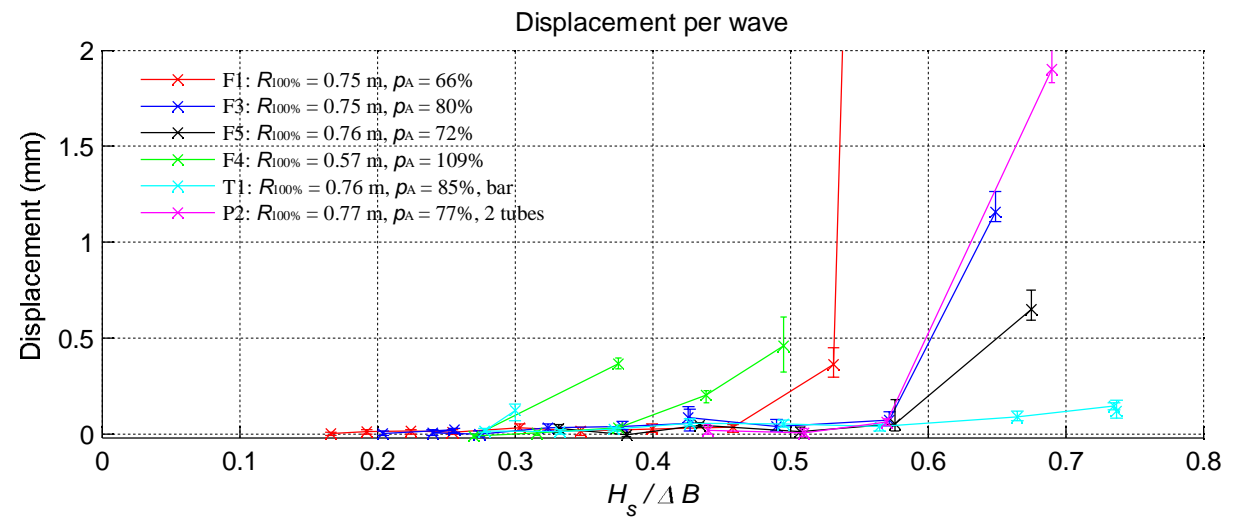
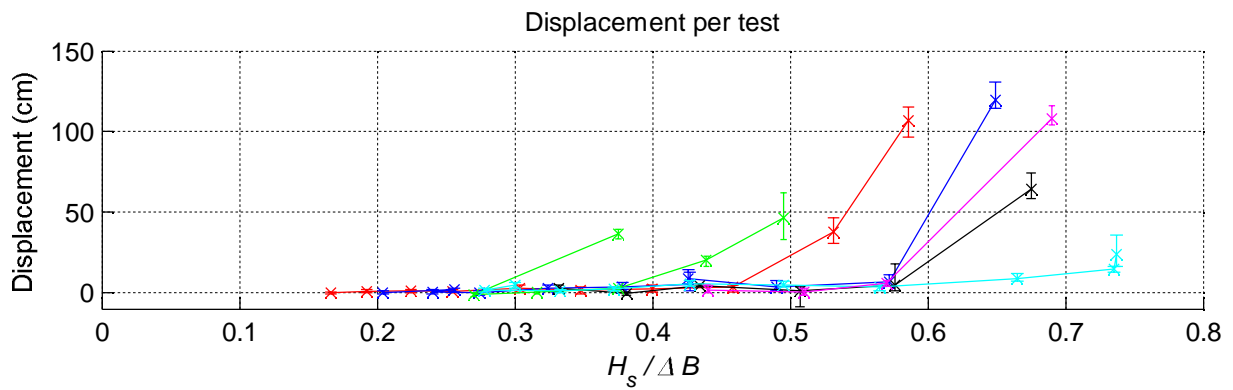
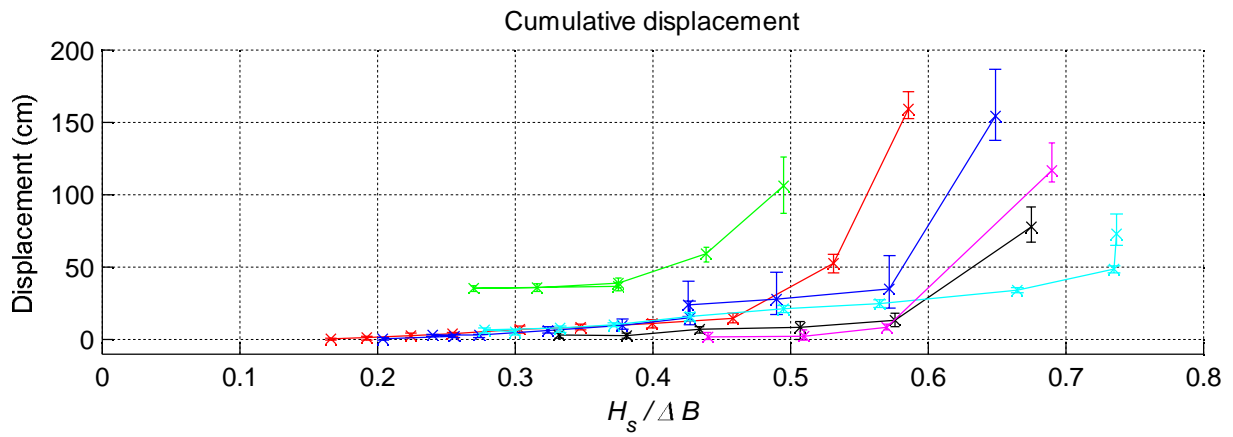
Overview displacement based on top view camera testseries

Geotextile tubes

**Deltares**

H5153

Fig. B.5a



Overview displacement based on top view camera testseries

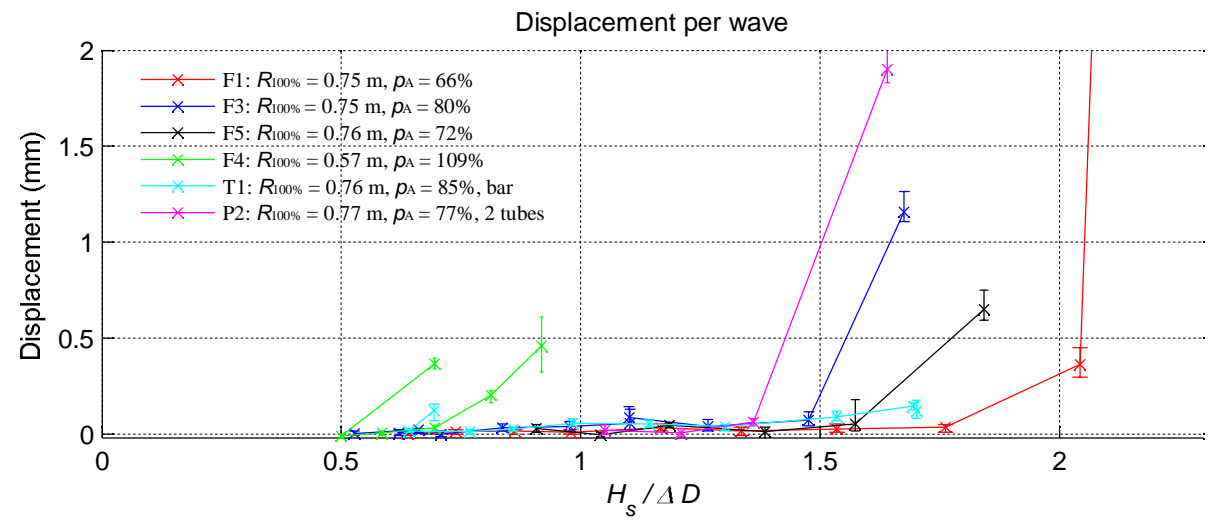
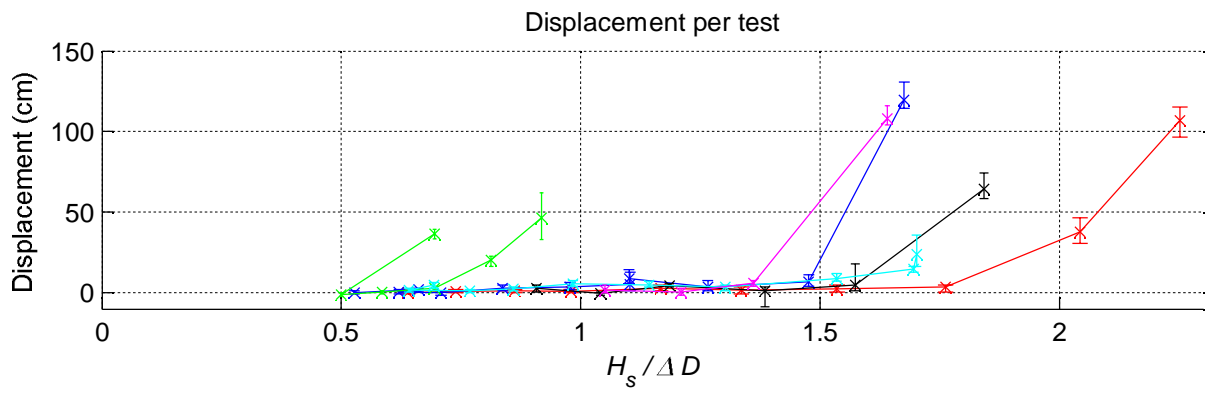
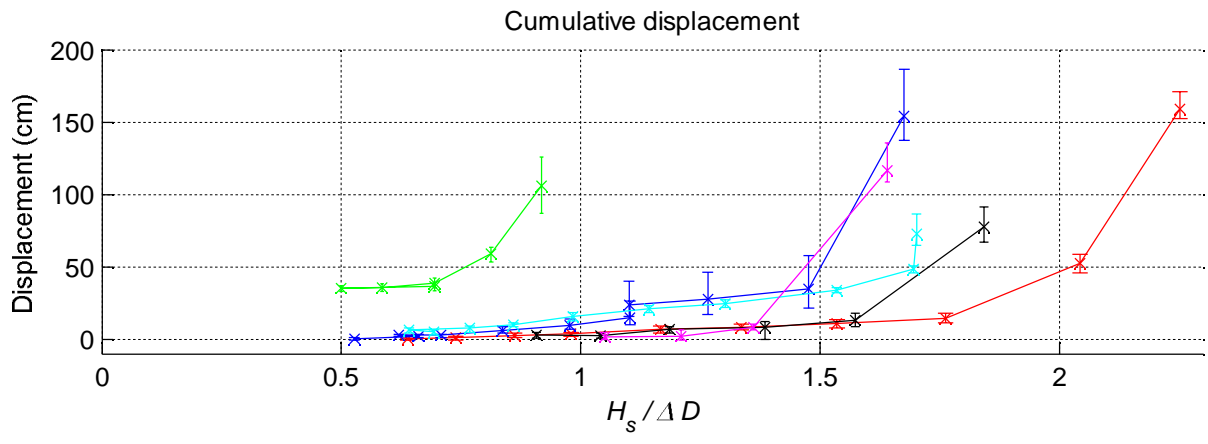
Geotextile tubes

Deltares

H5153

Fig. B.5b





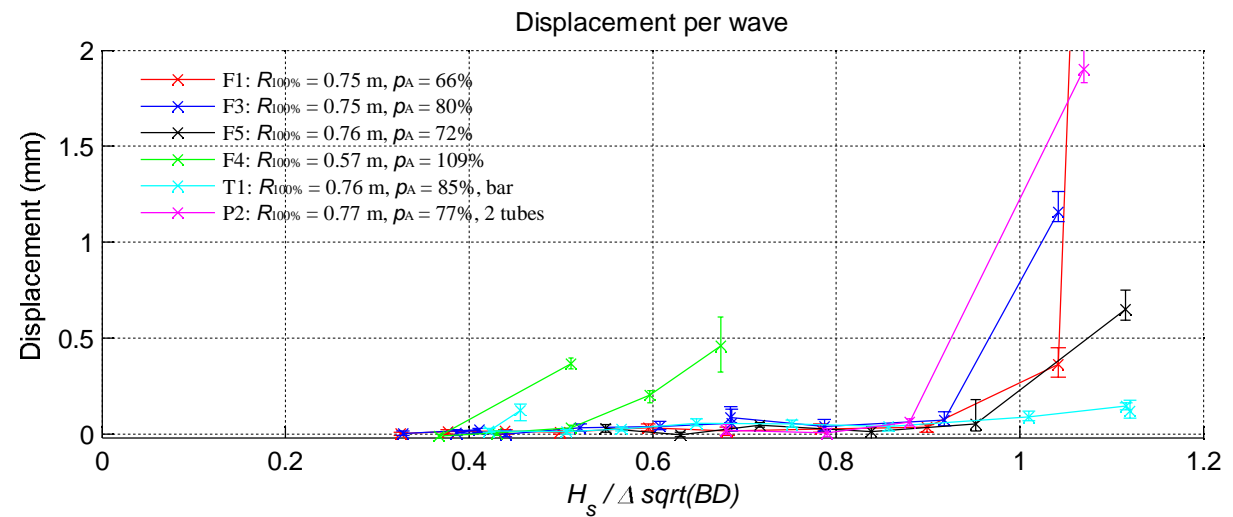
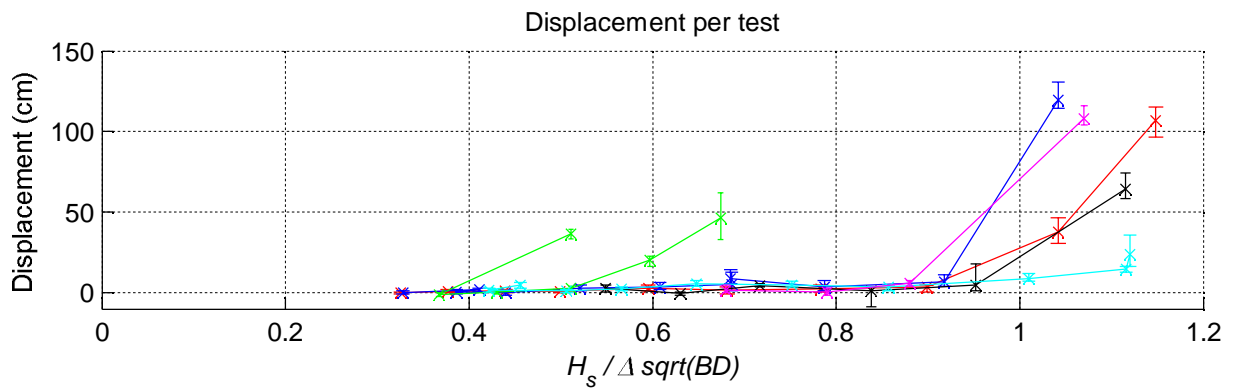
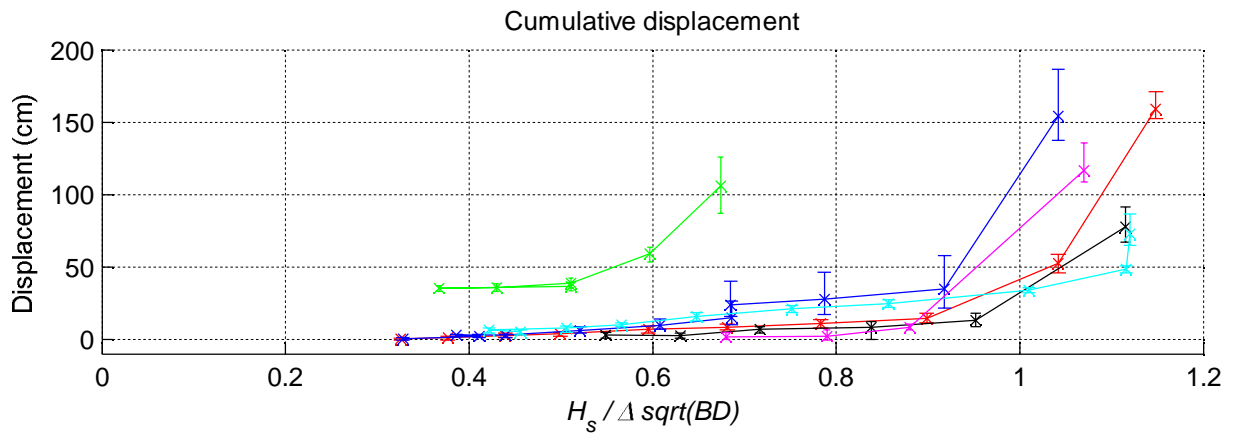
Overview displacement based on top view camera testseries

Geotextile tubes

Deltares

H5153

Fig. B.5c



Overview displacement based on top view camera testseries

Geotextile tubes

**Deltares**

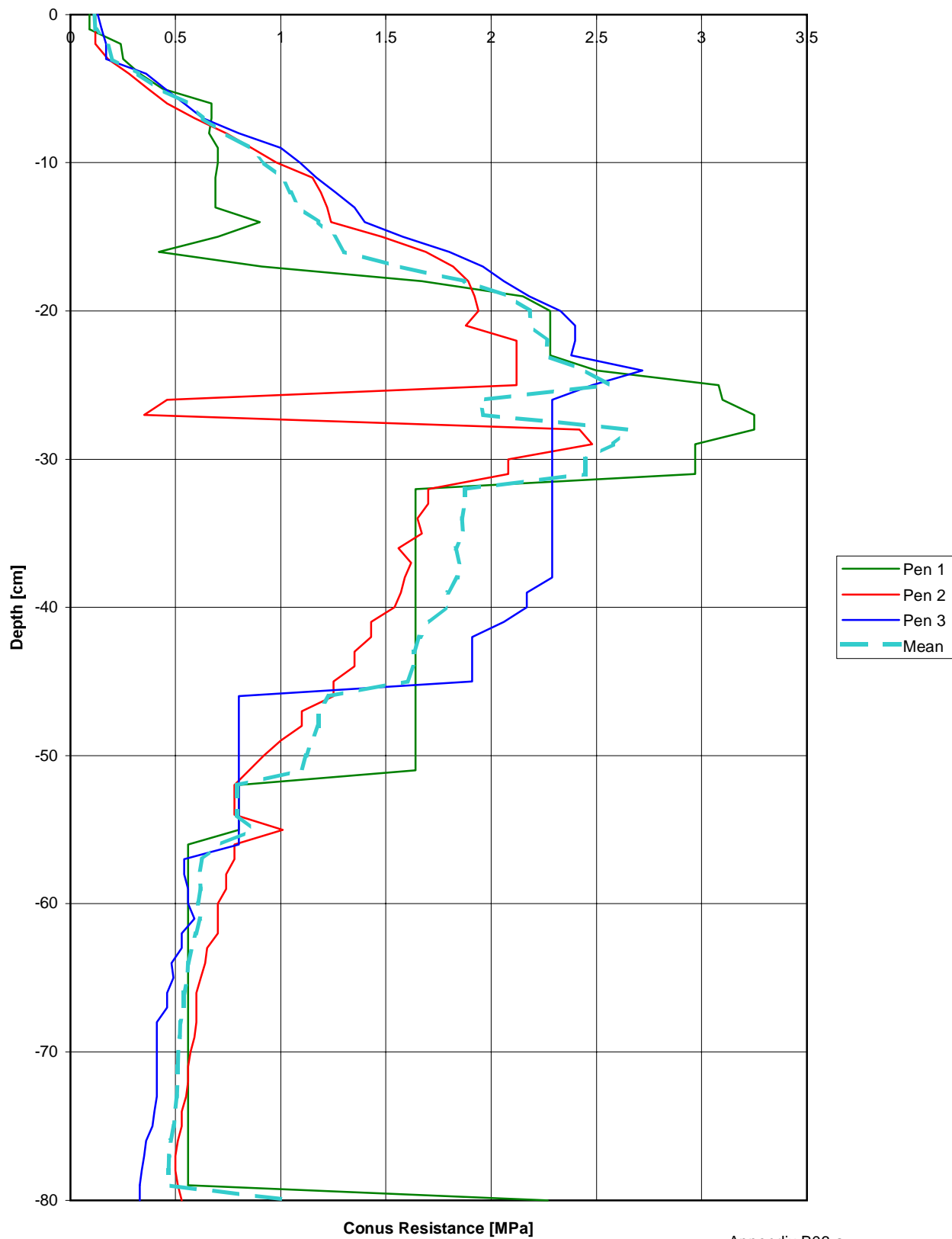
H5153

Fig. B.5d



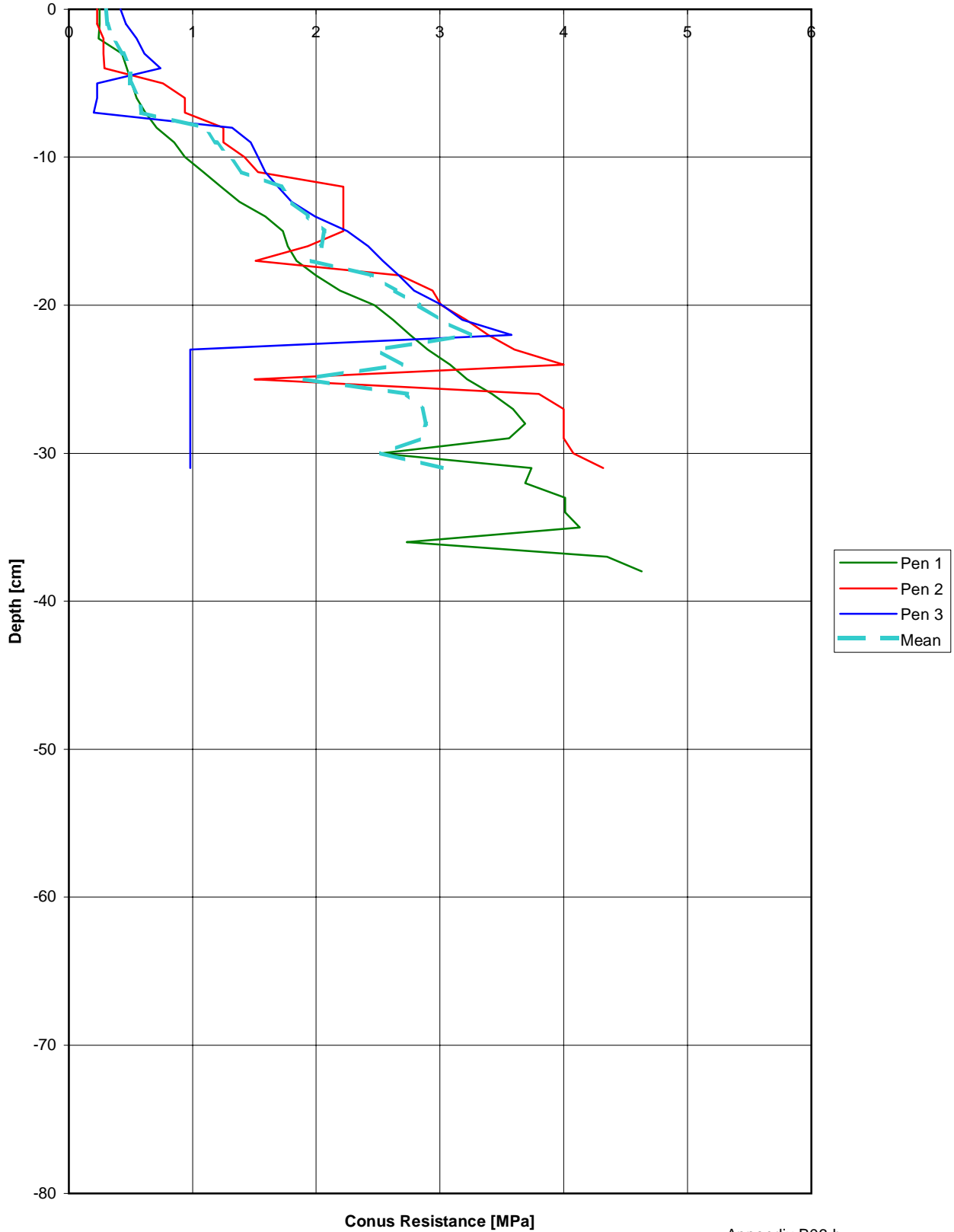
# Penetrologger measurements before test F4 - PLOTX001

conus type 2,0 cm<sup>2</sup>



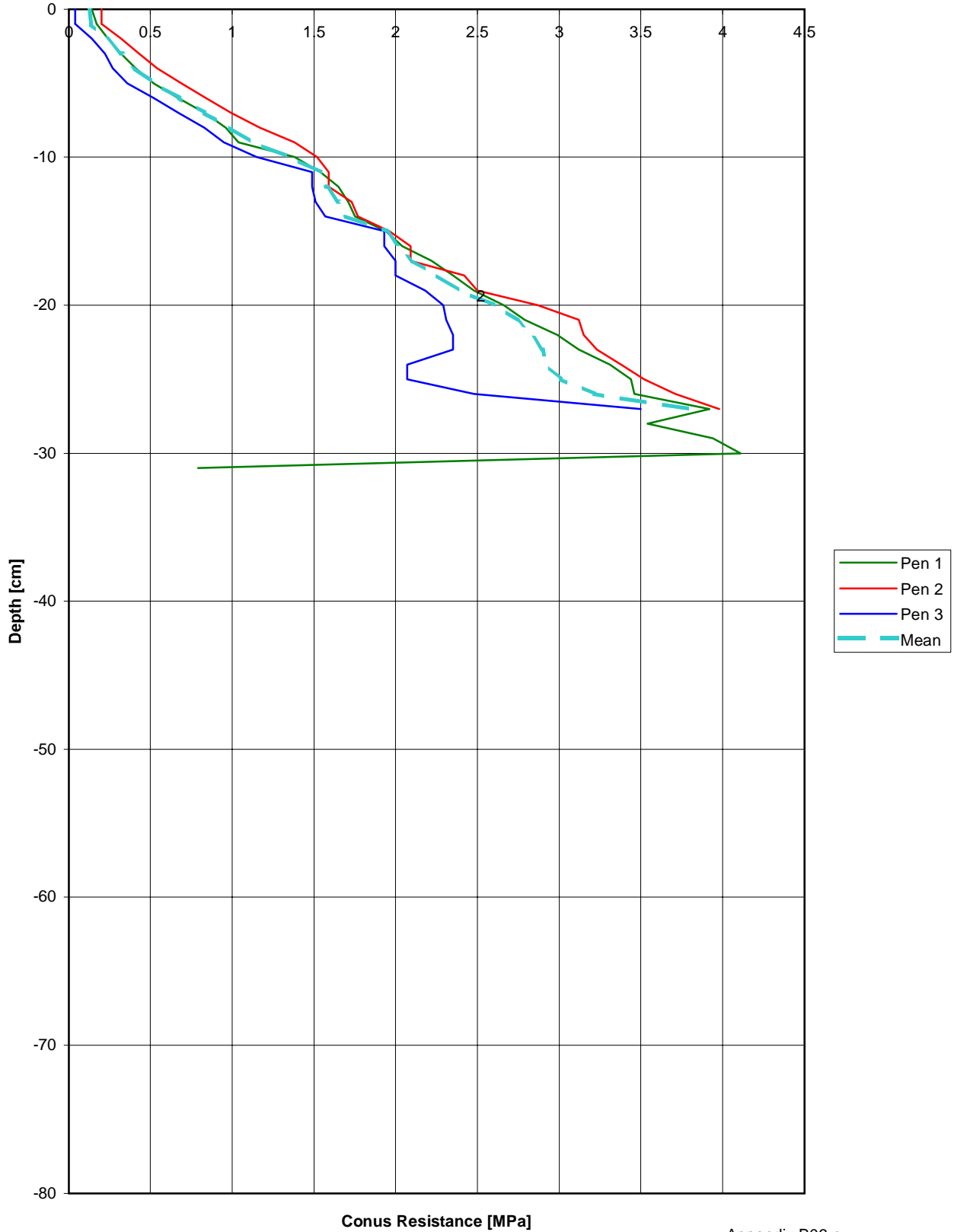
# Penetrologer measurements after test F4 - PLOTX002

conus type 2,0 cm2



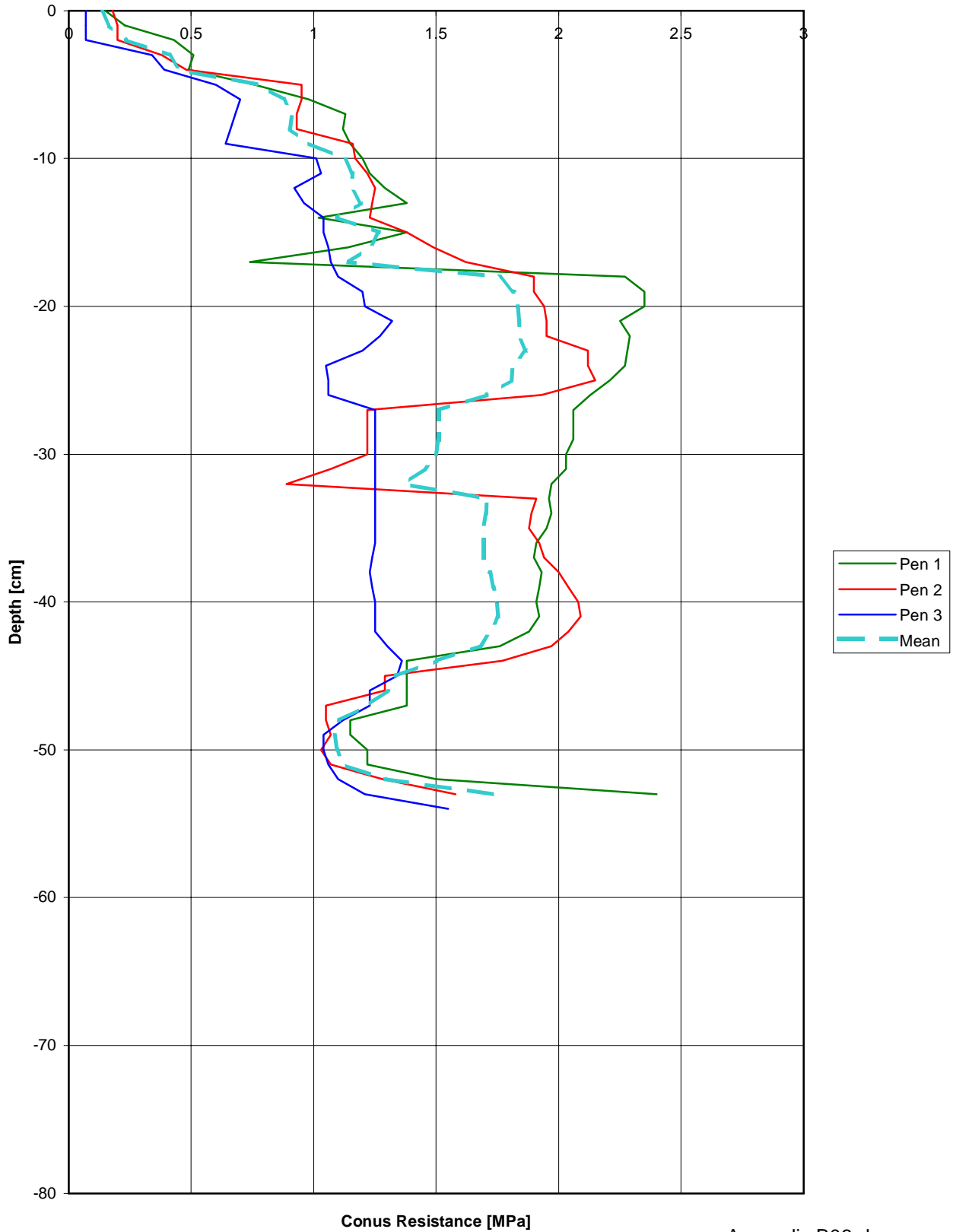
# Penetrologer measurements after test F4 - PLOTX003

conus type 2,0 cm<sup>2</sup>



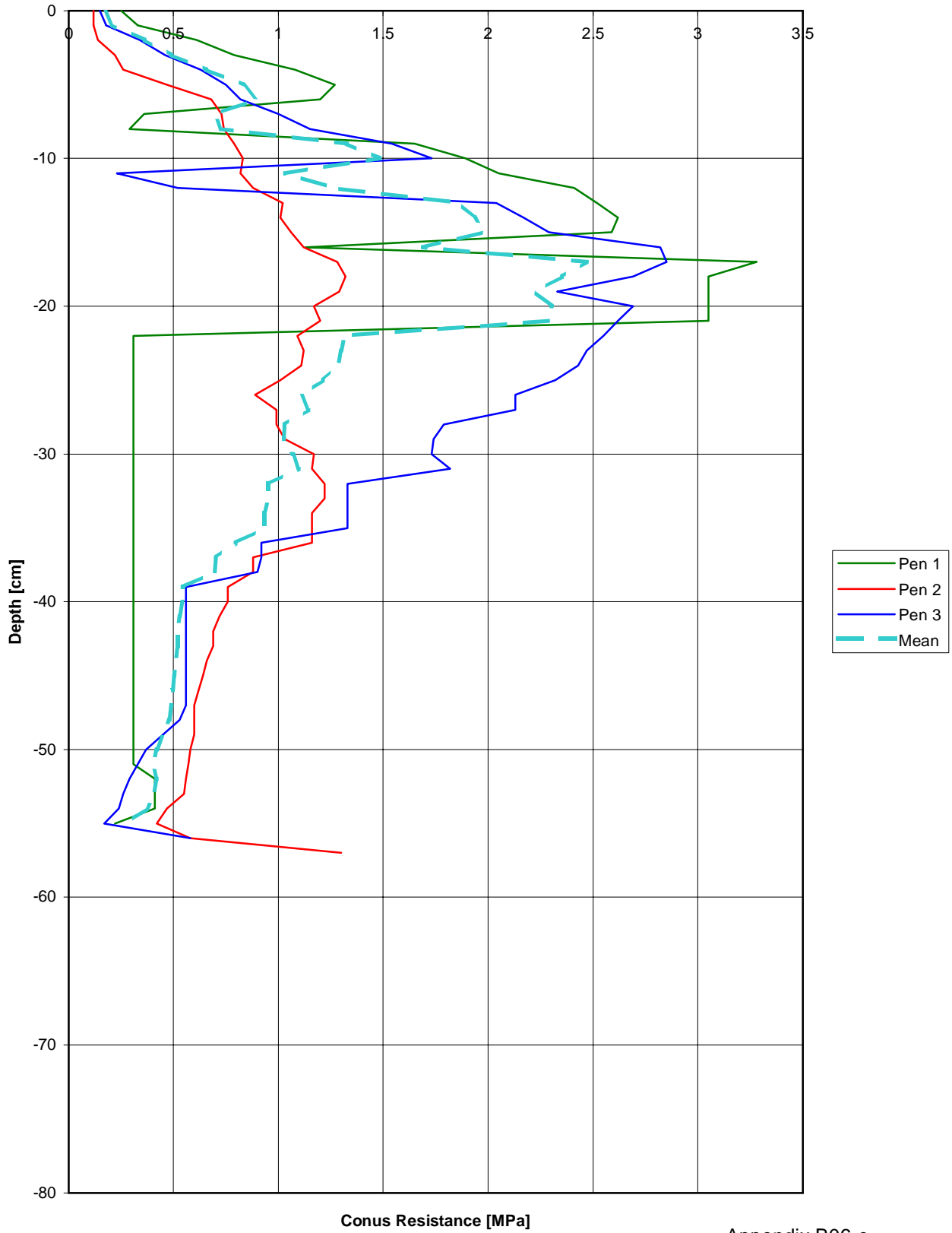
# Penetrologger measurements before test F1 - PLOTX001

conus type 2,0 cm<sup>2</sup>



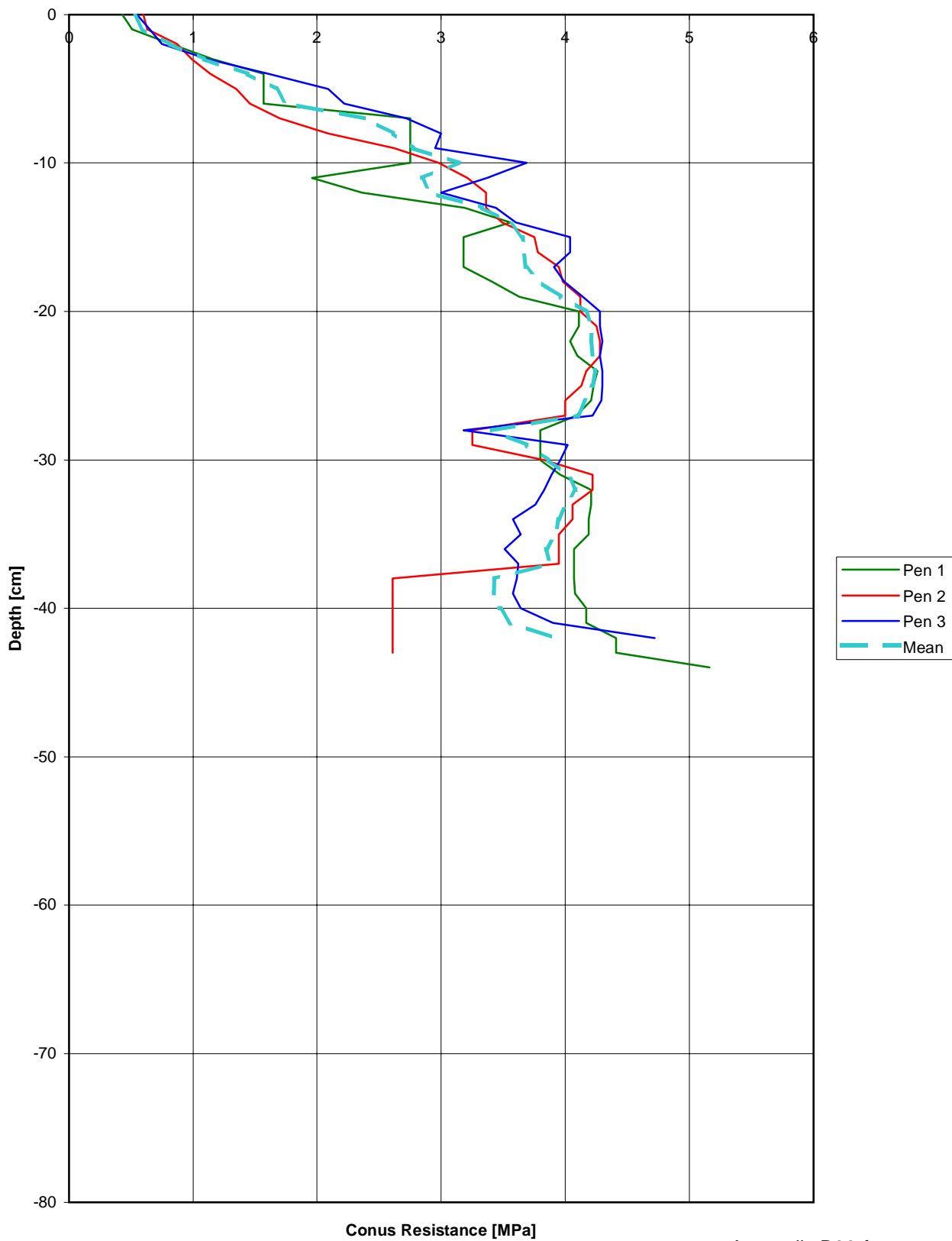
# Penetrologger measurements before test F1 - PLOTX002

conus type 2,0 cm<sup>2</sup>



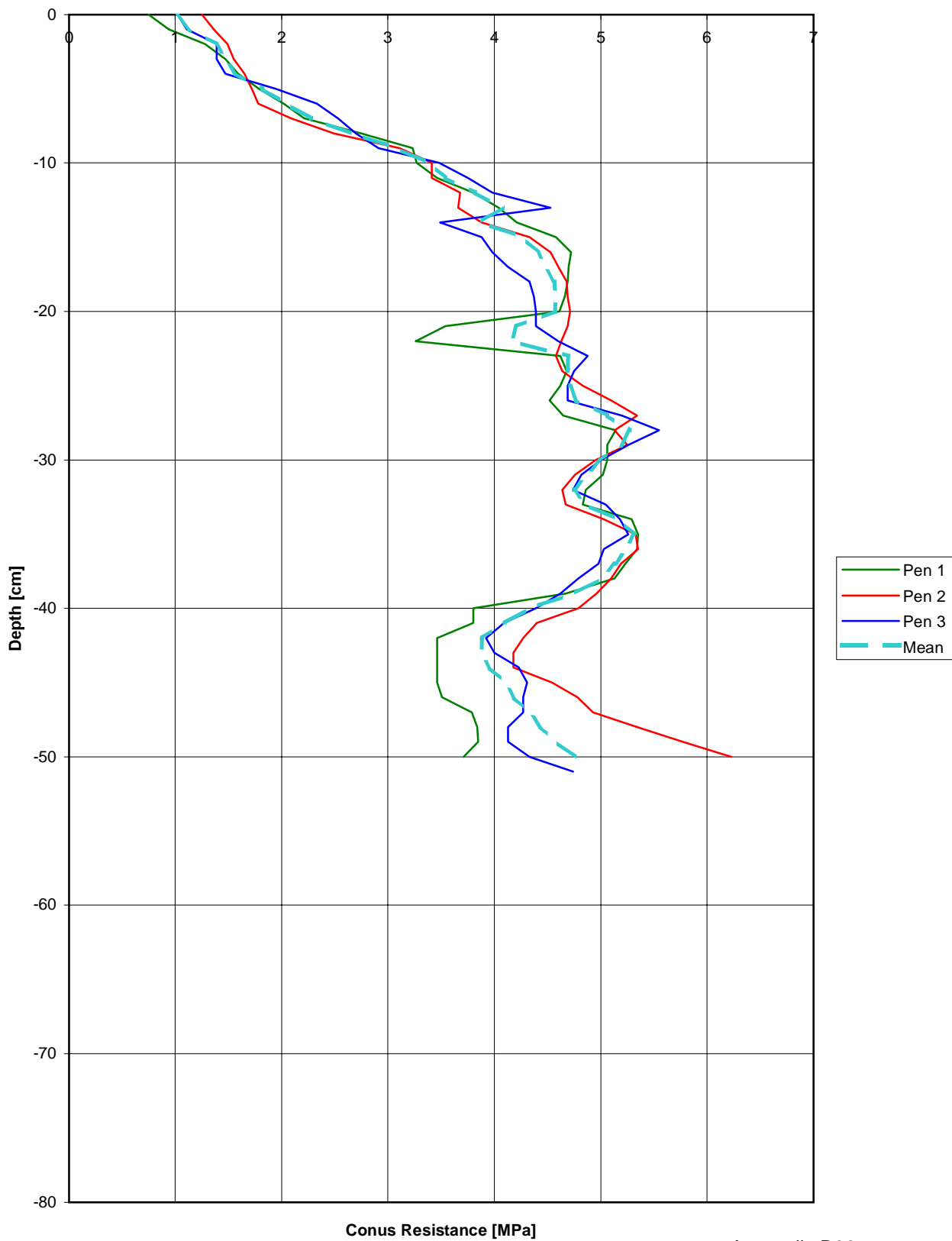
# Penetrologer measurements after test F1 - PLOTX001

conus type 1,0 cm<sup>2</sup>



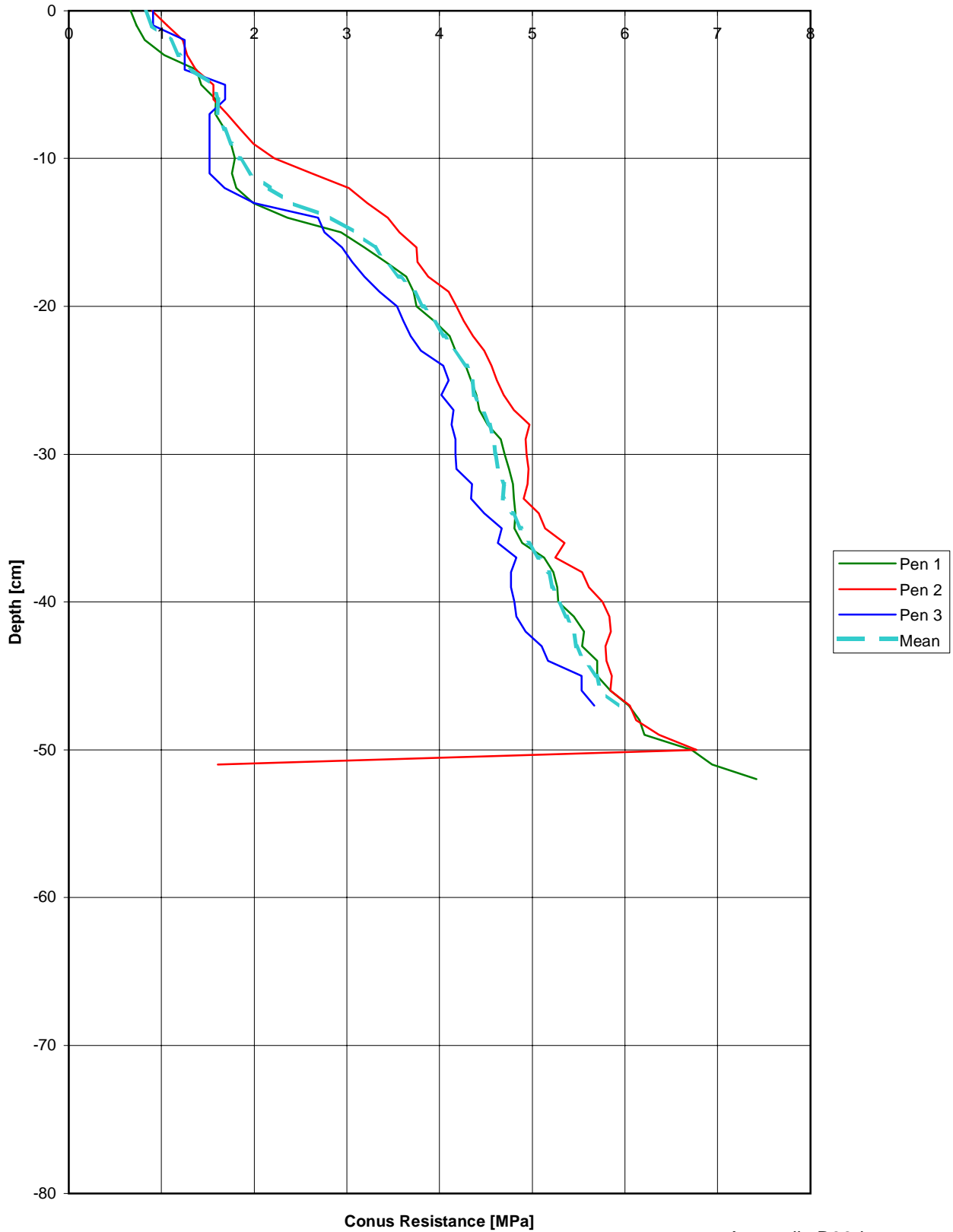
# Penetrologer measurements after test F1 - PLOTX002

conus type 1,0 cm<sup>2</sup>



# Penetrologer measurements after test F1 - PLOTX003

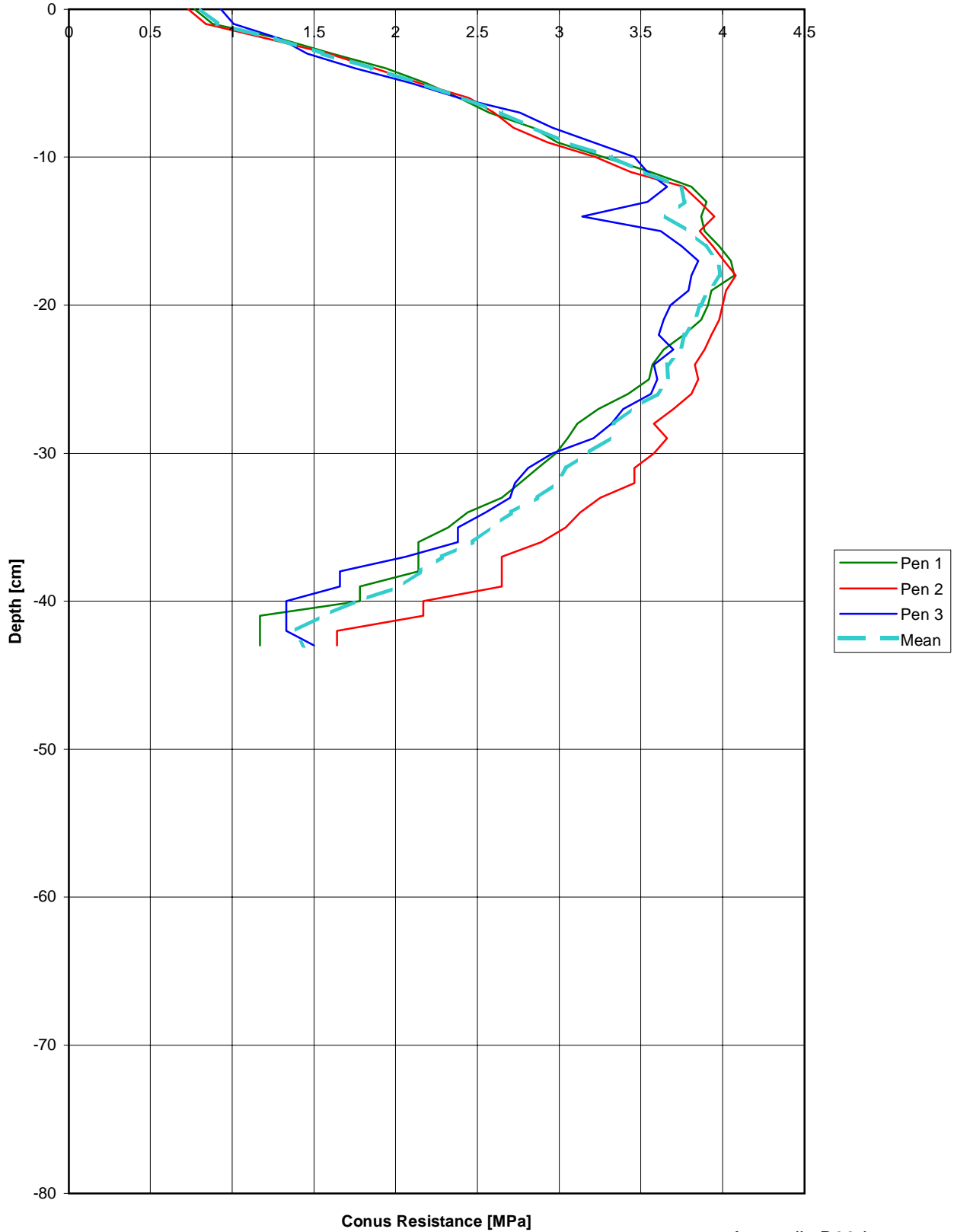
conus type 1,0 cm<sup>2</sup>





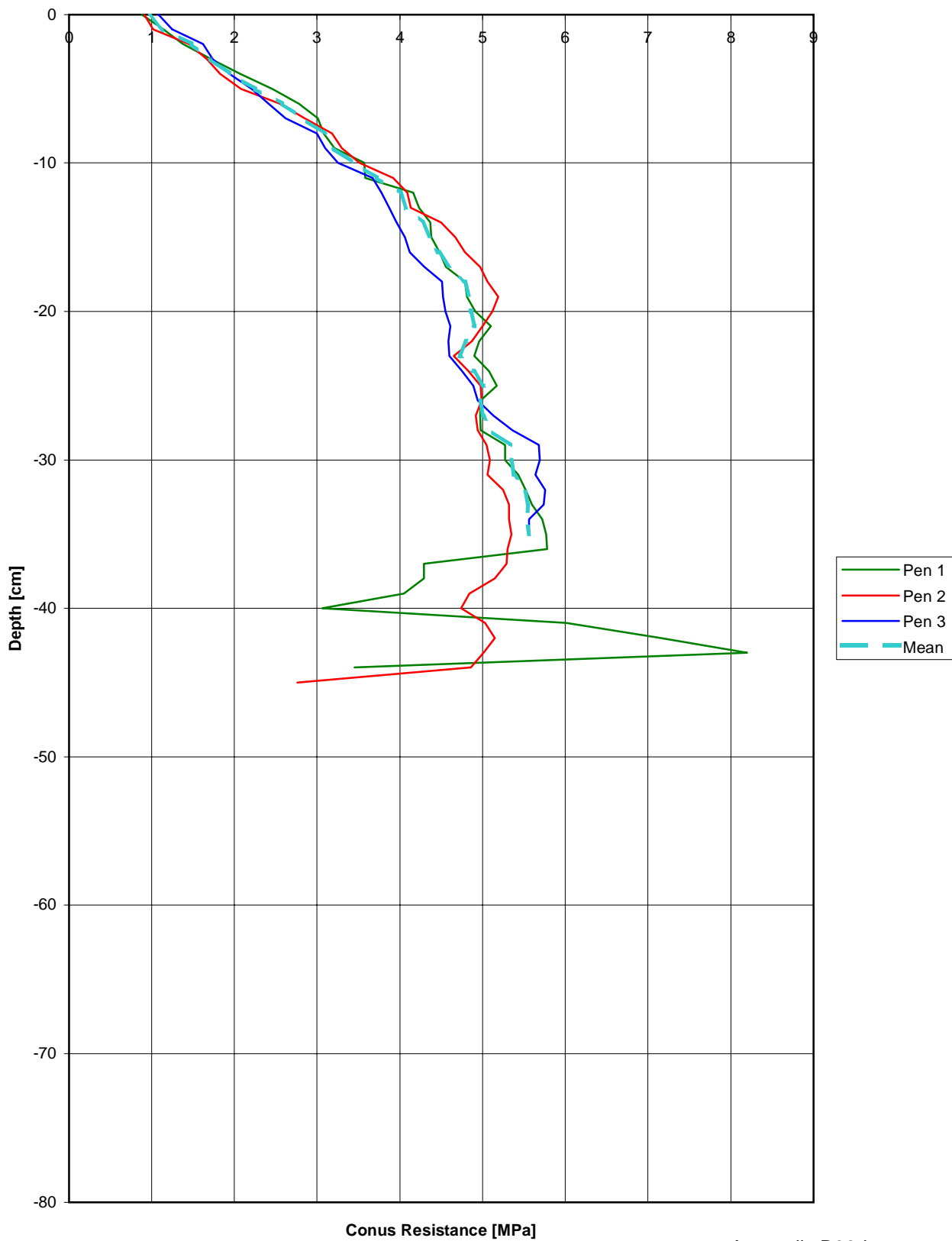
# Penetrologer measurements after test F1 - PLOTX004

conus type 1,0 cm<sup>2</sup>



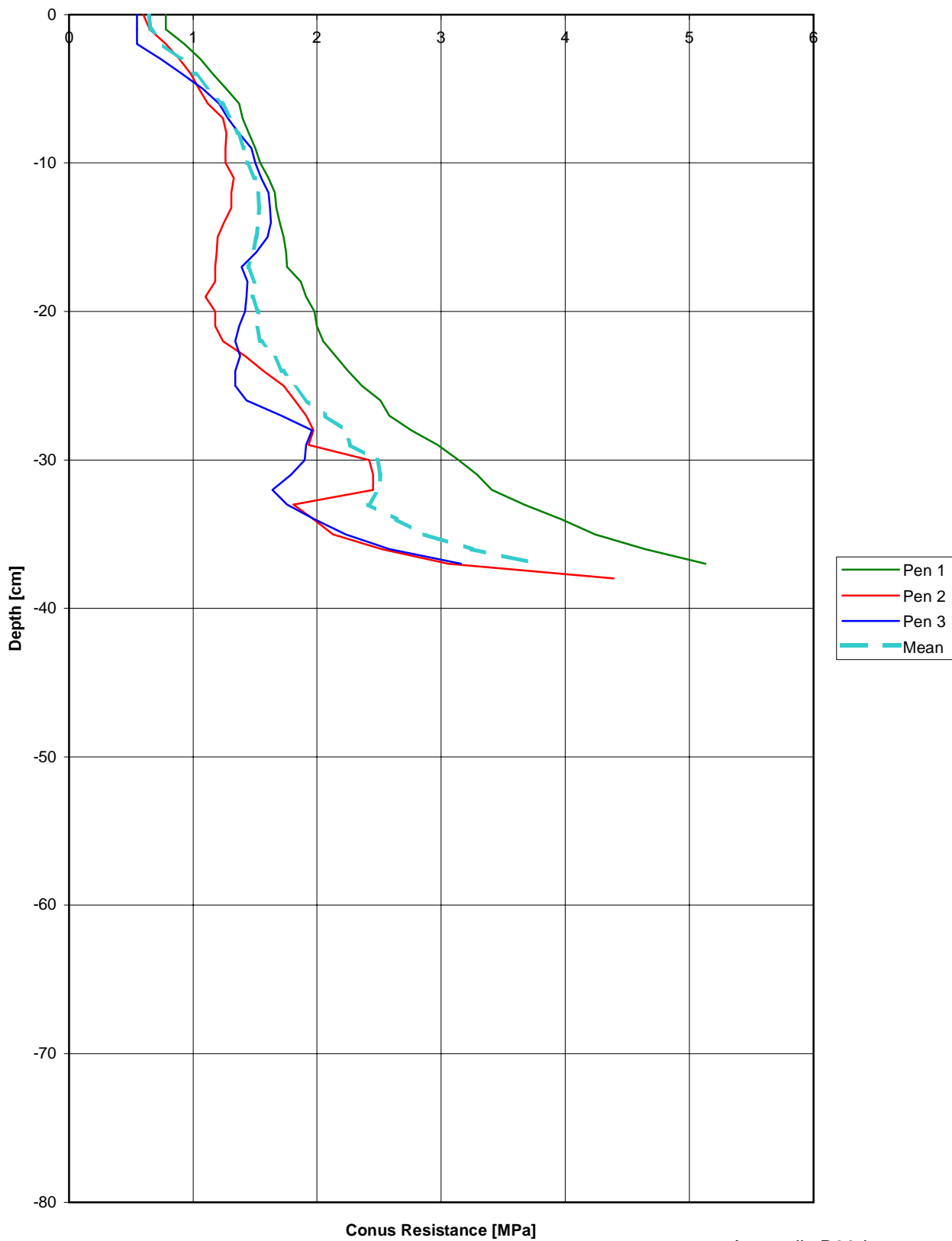
# Penetrologger measurements after test F1 - PLOTX005

conus type 1,0 cm<sup>2</sup>



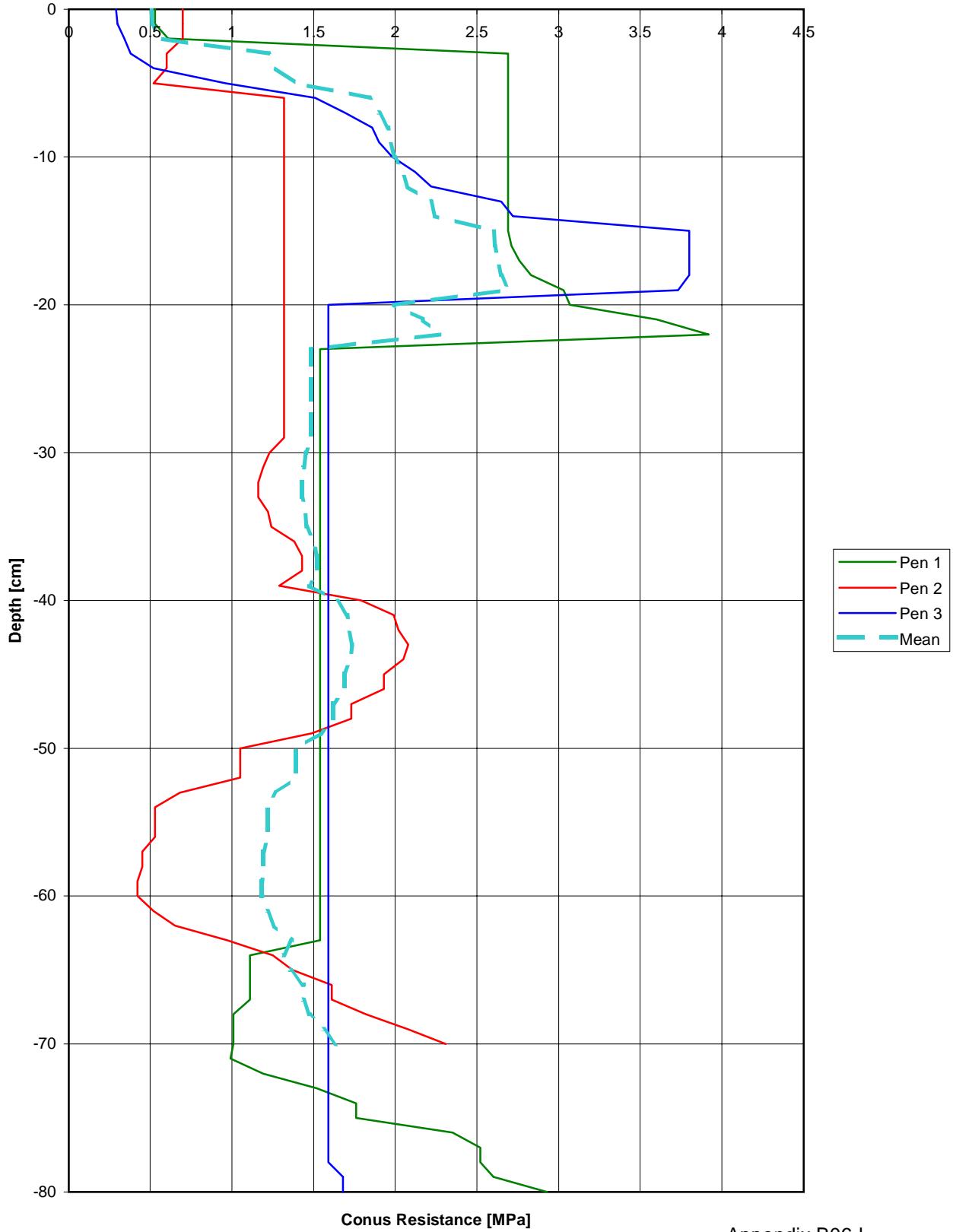
# Penetrologer measurements after test F1 - PLOTX006

conus type 1,0 cm<sup>2</sup>



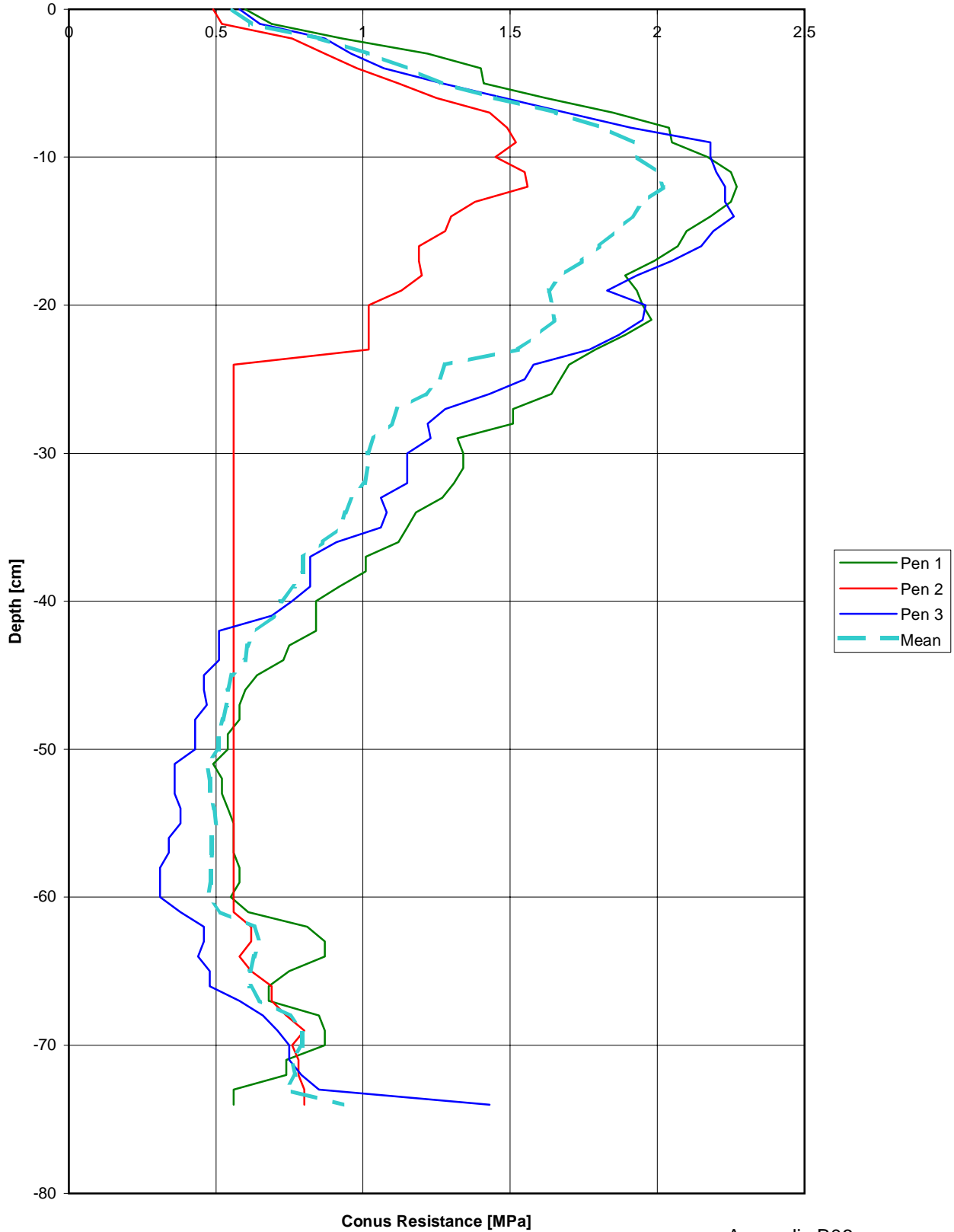
# Penetrologer measurements before test F3 - PLOTX001

conus type 1,0 cm<sup>2</sup>



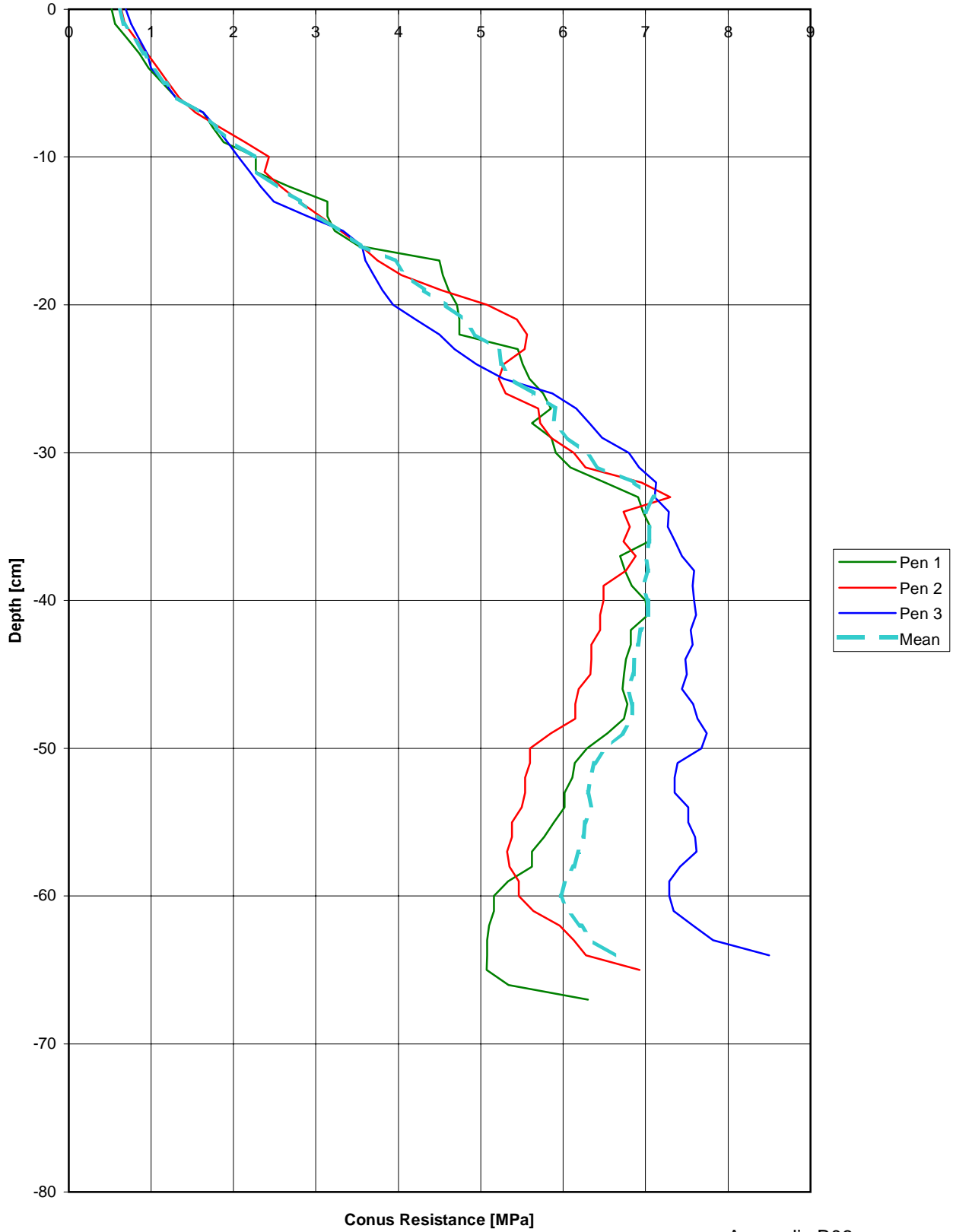
# Penetrologger measurements before test F3 - PLOTX002

conus type 1,0 cm<sup>2</sup>



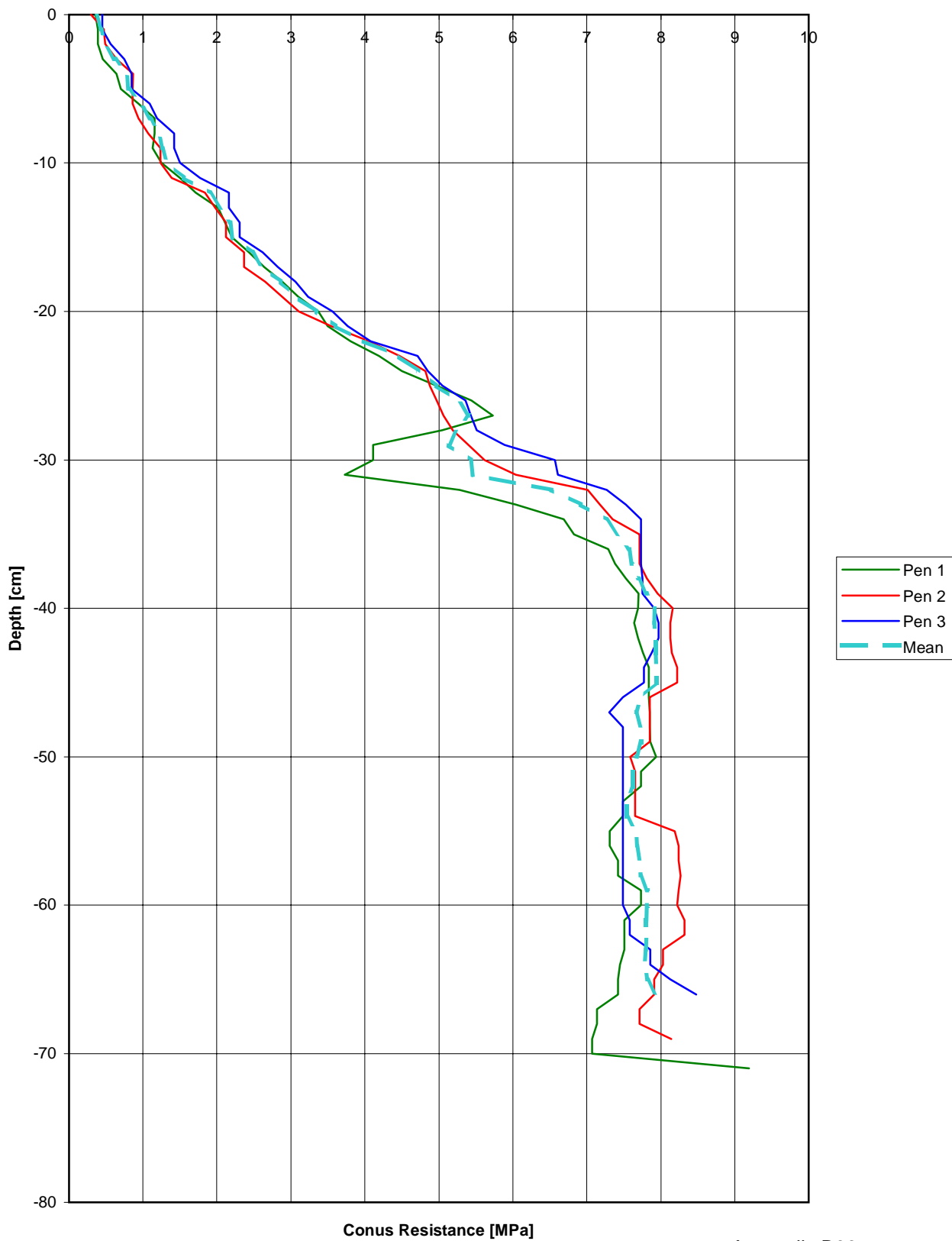
# Penetrologer measurements after test F3 - PLOTX001

conus type 1,0 cm2



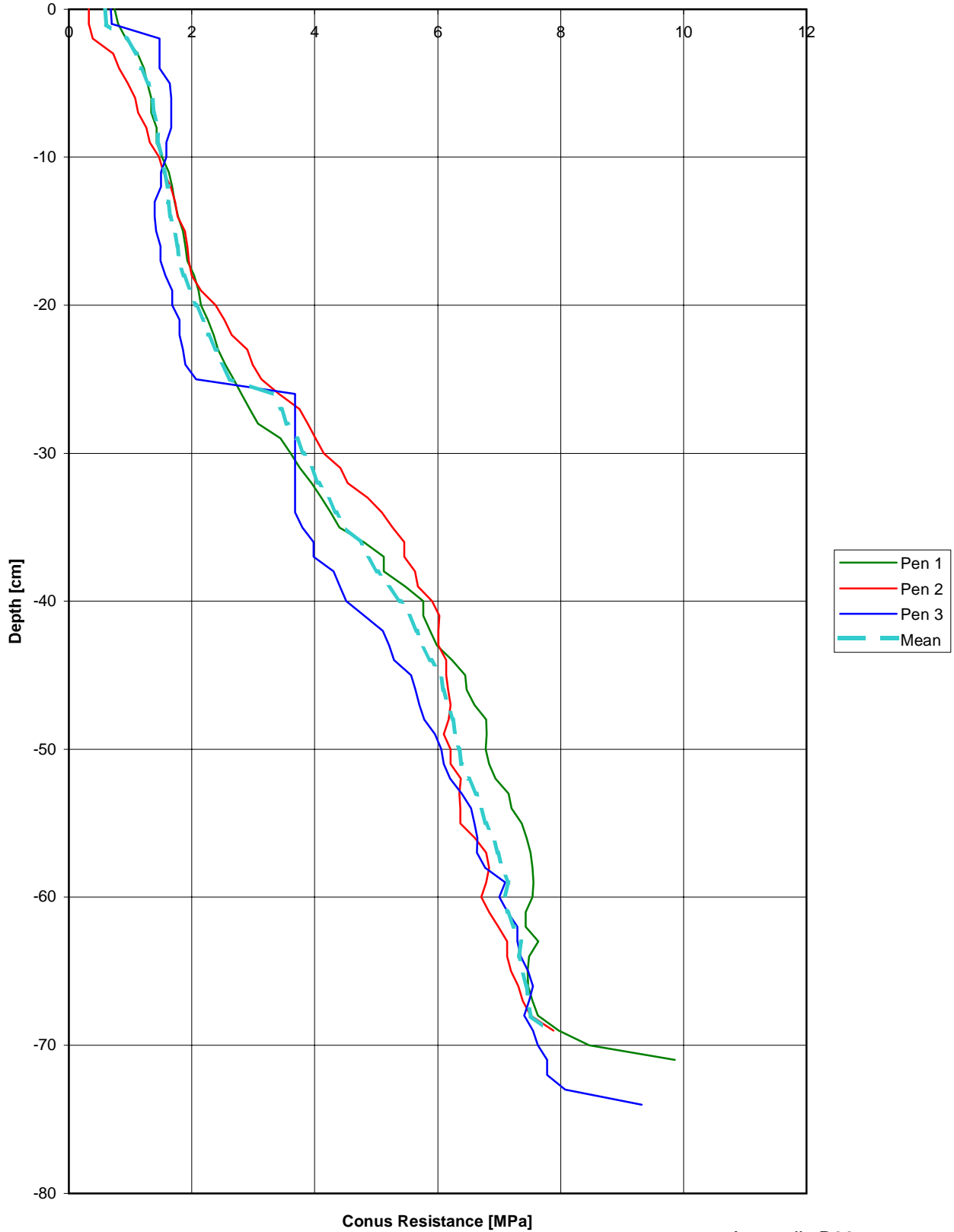
# Penetrologer measurements after test F3 - PLOTX002

conus type 1,0 cm<sup>2</sup>



# Penetrologer measurements after test F3 - PLOTX003

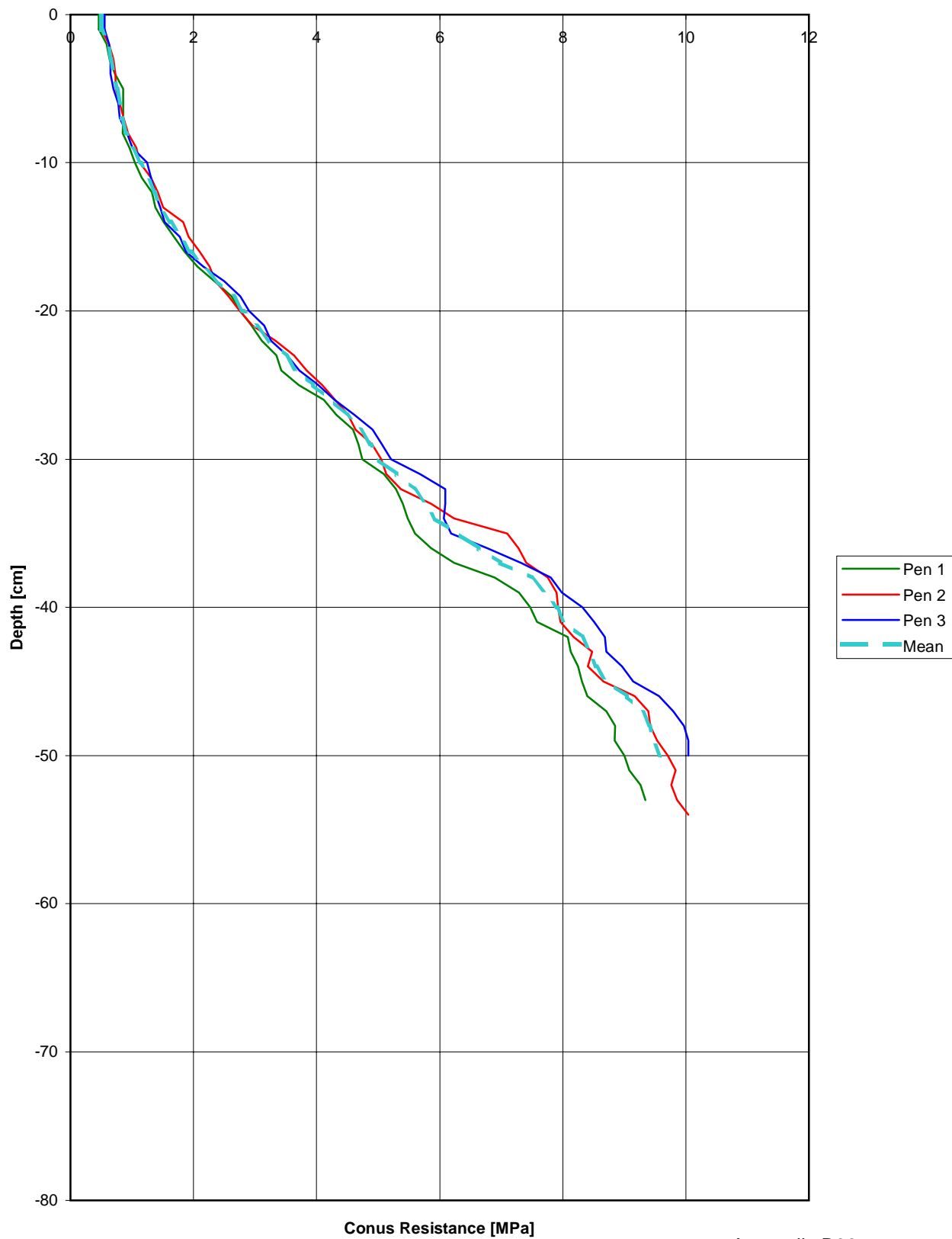
conus type 1,0 cm<sup>2</sup>





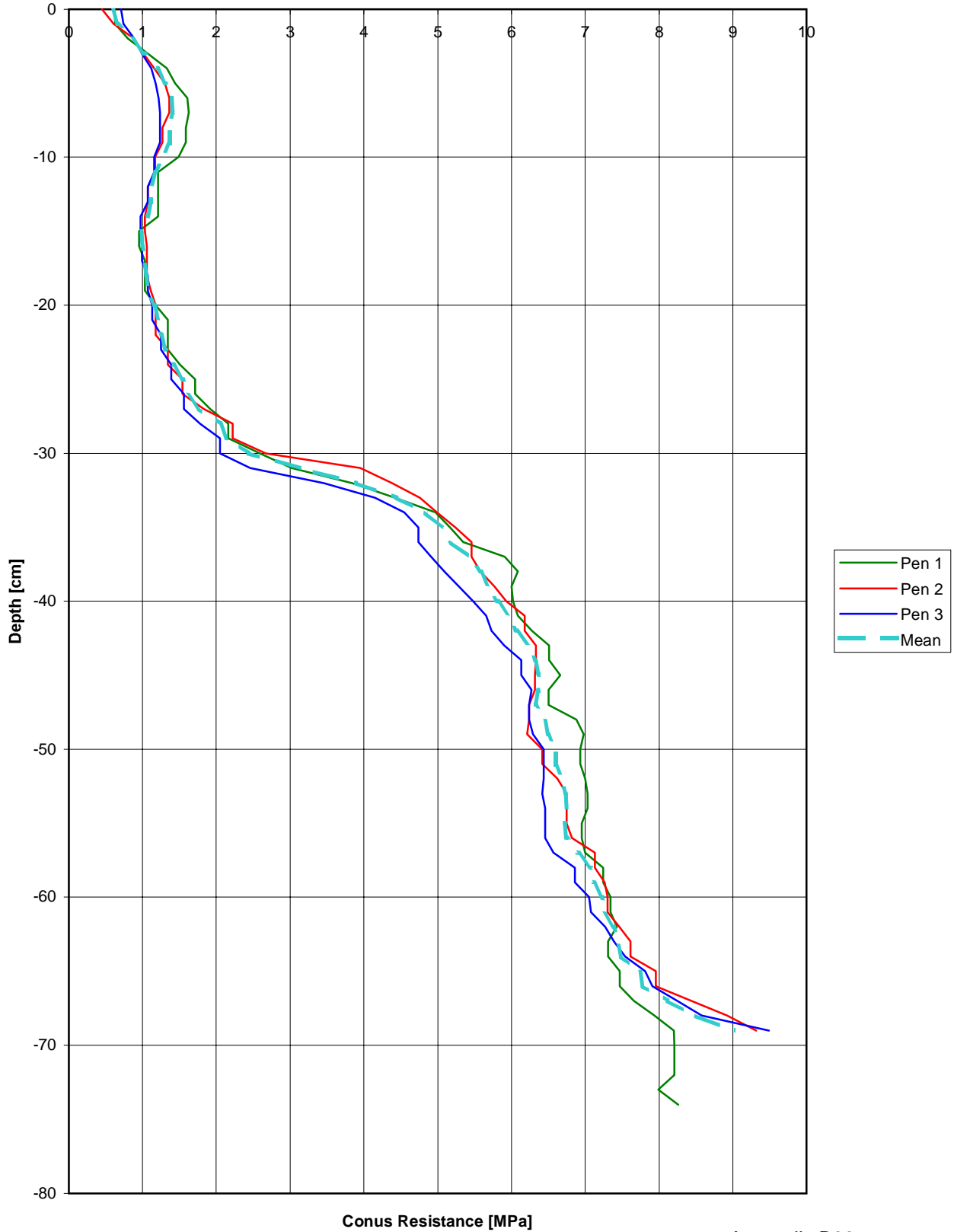
# Penetrologer measurements after test F3 - PLOTX004

conus type 1,0 cm<sup>2</sup>



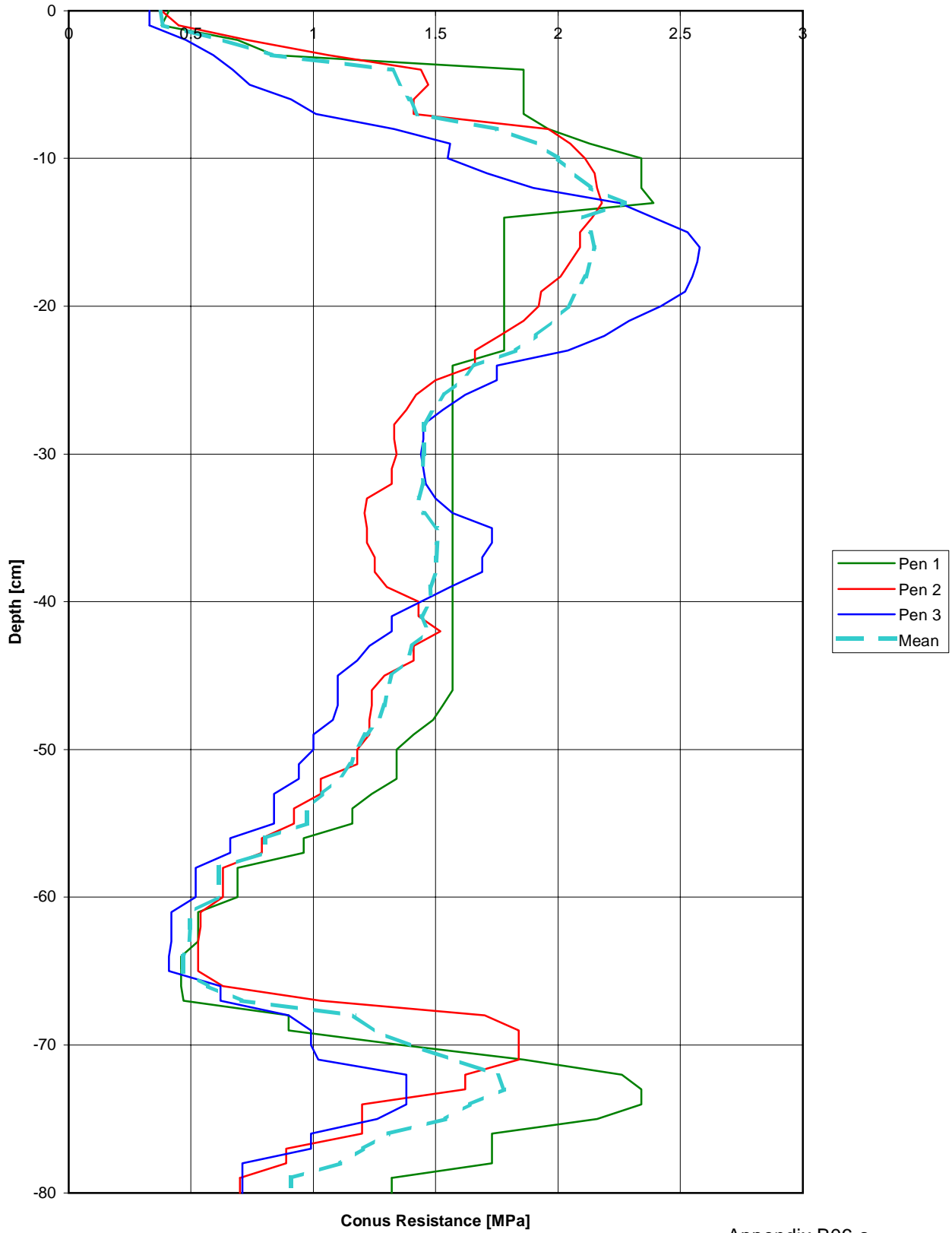
# Penetrologger measurements after test F3- PLOTX005

conus type 1,0 cm<sup>2</sup>



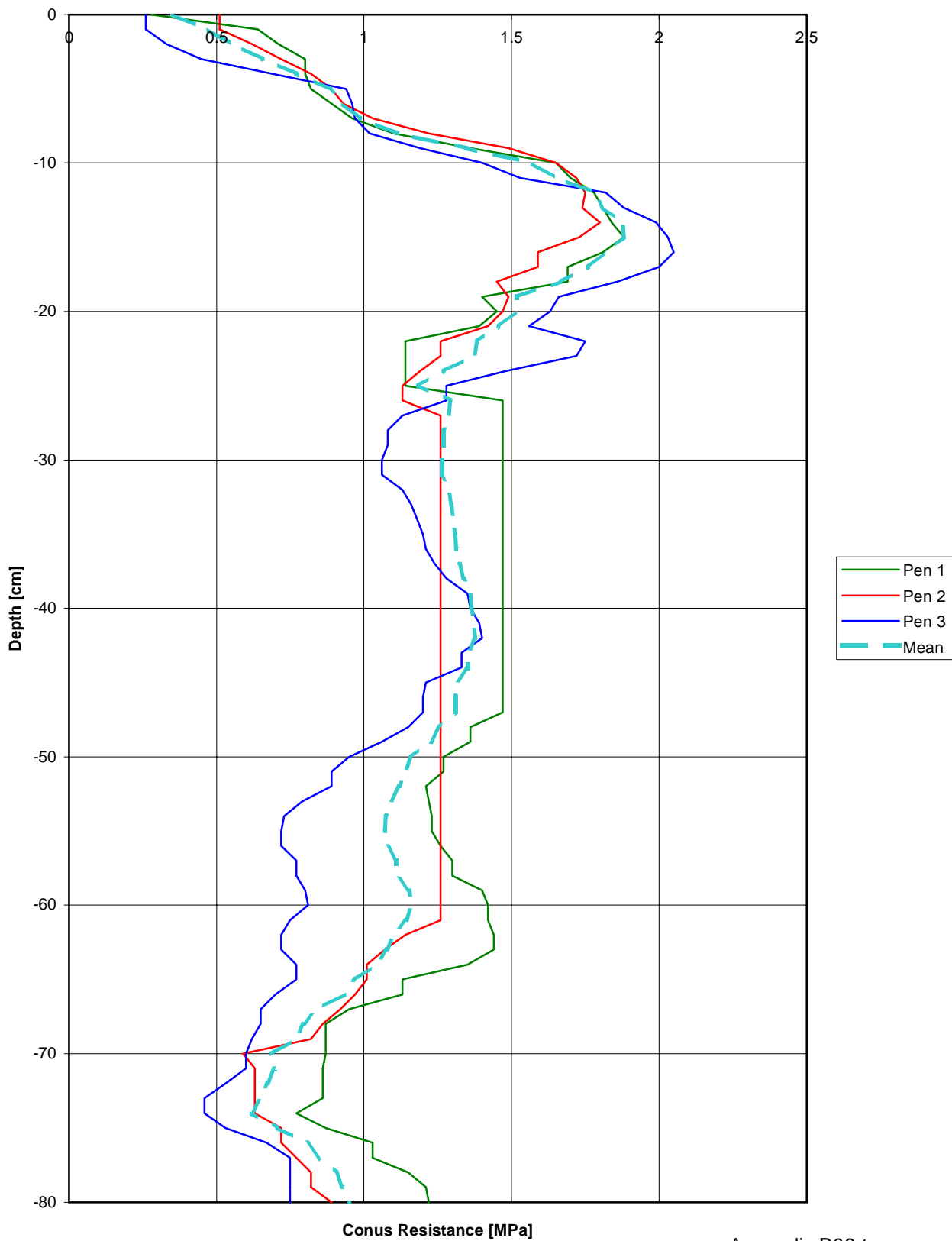
# Penetrologer measurements before test T1 - PLOTX006

conus type 1,0 cm<sup>2</sup>



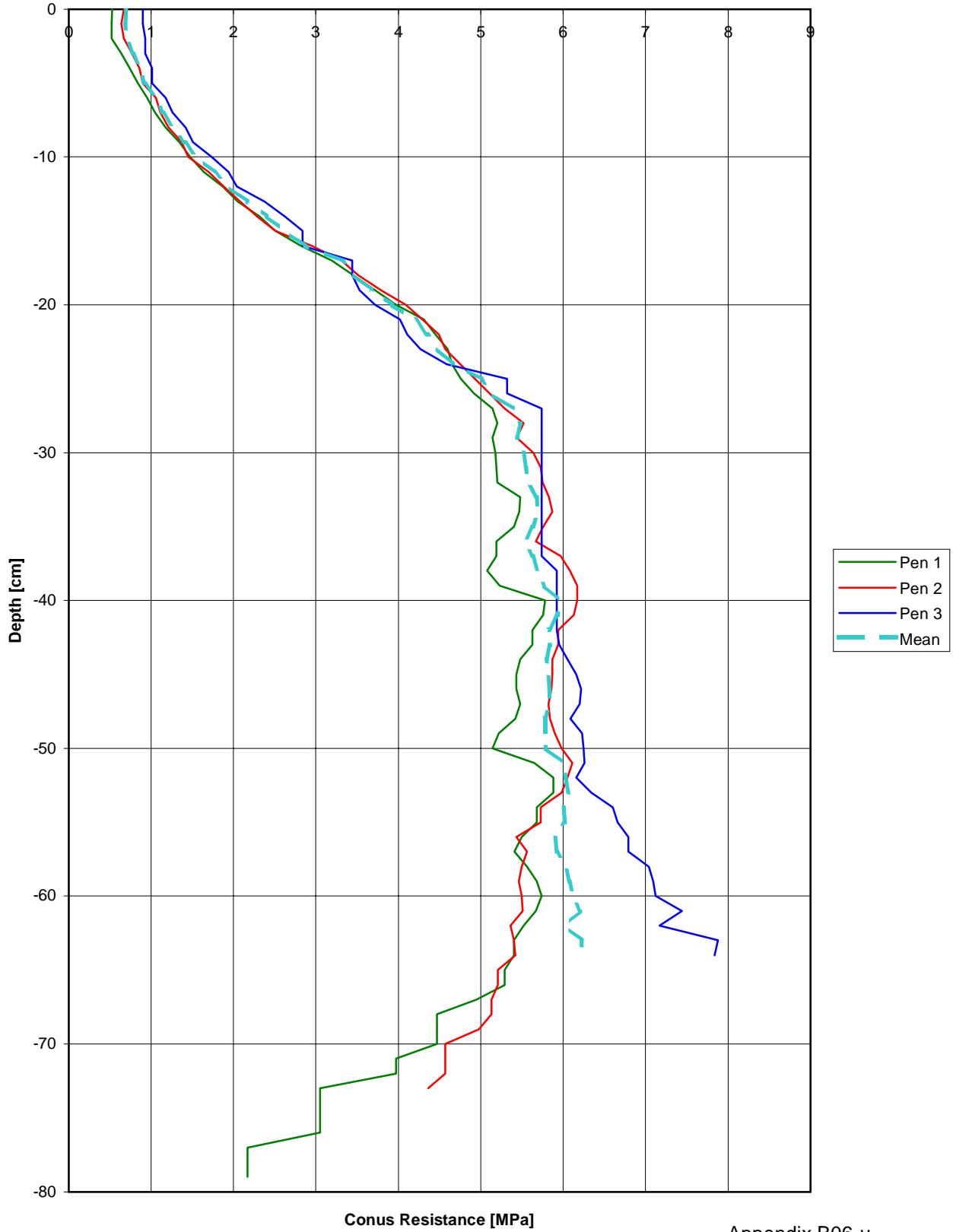
# Penetrologger measurements before test T1 - PLOTX007

conus type 1,0 cm<sup>2</sup>



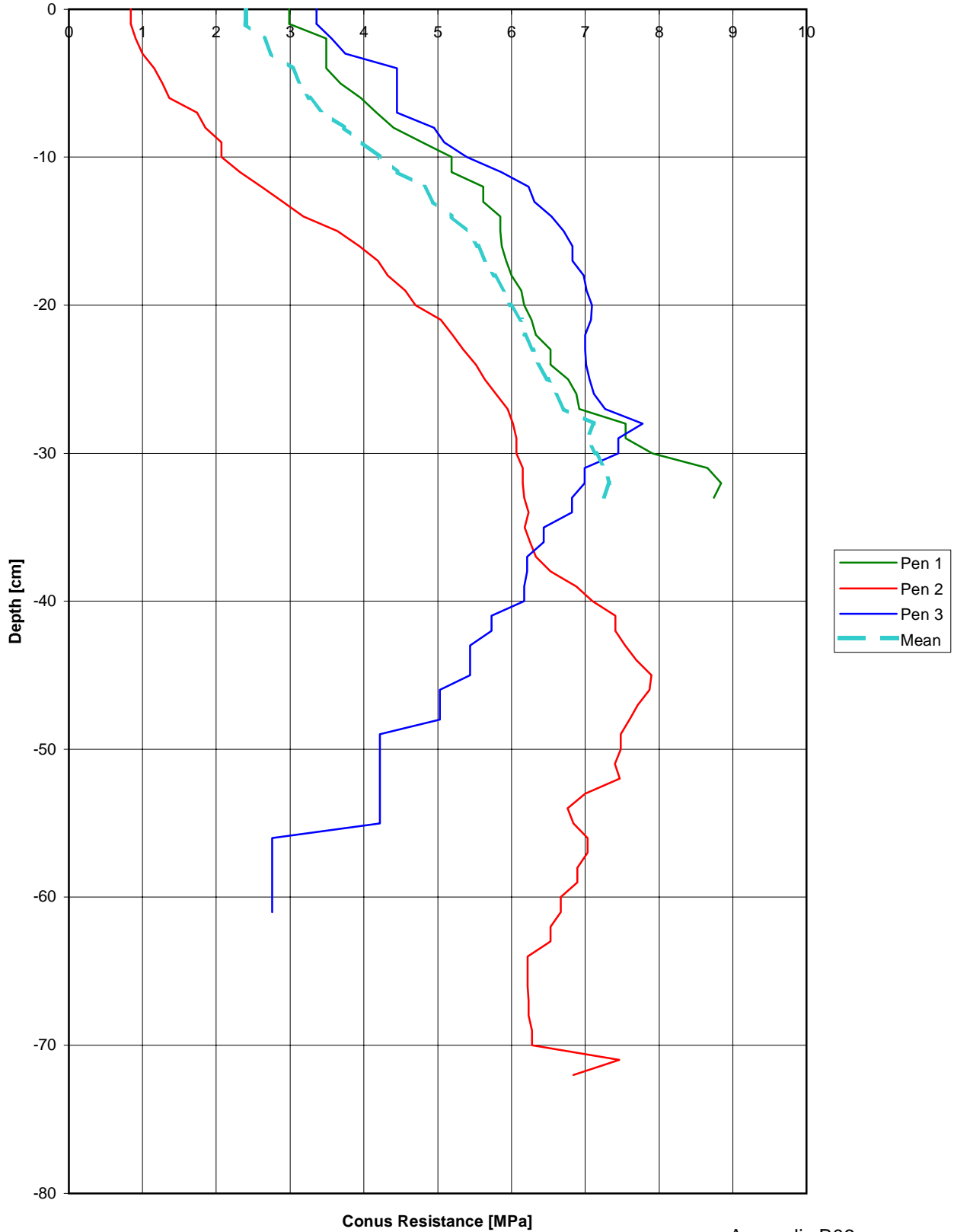
# Penetrologer measurements after test T1 - PLOTX001

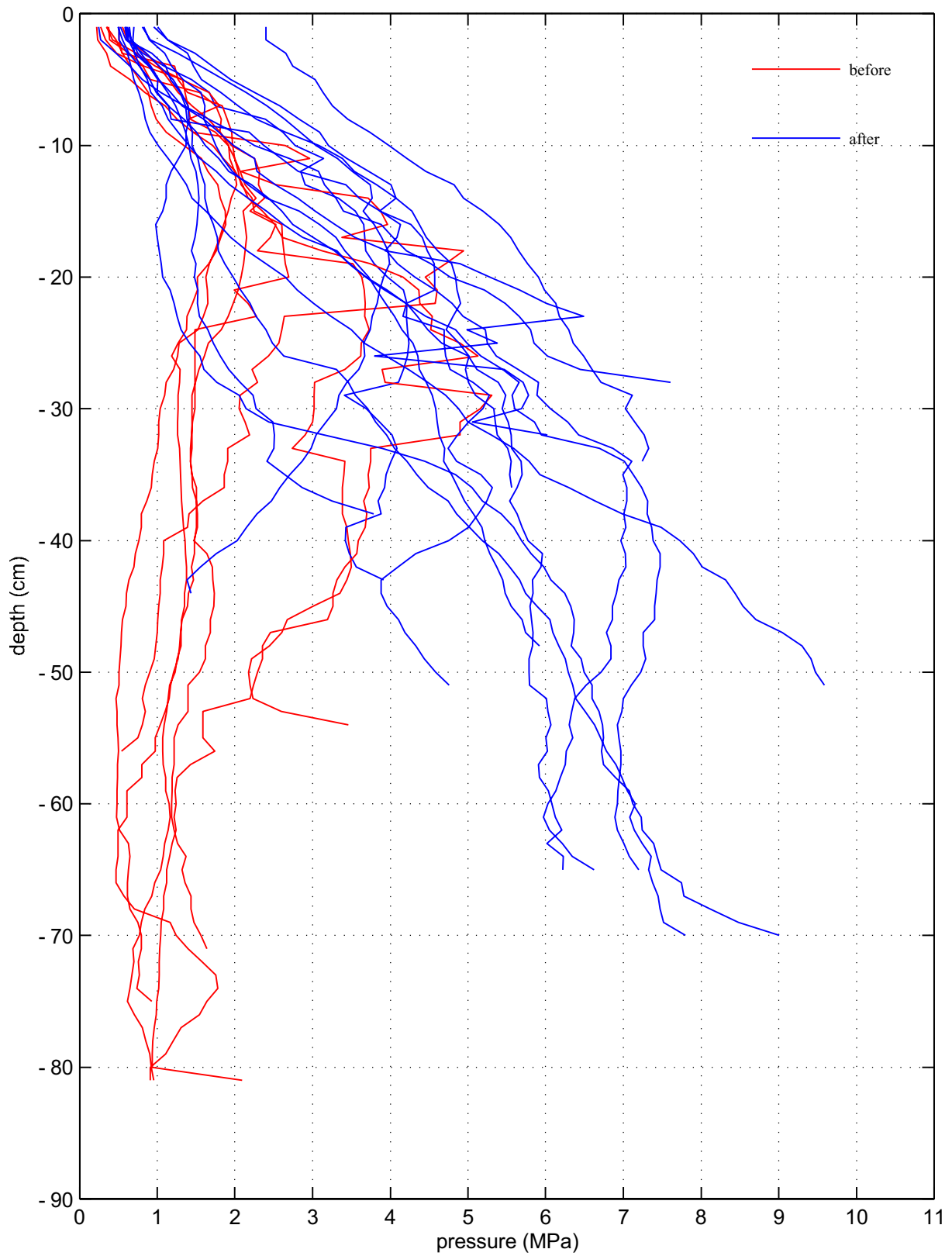
conus type 1,0 cm<sup>2</sup>



# Penetrologer measurements after test T1 - PLOTX002

conus type 1,0 cm<sup>2</sup>





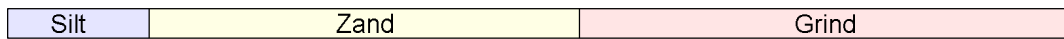
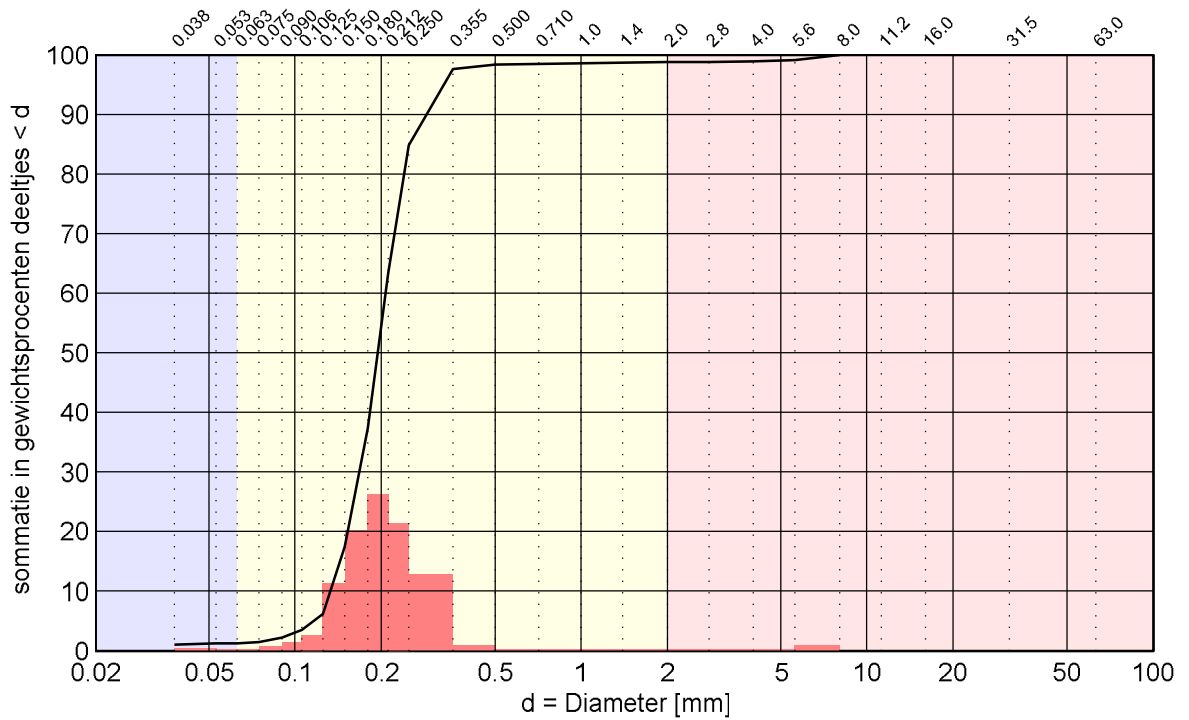
Results Penetrologer overview all

Geotextile tubes

**Deltares**

H5153

Fig B6-w



Kengetal	Waarde
$d_{10}$ [mm]	0.133
$d_{15}$ [mm]	0.144
$d_{50}$ [mm]	0.195
$d_{60}$ [mm]	0.207
$d_{60}/d_{10}$ [-]	1.6
$d_{90}/d_{10}$ [-]	2.2
$C_u$ [-]	1.03
$M_{63}$ [ $\mu$ m]	195
$M_{2000}$ [mm]	6.1
$D_m$ [mm]	0.199
$F_m$ [-]	1.15
$U$ [-]	53.7

Legenda	Boring	Monster	Diepte in m-MV
—	XXXX	1	. - . m

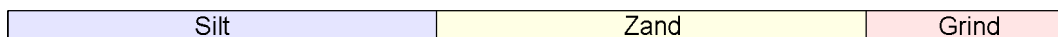
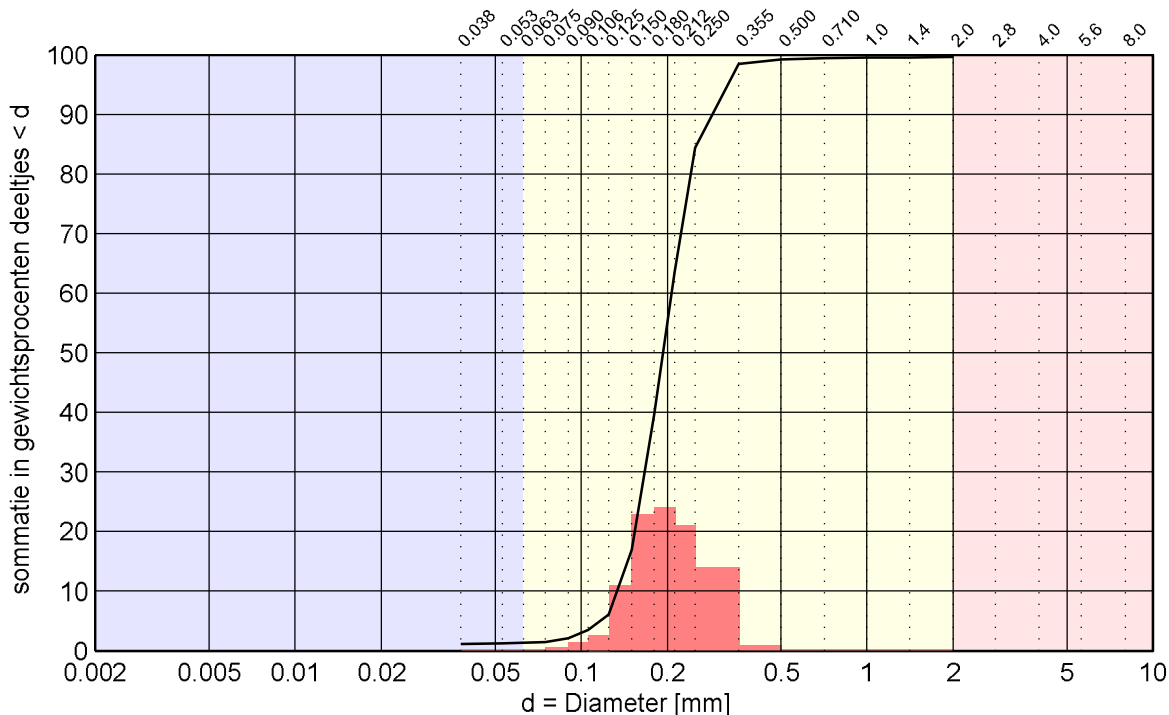
Bepaling fijn		Zandzeving: 100.42 g				Grind: - g	
d [mm]	%	d [mm]	%	d [mm]	%	d [mm]	%
-	-	-	-	0.180	37.4	-	-
0.001	-	0.038	1.0	0.212	63.4	2.8	98.7
0.002	-	0.053	1.3	0.250	84.8	4.0	98.9
0.004	-	0.063	1.3	0.355	97.6	5.6	99.1
0.006	-	0.075	1.5	0.500	98.4	8.0	100.0
0.008	-	0.090	2.2	0.710	98.5	11.2	-
0.010	-	0.106	3.5	1.0	98.6	16.0	-
0.016	-	0.125	6.1	1.4	98.6	31.5	-
0.030	-	0.150	17.3	2.0	98.7	63.0	-

**Beschrijving uitvoering proef**  
 Beschrijving volgens NEN5104: Zand, zwak siltig, zwak grindig  
 Volumieke massa  $2.65 \times 10^3 \text{ kg/m}^3$ . Aangenomen waarde.  
 Methode: GeoDelft  
 Bepaling fijne fractie: Geen  
 Bepaling grove fractie: droge zeving

**Commentaar**  
 Analyse uitgevoerd door: GeoDelft  
 Boormethode: -  
 Mengmonster: Nee

	datum	2008-10-06	Labo	Vrt
Delta-flume Geotextiele tubes				Contr.
Monster 1 - Before test F4, taken at the filling hose by line 4		436180/600		*)
<b>KORRELVERDELINGSDIAGRAM</b>		BIJL.B07-A		form
*) Vrijgegeven door Bijl op 2008-10-06 09:14				A4





Kengetal	Waarde
$d_{10}$ [mm]	0.134
$d_{15}$ [mm]	0.145
$d_{50}$ [mm]	0.193
$d_{60}$ [mm]	0.207
$d_{60}/d_{10}$ [-]	1.5
$d_{90}/d_{10}$ [-]	2.2
$C_c$ [-]	1.00
$M_{63}$ [ $\mu$ m]	194
$M_{2000}$ [mm]	0.0
$D_m$ [mm]	0.199
$F_m$ [-]	1.11
$U$ [-]	53.6

Legenda	Boring	Monster	Diepte in m-MV
	XXXX	2	. . . m

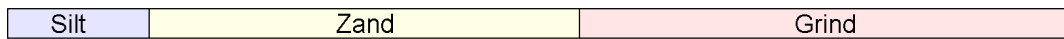
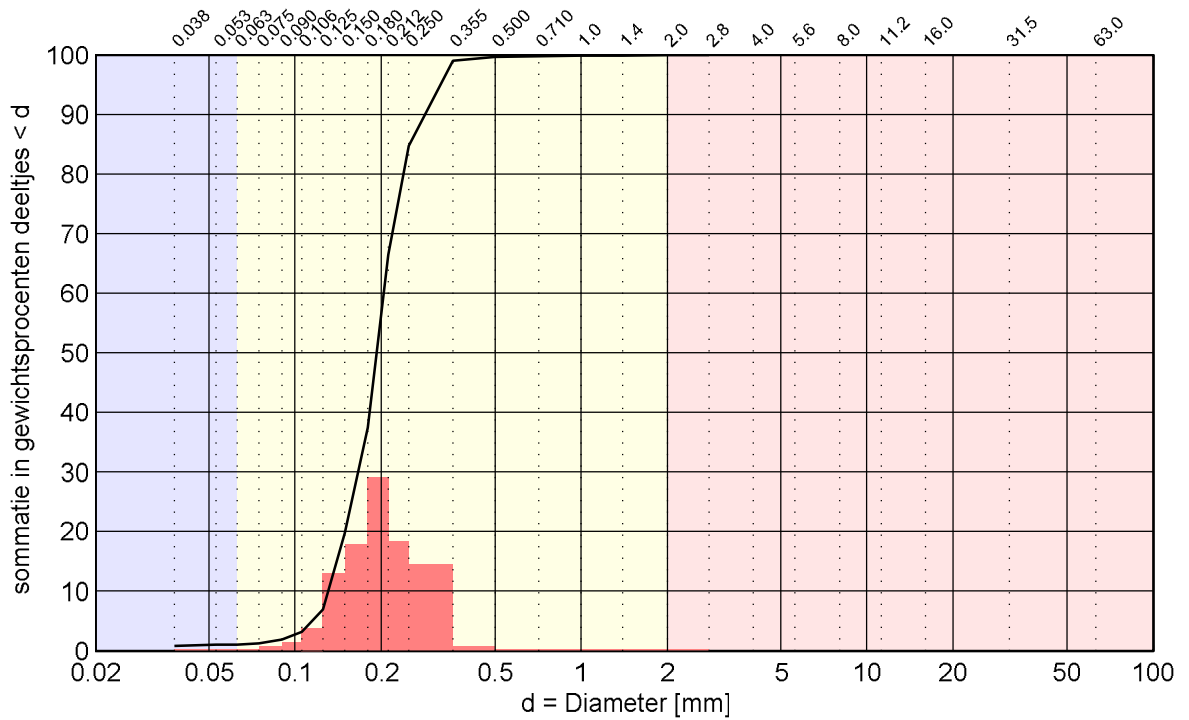
Bepaling fijn		Zandzeving: 100.58 g				Grind:	
d [mm]	%	d [mm]	%	d [mm]	%	d [mm]	%
-	-	-	-	0.180	39.6	-	-
0.001	-	0.038	1.1	0.212	63.5	2.8	-
0.002	-	0.053	1.2	0.250	84.5	4.0	-
0.004	-	0.063	1.3	0.355	98.4	5.6	-
0.006	-	0.075	1.5	0.500	99.3	8.0	-
0.008	-	0.090	2.1	0.710	99.4	11.2	-
0.010	-	0.106	3.5	1.0	99.5	16.0	-
0.016	-	0.125	6.1	1.4	99.6	31.5	-
0.030	-	0.150	16.8	2.0	99.7	63.0	-

**Beschrijving uitvoering proef**  
 Beschrijving volgens NEN5104: Zand, zwak siltig, zwak grindig  
 Volumieke massa  $2.65 \times 10^3 \text{ kg/m}^3$ . Aangenomen waarde.  
 Methode: GeoDelft  
 Bepaling fijne fractie: Geen  
 Bepaling grove fractie: droge zieving

**Commentaar**  
 Analyse uitgevoerd door: GeoDelft  
 Boormethode: -  
 Mengmonster: Nee

	datum	Labo.
	2008-10-06	Vrt
Delta-flume Geotextiele tubes Monster 2 - Before test F4, taken at the filling hose by line 4 <b>KORRELVERDELINGSDIAGRAM</b>	436180/600	Contr. (*)
	BIJL.B07-B	form. A4

\*) Vrijgegeven door Bjl op 2008-10-06 09:14



Kengetal	Waarde
$d_{10}$ [mm]	0.131
$d_{15}$ [mm]	0.140
$d_{50}$ [mm]	0.193
$d_{60}$ [mm]	0.204
$d_{60}/d_{10}$ [-]	1.6
$d_{90}/d_{10}$ [-]	2.2
$C_u$ [-]	1.04
$M_{63}$ [ $\mu$ m]	194
$M_{2000}$ [mm]	2.4
$D_m$ [mm]	0.197
$F_m$ [-]	1.09
$U$ [-]	54.3

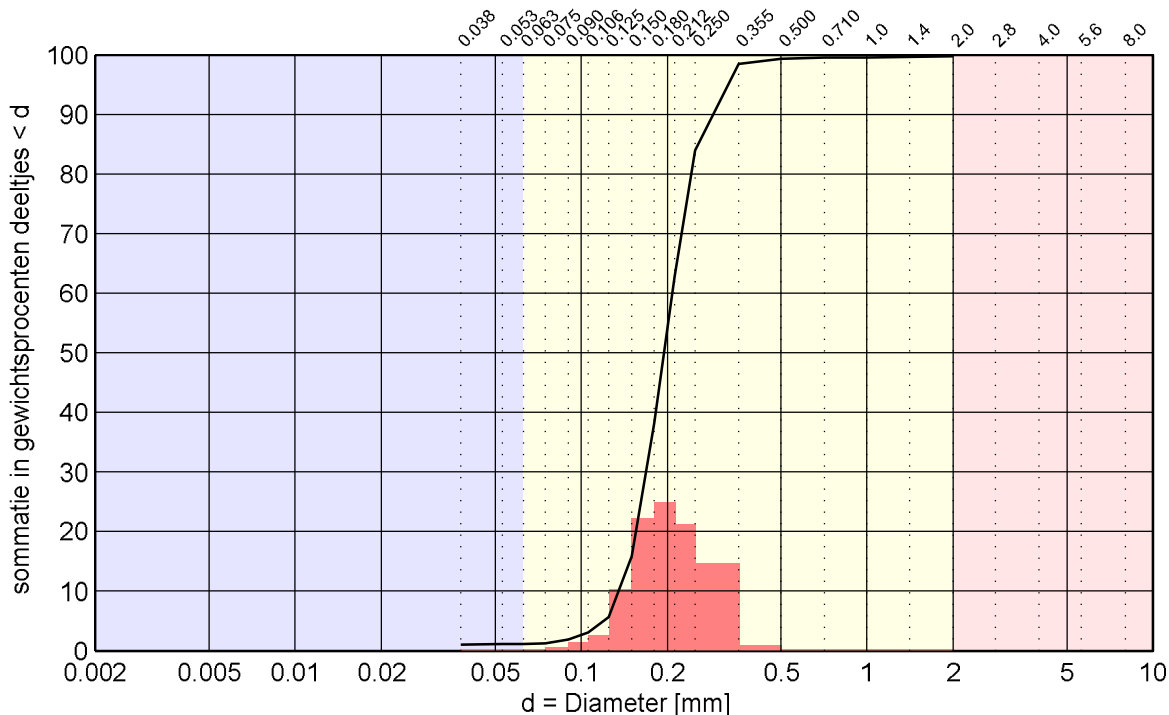
Legenda	Boring	Monster	Diepte
	XXXX	2A	. - . m

Bepaling fijn		Zandzeving: 100.86 g				Grind: - g	
d [mm]	%	d [mm]	%	d [mm]	%	d [mm]	%
-	-	-	-	0.180	37.5	-	-
0.001	-	0.038	0.8	0.212	66.5	2.8	100.0
0.002	-	0.053	1.0	0.250	84.7	4.0	-
0.004	-	0.063	1.0	0.355	99.0	5.6	-
0.006	-	0.075	1.2	0.500	99.7	8.0	-
0.008	-	0.090	1.8	0.710	99.8	11.2	-
0.010	-	0.106	3.2	1.0	99.8	16.0	-
0.016	-	0.125	6.9	1.4	99.9	31.5	-
0.030	-	0.150	19.7	2.0	99.9	63.0	-

**Beschrijving uitvoering proef**  
 Beschrijving volgens NEN5104: Zand, zwak siltig, zwak grindig  
 Volumieke massa  $2.65 \times 10^3 \text{ kg/m}^3$ . Aangenomen waarde.  
 Methode: GeoDelft  
 Bepaling fijne fractie: Geen  
 Bepaling grove fractie: droge zieving

**Commentaar**  
 Analyse uitgevoerd door: Deltares  
 Boormethode: -  
 Mengmonster: Nee  
 VOOR de proef

	datum	2008-11-10	Labo	Vrt
Delta-flume Geotextiele tubes				Contr.
Monster 3 - Before test F4, taken at the filling hose by line 1		436180/600		*)
<b>KORRELVERDELINGSDIAGRAM</b>		BIJL.B07-C		form
*) Vrijgegeven door Grw op 2008-11-10 10:28				
				A4



Silt	Zand	Grind
------	------	-------

Kengetal	Waarde
$d_{10}$ [mm]	0.135
$d_{15}$ [mm]	0.148
$d_{50}$ [mm]	0.195
$d_{60}$ [mm]	0.208
$d_{60}/d_{10}$ [-]	1.5
$d_{90}/d_{10}$ [-]	2.1
$C_c$ [-]	1.01
$M_{63}$ [ $\mu$ m]	195
$M_{2000}$ [mm]	0.0
$D_m$ [mm]	0.200
$F_m$ [-]	1.12
$U$ [-]	53.2

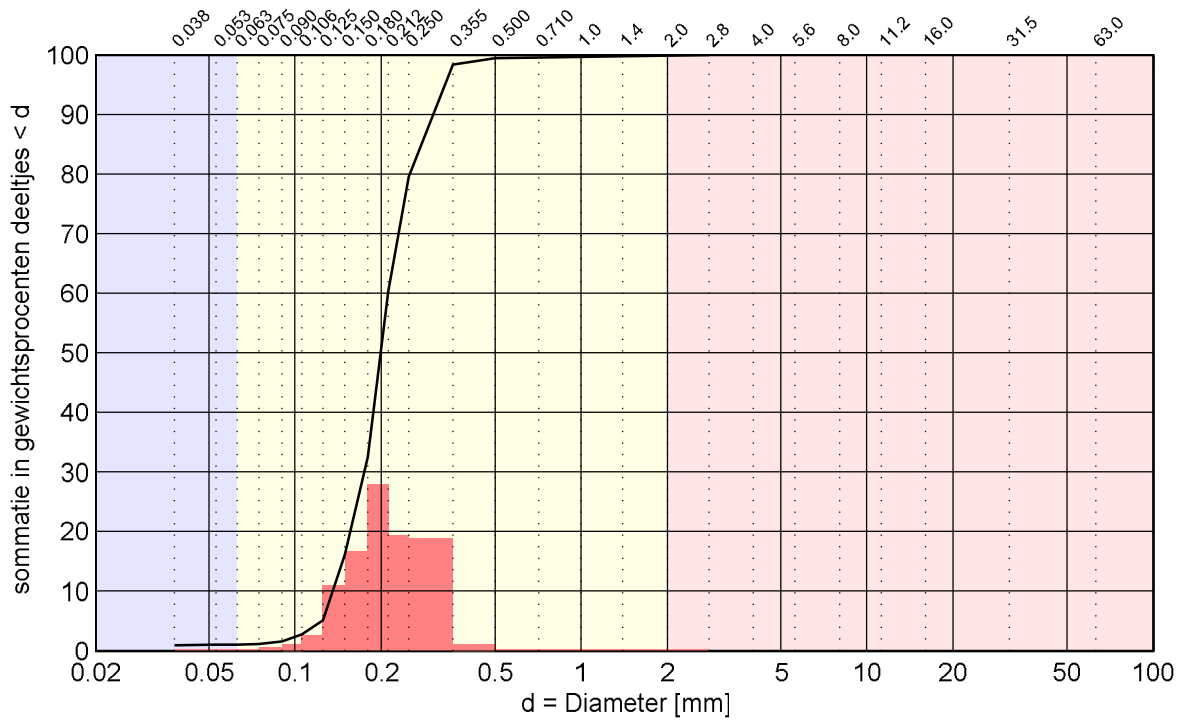
Legenda	Boring	Monster	Diepte in m-MV
	XXXX	3	. . . m

Bepaling fijn		Zandzeving: 100.28 g				Grind:	
d [mm]	%	d [mm]	%	d [mm]	%	d [mm]	%
-	-	-	-	0.180	38.1	-	-
0.001	-	0.038	0.9	0.212	62.8	2.8	-
0.002	-	0.053	1.0	0.250	83.9	4.0	-
0.004	-	0.063	1.1	0.355	98.5	5.6	-
0.006	-	0.075	1.3	0.500	99.4	8.0	-
0.008	-	0.090	1.9	0.710	99.5	11.2	-
0.010	-	0.106	3.1	1.0	99.6	16.0	-
0.016	-	0.125	5.6	1.4	99.7	31.5	-
0.030	-	0.150	15.9	2.0	99.7	63.0	-

Beschrijving uitvoering proef
Beschrijving volgens NEN5104: Zand, zwak siltig, zwak grindig
Volumieke massa $2.65 \times 10^3 \text{ kg/m}^3$ . Aangenomen waarde.
Methode: GeoDelft
Bepaling fijne fractie: Geen
Bepaling grove fractie: droge zeving

Commentaar
Analyse uitgevoerd door: Deltares
Boormethode: -
Mengmonster: Nee

	datum	2008-10-06	Labo	Vrt
Delta-flume Geotextiele tubes				Contr.
Monster 4 - After test F4, taken in the middle of the tube at line 3		436180/600		*)
<b>KORRELVERDELINGSDIAGRAM</b>				form
*) Vrijgegeven door Bijl op 2008-10-06 09:14		BIJL.B07-D		A4



Kengetal	Waarde
$d_{10}$ [mm]	0.136
$d_{15}$ [mm]	0.147
$d_{50}$ [mm]	0.200
$d_{60}$ [mm]	0.212
$d_{60}/d_{10}$ [-]	1.6
$d_{90}/d_{10}$ [-]	2.2
$C_u$ [-]	1.07
$M_{63}$ [ $\mu$ m]	200
$M_{2000}$ [mm]	2.4
$D_m$ [mm]	0.206
$F_m$ [-]	1.16
$U$ [-]	51.9

Legenda	Boring	Monster	Diepte
	XXXX	5	. - . m

Bepaling fijn		Zandzeving: 100.52 g				Grind: - g	
d [mm]	%	d [mm]	%	d [mm]	%	d [mm]	%
-	-	-	-	0.180	32.5	-	-
0.001	-	0.038	0.8	0.212	60.3	2.8	100.0
0.002	-	0.053	0.9	0.250	79.5	4.0	-
0.004	-	0.063	1.0	0.355	98.3	5.6	-
0.006	-	0.075	1.2	0.500	99.4	8.0	-
0.008	-	0.090	1.6	0.710	99.6	11.2	-
0.010	-	0.106	2.7	1.0	99.7	16.0	-
0.016	-	0.125	5.1	1.4	99.8	31.5	-
0.030	-	0.150	16.0	2.0	99.8	63.0	-

**Beschrijving uitvoering proef**  
 Beschrijving volgens NEN5104: Zand, zwak siltig, zwak grindig  
 Volumieke massa  $2.65 \times 10^3 \text{ kg/m}^3$ . Aangenomen waarde.  
 Methode: GeoDelft  
 Bepaling fijne fractie: Geen  
 Bepaling grove fractie: droge zeving

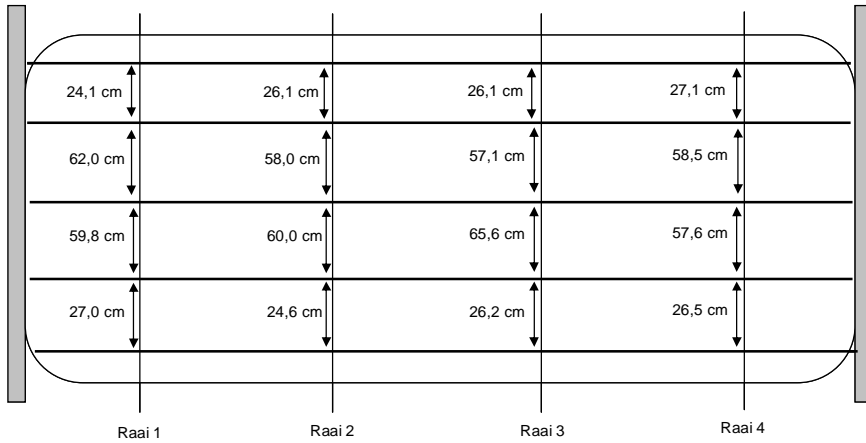
**Commentaar**  
 Analyse uitgevoerd door: Deltares  
 Boormethode: -  
 Mengmonster: Nee  
 NA de proef

	datum	2008-11-10	Labo	Vrt
Delta-flume Geotextiele tubes				Contr.
Monster 5 - After test F4, taken in the middle of the tube at line 2		436180/600		*)
<b>KORRELVERDELINGSDIAGRAM</b>		BIJL.B07-E		form
*) Vrijgegeven door Grw op 2008-11-10 10:28				
				A4

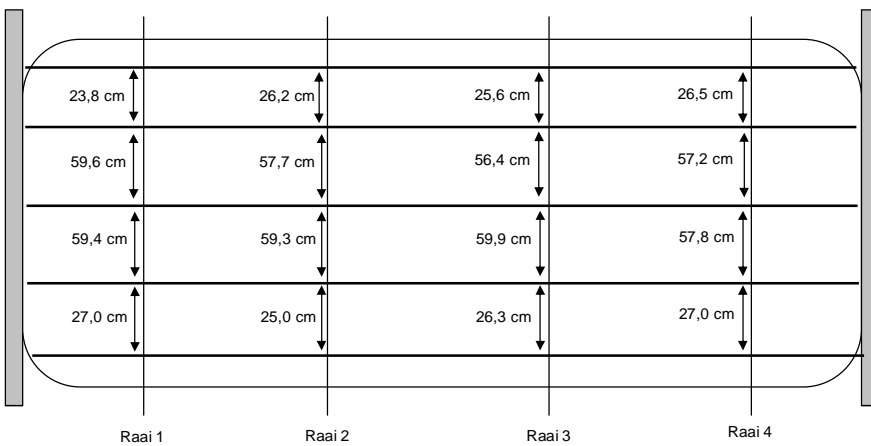
# Appendix B.8a Stretches in geotextile

The figures in this appendix show the measured distances between the mark lines on the geotextile. Figure B-A shows the difference between the measurements after and before a test series. This value is an indication for the stretches in the geotextile.

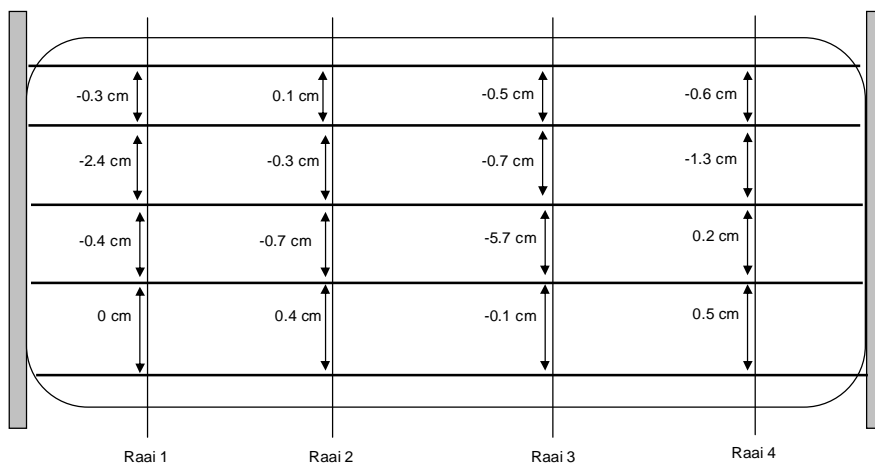
## Before test F1-1 (=A)



## After test F1-10 (=B)



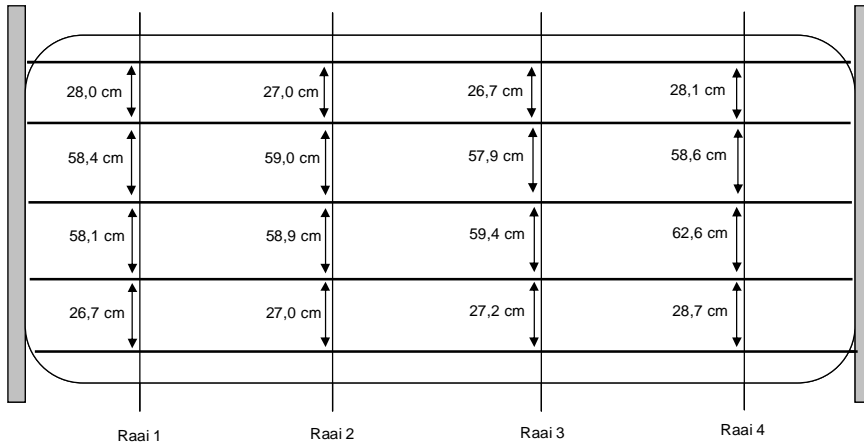
## B-A



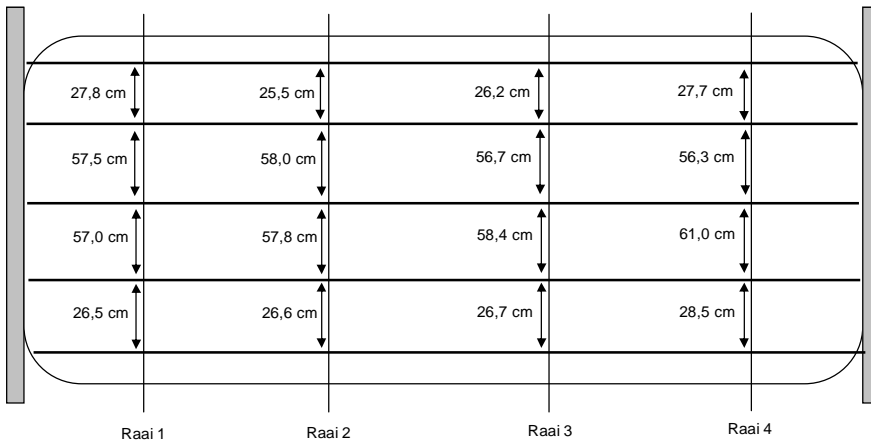
## Appendix B.8b Stretches in geotextile

The figures in this appendix show the measured distances between the mark lines on the geotextile. Figure B-A shows the difference between the measurements after and before a test series. This value is an indication for the stretches in the geotextile.

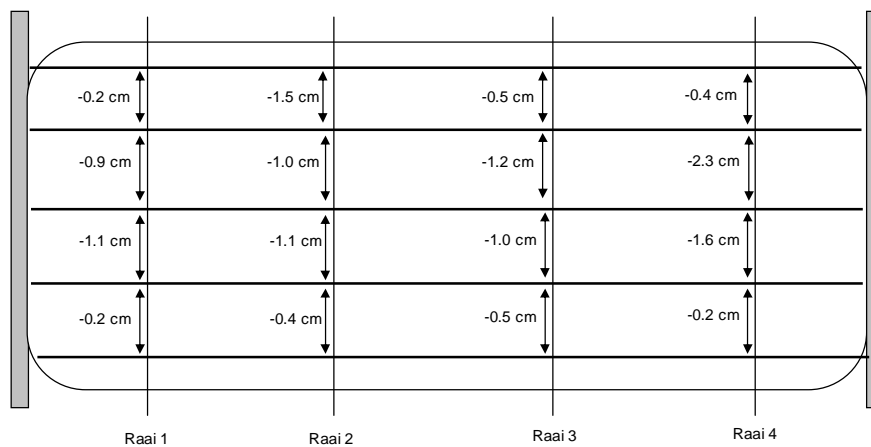
### Before test F3-1 (=A)



### After test F3-9 (=B)



### B-A



## C Photos

<i>Photo C.1</i>	<i>Lining out the Back flow structure</i>
<i>Photo C.2</i>	<i>Building the Back flow structure</i>
<i>Photo C.3</i>	<i>Placing concrete plates</i>
<i>Photo C.4</i>	<i>Back flow structure</i>
<i>Photo C.5</i>	<i>Geotextile on the concrete plates to avoid erosion</i>
<i>Photo C.6</i>	<i>Building the sand core</i>
<i>Photo C.7</i>	<i>Compacting the sand core</i>
<i>Photo C.8</i>	<i>Installing the reinforcement</i>
<i>Photo C.9</i>	<i>Application of the concrete</i>
<i>Photo C.10</i>	<i>Lay out geotextile tube</i>
<i>Photo C.11</i>	<i>Temporarily fixation geotextile tube</i>
<i>Photo C.12</i>	<i>Sand-water mixture</i>
<i>Photo C.13</i>	<i>Filling the geotextile tube and measuring the actual height</i>
<i>Photo C.14</i>	<i>Filling (over pressure) hose</i>
<i>Photo C.15</i>	<i>Walking over geotextile tube to prevent blocking</i>
<i>Photo C.16</i>	<i>Process water flows trough the geotextile during filling</i>
<i>Photo C.17</i>	<i>Markers on filled geotextile tube for image processing</i>
<i>Photo C.18</i>	<i>Bar behind geotextile tube to simulate trench</i>
<i>Photo C.19</i>	<i>Use of a slat at the landside to prevent damaging the profiler and geotextile tube.</i>
<i>Photo C.20</i>	<i>Use of a block at the seaside to prevent damaging the profiler</i>
<i>Photo C.21</i>	<i>Calibrating profiler</i>
<i>Photo C.22</i>	<i>Profiling geotextile tube</i>
<i>Photo C.23</i>	<i>Marking block</i>
<i>Photo C.24</i>	<i>Determine outermost point geotextile tube</i>
<i>Photo C.25</i>	<i>Measurements with Penetrologger</i>
<i>Photo C.26</i>	<i>Use of split ring</i>
<i>Photo C.27</i>	<i>Example of color injections</i>
<i>Photo C.28</i>	<i>During test series F4-1</i>
<i>Photo C.29</i>	<i>After test series F4-1</i>
<i>Photo C.30</i>	<i>During test series F1-6</i>
<i>Photo C.31</i>	<i>After test series F1-10</i>
<i>Photo C.32</i>	<i>After examining the geotextile tube (F1)</i>
<i>Photo C.33</i>	<i>During test series F3-9</i>
<i>Photo C.34</i>	<i>After test series F3-9</i>
<i>Photo C.35</i>	<i>Measuring height geotextile tube after test series F3-9</i>
<i>Photo C.36</i>	<i>During test series T1-6</i>
<i>Photo C.37</i>	<i>During test series T1-6</i>
<i>Photo C.38</i>	<i>During test series T1-6</i>
<i>Photo C.39</i>	<i>During test series T1-6</i>
<i>Photo C.40</i>	<i>Geotextile tube partly on bar after test series T1-9</i>
<i>Photo C.41</i>	<i>Determine dimensions after test series T1-9</i>
<i>Photo C.42</i>	<i>During test series P3-8</i>
<i>Photo C.43</i>	<i>During test series P3-9</i>
<i>Photo C.44</i>	<i>Sliding of geotextile tube during test series P3-9</i>
<i>Photo C.45</i>	<i>Prepared geotextile tubes before test series P2-1</i>
<i>Photo C.46</i>	<i>Movement of geotextile tube (left tube) after test series P2-4-2</i>
<i>Photo C.47</i>	<i>During test series F5-5</i>

- Photo C.48*      *During test series F5-5*
- Photo C.49*      *Deformed geotextile tube after test series F5-6*
- Photo C.50*      *Color injection test series F1. Injection at line 4, point 3*
- Photo C.51*      *Color injection test series F1. Injection at line 4, point 3*
- Photo C.52*      *Color injection test series F3. Injection at line1, point 3*
- Photo C.53*      *Color injection test series F4. Injection at line3, point 5*
- Photo C.54*      *Color injection test series F4. Injection at line 3, point 5*





Photo 1: Lining out the Back flow structure



Photo 2: Building the Back flow structure



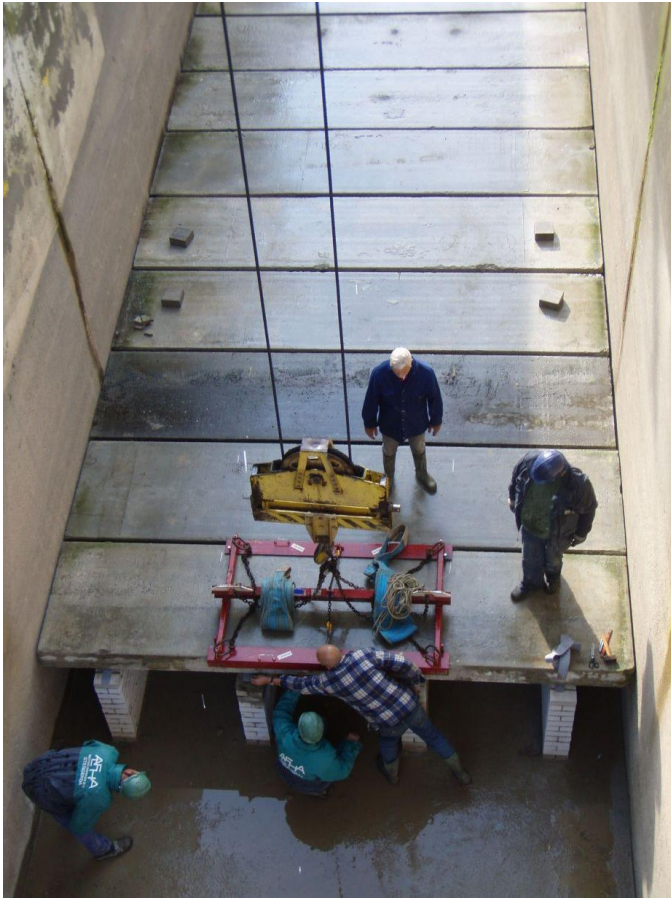


Photo 3: Placing concrete plates



Photo 4: Back flow structure



Photo 5: Geotextile on the concrete plates to avoid erosion



Photo 6: Building the sand core





Photo 7: Compacting the sand core



Photo 8: Installing the reinforcement



Photo 9: Application of the concrete



Photo 10: Lay out geotextile tube





Photo 11: Temporarily fixation geotextile tube



Photo 12: Sand-water mixture





Photo 13: Filling the geotextile tube and measuring the actual height



Photo 14: Filling (over pressure) hose





Photo 15: Walking over geotextile tube to prevent blocking



Photo 16: Process water flows through the geotextile during filling



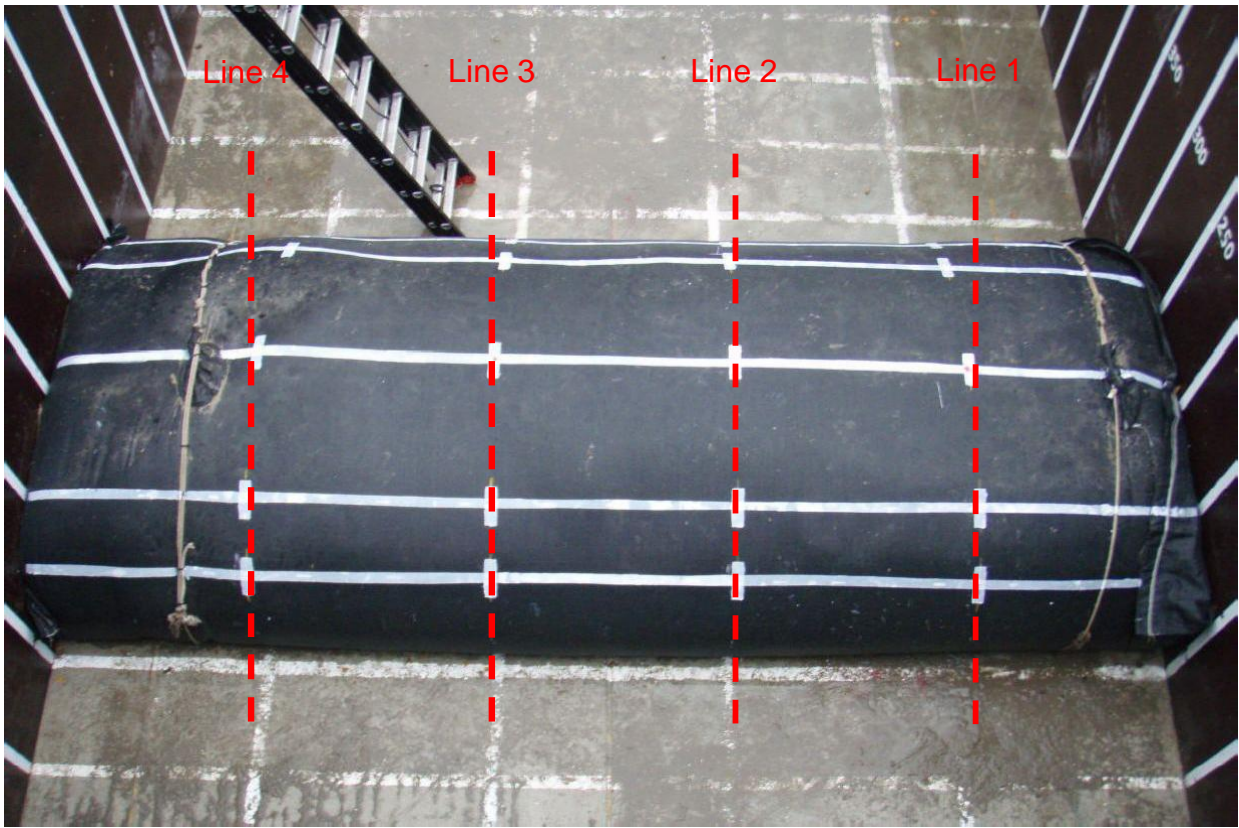


Photo 17: Markers on filled geotextile tube for image processing

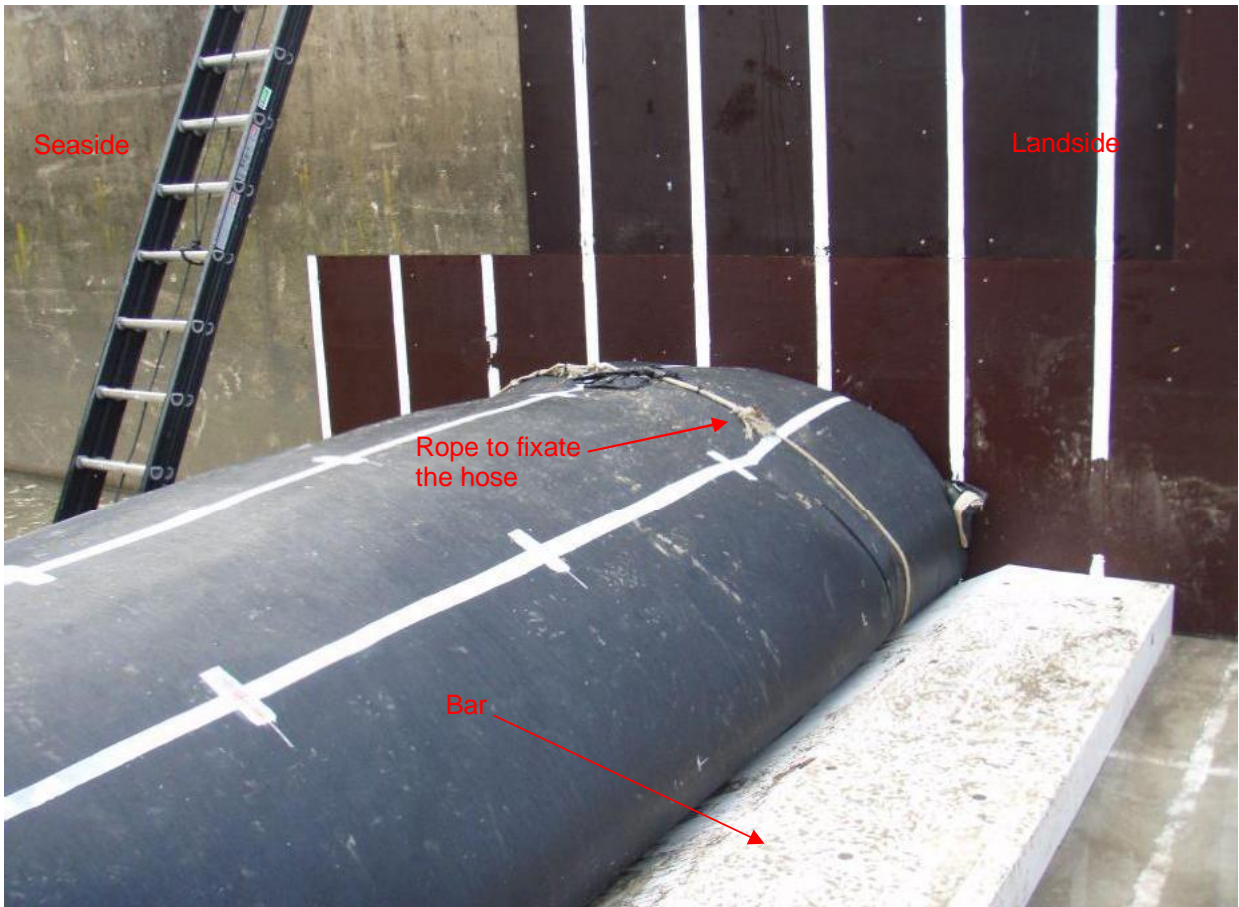


Photo 18: Bar behind geotextile tube to simulate trench





Photo 19: Use of a slat at the landside to prevent damaging the profiler and geotextile tube.

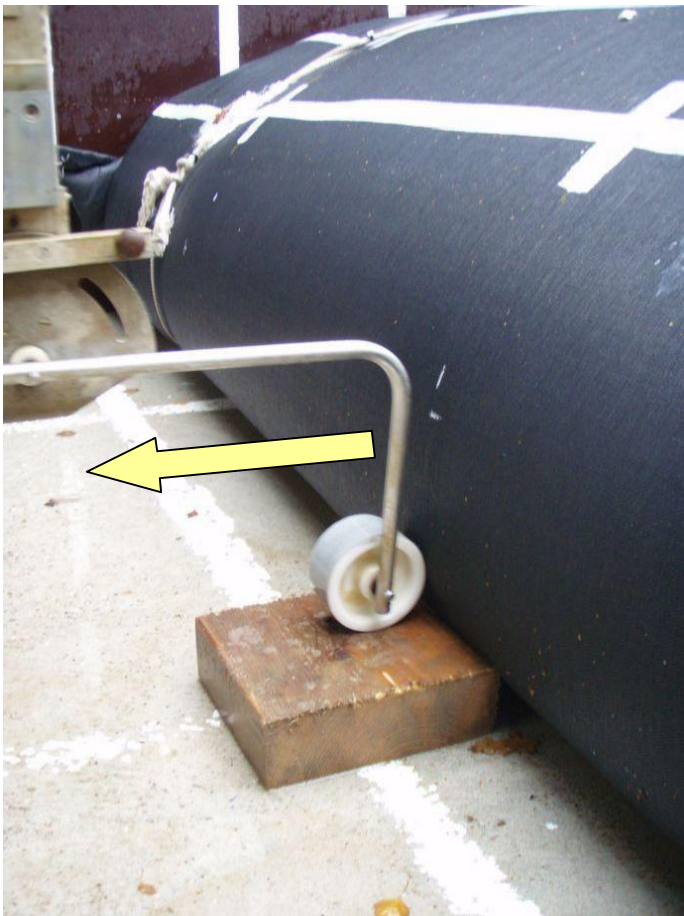


Photo 20: Use of a block at the seaside to prevent damaging the profiler



Photo 21: Calibrating profiler



Photo 22: Profiling geotextile tube



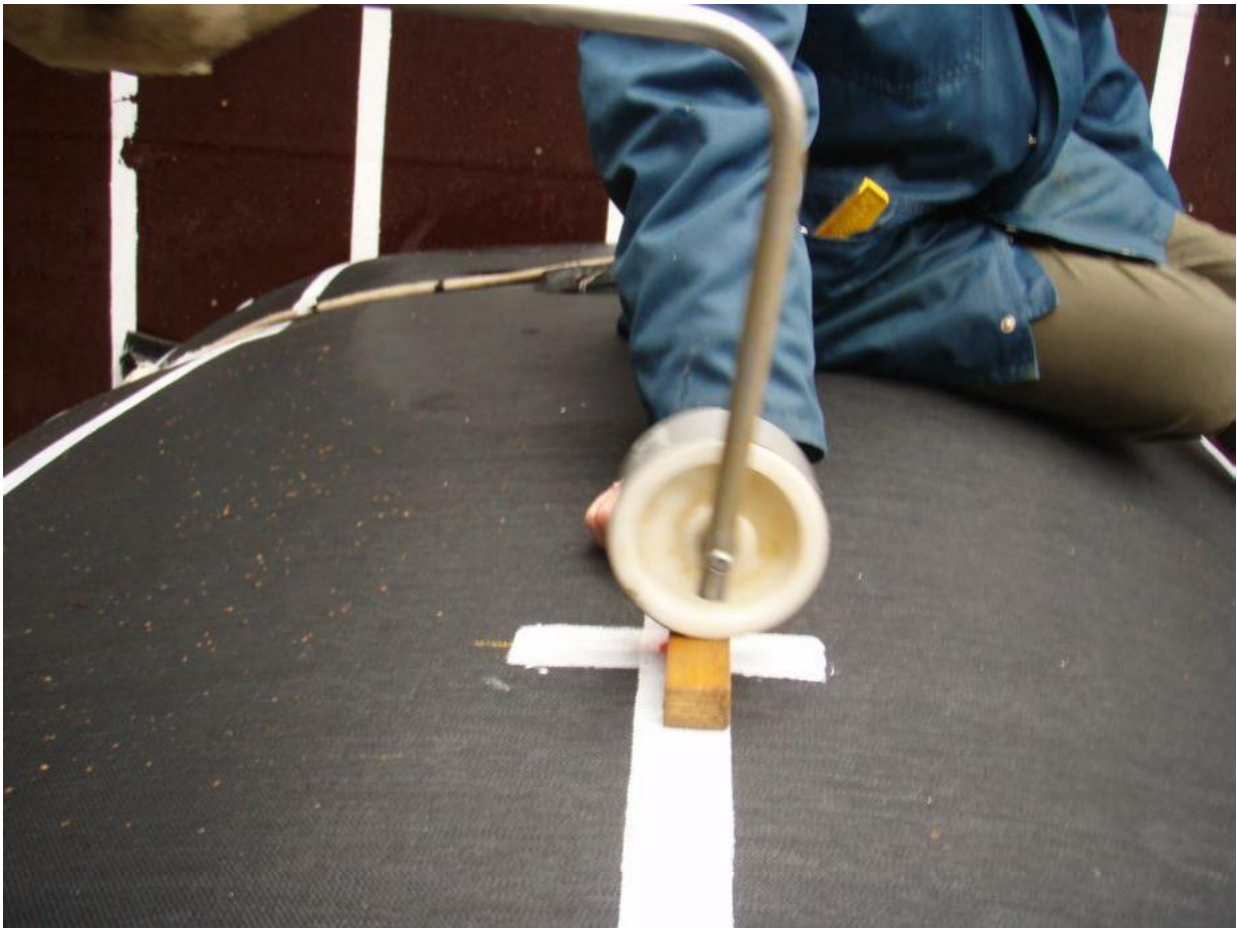


Photo 23: Marking block



Photo 24: Determine outermost point geotextile tube





Photo 25: Measurements with Penetrologger



Photo 26: Use of split ring





Photo 27: Example of color injections



Photo 28: During test series F4-1





Photo 29: After test series F4-1



Photo 30: During test series F1-6



Photo 31: After test series F1-10



Photo 32: After examining the geotextile tube (F1)





Photo 33: During test series F3-9



Photo 34: After test series F3-9





Photo 35: Measuring height geotextile tube after test series F3-9



Photo 36: During test series T1-6





Photo 37: During test series T1-6



Photo 38: During test series T1-6





Photo 39: During test series T1-6



Photo 40: Geotextile tube partly on bar after test series T1-9





Photo 41: Determine dimensions after test series T1-9



Photo 42: During test series P3-8





Photo 43: During test series P3-9



Photo 44: Sliding of geotextile tube during test series P3-9





Photo 45: Prepared geotextile tubes before test series P2-1



Photo 46: Movement of geotextile tube (left tube) after test series P2-4-2





Photo 47: During test series F5-5



Photo 48: During test series F5-5





Photo 49: Deformed geotextile tube after test series F5-6



Photo 50: Color injection test series F1. Injection at line 4, point 3





Photo 51: Color injection test series F1. Injection at line 4, point 3

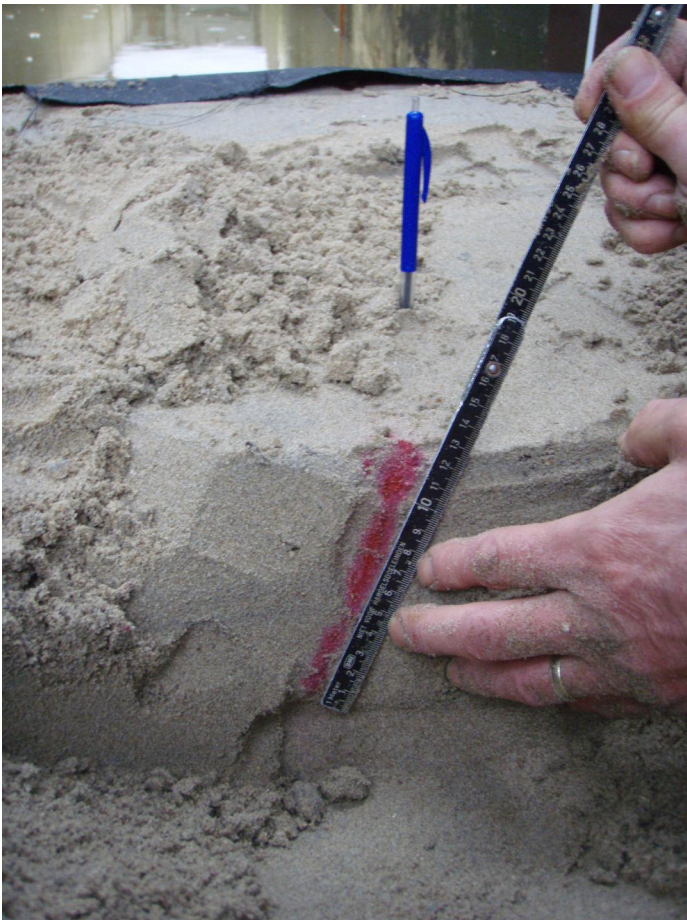


Photo 52: Color injection test series F3. Injection at line1, point 3





Photo 53: Color injection test series F4. Injection at line3, point 5



Photo 54: Color injection test series F4. Injection at line3, point 5





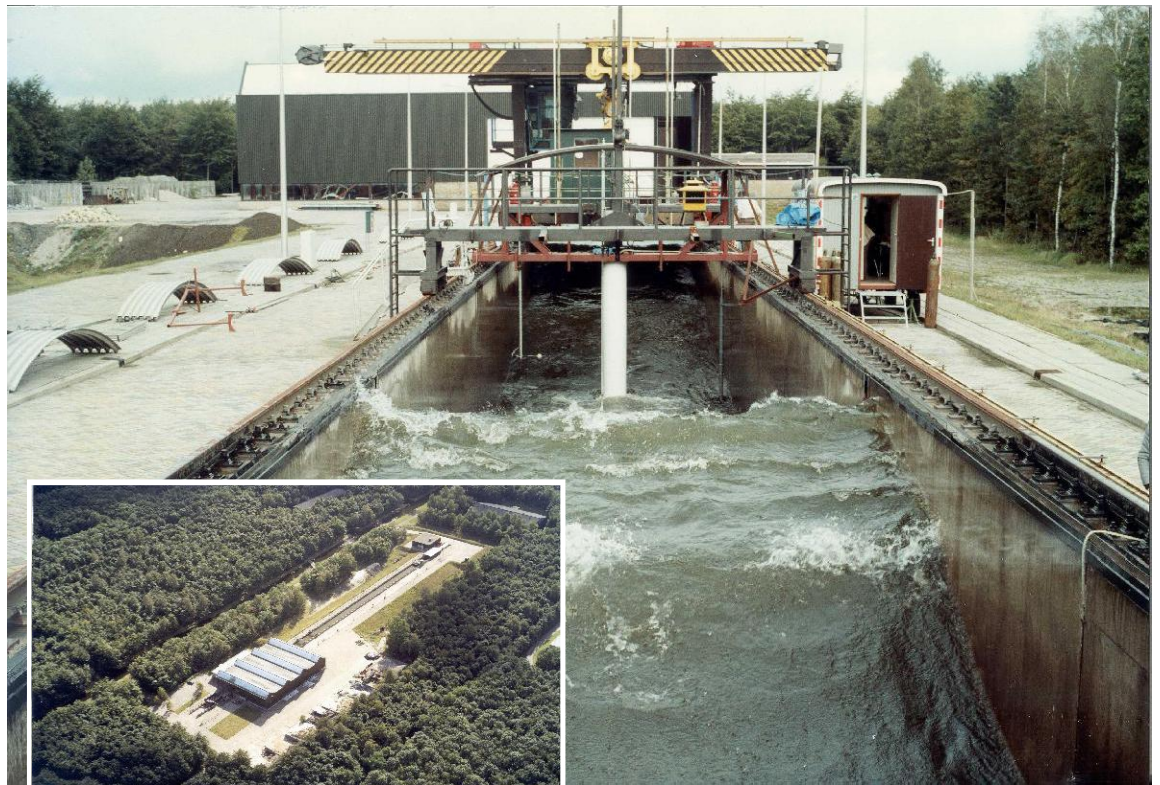
## **D Description Delta Flume**



## Delta flume

### introduction

The Delta flume is a wave flume which is unique because of its dimensions. The flume has a length of 240 m, a width of 5 m and a depth of 7 m (a deepened section of 9.5 m is also available). A flume with these dimensions allows for physical models on a scale which is near to prototype. This means that there are hardly any scale effects to take into account. The Delta flume is a state-of-the-art wave flume capable of generating both regular (periodic) and irregular (random) waves. The wave generator is equipped with online Active Reflection Compensation. This means that waves propagating towards the wave board are measured and that the wave board compensates for these reflected waves. In this way undesired waves do not re-reflect towards the structure and do not disturb the measurements. Also wave board control for random second-order waves is operational to compensate for spurious waves.



Measuring forces on a cylindrical structure in the Delta flume

Aerial photo of the Delta flume with on the left hand side the construction building and on the right hand side de the waveboard

### technical data

#### wave flume

Length: 240 m  
 Width: 5 m  
 Depth: 7 m

#### wave generator

Piston type (translatory) wave board  
 Full stroke: 5 m  
 Second-order wave steering system  
 Active re-reflection compensation  
 Installed electric power for wave generation: 800 kW

#### wave characteristics

Maximum height (regular): 2.5 m  
 Maximum sig. height (random) ( $H_s$ ): 1.6 m  
 Wave period: 1 - 12 s

#### features

Depth of deeper sections: 9.5 m  
 Wave-damping structures  
 Flexible water circulation system to fill or empty separate sections of the flume



## wave computation and processing software Delft-Auke/generate

The Delta flume is equipped with Deltares' second-order wave computation software Delft-Auke/generate which has been developed by Deltares. This software takes the second order effects of the first higher and first lower harmonics of the wave field into account in the wave board motion. It is designed to suppress spurious waves in order to generate a true-to-nature wave field in the flume with little laboratory side effects. The software is capable of generating regular waves as well as irregular waves according to well-known and user-defined spectral distributions.

Besides the reduction of the generation of spurious waves, it is very important to suppress the re-reflection of waves at the wave maker. To this end, the wave board is equipped with three wave gauges, which measure the wave height at the paddle. The wave gauge signals are used as input for the online active reflection compensation algorithm, which identifies any reflected waves and instantaneously compensates the wave board motion to absorb these waves.

## special features / possibilities

The size of the flume is a special feature in itself. The models are equally large which brings some construction problems along.

The models have to be constructed by using specialized equipment. A wide variety of special equipment is available on the Delta flume, including a large gantry crane. With this equipment it is for example possible to construct a model with a foreshore (both mobile and fixed) over the flume bottom.

Special equipment is also required for the measurements. This equipment is available on the Delta flume. Some 100 channels with instruments can be sampled in the standard configuration. If necessary more channels can be added.



Placement of antifer cubes in a breakwater model in the Delta flume



Model of a breakwater in the Delta flume



**projects**

Typical projects are hard to mention for the Delta flume. The size and available wave conditions make it possible to test almost every structure on a near-to-prototype scale. A few example projects are presented hereafter.

**breakwaters**

Several breakwaters have been tested in the Delta flume. See photographs for examples with tetrapods and antifer cubes. The stability of the armour layer and the overtopping discharge are typical measurements in such tests.



Typical breakwater model with tetrapods, measurements carried out: stability, overtopping discharge and overtopping events, waves

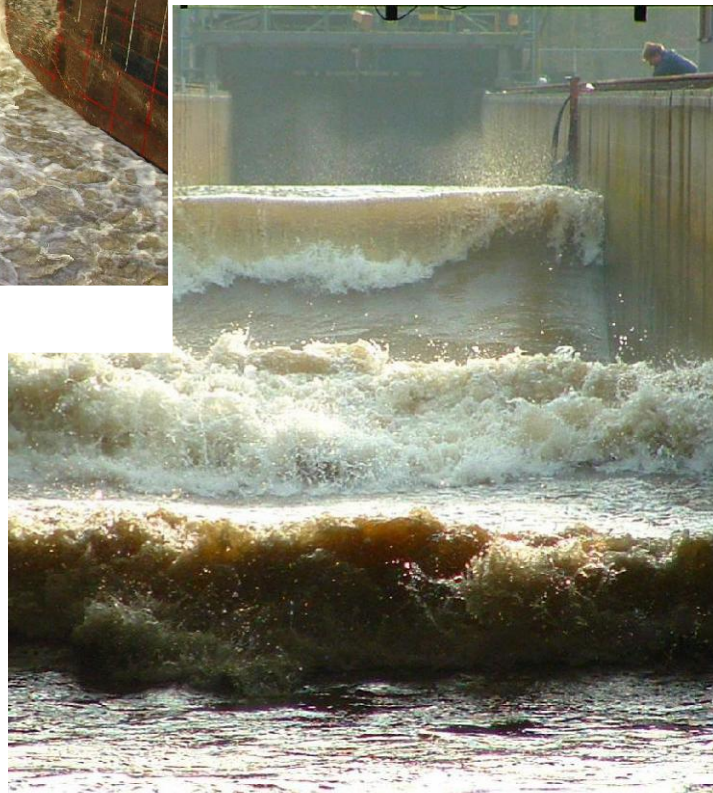


Wave impact during dune erosion test

**scour, bed protection**

Erosion of sediments is a phenomenon which is difficult to investigate on a smaller scale. Problems regarding grain size are difficult to solve in a small scale model. The Delta flume makes it possible to solve some of those problems because for instance the grain size can be one that is really found in nature.

An example of such a project is the dune erosion investigation which took place in 2005 and 2006. A cross shore profile was built at a scale of 1:6, for which a total volume of 3000m<sup>3</sup> sand was placed in the flume.



Series of waves during dune erosion tests



**placed block revetments**

A typically Dutch structure is a placed block revetment. With the help of the Delta flume the rules of thumb used until the flume went operational were replaced by a sound scientific argumentation. Recent investigations include grouted revetments which have been tested at a scale of 1:1.5.

**special projects**

The Delta flume is a versatile facility which can be put to use in numerous projects. Some have been mentioned before, but there are always special projects for which the flume can be useful. These projects range from testing underwater vehicles in combination with turbulent conditions to testing and calibrating field equipment.



Wave impact at a placed block revetment



Measurement of erosion resistance of grass on a dike



Determination of overtopping guidelines



Testing and calibrating a wave gauge

**Deltares**

Innovative solutions for water and subsurface issues.

Rotterdamseweg 185  
 P.O. Box 177  
 2600 MH Delft  
 The Netherlands  
 Telephone +31 15 285 85 85  
 Telefax +31 15 285 85 82  
 e-mail info@deltares.nl  
 internet www.deltares.nl

## E Analysis colour injections

To determine whether sand transport inside the geotextile tube occurs use has been made of colour injections. These colour injections with a needle of 20 cm length are applied before a test series was started. This injection 'labelled' the sand by giving the sand a red colour. After a test series the geotextile was removed and the location and length of the coloured sand was determined. This has been done for testseries F1, F3, F4 and T1.

### E.1 Theory

After a test series three characteristics of the sand injection have been determined. These are the deepest point of coloured sand below the geotextile ( $d_1$ ), the highest point below the geotextile ( $d_2$ ) and the relative distance between the needle insertion point in the geotextile and the highest point of coloured sand parallel to the geotextile ( $x$ ). These characteristics are shown in Figure E.1.

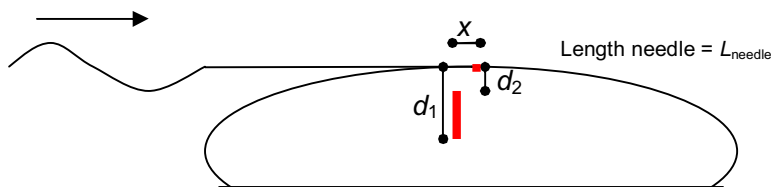


Figure E.1 Colour injection characteristics.

The amount of sand erosion can be determined when  $d_1$ ,  $d_2$  and  $L_{needle}$  are known. The following formula is used:

$$d_{erosion} = L_{needle} + d_2 - d_1 \quad (4.1)$$

Basically four scenarios can occur:

No sand movement at all

$$d_2 = 0, d_1 = L_{needle} \quad \rightarrow \quad d_{erosion} = 0$$

Sand is only disappearing from the location

$$d_2 = 0, d_1 < L_{needle} \quad \rightarrow \quad d_{erosion} = L_{needle} - d_1$$

Sand is added to the location

$$d_2 > 0, d_1 = L_{needle} + d_2 \quad \rightarrow \quad d_{accretion} = d_2$$

Combination of sand erosion and accretion

$$d_2 > 0, d_1 - d_2 < L_{needle} \quad \rightarrow \quad d_{erosion} = L_{needle} + d_2 - d_1$$

### E.2 Measurements and analysis of colour injections

Sand colour injections have been carried out for test series F1, F3, F4 and T1. For each test series the geotextile tube had several locations where injections were used. At every location three injections were applied. Not all parameters ( $d_1$ ,  $d_2$  and  $x$ ) were determined for every position since it was extremely time consuming to find the colour injections and the colored

path after the test series. The length of the needle was at every injection location  $L_{\text{needle}} = 20$  cm.

Sand colour measurements at testseries F4 can be found in Appendix A16a

Sand colour measurements at testseries F1 can be found in Appendix A16b

Sand colour measurements at testseries F3 can be found in Appendix A16c

Sand colour measurements at testseries T1 can be found in Appendix A16d

### **E.3 Conclusions**

The most interesting measurements with respect to sand movement are those performed after testseries F4 (high filling degree) and testseries F1 (low filling degree). At test series F4 (Appendix A15a) hardly any sand movement occurred. At test series F1 (Appendix A16b) sand erosion occurred at the top of the tube and sand accretion occurred at the landward side and the seaward side of the tube indicating a deformation of the tube due to sand movement within the tube.

## **F Specification Geolon PE 180 L**





PRODUCT GEGEVENS

# GEOLON<sup>®</sup>



## Geweven polyethyleen filter met lussen

		GEOLON <sup>®</sup> PE 180L	GEOLON <sup>®</sup> PE 525L	GEOLON <sup>®</sup> PE 1000L	STANDAARD
<b>CONSTRUCTIE</b>					
Constructietype		weefsel	weefsel	weefsel	
Garentype kettingrichting		monofil.	monofil.	monofil.	
Garentype inslagrichting		bandje	monofil.	monofil.	
Kleur		zwart	zwart	zwart	
<b>MECHANISCHE EIGENSCHAPPEN</b>					
<b>Kettingrichting:</b>					
Nominale treksterkte	kN/m	<b>40</b>	<b>40</b>	<b>37</b>	EN-ISO 10319
Rek bij nominale treksterkte	%	<b>24</b>	<b>25</b>	<b>32</b>	EN-ISO 10319
<b>Inslagrichting:</b>					
Nominale treksterkte	kN/m	<b>50</b>	<b>35</b>	<b>32</b>	EN-ISO 10319
Rek bij nominale treksterkte	%	<b>24</b>	<b>25</b>	<b>25</b>	EN-ISO 10319
<b>Statische doorpingssterkte (CBR):</b>					
Doorpingskracht	kN	<b>5</b>	<b>5</b>	<b>3,5</b>	EN-ISO 12236
Verplaatsing bij doorpings	mm	<b>50</b>	<b>50</b>	<b>45</b>	EN-ISO 12236
<b>Kegelvalproef</b>	mm	<b>9</b>	<b>12</b>	<b>12</b>	EN 918
Nominale treksterkte lussen	kN	<b>1,5</b>	<b>1,5</b>	<b>1,5</b>	Ten Cate Nicolon
<b>HYDRAULISCHE EN FILTER EIGENSCHAPPEN</b>					
<b>Waterdoorlatendheid</b>					
bij $\Delta h = 100$ mm	liter/m <sup>2</sup> s	<b>40</b>	<b>500</b>	<b>500</b>	NEN 5167
Waterkolom bij $v = 10$ mm/s	mm	<b>10</b>	<b>7</b>	<b>7</b>	NEN 5167
Permittiviteit $\Psi_s$	1/s	<b>1</b>	<b>1,5</b>	<b>1,5</b>	NEN 5167
Water permeability	m/s	<b>0,025</b>	<b>0,300</b>	<b>0,350</b>	EN-ISO 11058
Poriegrootte $O_{90}$	micron	<b>180</b>	<b>525</b>	<b>1000</b>	NEN 5168
Karakteristieke openingsmaat $O_{90}$	micron	<b>170</b>	<b>350</b>	<b>600</b>	EN-ISO 12956
<b>DUURZAAMHEID</b>					
<b>U.V.-bestendigheid:</b>					
Xenon test (50 MJ/m <sup>2</sup> )	U.T.S.	<b>&gt;90%</b>	<b>&gt;90%</b>	<b>&gt;90%</b>	ENV 12224
Classificatie	klasse	<b>D</b>	<b>D</b>	<b>D</b>	ISO 4892-2
Thermo-oxidatieve bestendigheid	klasse	<b>B</b>	<b>B</b>	<b>B</b>	NEN 5132
<b>FYSIEKE EIGENSCHAPPEN</b>					
Gewicht per eenheid (berekend)	g/m <sup>2</sup>	<b>250</b>	<b>195</b>	<b>200</b>	EN 965
Dikte (2kN/m <sup>2</sup> druk)	mm	<b>0,6</b>	<b>0,7</b>	<b>0,8</b>	EN 964-1
Lussenrooster	m	<b>0,5 x 0,5</b>	<b>0,5 x 0,5</b>	<b>1,0 x 0,5</b>	
Rollbreedte	m	<b>5,05</b>	<b>5,05</b>	<b>5,05</b>	
Rollengte	m	<b>200</b>	<b>200</b>	<b>200</b>	
Roldiameter	m	<b>0,45</b>	<b>0,36</b>	<b>0,36</b>	
Rolgewicht	kg	<b>265</b>	<b>210</b>	<b>215</b>	
Ten Cate Nicolon code		<b>392</b>	<b>373</b>	<b>447</b>	

De technische gegevens werden verkregen door interne en externe testprocedures.  
Bovengenoemde geotextielen kunnen geassembleerd worden tot geprefabriceerde panelen.

© GEOLON<sup>®</sup> is een geregistreerd handelsmerk van Ten Cate Nicolon bv  
© Copyright Ten Cate Nicolon bv, mei 2004. Eerdere uitgaven zijn niet meer geldig.  
Wijzigingen voorbehouden.



**Ten Cate Nicolon bv**  
Postbus 236, 7600 AE Almelo, Nederland - [www.tencate-nicolon.com](http://www.tencate-nicolon.com)  
Tel: +31 546 544811 Fax: +31 546 544490



## G Theoretical derivation stability number with respect to sliding

### G.1 Analytical model based on stability model of randomly placed rock mounds

#### G.1.1 Introduction

In this section it is assumed that the leakage length is smaller than the characteristic length of the external load or  $\lambda \ll L$ . This indicates that  $L$  determines the pressure gradients, leading to uprush and downflow velocities, which in turn cause forces on the individual element. Thus, the stability is governed by the local flow caused by the waves around the elements.

A more in-depth study to the stability of geotextile elements will be performed based on the theoretical approach of Iribarren (1938). In this approach Iribarren assumed that the length, width and height of a stone have the same dimensions. Iribarren's work will be reproduced in such a way that the length, width and height (thickness) of the element will be isolated. The hypothesis is that, based on this analysis, a new stability number will be created, which included both the thickness ( $D$ ) and the length ( $B$ ) of the geotextile element.

#### G.1.2 Definition of forces

A start is made by analysing the basic forces on an element. Reference is made to Figure G.1

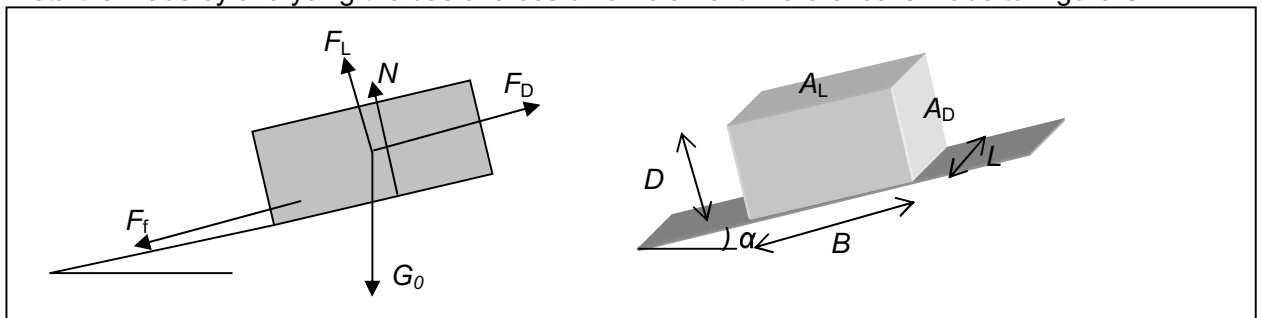


Figure G.1 Forces on an element

The hydrodynamic forces that act on the element are the drag force ( $F_D$ ) and the lift force ( $F_L$ ).

$$F_d = C_d \frac{1}{2} \rho_w u^2 A_D \quad (6.1)$$

$$F_L = C_L \frac{1}{2} \rho_w u^2 A_L \quad (6.2)$$

Where

$F_d$	=	drag force
$F_L$	=	lift force
$C_d$	=	drag force coefficient
$C_L$	=	lift force coefficient
$A_d$	=	(drag) surface of element
$A_L$	=	(lift) surface of element
$u$	=	velocity
$\rho_w$	=	density of the water

According to Pilarczyk (2000) the velocity in a breaking wave can be described by:

$$u = \varphi \sqrt{2gH} \quad (6.3)$$

Where  $g$  is the acceleration due to gravity,  $H$  is the wave height and  $\varphi$  is a coefficient which can vary between 1 and 1.5.

The surfaces of the element are given by:

$$A_D = D \cdot L \quad (6.4)$$

$$A_L = B \cdot L \quad (6.5)$$

Where  $D$  is the thickness or height,  $B$  is the width and  $L$  is the length of the element. Equation (6.1) and Equation (6.2) can now be rewritten:

$$F_d = C_d \rho_w \varphi^2 g H L D \quad (6.6)$$

$$F_L = C_L \rho_w \varphi^2 g H L B \quad (6.7)$$

The direction of the wave drag force  $F_d$  depends on the wave run-up or the wave run-down. Besides the drag and lift forces the following forces act on the element:

Friction forces:  $F_f = fN \quad (6.8)$

Normal forces:  $N = G_0 \cos \alpha \quad (6.9)$

Gravitational forces:  $G_0 = (\rho_s - \rho_w) g D B L \quad (6.10)$

Gravitation parallel to slope:  $G_{0\parallel} = G_0 \sin \alpha \quad (6.11)$

Where:

$F_f$	=	friction force
$f$	=	friction coefficient
$N$	=	acceleration due to gravity
$\alpha$	=	angle of slope
$G_0$	=	gravitational force
$g$	=	acceleration due to gravity
$\rho_s$	=	density of geotextile element

### G.1.3 Stability based on the drag force

Suppose that the lift force is negligible, thus  $F_L = 0$ :

Stability requires:

$$F_d < F_f + G_{0\parallel} \text{ for wave run-up} \quad (6.12)$$

$$F_d + G_{0\parallel} < F_f \text{ for wave run-down} \quad (6.13)$$

This can be rewritten in:

$$F_d < F_f \pm G_{0\parallel} \quad (6.14)$$

Combining the equations above gives:

$$C_d \rho_w \varphi^2 g H D L < f \cos \alpha (\rho_s - \rho_w) g D B L \pm \sin \alpha (\rho_s - \rho_w) g D B L \quad (6.15)$$

Rewriting gives:

$$\frac{H}{\Delta B} < \frac{f \cos \alpha \pm \sin \alpha}{C_d \varphi^2} \quad (6.16)$$

$$\text{With } \Delta = \frac{\rho_s - \rho_w}{\rho_w} \quad (6.17)$$

In case of no slope ( $\theta = 0$ ) the stability is:

$$\frac{H}{\Delta B} < \frac{f}{C_d \varphi^2} \quad (6.18)$$

This implicates that the stability is independent of the width,  $B$ , and the thickness,  $D$  of the geotextile element. The stability only depends on the slope angle,  $\theta$ , the friction coefficient  $f$  (between the element and its underground), the drag coefficient,  $C_D$  and the coefficient  $\varphi$ . However, one should realise that this is only valid if the lift forces are neglected.

#### G.1.4 Stability based on the drag and lift forces

The analysis presented above will be repeated but now the lift forces will be included:

Equation (6.8) is now rewritten as:

$$F_f = f(N - F_L) = f(\cos \alpha G_0 - F_L) \quad (6.19)$$

Applying Equation (6.14) gives :

$$C_D \rho_w \varphi^2 g H L D = f \left[ \cos \alpha (\rho_s - \rho_w) g D B L - C_L \rho_w \varphi^2 g H L B \right] \pm \sin \alpha (\rho_s - \rho_w) g D B L \quad (6.20)$$

Rewriting Equation (6.20) gives:

$$\frac{H}{\Delta} < \frac{B D}{\varphi^2 (C_D D + f C_L B)} (f \cos \alpha \pm \sin \alpha) \quad (6.21)$$

Or:

$$\frac{H}{\Delta \sqrt{B D}} < \frac{\sqrt{B D}}{\varphi^2 (C_D D + f C_L B)} (f \cos \alpha \pm \sin \alpha) \quad (6.22)$$

The use of separate length characteristics ( $B, D$ ) of a geotextile element has the consequence that it is not possible to express the stability number in a dimensionless parameter such as

$\frac{H}{\Delta D}$ ,  $\frac{H}{\Delta B}$  or  $\frac{H}{\Delta\sqrt{BD}}$  since the length and thickness is still in the right side of Equation (6.22).

However, for several elements the ratio between  $B$  and  $D$  are known. A shape factor is introduced:

$$\lambda = \frac{B}{D} \tag{6.23}$$

### G.1.5 Concluding stability formula

Using Equation (6.23), Equation (6.22) can now be rewritten:

$$\frac{H}{\Delta\sqrt{BD}} < \frac{\sqrt{\lambda}}{\phi^2(C_D + fC_L\lambda)} (f \cos \alpha \pm \sin \alpha) \tag{6.24}$$

| drag lift slope correction ('+':run-up, '-': run-down)  
Wave-velocity coefficient

Stability parameter

in which

$H$	=	characteristic wave height	(m)
$\Delta$	=	relative density	(-)
$B$	=	Width of element	(m)
$D$	=	thickness of element	(m)
$\lambda$	=	ratio between B and D, $\lambda = \frac{B}{D}$	(-)
$\phi$	=	wave-velocity coefficient (1~1.5)	(-)
$C_D$	=	drag force coefficient	(-)
$C_L$	=	lift force coefficient	(-)
$f$	=	friction coefficient	(-)
$\alpha$	=	slope angle	(°)

## G.2 Application of theoretical stability formula

### G.2.1 Introduction

Equation (6.24) can be rewritten for situation where drag or lift forces are not present or where no slope is applied. In some cases the ratio between the length and thickness ( $\alpha$ ) can be eliminated resulting in different stability numbers. Results are shown in Table G.1.



Table G.1 Overview stability formula for drag and lift forces with and without a slope

	no slope	slope
drag and lift	$\frac{H}{\Delta\sqrt{BD}} < \frac{\sqrt{\lambda}}{\phi^2(C_D + fC_L\lambda)}$	$\frac{H}{\Delta\sqrt{BD}} < \frac{\sqrt{\lambda}}{\phi^2(C_D + fC_L\lambda)}(f \cos \alpha \pm \sin \alpha)$
only drag ( $C_L = 0$ )	$\frac{H}{\Delta B} < \frac{f}{\phi^2 C_D}$	$\frac{H}{\Delta B} < \frac{1}{\phi^2 C_D}(f \cos \alpha \pm \sin \alpha)$
only lift ( $C_d = 0$ )	$\frac{H}{\Delta D} < \frac{1}{\phi^2 C_L}$	$\frac{H}{\Delta D} < \frac{1}{f\phi^2 C_L}(f \cos \alpha \pm \sin \alpha)$

Whether failure occurs due to drag, lift or a combination of drag and lift should be determined. A start is made by assuming that for tubes with a high filling rate the drag is dominating and that at a low filling rate the lift is dominating. This is visualized in Figure G.2.

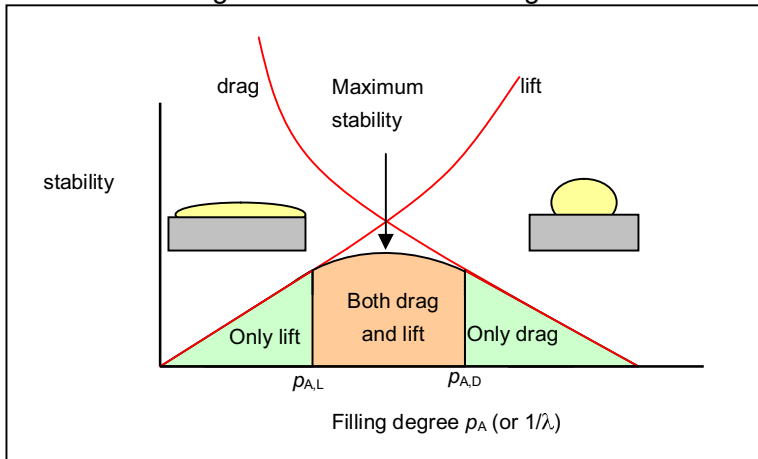


Figure G.2 Relevance of lift and drag

According to the above described model, lift can be denied for higher filling percentages and drag can be denied for lower filling percentages. The main question that raises is what the filling percentage values are at which lift or drag can be ignored (respectively  $p_{A,L}$  and  $p_{A,D}$ ).

G.2.2 Description of relevant parameters

It can be seen that for every situation given in Table G.1 different parameters influence the stability of the elements. An overview of these parameters is given in Table G.2.

Table G.2 Overview of parameters that influence the stability of an element under wave attack

	no slope	slope
drag and lift	friction coefficient ( $f$ ) thickness ( $D$ ), width ( $B$ ) drag ( $C_D$ ), lift ( $C_L$ )	friction coefficient ( $f$ ), slope angle ( $\alpha$ ) thickness ( $D$ ), width ( $B$ ) drag ( $C_D$ ), lift ( $C_L$ )
only drag ( $C_L = 0$ )	friction coefficient ( $f$ ) width ( $B$ ) drag ( $C_D$ )	friction coefficient ( $f$ ), slope angle ( $\alpha$ ) width ( $B$ ) drag ( $C_D$ )
only lift ( $C_d = 0$ )	thickness ( $D$ ) lift ( $C_L$ )	friction coefficient ( $f$ ), slope angle ( $\alpha$ ) thickness ( $D$ ) lift ( $C_L$ )

To determine the stability of a geotextile element in a theoretical way with the use of Equation (6.24), one should determine the following parameters:

*Friction coefficient,  $f$*

The friction coefficient between the element and its foundation layer can be determined by performing friction tests such as described in Appendix H.

*Ratio between length and thickness of element ( $\alpha$ )*

For several elements the ratio between  $B$  and  $D$  ( $\lambda$ ) is known:

Geotextile containers:  $B \approx 5D$  (Recio, 2008) (6.25)

Geotextile tubes:  $D \approx (1 - \sqrt{1 - p_A})D_{100\%}$  (CUR,2004) (6.26)

$$B = D + 0.5\pi(D_{100\%} - D) \quad (\text{CUR, 2004}) \quad (6.27)$$

Where  $p$  is the filling percentage and  $D_{100\%}$  is the diameter at 100% filling. Combining the given equations gives:

$$B = \left( 1 - 0.5\pi + \frac{1}{1 - \sqrt{1 - p_A}} \right) D \quad (6.28)$$

Rewriting gives:

$$\lambda = \frac{B}{D} = \left( 1 - 0.5\pi + \frac{1}{1 - \sqrt{1 - p_A}} \right) \quad (6.29)$$

Filling percentage of 80 %:  $p_A = 0.8 \rightarrow \lambda \approx 1.2$

Filling percentage of 60 %:  $p_A = 0.6 \rightarrow \lambda \approx 2.2$

An overview is given in Table G.3.

Table G.3 Overview of length-thickness ratio for several types of geotextile elements

Type of geotextile element	$\lambda$
Geotextile container	5
Geotextile tube (60% filling)	2.2
Geotextile tube (80% filling)	1.2
Geotextile bag	variable

*Slope angle,  $\alpha$*

The angle of the slope is known for each situation.

*Coefficient for velocity in breaking waves,  $\varphi$*

Pylarczyk (2000, section 5.5.3.1) uses a value between 1 and 1.5 for  $\varphi$ .

*Drag force coefficient,  $C_D$  and lift force coefficient  $C_L$*

The drag force coefficient  $C_D$  and the lift force coefficient should be determined for each type of geotextile element. Recio (2008) performed a literature study to find these coefficients but concluded that the available results were not appropriate to assess the drag and lift coefficients. Therefore, he performed systematic laboratory experiments for this purpose. This

is only done for geotextile containers in various set-ups. In a typical set-up of geotextile containers (a pile of geotextile containers with the crest container around the still water line) Recio found a drag coefficient of  $C_D = 4\sim 15$  and a lift coefficient of  $0.3\sim 1.2$ . These values are only given here to give an indication. However, for the various test set-ups, Recio found different values for these coefficients. This illustrates the main problem of the theoretical derived stability formulae against sliding.

### G.3 Comparison of analytical model and practical application

The above described theoretical approach is usually not applied for engineering purposes since the uncertainties in the several parameters is far too high (especially the drag and lift coefficient). For practical reasons the theoretical derived formula's are translated into a more simple formula with a 'dustbin coefficient'. This coefficient is based on extensive physical model tests. The most applied stability formulae are those of Hudson and Iribarren:

$$\text{Hudson} \quad \frac{H}{\Delta D} < \sqrt[3]{K_D \cot \alpha} \quad \text{or} \quad \frac{H_s}{\Delta D} < \frac{\sqrt[3]{K_D \cot \alpha}}{1.27} \quad (6.30)$$

The Hudson formula is applicable for slopes not steeper than 1:1 and not gentler than 1:4. The damage level is fixed, namely 0-5 per cent of the armour units displaced in the region of primary wave attack. Usually a  $K_D$  value of 1 is used for structures with an impermeable core and a  $K_D$  value of 4 is used for structures with a permeable core.

$$\text{Iribarren} \quad \frac{H}{\Delta D} < (f \cos \alpha \pm \sin \alpha) N^{-1/3} \quad (6.31)$$

The coefficients  $K_D$  and  $N$  are waste bins for all kind of unknown variables and unaccounted irregularities in the model investigations. The theoretical derived expression in this report is:

$$\text{Theoretical} \quad \frac{H}{\Delta \sqrt{BD}} < \frac{\sqrt{\lambda}}{\varphi^2 (C_D + f C_L \lambda)} (f \cos \alpha \pm \sin \alpha) \quad (6.32)$$

$$\text{Theoretical (only drag)} \quad \frac{H}{\Delta B} < \frac{1}{\varphi^2 C_D} (f \cos \alpha \pm \sin \alpha) \quad (6.33)$$

Similarities between the several approaches are clearly visible. The applied expression in CUR (2004) is

$$\text{Application (CUR,2004)} \quad \frac{H_s}{\Delta_t D_k} \leq F \quad (6.34)$$

With  $D_k = D$  when are tubes perpendicular to wave attack.

#### G.3.1 Suggested stability parameter

It can be seen that Equation (6.34) is a very rough approximation. The use of the parameter  $D_k$  (characteristic thickness) is very questionable since the width of the geotextile element might also play an important role. (In case of only drag forces, the thickness of the elements has no influence at all!) Therefore it is suggested to use the stability number as defined in Equation (6.24).

$$\text{Suggested new stability number} \quad \frac{H}{\Delta \sqrt{BD}} \quad (6.35)$$



## H Determination of friction coefficient

### H.1 Introduction

To determine the friction coefficient of the geotextile which has been used in the large scale experiments some small scale experiments have been performed which are described in this appendix. The theory of friction, the experiments and results are discussed.

### H.2 Theory of friction

The friction of several components is tested by placing an element on a slope which is increased by lifting the slope. At a certain moment the element starts to slide indicating that there is no balance between the friction force and gravitation or:

$$G_{\parallel} = F_f \quad (7.1)$$

Reference is made to Figure H.1.

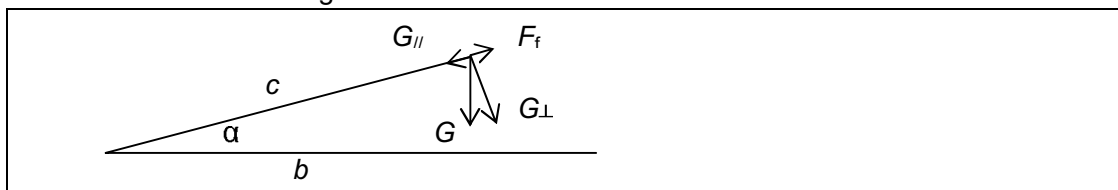


Figure H.1 Forces on an element placed on a slope

The gravitational force parallel to the slope is described by:

$$G_{\parallel} = G \sin \alpha \quad (7.2)$$

The friction force is described by:

$$F_f = f G_{\perp} \quad (7.3)$$

In which  $f$  is the friction coefficient between the element and the slope

And

$$G_{\perp} = G \cos \alpha \quad (7.4)$$

Combining Equations (7.1) until (7.4) gives the following relationship:

$$f = \tan \alpha \quad (7.5)$$

This implicates that, if the slope angle at which the element starts to slide is known, the static friction coefficient can be determined.

### H.3 Small scale experiments to determine the friction coefficient

Several small scale experiments have been performed to determine the friction coefficient between the geotextile (Geolon<sup>®</sup> PE180) and concrete and geotextile-geotextile. An impression of the experiments is given in Figure H.2

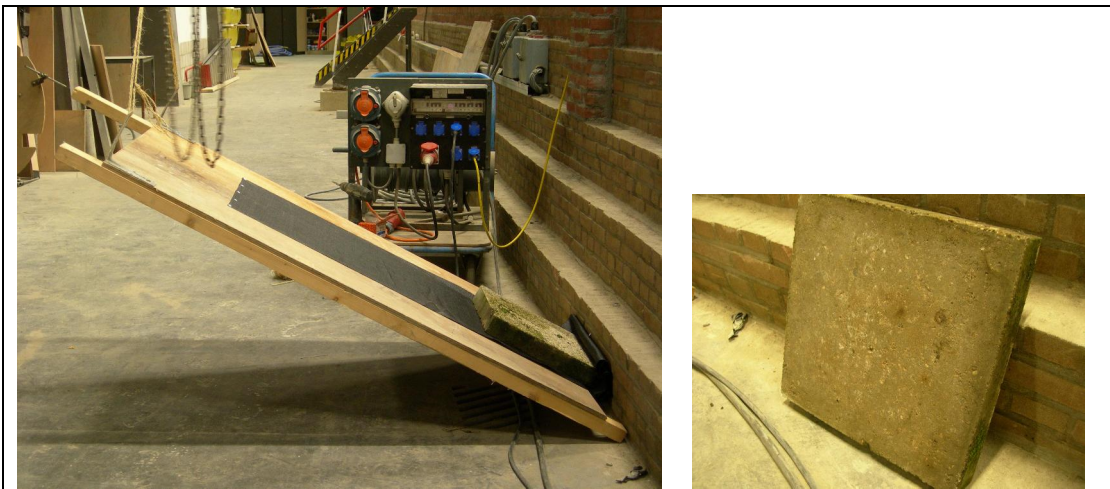


Figure H.2 Impression of small scale model tests to determine friction coefficients

Variations in the tests are the direction of the geotextile (in a particular direction the geotextile 'feels' a little rougher) and the use of a wet or dry geotextile. Each test is performed with a concrete tile of 0.40 m x 0.40 m x 0.063 m with a weight of approximately 23 kg. The surface of the concrete was smooth. (see also Figure H.2) After each test the length of the slope ( $c$ ) and the length of the projection to the floor ( $b$ ) has been measured. Based on these data, the slope angle  $\alpha$  and the friction coefficient are determined and shown in Table H.1.

Table H.1 Overview results small scale tests friction coefficient

Test	element surface	Geotextile on slope	b (m)	c (m)	slope $\alpha$ ( $^\circ$ )	friction coefficient $f$ (-)
1	geotextile (dry, smooth)	dry, smooth	1.744	1.815	16.1	0.29
2	geotextile (dry, rough)	dry, smooth	1.745	1.815	16.0	0.29
3	geotextile (dry, rough)	dry, rough	1.669	1.815	23.1	0.43
4	geotextile (wet, rough)	wet, rough	1.638	1.815	25.5	0.48
5	geotextile (wet, smooth)	wet, smooth	1.690	1.815	21.4	0.39
6	concrete	dry, smooth	1.590	1.815	28.8	0.55
7	concrete	wet, rough	1.553	1.815	31.2	0.61

## I Transmission coefficient and Energy losses

### I.1 Introduction

It is assumed that all the incoming wave energy ( $E_i$ ) is transferred into:

- 1 Dissipated wave energy on substructure ( $E_{ss}$ )
- 2 Dissipated wave energy on geotextile tube ( $E_{tube}$ )
- 3 Transmitted energy ( $E_t$ )

The dissipated wave energy on the geotextile tube leads to forces on this tube. This is shown in Figure I.1.

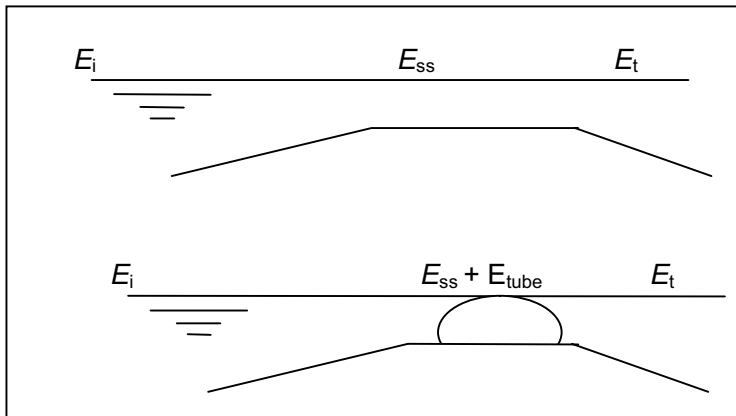


Figure I.1 Definition of energy

### I.2 Formula to determine ratio between effective and incoming wave height

The main interest is the ratio between the effective wave height on the tube and the incoming wave height:

$$\chi = \frac{H_{s,tube}}{H_{s,i}} = \sqrt{\frac{E_{tube}}{E_i}} \quad (8.1)$$

Where:

$\chi$	=	ratio between effective wave height on the tube and incoming wave height (-)
$H_{s,tube}$	=	dissipated energy on tube given as wave height (m)
$H_{s,i}$	=	incoming wave height (m)

This factor  $\chi$  can be used to adapt the significant wave height in the dimensionless parameter as described in Appendix G.

The effective wave energy on the tube is determined by comparing a situation where no tube is applied and a situation where a tube is applied.

The following relations based on energy balance are applied (see also Figure I.1):

$$\text{With tube} \quad E_i = E_{ss} + E_{tube} + E_{t,ss+tube} \quad (8.2)$$



$$\text{Without tube} \quad E_i = E_{ss} + E_{t,ss} \quad (8.3)$$

Combining Equation (8.2) and (8.3) gives:

$$E_{tube} = E_{t,ss} - E_{t,ss+tube} \quad (8.4)$$

With

$$E_{t,ss} = C_{t,ss}^2 E_i \quad \text{and} \quad E_{t,ss+tube} = C_{t,ss+tube}^2 E_i \quad (8.5)$$

Equation (8.4) is now rewritten:

$$E_{tube} = C_{t,ss}^2 E_i - C_{t,ss+tube}^2 E_i \quad (8.6)$$

Combining equation (8.6) and equation (8.1) gives:

$$\chi = \sqrt{C_{t,ss}^2 - C_{t,ss+tube}^2} \quad (8.7)$$

CIRIA, CUR, CETMEF (2007) uses several prediction methods relating the relative crest freeboard  $R_c/H_s$  to the coefficient of transmission  $C_t$ . A simplified method is summarized in Equation (8.8), Equation (8.9) and Equation (8.10):

$$-2.00 < \frac{R_c}{H_s} < -1.13 \quad : \quad C_t = 0.8 \quad (8.8)$$

$$-1.13 < \frac{R_c}{H_s} < 1.2 \quad : \quad C_t = 0.46 - 0.3 \frac{R_c}{H_s} \quad (8.9)$$

$$-1.2 < \frac{R_c}{H_s} < 2.0 \quad : \quad C_t = 0.1 \quad (8.10)$$

For a smooth low-crested structure a formula has been developed within the DELOS project (van der Meer *et al*, 2004):

$$C_t = \left( -0.3 \frac{R_c}{H_s} + 0.75(1 - e^{-0.5\xi_p}) \right) \cos^{2/3} \beta \quad (8.11)$$

With minimum and maximum values of  $C_t = 0.075$  and  $0.8$  respectively.

Where  $\beta$  is the wave angle and  $\xi_p$  is the breaker parameter.

Since the above described parameters are known, it is now possible to determine the ratio between the effective wave height on the tube and the incident wave height,  $\chi$ .

### 1.3 Graphic presentation of reduction parameter $\chi$

Applying Equation (8.7) requires some calculation to determine the reduction parameter  $\chi$ , which makes it difficult to use for a 'quick' calculation. Therefore a graphical application has been derived which is described below.

Equation (8.11) is rewritten as

$$C_t = a \frac{R_c}{H_s} + b \quad (8.12)$$

With

$$a = -0.3 \cos^{2/3} \beta \quad (8.13)$$

And

$$b = 0.75(1 - e^{-0.5\xi_p}) \cos^{2/3} \beta \quad (8.14)$$

Equation (8.7) is rewritten as

$$\chi = \sqrt{C_{t,1}^2 - C_{t,2}^2} \quad (8.15)$$

(8.12) in (8.15) gives:

$$\chi = \sqrt{\left(R_{c,1}^2 - R_{c,2}^2\right) \frac{a^2}{H_s^2} + \left(R_{c,1} - R_{c,2}\right) \frac{2ab}{H_s}} \quad (8.16)$$

The following is assumed:

- The waterlevel is equal to the highest point of the tube:  $R_{c,1} = -D$  (8.17)

- $R_{c,2} = 0$  (8.18)

(8.17) and (8.18) in (8.16) gives:

$$\chi = \sqrt{a^2 \left(\frac{D}{H_s}\right)^2 - 2ab \left(\frac{D}{H_s}\right)} = f\left(a, \frac{D}{H_s}, b\right) \quad (8.19)$$

$$a = f(\beta) \quad (8.20)$$

$$b = f(\xi_p, \beta) \quad (8.21)$$

The following condition is assumed:

Perpendicular wave attack:  $\beta = 0$  (8.22)

#### 1.4 Restrictions for applying the graph

Equation (8.11) is restricted for the following condition:

$$0.075 < C_t < 0.8 \quad (8.23)$$

This influences  $C_{t,1}$  (wave transmission when no tube is applied)

$$C_{t,1} < 0.8 \quad (8.24)$$

Applying Equation (8.12) and (8.17) gives

$$a \frac{-D}{H_s} + b < 0.8 \quad (8.25)$$

Rewriting gives:

$$\frac{H_s}{D} > \frac{-a}{0.8-b} \quad (8.26)$$

According to CIRIA, CUR, CETMEF (2007) a transmission coefficient of  $C_t = 0.8$  should be chosen if Equation (8.26) is not fulfilled. This results in values for the wave reduction parameter  $\chi$  such as given in Table I.1.

Table I.1 Value of  $\chi$  below a threshold value of  $H_s/D$

$\xi_p$	$H_s/D \leq$	$\chi$
1	0.59	0.74
2	0.92	0.65
3	1.38	0.55

The design graph for conditions where  $\beta = 0^\circ$  (perpendicular wave attack) is shown in Figure I.2. This graph is based on Equation (8.19) and Table I.1.

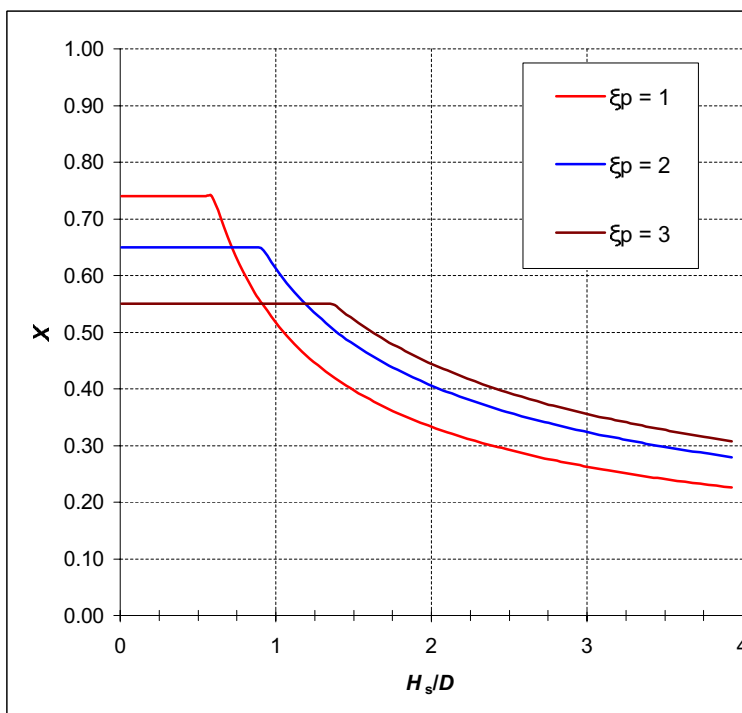


Figure I.2 Design graph for determining  $\chi$